MICROWAVE RADAR TECHNIQUES AND DEDICATED SIGNAL PROCESSING FOR VITAL SIGNS MEASUREMENT

DOCTORAL THESIS

PRESENTED FOR THE DEGREE OF DOCTOR OF PHILOSOPHY IN

ELECTRONICS MICROELECTRONICS NANOELECTRONICS MICROWAVE

DOCTORAL SCHOOL

ENGINEERING AND SYSTEMS SCIENCE (ENGSYS)
UNIVERSITY OF LILLE

By

FATIMA SEKAK

DEFENDED ON 14 DECEMBER 2021

THESIS COMMITTEE:

Aziz BENLARBI DELAI	Prof.at Sorbonne University	Reviewer
Christophe LOYEZ	Research Director at IEMN-IRCICA	Examiner
Fouzia BOUKOUR	Research Director at University Gustave Eiffel	Thesis director
Kamel HADDADI	Asst. Prof at University of Lille	Thesis director
Madjid HADDAD	R& I Manager at SEGULA Engineering	Invited
Maria-Gabriella DI BENEDETTO	Prof. Sapienza University of Rome	Reviewer
Raja ELASSALI	Prof. ENSA Marrakech	Examiner

Techniques radars hyperfréquence et traitement de signal associé pour la mesure de signes vitaux

Thèse pour obtenir le grade de docteur

de l'université de Lille en

ÉLECTRONIQUE MICROÉLECTRONIQUE
NANOÉLECTRONIQUE MICRO-ONDES

Ecole Doctorale

Ecole doctorale Science de l'ingénierie et des systèmes (ENGSYS)

Université de Lille

Présentée par

Fatima SEKAK

le 14 décembre 2021

Comité de thèse:

Aziz BENLARBI DELAI	Professeur à l'université de Sorbonne	Président du jury
Christophe LOYEZ	Chargé de Recherche à IRCICA	Examinateur
Fouzia BOUKOUR	Directrice de recherche à l'université Gustave Eiffel	Directrice de thèse
Kamel HADDADI	Maître de conférences à IEMN-IRCICA	Directeur de thèse
Madjid HADDAD	Responsable R&I SEGULA Engineering	Invité
Maria-Gabriella DI BENEDETTO	Professeur à l'université Sapienza de Rome	Rapporteure
Raja ELASSALI	Professeur à l'ENSA de Marrakech	Examinatrice

To my late grandmother

You will always be loved...

To the one who taught me to dream big and to break the glass ceiling. She always tell me: do what you say you will do, do it right, and do it with excellence. When you don't do something the right way just own it.

She played a big role in my whole life. She was never just "my grandmother", but my guardian, my friend and my inspiration. His spirit and strength lives in me and in all who have been touched by the love, strength, conviction, wisdom and beauty of his soul.

You taught me more than I ever knew. You gave me reason to continue the fight, saying a better day comes after the night.

Abstract

In the context of securing transportation systems, short-range monitoring of people's activity, in particular the driver's activity in a vehicle, is a major issue in the improvement of the driver assistance system. The application targeted concerns mainly the railway domain. Respiratory and heart rates of the driver are key indicators for the evaluation of the physiological state. Conventional methods of measuring these vital signs rely on sensors operating in direct contact with the skin. Therefore, the intrusive character of these solutions is not suited for the transportation domain, especially because of the induced discomfort and sometimes the driver needs to move freely in his environment.

A microwave radar solution operating at low power is proposed for the continuous measurement of respiratory and cardiac activity signals deducted from the mechanical movement of the rib cage. These vital signs are indicators of human activity that can be detected at a distance using radiated microwave electromagnetic waves. Signal processing based on developing the cyclic features of the reflected signal using the first, second and third order of the cyclostationary approach, is implemented in order to extract the parameters of the breathing and the heartbeat frequencies. The proposed hardware solutions are given a comprehensive guide setting for better estimation of the breathing and heartbeat rates.

Key words: Cyclostationary approach, Cyclic cumulant, cyclic moment,high order statistics, Radar, monitoring vital signs, heart rate, respiration rate, movement of the chest.

Résumé

Dans le cadre de la sécurisation des systèmes de transport, la surveillance à courte distance de l'activité des personnes, en particulier de l'activité du conducteur dans un véhicule, est un enjeu majeur dans l'amélioration du système d'aide à la conduite. L'application visée concerne principalement le domaine ferroviaire. Les rythmes respiratoire et cardiaque du conducteur sont des indicateurs clés pour l'évaluation de l'état physiologique. Les méthodes classiques de mesure de ces signes vitaux reposent sur des capteurs fonctionnant en contact direct avec la peau. Par conséquent, le caractère intrusif de ces solutions n'est pas adapté au domaine du transport, notamment à cause de l'inconfort induit et parfois le conducteur a besoin de se déplacer librement dans son environnement.

Une solution de radar hyperfréquence fonctionnant à faible puissance est proposée pour la mesure en continu des signaux d'activité respiratoire et cardiaque déduits du mouvement mécanique de la cage thoracique. Ces signes vitaux sont des indicateurs de l'activité humaine qui peuvent être détectés à distance à l'aide d'ondes électromagnétiques à micro-ondes rayonnées. Un traitement du signal basé sur le développement des caractéristiques cycliques du signal réfléchi à l'aide du premier, deuxième et troisième ordre de l'approche cyclostationnaire, est mis en œuvre afin d'extraire les paramètres de la respiration et les fréquences cardiaques. Les solutions matérielles proposées bénéficient d'un réglage de guide complet pour une meilleure estimation des fréquences respiratoires et cardiaques.

Mots clés: Approche cyclostationnaire, cumulant cyclique, moment cyclique, statistiques d'ordre supérieure, radar, surveillance des signes vitaux, fréquence cardiaque, fréquence respiratoire, mouvement de la cage thoracique.

Contents

List of Figures

List of Tables

Acronym List

AWGN	Additive White Gaussian Noise
BPF	BandPass Filter
BPM	Beats Per Minute
BW	BandWidth
CPM	Cycles Per Minute
CW	Continuous-Wave
CWT	Continuous Wavelet Transform
DUT	Device Under Test
ECG	ElectroCardioGram
EM	ElectroMagnetic
EMR	ElectroMagnetic Radiation
FCC	Federal Communications Commission
FFT	Fast Fourier Transform
FMWC	Frequency-Modulated Continuous Wave
HFSS	High Frequency electromagnetic Simulation Software
HR	Heart Rate
ICNIRP	International Commission on Non-Ionizing Radiation Protection
IF	Intermediate Frequency
BPF	Bandpass Filter
IFBW	Intermediate Frequency BandWidth
IPI	Inter-Pulse Interval
IR-UWB	Impulse Radio Ultra-Wideband
ISM	Industrial Scientific and Medical
MRI	Magnetic Resonance Imaging
PRF	Pulse Repetition Frequency
RADAR	RAdio Detection And Ranging
RCS	Radar Cross Section
RF	Radio Frequency
RR	Respiration Rate
SAR	Specific Absorption Rate

SFCW	Stepped-Frequency Continuous Wave
S-parameters	Scattering parameters
TOCM	Third-Order Cyclic-Moment
UWB	Ultra-Wideband
VNA	Vector Network Analyze
VSWR	Voltage Standing Wave Ratio

Introduction

Vital signs can be thought of as the black box containing the person's state of health. Respiratory Rate (RR) and Heart Rate (HR) are classified as the most important vital signs indicators. Subtle changes in those physiological signals are linked to physical or physiological stress responses that may be associated with critical conditions.

The reliability and capacity to remotely detect vital signs particularly useful in situations where direct contact with the subject is impossible, uncomfortable or undesirable. It is desirable to avoid problems such as skin irritation, restriction of breathing, and contact with electrodes in a number of healthcare applications, including monitoring of geriatrics, person with compromised skin and sleep monitoring, and situations where individuals need to move between the measurement without any restrictions of electrodes, leads or cuffs.

Alternative devices should be non-invasive, non-contact, more comfortable, cost effective and accurate. These characteristics are most important in case of infants, burnt victims,etc. All of the reasons mentioned above have seen an increase in research in this area. Due to the microwave sensitivity toward small movements,non-contact and noninvasive continuous monitoring radar has been pointed out as one of the most promising technologies which have been suggested in recent years for monitoring of human cardiopulmonary activity. Radar monitoring provides a method to determine the heart and respiration rates of a subjects without any contact and through clothing.

In the context of securing transportation systems, short-range monitoring of people's activity, in particular the driver's activity in a vehicle, is a major issue in the improvement of the driver assistance system. The application targeted in this work concerns mainly the railway domain. Respiratory and heart rates of the driver are key indicators for the evaluation of the physiological state. Conventional methods of measuring these vital signs rely on sensors operating in direct contact with the skin. Therefore, the intrusive character of these solutions is not suited for the transportation domain, especially because of the induced discomfort and sometimes the driver needs to move freely in his environment.

In this work, a microwave radar solution operating at low power is proposed for the continuous measurement of respiratory and cardiac activity signals. In particular, physiological signals (heartbeat,breathing and mechanical movement of the rib cage) are indicators of human activity that can be detected at a distance using radiated microwave electromagnetic waves.

Although the literature shows a growing interest in the development of radar techniques dedicated to the surveillance of people, there is no robust, sensitive and accurate commercial device available to date. Several radar technologies are presented in the literature for the vital signs extraction. Depending on the radar system hardware and the type of signal used.

Radar based on the RF system was used to detect the heart and respiration rates, this radar presented the obvious choice to perform this study as it allows to test several configurations, provides a wide range of several parameters that can be changed very easily like the frequency, the the Intermediate Frequency Band Width, the input power,etc. One of the most important features of radar monitoring of heart and respiration motion is the choice of operating frequency. In this thesis we will use three ISM frequencies 2, 10 and 17 GHz. the instrumentation for its frequencies is also accessible, the equipment present in our laboratory can only cover this frequency range. A detailed analysis of the electrical and geometrical parameters of the radar technique is proposed in this work in order to identify the sources of uncertainties, to define the optimal parameters, to validate experimentally the proposed solution.

The extraction of vital signs becomes even more difficult in the presence of other parameters related to the application such as the random movement of people, or the presence of other types of disturbances (noise, attenuation, clutter,etc). In order to accurately estimate the heart and respiration rate from the signal reflected from the displacement of the chest, various signal processing methods have been proposed in the literature. A study on the part of the associated signal processing made it possible to highlight the various reliable techniques for detecting and identifying radar signals. An original signal processing, based on developing the cyclic features of the reflected signal using the first, second and third order of the cyclostationary approach, is implemented in order to extract the parameters of interest in reference or disturbed measurement environments. The proposed hardware solutions associated with an optimal signal processing allow to foresee radar architectures adapted to non-laboratory contingencies and given a comprehensive guide to settings for better estimation of the breathing and heartbeat rates.

Chapter 1

General context of the thesis

1.1 Introduction

Recently, the measurement of non-contact vital signals has attracted a great deal of research interest. This research concerns the measurement of basic body functions several fields of application. These measurements are taken to help assess the general physical health of a person, to give clues to possible illnesses, and to show progress towards recovery. We can cite, for example, the detection of people under the rubble following earthquakes, or the measurement of heartbeats at a distance for people for whom traditional electrocardiographs are not indicated. Due to the high sensitivity of microwaves to small movements, Doppler radar has been used as a non-contact and non-intrusive monitoring system for cardiopulmonary activity.

Measuring heart and respiratory rates using Doppler Radar is a non-contact, non-obstructive way to remotely monitor vital signs at depth. The modulated reflected radar signal in the presence of high noise and interference is non-stationary with hidden periodicities, which cannot be detected by ordinary Fourier analysis [89].

The aim of this thesis is to be able to propose a reliable solution to measure without contact the heartbeat and breathing of a person inside his house. This is of great interest to the elderly, burnt people or babies. Thus, monitoring their cardiac activity remotely allows them to live their own lives normally. This thesis presents a comparative study in the detection of heartbeat signals, considering different frequencies and emission powers. This makes it possible to specify the optimum operating frequency, which gives a compromise between the complexity of the measurement system, the precision as well as the minimum power emitted. In addition, a comparative study between several signal processing methods is proposed in order to extract the best method which makes it possible to measure the cardiac signal and consequently to extract its parameters.

1.2 Scientific problematic and motivation

The growth of signal processing techniques and the development of different architectures of good and precise systems for the detection of vital signs, has contributed significantly in the establishment of diagnostics and prevention to give good treatments and rapid therapies. and appropriate for person under tests.

There are several contact medical devices available to monitor people's vital signs, such as an ECG [87], stethoscope, oximeter, or phonocardiogram. These devices are often annoying and unpleasant for daily and long term use. People tend not to like wearing or charging them. We can cite, for example, the detection of people under the rubble following earthquakes [13], or the measurement of heartbeats at a distance for people for whom traditional electrocardiographs are not indicated. person under tests whose conditions may be disturbed or worsened by contact sensors include newborns, infants at risk for Sudden Infant Death Syndrome [50], adults with sleep disorders [90], and burns; Most alternatives to standard heart and respiratory monitors require contact and generally precise control or placement, which may be impossible or undesirable in many situations [89].

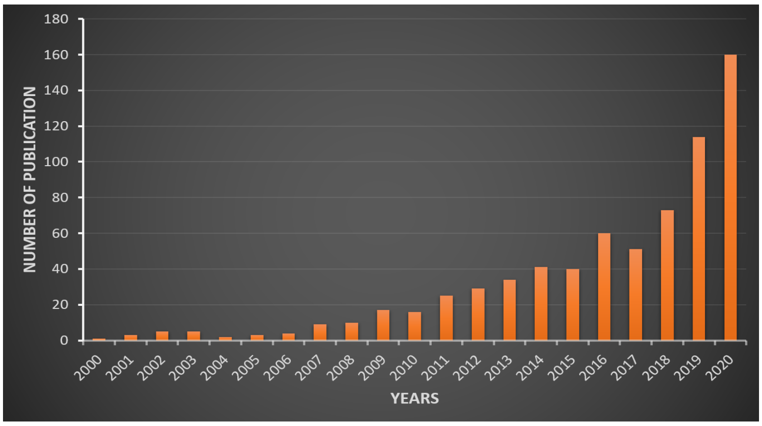

Figure 1.1: Evolution of publication over a years [IEEE : Vital signs radar]

A non-contact heart and respiratory rate monitor could provide vital signs monitoring without attached electrodes for these person under tests. Additionally, a non-contact sensor could be used in several situations where individuals need to move between measuring stations without restriction of electrodes, wires or cuffs; a vital signs monitor capable of detecting the absence of contact and through clothing would be ideal in these situations. Non-contact detection and monitoring of human cardiopulmonary activity through clothing and bedding could also be a valuable tool for sleep monitoring and home health care applications.

Radar is the acronym for RAdio Detection And Ranging translated as "radio detection and telemetry". The radar system was created in the late 1930s, and was instrumental in the Battle of Britain during the Second World War. Radar technologies are used in the civilian sectors for a large number of applications, such as automotive, marine navigation, domestic applications, transport, consumer applications (control badges, identity or tickets), medical diagnoses (MRI: Magnetic Resonance Imaging) and therapies (physiotherapy, hyperthermia, etc.). The use of radiofrequency waves in healthcare is a relatively recent phenomenon (early 1980s) [53] but very competitive. The development of radar for monitoring vital signs such as respiration and heart rate has attracted much attention in recent years, and is a proven issue for this application due to the high sensitivity of microwaves to small movements (chest millimeter movement)[89]. Doppler radar has been used as a non-contact monitoring system for cardiopulmonary activity .

In the context of securing transport systems, the short-distance monitoring of the activity of people, in particular the driver in a vehicle, is a major challenge to improve the driver assistance system. Currently the train driver must signal that he is awake by operating a small lever on a regular basis. When this repetitive gesture is not accomplished, the train comes to a stop on the track and the control center is notified. This causes considerable delays, and therefore a significant financial loss. In addition, the repetitive gesture of activating the lever is a hardship factor which must be reduced or even eliminated for the well-being of the railway workers. Also, this driver's watch system does not allow control of his vigilance.

A solution based on Doppler radar for real-time monitoring and detection of periodic movement, such as mechanical vibration and physiological movements [37] [100], was proposed. The radar-based approach features non-invasiveness, non-contact detection, continuous operation, low cost and low power consumption. This solution is proposed in this report for the control of the driver vigilance. The ISM band is used because it is unlicensed band intended for low data rate communications often used for this type of application.

1.3 Benefits of non contact vital signs monitoring

There are several contact medical devices available for monitoring vital signs of people. Otherwise, the noninvasive and non-contact detection and estimation of vital signs, such as heart beat and respiration are a powerful tool. It is useful in situations where direct contact with the subject is either undesirable or impossible. These devices are often inconvenient and unpleasant for daily and long-term use. It can be used for different applications in different fields, such as the burn person under tests where the use of traditional electrodes to measure heartbeat is not an option, infants, monitoring of person under tests with irritated skin, monitoring of sleep apnea, as well the detection of survivors on rubble, home monitoring of the elderly, rhythm monitoring for athletes or for car and train drivers [49].

Various levels of details can be obtained by measuring the breathing and the heart rates. Firstly, the data can be used to verify that the subject under test is alive so the subject is breathing and that the heart is beating. Respiratory rate and pattern are indicators of respiratory physiology, whereas an irregular pulse rate can indicate cardiac abnormality. The shapes or the range of the heart and respiration signatures could potentially be used as an additional diagnostic tool; for example respiratory effort could be measured through the amount of motion [49] [21].

1.4 Objectives

The estimation of non-contact vital signs is based on the detection of phase-shift modulation induced by small mechanic movements of the chest which is of the order of a millimeter, the presence of environmental noises and random body movements are difficult challenges to get precise results. The use of radar concept associated to signal processing techniques aim to improve detection sensitivity, reduce noise and increase detection range. The state of the art is quite rich concerning the hardware part of the radar [100] [8] [6].

Nevertheless, a parametric study of the system remains necessary for each given application. The main difficulty remains on the choice of the optimal input parameters which make it possible to receive the precise signal comprising the useful information. A parametric study is conducted to determine the best parameters for accurate operation of radar for monitoring vital signs. This study considered the impact of several parameters like, the operating frequency, the input power, the distance separating the person under test and the RF system, the electric parameters;etc. Associated signal process-

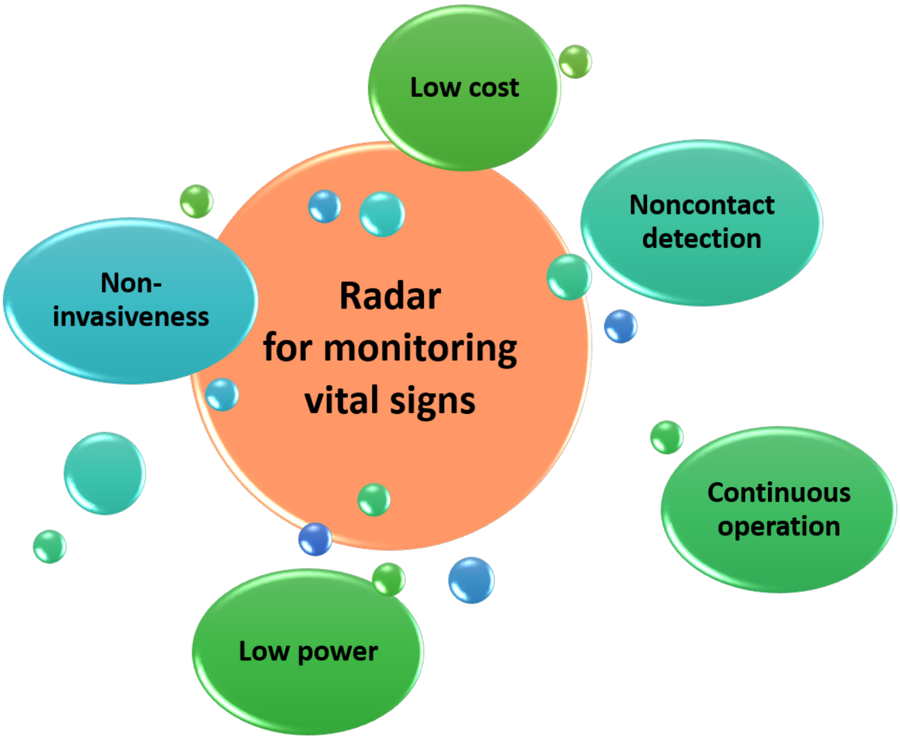

Figure 1.2: Radar for monitoring vital signs objectives

ing technique was developed in order to extract the vital signs (breathing and heartbeat). However, the harmonics (combination of frequencies) of the breath mixing with the frequencies of the heartbeat. It is currently almost impossible to separate these two signals with a classic filter because of the pseudo-periodicity of the two rhythms.

Indeed, the reflected radar signal is modulated by the displacement of the thorax, and the choice to use a signal processing algorithm based on the cyclostationary approach, makes it possible to extract the cardiac and respiratory frequencies from the reflected signal which is contaminated by various noises, body movement artifacts and shifting continuously and without demodulating. Cyclostationary theory is one of the most powerful tools for analyzing signals with a hidden cyclic statistical pattern. This theory mainly uses cyclic statistics to detect and estimate the cyclic components of signals. It is commonly used in the analysis of communication signals and the estimation of micro-movements. The challenge with this approach is to develop the theoretical part then the simulations and the application on the real measurements.

1.5 Challenges

The most significant challenges in completing the project were:

- Developing novel ideas for original research
- Vector Network analyzer programming.
- Measuring results from all devices (Airflow and ECG reference sensors) and VNA simultaneously for comparison.
- Statistical analysis including the development of the first, second and third order cyclic moment and cyclic cumulant.
- Find out the effect of several parameters, like frequency, power, polarization, body position, distance between antenna and the person's chest.
- Analyze and validation of the results obtained using the proposed algorithm with the simulations, then with the measurements.
- Verify accuracy of the cyclostationary approach with reference system.

1.6 Organization of the thesis

This thesis is divided into five chapters. In the chapter 2, after a brief description of vital signals and the constraints of existing technologies for monitoring them, the advantages of non-invasive and contactless detection are presented. This chapter also describes radar technologies for the detection of cardio-respiratory signals. Moreover, its cover the CW radar theory and comparison of different topology of radar architectures. The reasons justifying the choice of using the Vector Network Analyzer (VNA) as a continuous radar for monitoring vital signs is presented.

In the chapter 3, the state of the art of the different techniques in signal processing to estimate and extract the heart and respiration rate was described. Then, we have chosen to carry out simulations of an existing method based on demodulation and ellipse adjustment to separate the respiratory and cardiac frequencies.As well as we present the theory of the cyclostationary approach proposed in this work, for the detection of vital signs. Furthermore, we explore the assessment of second and third orders cyclostationary signal processing performance by developing the cyclic features of each order. A comprehensive simulations study was undertaken to investigate and evaluate the impact of different parameters (noise, distance, frequency,etc) on the cyclic features of the reflected signal.

Chapter 4 on free space calibration for microwave radar vital signs. Heterodyne CW radar built up with reference measurement instrument is used to accurately identify sources of errors.The aim of this chapter is to carry out a study that will allow us to optimize the measurement bench before starting the first application measurements. Several parameters influence the signal of interest, which reflects the mechanical displacement of the rib cage in millimeter order. A detailed analysis of the electrical and geometrical parameters of the radar technique is proposed in this work in order to identify the sources of uncertainties, to define the optimal parameters, to validate experimentally the proposed solution.

Chapter 5 investigate the effect of the parameters of the measurement environment like the polarization of the emitted and received antennas, the distance between the subject under test and the radar and different scenarios with several sides of the subject. As well as the study of the internal parameters of the VNA like the input power, the Intermediate Frequency Bandwidth (IFBW), the operating frequency and the number of samples of the emitted signal. A study involving . The algorithm proposed based on the cyclostationary algorithm was applied on the results of the measurements. The results was compared to a reference system to validate the performances of the algorithm.

At the end there are conclusions and suggestions for future work.

Chapter 2

State of the art on techniques for characterizing vital signs

2.1 Introduction

In the topic of improving the driver assistance system and the working conditions of train drivers while increasing the safety and reliability of rail traffic, the short-distance monitoring of driver activity in a vehicle is a major challenge. The non contact detection of vital signs (DESIS) project aims to predict general physical health of a driver's condition: lack of attention, stress, fatigue, insomnia, sleepiness, etc, and to develop alternative solutions for controlling driver vigilance. These parameters altering the driver's vigilance are directly linked to physiological signals such as heart rate and breathing rate. These vital signs are recorded in all person under tests regularly in both clinical and emergency situations, and changes in their values can be an early warning sign of a changing physiological condition. Therefore, each driver has a unique and different value of this signs and the normal ranges of a person's vital signs vary with age, weight, gender, and overall health.

This section describes the location and anatomy of the heart and the chest, the electrical and mechanical events that cause contraction and respiration, the motion of the heart and the chest during contraction, and how that motions affects chest wall motion. Then, vital signs and their usual monitoring techniques are presented.

The evaluation of cardiopulmonary functions is most often performed with contact sensors when direct access to the subject is available. Non-contact physiological monitoring can have a significant impact beyond healthcare applications, particularly in situations where direct subject access is not available or difficult. Our goal in this thesis is to determine the heart and the breathing rates concentrated in the chest, where the lungs and heart are located, but also include the abdomen. The small mechanical movements of the rib cage, caused by the breathing and the heart beats will be measuring using radar.

The principle of the radar for monitoring vital signs, is based on the detection of the mechanical movements that occur due to periodic physiological events, including heart and respiration rates. Currently available techniques for measuring heart and respiratory rates are discussed in this chapter, including commonly used clinical measurements, alternative measurements, and measurements of cardiac and respiratory movement by movement on the surface of the skin. The radar measurement of these movements is examined and compared to other methods of measuring heart and respiratory rates.

2.2 Elements of physiology

2.2.1 Heart motion:Anatomy and physiology of the heart

The heart is located in the chest between the lungs behind the sternum and above the diaphragm, an overall view is given in Figure 2.1. It is surrounded by the pericardium. Its size is about that of a fist, and its weight is about 250-300 g. Its center is located about 5 cm to the left of the midsagittal plane. Located above the heart are the great vessels: the superior and inferior vena cava, the pulmonary artery and vein, as well as the aorta [58].

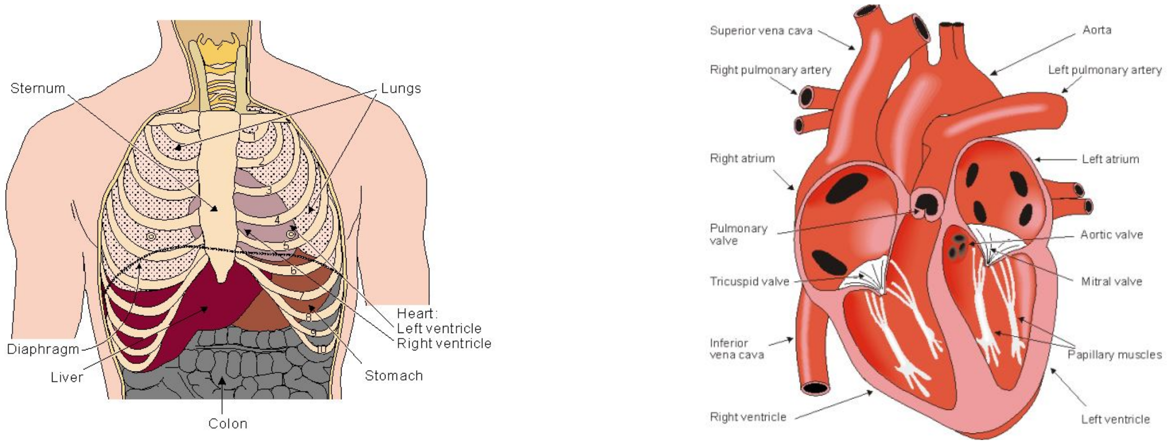

(a) (b)

Figure 2.1: (**a**) Location of the heart in the thorax; (**b**) Anatomy of the Heart

The heart is a muscular organ in the middle of the chest, which pumps blood containing oxygen and nutrients around the body through the blood vessels of the circulatory system Figure 2.1.
The heart rate is measures the number of times per minute that the heart contracts or beats. The speed of the heartbeat varies as a result of physical activity, threats to safety, and emotional responses. It is not only the speed of the heart rate that is important. The rhythm of the heartbeat is also crucial, because an irregular heartbeat can be a sign of a serious health problem. The resting heart rate refers to the heart rate when a person is relaxed. The normal resting heart rate is called the sinus rhythm.

According to a clinical study described in the article [93], the results produced extremes of 51 and 95 beats/min for women and 46 and 93 beats/min for men [93].

The heart rate is lower during sleep with rates around 40-50 bpm is common and is considered normal and it increases as a result of physical activity, so an athlete's heart rate at rest can be lower than 50 bpm[105].

2.2.2 Abnormal heart rhythms

- **Tachycardia:** a sinus rhythm of higher than 100 bpm is called sinus tachycardia. It occurs most often as a physiological response to physical exercise or psychical stress, but may also result from congestive heart failure.
- **Bradycardia:** is a pulse rate less than 50 bpm. The heart rate may be slow (less than the arbitrarily defined lower limit of 50 bpm) for one of two reasons: The atria are slow—atrial bradycardia; or there is a block in conduction between the atria and ventricles—atrioventricular or AV block.

2.2.3 The electrical activity of the heart

The electrocardiogram (ECG) is the electrical manifestation of the contractile activity of the heart, and can be recorded with surface electrodes on the limbs or chest. The rhythm of the heart in terms of beats per minute (bpm) may be easily estimated by counting the readily identifiable waves [108]. An ECG trace shows a series of waves that each has a name.It starts with a P wave, which initiates the cycle, continues with the QRS interval and completes with the T wave. The normal electrocardiogram is illustrated in Figure 2.2. The figure also includes definitions for various segments and intervals in the ECG.

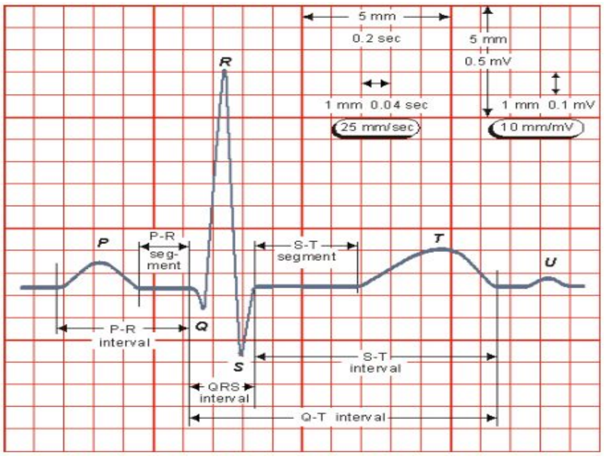

Figure 2.2: Schematic of normal electrocardiogram signal [67]

The sequence of events and waves in a cardiac cycle is as follows [67]:

- **P-wave**: a small low-voltage deflection caused by the depolarisation of the atria prior to atrial contraction. Due to the slow contraction of the atria and their small size, it is a slow, low-amplitude wave.The P wave should not exceed 2.5 mm (0.25 mv) in height and 0.11 second in width.
- **Q-wave:** It is the first negative deflection from the baseline after the P wave, but preceding an upward deflection. Normally, the Q wave reflects ventricular septal depolarization, and its duration does not exceed 0.03 second, and its depth generally does not exceed 3 mm.
- **R-wave:** It is the first positive deflection after the P wave, reflecting depolarization of the ventricular mass.The height of the R wave generally does not exceed 20 to 25 mm.
- **P-R interval**: The stimulation then reaches the atrioventricular node. There, the stimulation is blocked to allow the filling of the ventricles. The PR interval is normally 0.12–0.20 seconds [3].
- **QRS complex**: the largest-amplitude portion of the ECG, caused by currents generated when the ventricles depolarise prior to their contraction. The duration of the QRS complex measures between 0.06 and 0.10 second.
- **T-wave**: ventricular repolarisation.
- **P-Q interval**: the time interval between the beginning of the P wave and the beginning of the QRS complex.

- **Q-T interval**: characterises ventricular repolarisation.

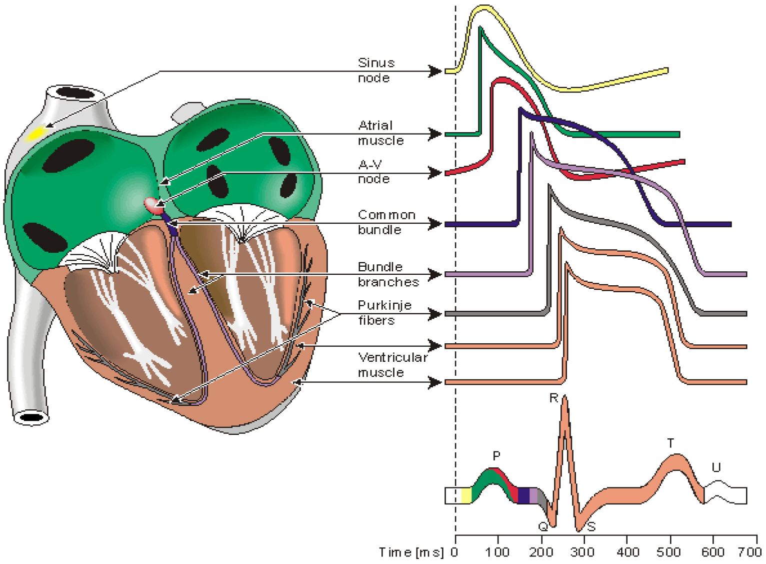

Figure 2.3: Electrophysiology of the heart showing all the waveforms [58]

2.2.4 Respiratory motion

When breathing, muscles contract to generate changes in chest volume, which create pressure differences between the chest and the external environment. Figure 2.4 shows the location of the muscles associated with respiration, the lungs, and the ribs.

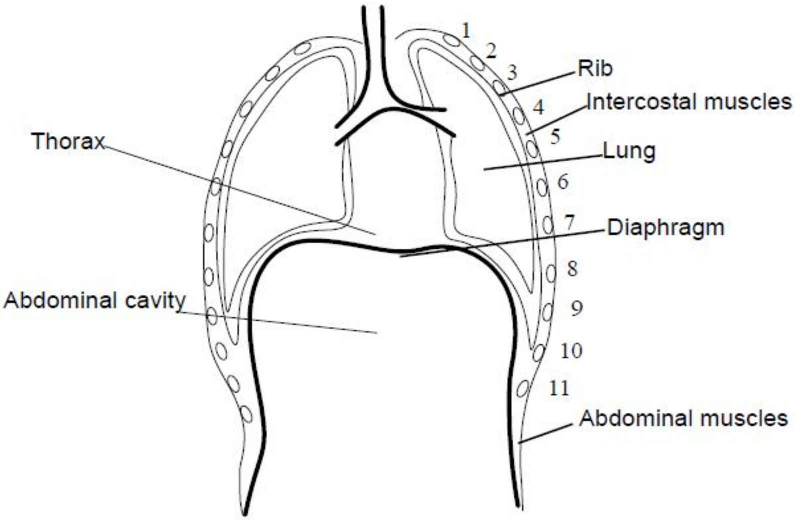

Figure 2.4: The thoracic wall and body cavities [71]

Breathing is the increase of alveolar pressure created by inspiration, where the thorax expands by the movement of the rib cage equally and bilaterally upwards and towards by the external intercostal muscles. The respiratory rate is the number of breaths for one minute through counting how many times the chest rises, is defined as one breath to each movement of air in and out of the lungs, expressed in cycles per minute (cpm)(1 Cycles Per Minute = 0.0167 Hertz). It is measured while the clinician is holding the person under test's wrist and ostensibly measuring the pulse, primarily because the respiratory rate may change if attention is drawn to it. This practice seems reasonable because the respiratory rate is the only vital sign under voluntary control, which mean that the respiration rates may increase with fever, illness, or other medical conditions [61]. The ideal length of time to take a respiratory rate measurement continues to be 1 minute In general, the respiratory rate for an adult sits between 10 (0.16 Hz) and 20 (0.33 Hz) breaths per minute , but there will be some variation depending on age and medical condition [83] [12]. Children have a higher respiratory rate than adults. During slow sleep, the respiratory rate decreases.

2.2.5 Abnormal respiratory rate

Respiratory rate can help identify deterioration in the person under test, assess response to treatment, and identify when a person under test needs care. It is accepted that a respiratory rate of above 25 breaths per minute or an increasing respiratory rate can indicate that a person under test could be deteriorating. A reduction in respiratory rate to 8 or fewer breaths per minute is also indicative of person under test deterioration.

TACHYPNEA Definitions of tachypnea vary, but the most reasonable one, based on the normal range and clinical studies, is accelerated respiratory rate 25 breaths/min or more.

BRADYPNEA Bradypnea is defined as slowed respiratory rate less than 8 breaths/min and it can happen during sleep or when you're awake. It is not the same thing as apnea, which is when breathing completely stops.

2.2.6 Chest movement due to breathing and heartbeat

Depolarization of the heart triggers atrial and ventricular contractions. This depolarization and polarization form a cycle of contractions. These contractions are responsible for cardiac displacement and movement of the ribs and tissue near the heart. In particular, the ribs and tissues move due to changes in the shape and volume of the heart. These movements also move the chest. The phase-shift variations due to the limits of the chest displacement caused by heart-beatings is about 0.2 mm to 0.5 mm [69].

As the diaphragm contracts, its dome descends into the abdominal cavity, causing the thorax to elongate and increase in volume, and pushing the abdominal viscera out against the compliant abdominal wall. In normal inspiration the diaphragm extends 1-2 cm into the abdominal cavity. In deep inspiration the diaphragm can descend as much as 10 cm [71]. During the breathing also, the contraction of the muscles generates changes in the volume of the chest and arises from pressure differences between the chest and the external environment. These muscles include the intercostal muscles (the muscles between the ribs), the muscles of the neck, the muscles of the abdomen and the diaphragm which is the most important muscle and which separates the abdomen and the thoracic cavity,Vibrations of the thorax and abdomen cause large displacements on the surface of the skin. The chest motion, caused by respiration, varies from 4 mm to 12 mm [69].

2.3 Interaction of radio-frequency waves with human body

In this section, we summarize the main laws that govern the interaction of electromagnetic radiation with matter. Electromagnetic radiation (EMR) is energy that propagates through free space (air) at the speed of light or through material in the form of an advancing interaction between electric and magnetic fields. It can make itself manifest by its interaction with matter. When electromagnetic radiation hits a target, some wavelengths are absorbed while others are reflected by the object. A portion of the energy can possibly be transmitted through the object if it is more or less transparent, with a change in the direction of the propagation due to refraction, Figure 2.6 below. The part of the radiation that is absorbed changes the internal energy of the object and produces heat that will be re-emitted as radiation at a longer wavelength. The total incident energy will interact with the surface according to one or the other of these modes of interaction or according to their combination. The proportion of each interaction will depend on the wavelength of the energy, as well as the nature and conditions of the surface [56].

- **Absorption** occurs when radiation energy is absorbed by the target.
- **Transmission** when radiation energy passes through the target.
- **Reflection** the electromagnetic waves are reflected if they encounter a

material with a different dielectric constant.

The human body can be modelled as a multi-layer structure, in which each layer corresponds to a specific tissue, as depicted in Figure 2.5 [75].Despite RF waves in low frequency conditions being able to penetrate the human tissue, the major quantity of detected energy on the radar is coming from the reflection of radiation in air/ skin boundary surface.

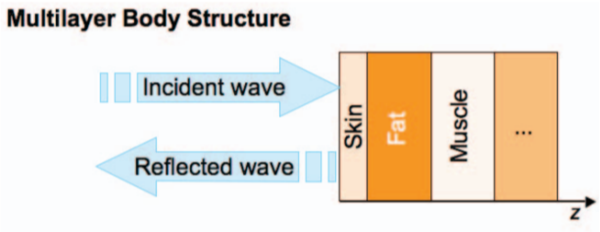

Figure 2.5: Multilayered model structure of the body [75]

The electrical properties of the biological tissue affect how much of the signal is reflected and transmitted, both at the skin–air interface and at interfaces between different tissues within the body. Of the radiation that enters the body, the electrical properties determine how much of it is attenuated per unit distance, how much is transmitted to the next layer, and how much is reflected back toward the skin surface.

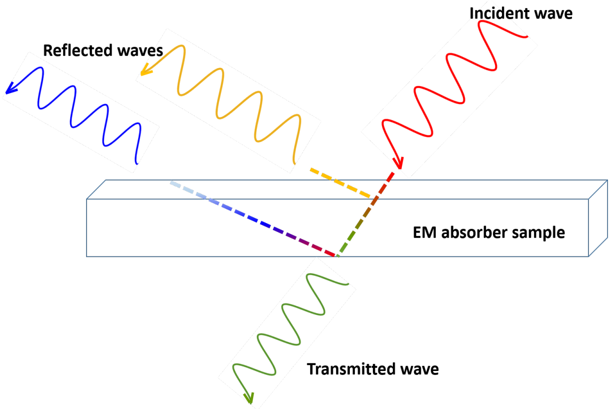

Figure 2.6: Concept of electromagnetic (EM) absorption, reflection, and transmission

Therefore, the analysis of physical effects beyond the interaction of radio waves with human targets is very important for a better understanding of the information from cardiovascular radar data. Radio-frequency waves present advantages but also a risk for the individual, due to uncontrolled emissions. In general, the increase in power leads to an increase in the signal-to-noise ratio, hence the increase in precision. But the health of the person can be affected. It is therefore necessary to reduce the emitted power in order to reduce the radiated energy to which the individual under test is exposed during the measurements. These limits related to the operated frequency. The exposure limits recommended by recognized health organizations are established in such a way as to prevent the harmful effects of radio-frequencies on health and offer equivalent protection [24].

In order to quantify the energy absorbed by a person's body, a parameter is taken into consideration which is Specific Absorption Rate (SAR). SAR represent the amount of power absorbed per unit mass, and it is expressed in Watt per Kilogram. It has the advantage of allowing a comparison of the exposure of near-field and far-field sources. The amount of radiation absorbed depends on the characteristics of the incident field (frequency, intensity, polarization, etc.), the characteristics of the exposed body (size, external geometry and dielectric properties of the tissues), grounding effects and reflections by objects located near the body of the exposed person (Non-Ionizing Radiation Protection, 1998). The SAR can be calculated for the whole body, a part of the body, a particular organ or for an arbitrary volume [31].

Many commission and organisms limit and set the radiation exposure for the health of the human body, like International commission on Non-Ionizing Radiation Protection (ICNIRP) and U.S Federal Communications Commission (FCC) [24]. A safety factor of 10 was then incorporated to arrive at the final recommended protection guidelines. The occupationally exposed population consists of adults who are generally exposed under known conditions and are trained to be aware of potential risk and to take appropriate precautions. By contrast, the general public comprises individuals of all ages and of varying health status, and may include particularly susceptible groups or individuals.

However, the SAR (Specific Absorption Rate) is the magnitude set by researchers to quantify and limit energy dissipation in living matter [5]. It is defined by 2.1:

$$SAR = \frac{\sigma E^2}{\rho} \tag{2.1}$$

where σ is the electrical conductivity of body tissue in S / m, ρ is the density of body tissue in kg/m^3 and E is the peak value of the electric field in V / m. There are two types of SAR: Whole body averaged SAR characterizes thermal effects, and Local SAR is used to assess and limit excessive potency in small parts of the body resulting from special exposure conditions.

A study [7] of the propagation of electromagnetic waves in human tissues proves that half of the incident energy is reflected at the surface of the skin and the other half propagates in the tissues, but is attenuated in each layer by the reflection 2.7. Hence, for our application, the majority of the power received at the receiving antenna is the power reflected at the surface of the moving person's chest. The penetration of waves inside human tissues decreases at higher frequencies (greater than 10 GHz, the penetration does not exceed 3 mm) [7]. Therefore, power density (S) is the appropriate magnitude used for microwave frequencies when the depth of penetration into the body is low. It is the quotient of the incident radiated power perpendicular to a surface by the area of this surface. It is expressed in Watts per m^2 (W / m^2).

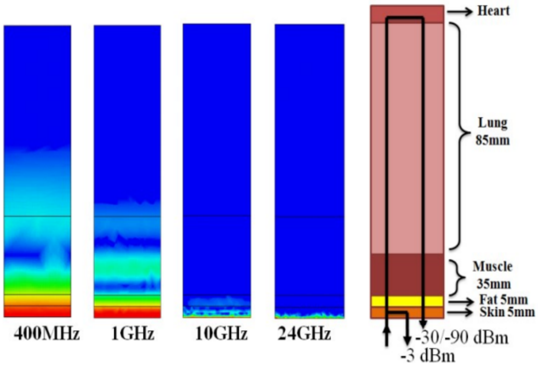

Figure 2.7: Propagation of electromagnetic waves in human tissues for various carrier frequencies (Simulation with HFSS) [7]

Over the entire near field area, the power density is given by[7]:

$$S = \frac{16\eta P}{\pi D^2} \tag{2.2}$$

where η is the efficiency of the antenna, P is the power of the transmitter (W), and D is the diameter of the antenna (m).

While, in the far-field area, the wave front incident on the rib cage of the person under test, from the emission radar, then exhibits a planar wave structure. Likewise, upon reception, the electromagnetic field diffracted from the patient's chest and received at the antenna satisfies the conditions for plane wave radiation. The power density in this area is given by[7]:

$$S = \frac{GP}{4\pi D} \tag{2.3}$$

where G is the gain of the antenna, P is the power of the transmitter (W), and d is the distance between the antenna and the target (m).

The level of the exposure of individuals under moderate environmental conditions to a whole-body SAR is approximately 4 W/kg for about 30 min. A whole-body average SAR of 0.4 W/kg has therefore been chosen as the restriction that provides adequate protection for occupational exposure. An additional safety factor of 5 is introduced for exposure of the public, giving an average whole-body SAR limit of 0.08 W/kg [68][98].

Table 2.1: Conditions and limits of the SAR for the frequency range 2-300 GHz [68] [98]

Exposure characteristics	Average SAR Whole body (W/Kg)	Average SAR for head and trunk (W/Kg)	Average SAR for limbs (W/Kg)	Power density S (W/m^2)
Occupational exposure	0.4	10	20	-
General public exposure	0.08	2	4	10

For example, in the far-field area at the frequency 10 GHz, the power density for -6 dBm input power is $7.95e^{-4}W/m^2$ and $3.16e^{-3}W/m^2$ for the input power 0 dBm. The parameters set for this calculation are resumed in Table 2.2. The calculated values show that we are very low than the standards described (10 W/m^2).

Table 2.2: Parameters used to calculate the power density

Distance between target and antenna	1 m
Gain of antenna at 10 GHz	11.56 dB
Power of the transmitter	0 dBm
Diameter of the antenna	24.4cm

Note that these ranges depend on frequency. In addition, the aspect of time is taken into consideration especially that sensation of fatigue is linked to exposure over a longer period of time.

2.4 Monitoring techniques of vital signs rate

This section review some of different systems for measuring human respiratory and cardiac rates. The review highlights the various technologies as well as some of their shortcomings and limitations. There are various ways of grouping the commercially available systems for measuring breathing and heart rates, by their (contact or non-contact), by their application domain (medicine or public use) or by the covered area (short-range, mid-range and long-range radar). This section presents a brief overview of the current systems for monitoring vital signs.

Non-contact detection and monitoring of cardiopulmonary activity is one of the most promising solutions for controlling driver vigilance in different situations. The devices that allow the measurement of vital signals are more or less expensive and cumbersome according to their complexity, ranging from simple using to complex where should be used by qualified personnel when taking measurements.

2.4.1 General public embedded diagnostic techniques

Mobile devices, smartwatch, wristband (bracelet) and patch have become essential daily tools. The smartwatch and the bracelet are a wearable medical device that collects vital signs data such as blood pressure, oxygen level in the blood (SPO2) [40], heart rate, and respiratory rate with the possibility of synchronization with a smartphone. Connectivity either via a smartphone with Bluetooth, or via a dedicated gateway. The watch should be worn on the wrist while the patch should be placed anywhere on the upper torso.
Modern smartphones equipped with sensors (accelerometers,microphone and camera...). These sensors can be used for capturing body movements as well as interpreting certain physiological functions from their analysis. For example, smartphone-based accelerometers and ballistocardiogram (BCG) may provide physiological parameters (i.e., the RR and HR) [33]. Another way to measure vital signs is applications installed in the smartphones, like google fit, using the phone's camera: the back one for heart rate and the front one for breathing. In the first case, the user will have to place his finger on the main sensor. Due to technique of photoplethysmography, the application record the color changes of the fingers to estimate the heart rate. For the respiratory rate, Google Fit recommends placing the smartphone on a stable surface so that can frame using the front camera.The algorithm analyze the data obtained by observing the user's face and the movement of the chest to produce the result [1].

An other technology is MySignals, which is an eHealth IoT Development platform for remote health monitoring, equipped with 17 different sensors with contact that measure the vital signs such as pulse and breath rate [105].The data gathered by MySignals is encrypted and sent to the developer's private account at the Libelium Cloud.

2.4.2 Monitoring techniques of vital signs rate

This section addressed different types of medical methods for monitoring heart and respiration rates.

2.4.2.1 Respiration rate (RR)

The respiratory rate is typically measured through observation or palpation of the chest. An accurate reading requires counting for a full minute, because the rates are so low [28]. The measurement of respiratory rate by different examiners can vary significantly, and if the person under test realizes that their respiration is being monitored, they may change their breathing rate and pattern. Clinically, RR could be recorded with a range of techniques listed in table 2.3.

Table 2.3: Different techniques for recording RR, clinically

Methods	Advantages	Limitations
Manual counting	Easy to perform, non-contact	Inaccurate, time-consuming
Spirometer	Accurate, simultaneous measurement of multiple respiratory parameters	Interfere with natural breathing, difficult for continuous RR monitoring
Capnometry	Accurate, easy to perform, able for continuous RR monitoring, simultaneous measurements of biochemical parameters	Uncomfortableness caused by contact, special devices needed for analysis
Impedance pneumography	Accurate, continuous, simultaneous measurement of multiple respiratory parameters	Difficult to perform, special devices respiratory parameters needed for analysis

2.4.2.2 heart rate (HR)

The two most common method for measuring the heart rate are the **electrocardiogram (ECG)** and the **Photoplethysmography (PPG)** . ECG is the measure of electrical potential generated by the cardiac muscle which is usually acquired at multiple points on the surface of the body, the electrocardiogram provides information about the part of the heart that triggers each heartbeat (the pacemaker), nerve conduction pathways of the heart and the rhythm of the heart.

PPG is an optical technique that uses a light source (with wavelengths between 500 nm and 600 nm, corresponding to the green and yellow regions) and a photo-detector at the surface of skin to measure the volumetric variations of blood circulation. A portion of the emitted light is absorbed by human tissue while the other portion is reflected. A Photo-Detector (PD) is used to record the intensity of the received light. This intensity changes during the systolic and diastolic phase-shifts of the cardiac cycle [95].

2.4.3 Microwave techniques for measuring vital signs

Radio Frequency (RF) radars have been used in wireless sensors applications for decades. Compared to other technologies, wireless radars are interesting for their benefits of non-contact and non-invasive detection based on RF. The advantages of non-contact vital signs detection by radar methods have been demonstrated in [21, 14]. These vital signs are estimated from the acquired waveform that reflects the chest volume variation and displacement during the inspiration and expiration.

The first use of radar systems for the detection of vital signs dates back to the 1975 s for measuring RR [53], a 10 GHz system was used for measuring the respiration of a rabbit located at 30 cm away from the system antennas but the system was not sensible enough to detect the heartbeat. Besides that, the heart beats was measured with a breath hold required [54]. Since then, the interest in radars for the monitoring of breathing and heart rate has increased considerably. These developments involved analog and digital signals processing to separate the small heart signal from the much larger respiratory signal, so that the person does not need to hold their breath for the heart rate to be measured, and the heart and breathing can be measured simultaneously [6].

An Ultra-Wide Bandwidth (UWB) pulses was employed to detect the heart rate and breath rate by sending very short and repetitive waveforms toward the target person's chest surface in [41, 81]. Hence, the papers [11, 115] focuses on continuous monitoring of vital sings using an Impulse-Radio (IR) UWB radar. The echoes will be received by carrying a round-trip time delay proportional to the movement of the chest surface with respect to the transmitted waveform, which can focus on the phase-shift information introduced by the modulated time delay. The hybrid UWB-Doppler system aided with Kalman Filter is demonstrated in [102], where the system setup consisted of an UWB positioning subsystem, a K-band Doppler radar.

Three prototypes of radars operating at 5.8 GHz, 24 GHz and 35GHz separately are presented by Chioukh [9]. These systems are different in frequency of operation, in their architectures and in manufacturing techniques 2.8. The first proposed architecture is a 5.8 GHz Doppler bistatic radar, which is based on the 4x4 patch antenna and a coupler which separates the transmitted wave and the reflected wave. The second architecture, used at the 24 GHz frequency based on two horn antennas, a power divider and a mixer. And the third system operating at 35 GHz, which this time is composed of a single 8x16 element slot antenna, a circulator, a mixer and a filter.

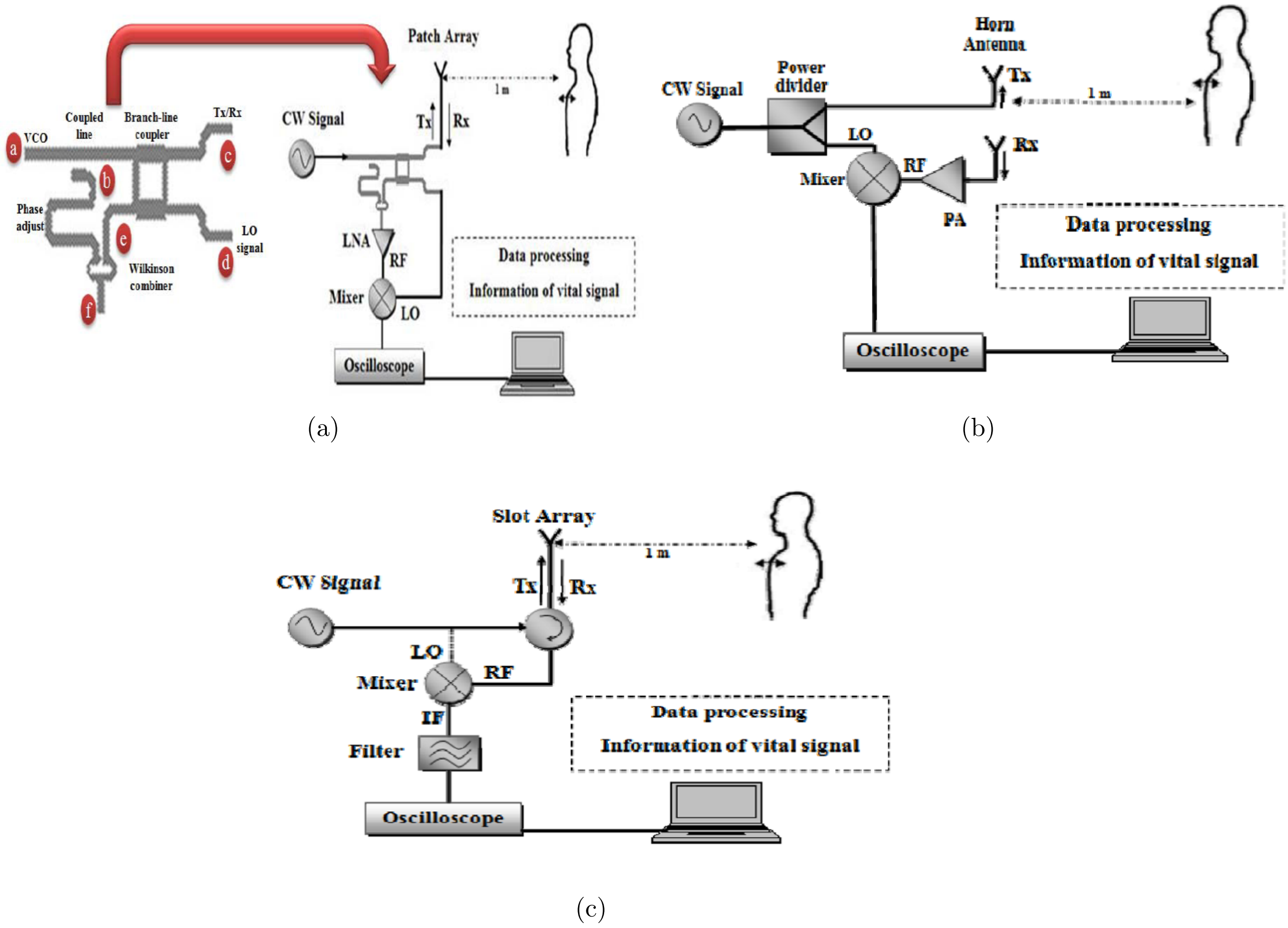

(a)

(b)

(c)

Figure 2.8: Radar diagrams at frequencies (a) 5.8 GHz; (b) 24 GHz and (c) 35 GHz [10]

Other work shows harmonic radar based on frequency diversity to provide improvements, more sensitivity and reliability. These works proposed a 24 GHz radar based on the six-port receiver [9]. The measurements collected, at a distance of 50 cm between the person under test and the antenna, are very noisy, and the peaks due to the harmonics of breathing and intermodulation are important. It is therefore difficult to discriminate the heart rate (Figure 2.9). The use of multi-frequency radar aimed to show that the detection improvement can be obtained by using a system operating at multiple frequencies [10]. This concept is then validated after in [8] by the measured results of an experimental prototype using the proposed harmonic six-port radar platform operating both the fundamental frequency 12 GHz and its second harmonic frequency 24 GHz.

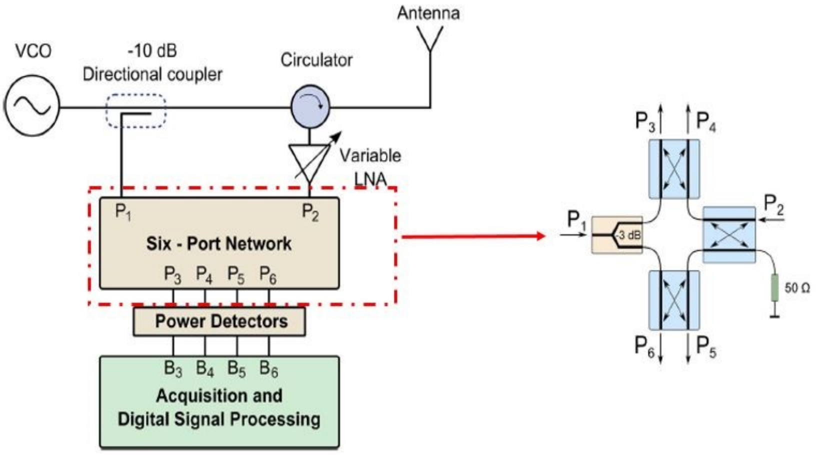

Figure 2.9: Six-Port Receiver Radar Schematic [8]

Using the same receiver, a continuous-wave (CW) monostatic radar with interferometric evaluation is proposed in [100]. The radar is based on the six-port receiver network to perform a relative phase-shift measurement between the received signal from the antenna and a reference signal derived through a directional coupler from a microwave source generating a 24-GHz CW signal. The received signal is amplified by a low-noise amplifier (LNA) and a variable attenuator chain to guarantee that the amplitude of the input signal at the second port of the six-port receiver is comparable to the amplitude of the reference signal at the first input port. The results show a difference between the heart rate detected for different positions which is due to erroneous periodic peak detection, mainly due to non-ideality of the environment which influence the measurement. An improvement is proposed in [99] where the idea of integrating the radar in the driver's seat using the same six-port system while modifying the treatment part. In this regard, the system configuration has been designed to be the best way to emulate realistic conditions with different measurement scenarios.

Figure 2.10: (a) The radar is 0.5 m in front of the person, (b) The radar is installed behind the seat [99]

Quadrature CW radar with I/Q channel demodulation has been proposed in [35]. I/Q channel demodulation with calibration method is added to alleviate the null point problem occurring in direct-conversion single-channel receiver [20] and acquire an accurate phase-shift demodulation result with high linearity. In [70] a vector network analyzer (VNA) system was reported, this system tuning both frequency and power to determine the optimum frequency and the minimum power able to extract vital signal.the authors used a VNA as a suitable Doppler radar with different parameters optimized.

Besides the vector network analysis, measurements of minor variations in distance can be made by interferometric methods. Lately, much research has been carried out on alternative microwave interferometric radar techniques. The architecture of the six-port receiver, used as an interferometer, for angle, displacement and vibration measurements[99] [100]. Where they have integrated a six-port radar in the driver's seat for monitoring of vital signs.

With the growing interest in measuring and monitoring vital signs, many researchers have contributed to technological advancements and signal processing in this area. This has led to various front-end radar architectures and different methods for detecting and extracting these signs.

In the previous part, a non-exhaustive bibliographical study of the progress of research for the detection of vital signs was presented. Supplemented by a summary table thus allowing to have a global vision of the state of progress of research in this field. as well as the dedicated techniques to achieve the detection of vital signs. The works is briefly described in table 2.4 with year of publication, reference, description and results.

Years	References	Description and results
1975	J.C. Lin [53]	Respiration measured on rabbit and human at 30 cm using sweep oscillator for the output power 10 mW at 10 GHz
1979	Lin et al.[54]	Measuring the heart in the apex region while the subject hold his breath lies in the supine position at 3 cm from apex
1986	Seals et al.[88]	Analog signal processing for detection and separation of heart and respiration signs at 3 and 10 GHz using quadrature radar
1990	Chuang et al.[13]	Heart and respiration for detecting victims through the rubble at 2 and 10 GHz with the clutter cancellation
2000	Chen et al.[6]	Life-detection system under rubble or behind barriers at 450 and 1150 MHz.Heart and respiration were measured
2002	Lubecke et al.[57]	Add-on module uses signals from existing wireless devices to measure heart and breathing with a 2.4 GHz cordless phone and a signal generator
2004	Droitcour et al.[20]	Range correlations and I/Q performance benefits in single-chip Doppler radars
2004	Ossberger et al. [72]	Respiratory detection of persons through a wall at 85 cm using an UWB pulse radar and wavelet transform algorithm
2005	Matsui et al.[60]	Used 1215-MHz radar to detect RR-intervals for heart rate variability on one subject using detect peaks methods
2006	Xiao et al. [107]	Heterodyne Ka-band radar that detect the heartbeat and breathing signals using double-sideband transmission to avoid null detection point
2007	Park et al.[76]	Quadrature receiver at 2.4 GHz using arctangent demodulation with DC offset compensation to detect heart and respiration rate
2008	Changzhi Li	Random motion suppression technique measurements

	et al.[47]	for different positions at 5 - 6 GHz
2009	Massagram et al.[59]	2.4 GHz quadrature system with linear demodulation method to detect heart rate variability (HRV) and respiratory sinus arrhythmia (RSA)
2010	Wang et al.[103]	Frequency demodulation of a scanning oscillator under injection-locking and self-injection-locking for vital signs detection using a single antenna
2011	Pan et al.[74]	A voltage-controlled tunable phase shifter is introduced in the Doppler radar to eliminate the null point problem in the non-contact vital sign detection
2011	Chuang et al.[15]	Radar CMOS based on wave-guide component at 60 GHz including a clutter canceller from distances of 1 and 2 m
2011	Kiriazi et al.[42]	Dual-frequency (2.4,5.8-GHz) radar for cardiopulmonary effective radar cross section (ERCS) of human subject
2013	Vinci et al.[100]	Monostatic radar based on a six-port interferometer operating a continuous-wave signal at 24 GHz
2013	Singh et al.[90]	Doppler radar for clinical sleep monitoring Doppler radar is being investigated as a cost-effective solution for long-term monitoring of sleep apnea

Table 2.4: Radar measurement for monitoring vital signs

Several characteristics make the vector network analyzer attractive in the implementation, it is one of the main RF system used for microwave measurements. One of the objectives of this thesis is to do a general parametric study, for that the choice of radar opted is the vector network analyzer (VNA). It offers the possibility to vary several parameters (frequency, power, sweep time,etc.). In addition, it measures the phase and amplitude of S-parameters.

2.5 Radar measurement of vital signs

Bibliographical research was carried out on the various technologies for monitoring vital signs using radar. This research concerns the development of radar systems, their advantages and their reliability for cardiac and respiratory signal monitoring applications.

2.5.1 Radar equation

The signal-to-noise ratio (SNR) is derived to assess the theoretical limits of the radar system. The received power is determined by the radar equation. The received power approximation is based on the transmitted power, the range to the target, and the properties of the transmit antenna (gain), the radar cross section, and the receive antenna. The power radiated in the desired direction is known as the Effective Radiated Power, ERP, and is equal to the Gain multiplied by the Transmitted Power (G P_T):

$$ERP = GP_T \tag{2.4}$$

Where P_T is the transmitted power and G is the gain of the antenna. When the same antenna is used for transmitting and receiving, the gain is the same for both antennas, and the equation can be simplified to:

$$P_R = \frac{P_T G^2 \sigma \lambda^2}{(4\pi)^3 R^4} \tag{2.5}$$

Where σ The radar cross section, , is determined by the amount of power incident on the target that is re-radiated toward the antenna, and R the range.

2.5.2 Antenna considerations

Antennas are a critical component for the overall performance of the radar. The role of an antenna is to convert the electrical energy of a signal into electromagnetic energy radiated in all directions of space and vice versa. This power depend on the characteristics of the antenna. For a bistatic radar, where we have two antennas, a transmitting antenna is a device that transmits energy between a transmitter and the free space where that energy will propagate. Conversely, a receiving antenna is a device that transmits the energy of a wave propagating in space to a receiving device. [25]

2.5.2.1 Directivity

The directivity of an antenna relates to its ability to concentrate the radiation in the desired direction. An antenna which radiates uniformly in all directions in three-dimensional space is called an isotropic antenna. Such an antenna does not exist, but it is convenient to refer to it when discussing the directional properties of an antenna [82]. The directivity means the ratio between the power emitted in the maximum direction and its entire spatial distribution. We will therefore say that a strongly directive antenna admits a low radiation aperture, and a weakly directive antenna admits a large radiation aperture. A directional antenna then concentrates its energy in a single direction. This phenomenon results in a main lobe on the radiation pattern. The directivity of the hypothetical isotropic radiator is 1 or 0 dB. Antennas can be omnidirectional, sectorial or directive:

- Omnidirectional antennas radiate the same pattern all around the antenna in a complete 360 degrees pattern. The most popular type of omnidirectional antenna is the Dipole-Type.
- Sectorial antennas radiate primarily in a specific area. The beam can be as wide as 180 degrees, or as narrow as 60 degrees.
- Directive antennas are antennas in which the beam-width is much narrower than in sectorial antennas. They have the highest gain and are therefore used for long distance links. Types of directive antennas are the horn, the patch antenna and many others.

2.5.2.2 Bandwidth

Antenna bandwidth refers to the range of frequencies over which the antenna can operate correctly. It is corresponds to the frequency band where the transfer of energy from the power supply to the antenna (or from the antenna to the receiver) is maximum.

The bandwidth can also be described in terms of percentage of the center frequency of the band [82].

$$BW = 100 \times \frac{Higherfrequency - Lowerfrequency}{Centrefrequency} \tag{2.6}$$

Beamwidth is the angular separation between the half power points (3dB points) in the radiation pattern of the antenna in any plane.

2.5.2.3 Gain

Antenna gain is the ability of the antenna to radiate more or less in any direction compared to a theoretical antenna. If an antenna could be made as a perfect sphere, it would radiate equally in all directions. Such an antenna is theoretically called an isotropic antenna and does not in fact exist. However, its mathematical model is used as a standard of comparison for the gain of a real antenna [82].

It is defined as the product of the antenna efficiency and its directivity. The gain is obtained by concentrating the radiated power into a narrow beam. A high gain is achieved by increasing the effective aperture area A_e of the antenna in square meters. We write the gain G as [31]:

$$G = \frac{4\pi A_e}{\lambda^2} \tag{2.7}$$

Antenna gain is typically given the symbol G, and is defined as the maximum radiation intensity produced by the antenna compared to that given by a lossless isotropic radiator supplied with the same level of power. If an antenna's gain is 2 (3 dB), it means that twice the amount of effective power will be sent in the direction of a target than from an isotropic radiator.

2.5.2.4 Radiation zones

When a signal from a transmitter is applied to an antenna, it sends out electromagnetic waves in to free space. The EM field characteristics vary as a function of distance from the antenna. They are broadly divided into two regions, the near-field region, and the far field region. Depending on D which is the maximum dimension of the antenna, and on the wavelength λ, there are three zones starting from the emitting source:

- The Rayleigh zone is located at distances from the antenna between $\frac{\lambda}{2\pi}$ and $\frac{D^2}{2\lambda}$
- The Fresnel zone This is an intermediate zone located between $\frac{D^2}{2\lambda}$ and $\frac{2D^2}{\lambda}$
- The far field zone (Fraunhofer zone) is beyond $\frac{2D^2}{\lambda}$ and the electromagnetic wave is plane.

2.5.3 Antenna consideration for monitoring vital signs

Choosing to use a highly directional, wide beam, or omnidirectional antenna requires taking into account compromises between size and directivity. The higher the directivity of an antenna, the larger its area.In this case, the abdomen of the subject faces the antenna.

Nevertheless, if the beam is focused to cover a small area on the subject's chest, it may be though to guarantee that the beam is on the correct part

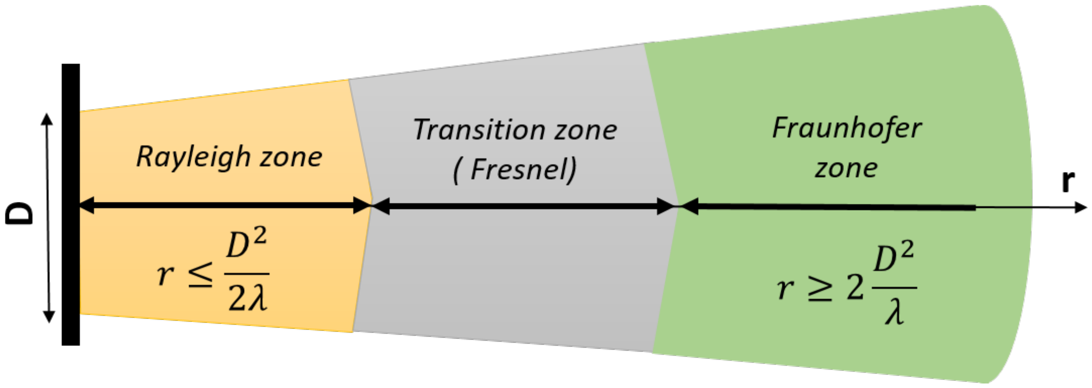

Figure 2.11: Representation of field zone

of the subject [20]. Besides, in applications where the subject may move while monitoring, a highly directional antenna should follow the subject's movement to avoid losing contact. In a bistatic radar system which use two antennas, can affect the radar cross section of the target. In this manner, as long as the two antennas are kept close to each other, this effect will be minimal [91]. If the antennas are close to each other, care should be taken to minimize the leakage between the two antennas. When the antennas are spaced and angled appropriately, the dominant source of leakage is usually backscatter from nearby clutter, which is unavoidable [20].

2.5.4 Operating frequency

The detection of vital signs is based on a reflected signal from the subject's chest. Therefore, the most important feature is that the RF signal penetrates clothing with minimal reflection and has a higher reflection at the air/skin interface.However, the signal reflects at the air/skin interface less as the frequency decreases,and it has more significant reflections as the frequency increases. Parameters such as antenna size, measurement environment, and distance between antenna and the target, will determine optimum operation frequency for a particular application. These features turn on the operational frequency Besides the signal processing. Operating frequencies varying in millimeter-wave band, for non-contact monitoring of vital signs with CW radar, have been evaluated in [78].

An important feature in frequency choice is the resolution. a direct relation exists between the variation of phase-shift and the operating frequency. The signal-to-noise ratio is dependent on the wavelength of the carrier and the variation of phase-shift proportional to the carrier wavelength, hence higher is the operating frequency better is the detection sensitivity [18]. phase-shift modulation in radians is:

$$\frac{4\pi x(t)}{\lambda} \tag{2.8}$$

where $x(t)$ is the chest motion. If the frequency is high then the wavelength is short and the phase-shift modulation is large. If the phase-shift noise is the same across different frequencies, increasing the frequency increases the SNR.

The hardware complexity and cost of the system should be taken into consideration; the cost increases when using higher operating frequencies.The choice of an unlicensed band is important for FCC compliance, and also in order to have a range of commercially available antennas to choose from. All the selected frequencies evaluated in the literature belongs to the Industrial Scientific and Medical Band (ISM) are used essentially due to the vast availability of low-cost RF/microwave components and integrated circuits in this bands [18].

A higher frequency also means that the same antenna gain can be obtained with a physically smaller antenna. The maximum directivity that can be obtained from an antenna with aperture area is:

$$D_{max} = \frac{4\pi A}{\lambda^2} \tag{2.9}$$

2.5.5 Principle of radar for monitoring vital operation of the radar

Radar is a transmitter and receiver of electromagnetic waves. It sends an electromagnetic (OEM) wave and receives an echo signal, and gives information on the targeted objects. The time of flight between transmitted and received signals indicates the distance of the target from the transmitter.

As shown in Figure 2.12, a radar system consists of a transmitter, an antenna, a duplexer, a receiver, and equipment for signal processing. The emitting part of the radar creates, emits, an electromagnetic wave towards a precise direction, which in our case is the driver's chest. The OEM spins through the air at the speed of light (about 300,000 km / s). If it encounters an obstacle, part of the OEM continues possibly being modified, this part of the initial

OEM is the refracted OEM, and the other part is reflected and it returns to the radar, which detects this return.

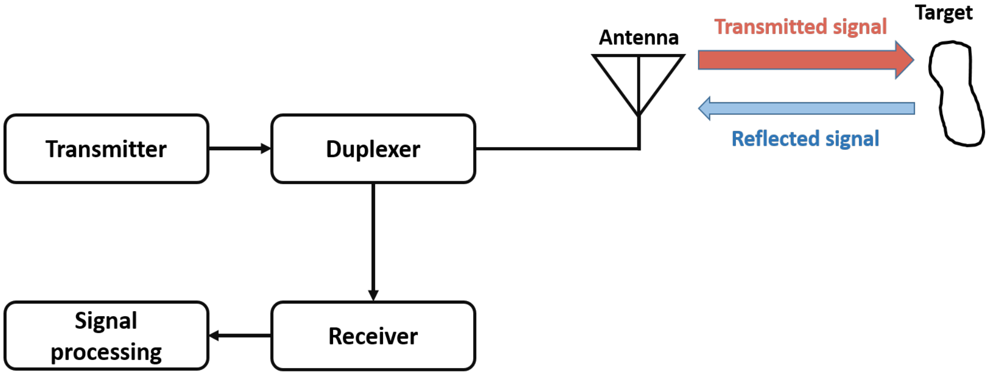

Figure 2.12: Block diagram of the radar system

2.5.6 Radar for monitoring vital signs

The heart and respiratory rates are the two most important vital signs that indicate the body's functioning state. The movement of the rib cage is caused by breathing and the heart rate. The principle of a radar for monitoring vital signs is based on the phase-shift modulation induced by the movement of the thorax.

Vital signs are detected by the radar transmitting electromagnetic (EM) waves toward the person, and recording the received reflections. When the person is breathing and the heart is beating, modulations occur in the received radar reflections from the person. EM waves can propagate inside the body and a part of this wave will be reflected at the boundaries of each tissue back toward the receiving antenna. However, the electric field attenuation in body tissues is high. This coupled with the fact that the air/skin interface provides a strong back-scattering suggests that reflections from inside the body do not contribute significantly to the modulations, even though the heart itself has a larger motion than the chest surface.

The human chest moves because of the heart beating and the respiration cycle. These movements form a quasi periodic motion applies an offset to the return signal and have its phase-shift modulated proportionally to that time varying position. Hence, when the continuous wave (CW) from the radar at a certain frequency is incident upon the chest it is reflected with the quasi periodic motion modulated on it. The phase-shift of the reflected signal in its base band form contains information about the chest motion from which heart and breathing rate can be extracted using signal processing. In order to accurately estimate the information of interest, various signal processing techniques have been used.

For the right choice of radar for monitoring chest movement for detection of vital signs, the receiver should maximize the ability to distinguish between physiological signals and noise sources. In such a system, the signal-to-noise ratio, cost, weight, size, and bandwidth depend on the chosen architecture. Nevertheless, the receiver must have a reduced size, while presenting low costs. On the other hand, they must operate on an important frequency band in order to respond the needs of high data rates, all these instructions to reduce the complexity and cost of the components.

2.5.7 Monostatic and bistatic radar architectures

One of the core component of the radar system is antenna. There are two basic radar configurations based on the spatial relationship between the transmitting and receiving antennas: monostatic and bistatic. An overview about bistatic and monostatic radar architecture is described in this section.
Bistatic radar contains separated antennas [39]. The first antenna is dedicated for the transmitted signal (Tx) and the second for the received signal (Rx). In monostatic radar architecture, a single antenna performs both the transmission and reception of the radar signal. Signals generated in the transmitter are passed directly to the same antenna. The receiving signal is routed to the receiver part. The transmitted and received signals are separated through a circulator. Figure 2.13 shows monostatic and bistatic radar architecture [86].

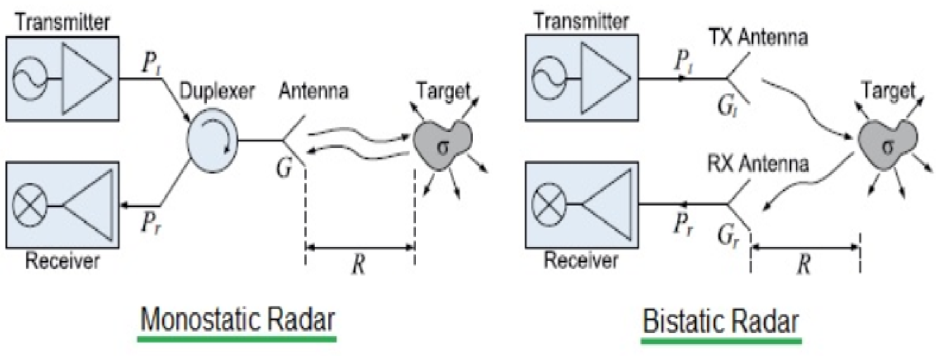

Figure 2.13: Monostatic and bistatic radar

2.5.8 Heterodyne and homodyne architectures receivers

In architecture of radar, a receiver is used to amplify and down-convert a radio frequency (RF) signal with minimal deformation. However, the requirements for the receiver hardware performance should provide high dynamic range, low noise, and high local oscillator (LO) isolation so as to avoid radiation emission. The option of receiver architecture is usually determined by the hardware complexity, power dissipation and system considerations. There are two main architecture prevails in radio receiver of any system i.e. Heterodyne and Homodyne.

A reference signal is commonly used in CW radars to down-convert the received signal. The simplest phase-shift detector involves mixing the received signal with a signal of the local oscillator (LO) that was used to generate the signal at the transmission at the same frequency as its carrier. So that the RF frequency is converted directly to baseband.Such a receiver that uses a reference signal at the same frequency as the carrier signal is known as either direct conversion receiver or homodyne [18] [97].

Figure 2.14 represents the homodyne receiver architecture. Where the RF BPF is a bandpass filter that is sometimes included to attenuate signals to avoid inter-modulation resulting from receiver nonlinearities. The LNA is a low-noise amplifier that rise the receiver noise figure. The local oscillator is at the same frequency as the RF carrier, and when mixed with the received signal after the baseband low-pass filter. The reference signal is mixed with the received signal using a mixer for down-conversion. Then the mixer output passes through a low-pass filter to reduce high-frequency signals and harmonics resulting from the mixing operation to obtain the down-converted signal as a baseband signal. An LNA and an RF band-pass filter may be used to amplify and filter the received signal to enhance the signal-to-noise ratio (SNR) [97]. One of the challenges of this architecture is to manage the DC component of the baseband signal which relates to the reflections from fixed objects and to the energy of the transmitted signal itself [18].

A heterodyne receiver differs from a homodyne receiver in that it uses an LO at a frequency distinct from the carrier signal as the reference signal for down-conversion. It instead mixes the received signal with a LO signal at a different frequency. Then the down-converted signal becomes a signal

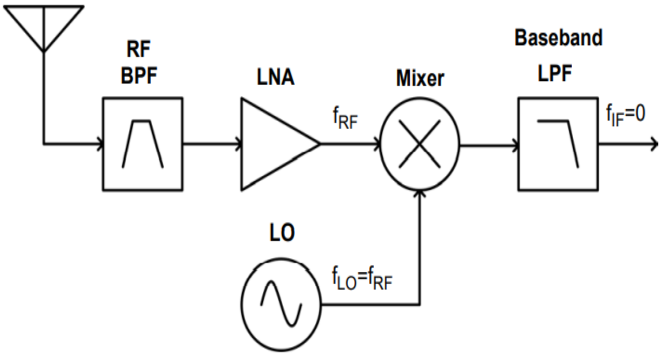

Figure 2.14: Homodyne receiver architecture

modulated on an intermediate frequency (IF) rather than being converted directly to a baseband signal, after filtering is applied. A basic architecture of a heterodyne receiver is shown in figure 2.15.

As with the homodyne, an LNA may be used to amplify the received signal prior to the mixing operation. The presence of an IF stage allows to use of high-quality components tuned to the carrier frequency, and band-pass filters at the RF and IF stages help eliminate unwanted signals an improve SNR. The issue with the DC component pertaining to a homodyne receiver is eliminated in a heterodyne receiver. However, the architecture of a heterodyne is more complicated compared to that of a homodyne receiver [18].

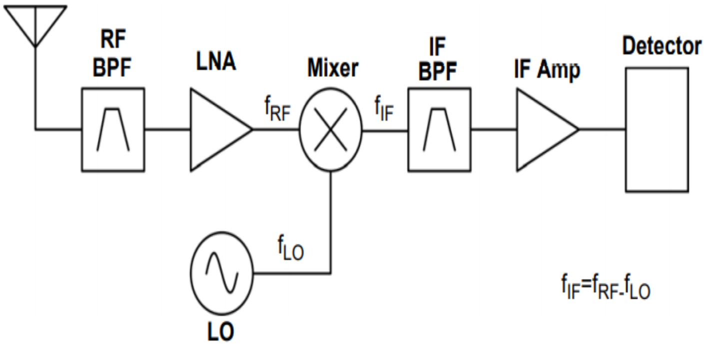

Figure 2.15: Heterodyne receiver architecture

The detector may be a mixer to baseband, a quadrature demodulator, or another type of detector that functions at the intermediate frequency. The RF BPF is a high-quality radio-frequency bandpass filter designed to eliminate the image frequency, the undesired signal capable of producing the same IF as the desired signal produces when mixed with the LO. The low noise

amplifier (LNA) decreases the receiver noise figure by increasing the signal power at the input before the rest of the receiver adds noise. Then, the signal is mixed with the LO to down-convert it to the intermediate frequency. The IF BPF is a high-quality bandpass filter at the intermediate frequency used for channel selection, and the IF Amp is an amplifier at the intermediate frequency. The IF amplifier is often a gain-controlled amplifier that adjusts the signal to the appropriate amplitude for the detector [97].
The type of detector varies with the application and depending the modulation and the information that is modulated. It may consist of down-conversion to baseband, an envelope detector, a phase-shift-locked loop, or other topologies. The LO is typically tuned to select the desired channel [18].

2.6 Types of Radar

Depending on the radar system hardware and the type of signal sent, it may be possible to classified the radars according to the waveform into two groups: pulse radars like ultra-wideband (UWB) which is a special case of pulsed radar, that provides good range resolution due to the short pulse duration [102, 41, 81] radars, and continuous wave radars such as continuous wave (CW) Doppler radars [62, 9, 113], frequency-modulated continuous wave (FMWC) [77, 45] and six-port [43, 100].

2.6.1 Continuous-wave radar

Continuous wave (CW) radar represents one of the simple hardware implementations in which a narrow bandwidth fixed frequency signal, usually sinusoidal in low cost applications, is transmitted, and the reflections of that signal from any obstacle in the range are received and mixed with the transmitted carrier. A CW radar detects the radial velocity of a moving object, which changes the frequency of the signals it reflects. The frequency shift of the received signal is known as the doppler effect. Based on the effect, doppler radar can be exploited to detect periodic movements like physiological movement and mechanical vibration. Objects approaching or moving away from a radar cause the reflected signals to move up and down in frequency, respectively, compared to the signal transmitted by the radar.

The main limitations of a CW radar is the fact that it does not have the ability to unambiguously detect the distance to a moving object. Besides, the signal radiated by the transmitting antenna of a CW radar may couple to its received antenna, which will affect the DC component of the baseband signal at the receiver and may interpreted as a reflection from a stationary object requiring the TX-RX isolation to be sufficiently high.

2.6.2 Frequency-Modulated Continuous Wave radar (FMCW)

CW Doppler radar has drawn more research interests due to the advantages cited in the table 2.5 and the limitations to detect the distance can be eliminated by modifying the radar via frequency modulation (FM). The FMCW can be seen as an extension to the CW radar in which the frequency of the continuously over a fixed time period by a modulating signal of triangular (linear FM), sinusoidal or other waveforms. A common FMCW radar is the linear FMCW (LFMCW) radar, which linearly increases and decreases the frequency of the CW signal as shown in Figure 2.16 [77, 45, 101]. This characteristic gives these devices both Doppler and distance information which permits a significant number of radar applications such as the measurement of multiple-target vital signs detection, the distance from the antenna to the two targets is 1.3 m and 2 m respectively [23].

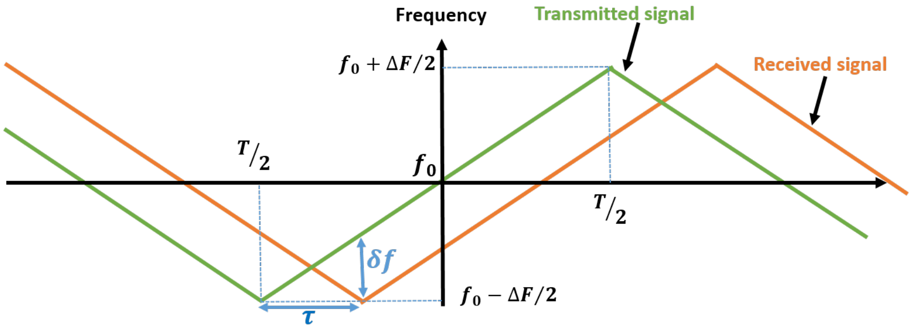

Figure 2.16: Modulated waveforms at the TX and RX for the FMCW radar

The propagation time τ of the return signal between the times it was transmitted and received can be expressed as:

$$\tau = \frac{2R}{C} \tag{2.10}$$

Where R is the range between the received and the stationary target, and C is the speed of light. According to this Figure 2.16, the frequency difference between the transmitted signal and the received signal is proportional to the delay and therefore to the distance from the target. When the latter is in motion a Doppler shift is added to the frequency difference caused by the delay.

Although not generally compared to CW and FMCW, stepped-frequency continuous-wave radar (SFCW) can also be used for the detection of vital signs [94, 80]. Nonetheless, continuous wave modulated devices have a more complex hardware architecture than simple CW radars, consuming more power from the power supply and requiring more complex radar signal processing methods.

2.6.3 Six-port radar

The name "six ports" is acquired from the structure itself: it has two input ports and four output ports, hence six ports. The concept of six-port technology can be summarized by phase-shift controlled superposition of two input signals that are superimposed under four different relative and static phase-shift shifts. The resulting four sum signals can be observed at the respective output ports of the structure. The six-port concept was introduce as an alternative of the heterodyne detection principle of network analyzers [22].
the block diagram of a typical six-port receiver. The received signal from the antenna is amplified by a low-noise amplifier (LNA)] and the local oscillator (LO) are connected to the two input ports of the passive structure. Its output signals are converted to baseband and the complex-valued in-phase-shift and quadrature (I/Q) information can be reconstructed [44].

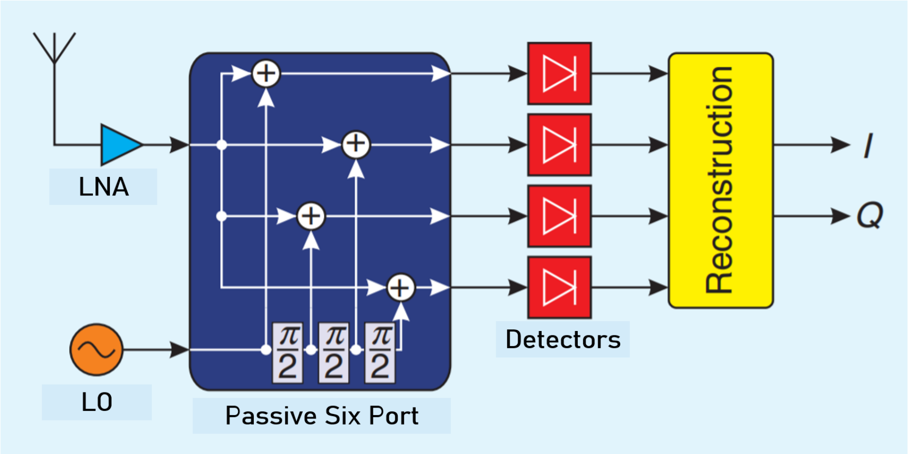

Figure 2.17: Block diagram of a six-port receiver [44]

The main advantages of the six-port interferometer are its low complexity hardware setup and its phase-shift resolution. The latter is based on the fact that compared to mixer-based I/Q receivers, the I/Q generation and down conversion are split into separate stages: the passive six-port structure generate the I/Q directly in the RF domain. There is neither noisy circuitry nor non-linear processing stages involved, resulting in strictly linear behavior.

The resulting differential I/Q signals are then brought to the baseband in a subsequent step by diode detectors. One major drawback of the six-port concept is its low sensitivity and limited noise performance.

2.6.4 Ultra-Wideband (UWB) radar

Ultra-Wideband UWB technology is based on the transmission of very short pulses that result in large spectrum signals. A signal can be classified as an ultra-wideband (UWB) signal if its fractional bandwidth is> 0.2 and the bandwidth is $\geq 500MHz$ according to the Federal Communication Commission (FCC) in 2002 [97], assigning an unlicensed band for commercial purposes [73]. The fractional bandwidth B_f is define as the ratio of signal bandwidth to the center frequency which given by Equation 2.11:

$$B_f = \frac{f_H - f_L}{f_c} \tag{2.11}$$

Where f_H and f_L are the higher and lower points in the spectrum, respectively, and f_c is the center frequency, or carrier signal frequency.

Typically, most UWB radars transmit via large bandwidth over short pulse periods, usually on the order of a nanosecond, or even a picosecond; we generally refer to this type of UWB signalling as impulse radio UWB (IR-UWB) radar [36]. IR-UWB radar systems, are based on the pulse radar architecture in which target distance is achieved with pulse-timing technique. IR-UWB radar has been introduced as a high resolution radar system capable of measuring vital signs using pulse synchronization techniques [102, 41, 81]. Like FMCW devices, the IR-UWB is a short range radar capable of providing range information as well as high speed measurements. The new regulations have encouraged an increase in research into remote surveillance systems based on this type of radar also.

The typical IR-UWB signal is a gaussian waveform of pulse-width τ_p modulated by a carrier wave of frequency f_c . These pulses are periodically emitted at a Pulse Repetition Frequency (PRF). The Inter-Pulse Interval (IPI) is inversional proportional to PRF and defines the time occurred between two pulses emission. A IR-UWB signal is represented below in Figure 2.18.

A continuous-wave radar transmits and receives a very narrow bandwidth signal and the FMWC system emit a beam whose frequency is modulated

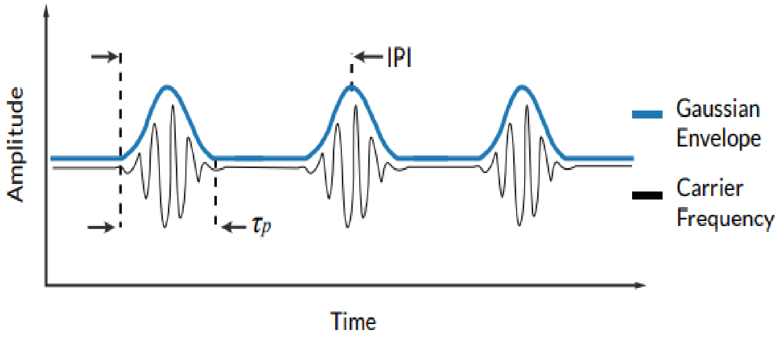

Figure 2.18: IR-UWB signal representation: a short pulse train of RF signal modulated by a gaussian function

over a determined bandwidth. However, a pulsed radar switches between transmitting and receiving, and the signal has a somewhat wider bandwidth due to the pulses. These radars are distinguished by the type of transmitted signal which could differ in waveform, frequency,and power of the modulated Radio Frequency (RF) wave. Various studies have already demonstrated the capacity of these radar systems in the measurement of respiratory and heartbeat signals in the microwave frequency band [79]. However each of these types has its own advantages and disadvantages and the detection performance and accuracy of different type of radar are distinct, due to the different hardware architectures.

Table 2.5: Advantages and Disadvantages of each type of radar

Type of radar	Advantages	Drawback
UWB	Instantaneously measure target range Elimination of leakage	Limited transmit power Short detection range
FMWC	Measure of velocity and range Uses low power for transmission Good sensitivity and stability	Attenuation of the signal Short ranges due to power
Heterodyne	simple topology and architecture Low power consumption Large detection range [49] Higher measurement accuracy	Leakage of the transmitted signal to the receiver, null-point problems

2.7 The choice of measurement system

Since the six-port concept was introduced as an alternative of the heterodyne detection principle of network analyzers [22], the vector network analyzer (VNA) was used as experimental system in this PhD due to its advantages.

The VNA permit access and controlling different parameters, such as frequency of the system, number of sampling points and time of measurement. As well, it measure the phase-shift and the amplitude of the S-parameters (reflection and transmission coefficients) allowing the use of different configurations at the same time, either monostatic or bistatic architectures. Given that the VNA measures the time variation of the phase-shift of the transmission and reflection coefficient which corresponds to the difference between the phase-shift of the received and the transmitted signal. Therefore, setting up a measurement system by pairing the antennas with the coaxial cables and the VNA makes setting up the experiment easy and simple.

2.7.1 The scattering parameters (S-parameters)

The propagation phenomena results in a variation of the voltages and currents along the transmission lines. The H, Y or Z matrices are used to describe the low frequency circuit, but in the microwave domain, the geometric dimensions of the structures guiding the electrical signal become of the same order of amplitude as the wavelength. This does not allow us to use the notions of voltage and current Figure 2.19. We introduce the notion of power, which is a quantity easy to measure in hyper-frequencies, which makes it possible to use the distribution matrix [S]. The dispersion parameters are measured on an input and an output adapted to an impedance generally equal to 50 Ω . On the other hand, these parameters require the measurement of the incident and reflected waves. Appropriate devices called network analyzers provide access to these quantities [70].

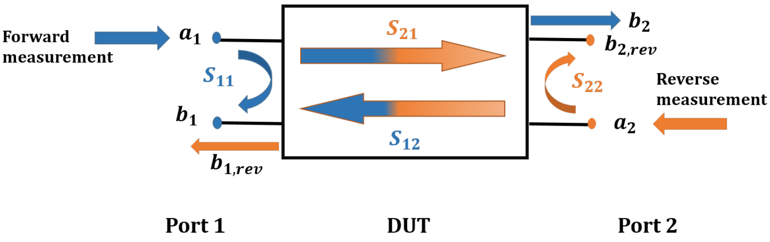

Figure 2.19: A two-port network

The S-parameters of the device under test (DUT) can be defined as follows:

- $S_{11} = \frac{b_1}{a_1}$, switch in forward direction.
- $S_{21} = \frac{b_2}{a_1}$, switch in forward direction.
- $S_{12} = \frac{b_1}{a_2}$, switch in reverse direction.

- $S_{22} = \frac{b_2}{a_2}$, switch in reverse direction.

2.7.2 The vector network analyzer (VNA)

The VNA is used to determine the amplitude and phase-shift S-parameters of a quadrupole. Its principle consists in exciting the device under test (DUT) at one of its ports, then in measuring the signals, in amplitude and in phase-shift, reflected and transmitted by the DUT while closing the other ports on the reference impedance. By successively exciting all the accesses one obtains the terms of the matrix of distribution [S] according to the frequency.The figure 2.20 shows the block diagram of the Vector Network Analyzer.

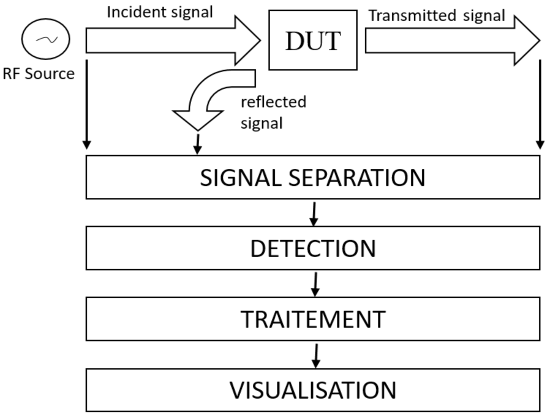

Figure 2.20: Block diagram of the network analyzer

We mainly distinguish two classes of network analyzers:

- Heterodyne vector network analyzers (Agilent, Rhode Schwarz, etc.) which measure S-parameters after transposition of microwave signals into low frequency signals.
- Six-port reflectometer type direct detection vector network analyzers.

2.7.3 Configuring the VNA

The use of a measuring device requires a knowledge of the operation of its internal mechanisms, in order to better understand the results of the measurement and to avoid interpretation errors. Components of the measurement setup, such as connectors, cables, and even the response of test instruments, can introduce errors in measurements, both for transmission and for reflection, which translate by superimposed undulations. The experimental errors are mainly due to the defects of the measuring devices (unstable generators ...), to the experimenter (repeatability of connections, reading errors ...) and finally to the measurement environment (temperature, pressure ...). These errors change the result of the ideal measurement.

Calibration is described as the process that establish, under stated conditions, the link between values of quantities indicated by a measuring instrument or measuring system, or values represented by a material measure or a reference material, and the corresponding values realized by standards. While calibration is required for accurate measurements and takes a few minutes, it saves time as a tool for correcting these imperfections, as well as other defects. There are several types of calibrations, defined by the ports used and the level of correction achieved. We are interested in these two types:

Table 2.6: Types of calibration with the VNA

Type	Calibrated parameters	Limitations
Full 1-Port	S_{11} and S_{22}	Only one reflection parameter is corrected (S_{11} or S_{22}). Both ports can be covered, but only reflection measurements will be corrected. This type of calibration is useful for reflection only measurements.
Full 2-Port	S_{11} , S_{12}, S_{21} and S_{22}	This is the most widely used and comprehensive calibration involving two ports. The four S-parameters (S_{11}, S_{12}, S_{21} and S_{22}) are fully corrected

A sweep is a series of consecutive data point measurements made on a specified sequence of stimulus values. There are several types of sweep (Linear Frequency, Log Frequency, CW Time...). In our case we choose at the beginning a linear frequency sweep while specifying the start value of the frequency sweep, the end value of the frequency sweep, the number of points, the power and bandwidth because we have broadband devices. Thus, to configure the analyzer on a single frequency (which is in the band chosen before) we change the sweep to CW time mode and we define the duration of the measurement, and the data is displayed versus time

For the configuration of the VNA, there are parameters which are used during the calibration. Therefore, it can be particularly useful to configure the VNA in advance. The parameters of interest are:

- Frequency range: Segmented scanning must also be configured in advance if a more personalized frequency list is desired.
- Number of points: The number of data points that the analyzer measures during a scan.
- Bandwidth and IFBW: The received signal is converted from its source frequency to a lower intermediate frequency (IF). Reducing the IF re-

ceiver bandwidth reduces the effect of random noise on a measurement. Each reduction in the IF band decreases the background noise. However, smaller IF bandwidths result in longer scan times.

- The power level: the power level is defined at the output of the source.
- Sweep Time: Specifies the time the analyzer takes to acquire data for a sweep.

2.8 Different source of signal perturbation

The amplitude of the signal at the baseband depends on the received power and phase-shift modulation. There are different sources of noise and disturbance for the physiological signals: residual phase-shift noises from the LO, downconverted RF additive white gaussian noise (AWGN) from the front end of the receiver, and baseband noise from the components and the mixer.

2.8.1 The residual phase-shift noise

The residual phase-shift noise includes the phase-shift noise by the chest signal itself, the stationary human body reflection, the antenna leakage signal, and the mixer leakage signal. Because the frequency range concerned in the radar for monitoring vital signs system is less than 10 Hz, the phase-shift noise itself may be large enough to affect the signal detection. However, when the same oscillator is used for transmitting and down-converting operations, the phase-shift noise of the received signal is correlated with that of the LO, and the phase-shift noise is dramatically reduced. In radar applications, such as bio-radar, this phase-shift noise reduction phenomenon is called the range correlation effect [37].

The residual phase-shift noise power from the vital signs can be given by [40]:

$$N_{\Delta\varphi_h} = \frac{P_{Tx} G_T G_R G_{Rx} \sigma L_h}{2\pi f^2 d^2} S_\varphi(1) ln(\frac{f_{max}}{f_{min}}), \tag{2.12}$$

where P_{Tx} is the transmitted power, G_T and G_R are transmitter and receiver antenna gains,G_{Rx} is the receiver gain. σ is $theRCS$, L_h is the reflection loss of the heart. $S_\varphi(1)$ is the phase-shift noise at 1 Hz. As can be seen from (2.12), the residual phase-shift is inversely proportional to both the operating frequency as well as the distance. This power is used to generate the residual phase-shift noise $\Delta\varphi\,(t)$.

There are other residual phase-shift noise causing by clutter, antenna leakage, and mixer leakage depending on the radar architecture [37].

2.8.2 The thermal noise

The dominant RF noise at the input to the receiver is thermal noise, thermal noise is zero-mean, has a gaussian distribution, and does not vary with frequency. This is additive to the RF signal. The thermal noise power is expressed as follows [37]:

$$N_{Thermal} = 8 G_{Rx} k T B N_f, \tag{2.13}$$

where k is Boltzman' s constant, T the absolute temperature, B is the bandwidth. N_f is the noise figure. Unlike phase-shift noise, thermal noise is independent from distance and frequency. It means that the noise is fixed regardless of the attenuation of the reflected signal. The thermal noise power is used to generate the additive complex noise $Z(t)$.

2.8.3 Attenuation

The attenuation A_{HR} for the complex-valued reflected signal is [57] [37]:

$$A_{HR} = \sqrt{\frac{P_{Tx} G_T G_R \sigma_h L_h \lambda^2}{(4\ \pi)^3 d^4}}, \tag{2.14}$$

where P_{Tx} is the transmitted power, G_T and G_R are transmitter and receiver antenna gains. σ_h is the RCS, L_h is the reflection loss of the heart.

2.9 Conclusion

Vital signs are key indicators in assessing an individual's health. Conventional methods rely on direct contact with the person under test's skin and can therefore cause discomfort and reduce autonomy. This chapter was devoted to the state of the art of different techniques for measuring vital signs including the microwaves method based on the radar. The principle of several type of radar for measuring the movement of a person under test's chest was introduced. Then, a brief background on radar was presented along with to the art and science of non-Contact cardiopulmonary monitoring with different type of radar.

Doppler radar was introduced for the non-contact detection or monitoring of human cardiopulmonary activity. These functions can be a promising tool for medical, emergency, military or security service applications if reliable and robust detection can be provided. The sensitivity of detection relative to the position of the target is nevertheless a challenge due to the periodic phase-shift relationship between the received signal and the local oscillator (LO). Several researches and studies have been carried out in recent years with the aim of improving this system. They relate to the different architectures for the improvement of the sensitivity of the system.

Different type of radar was reported in this chapter, each of these type has it own advantages and disadvantages depending in the performance and accuracy of the architectures. The choice of the measurement system was presented. This choice based on the vector analyzer network (VNA) Due to its simplicity of manufacture and therefore its allowing the access and controlling different parameters. The signal processing techniques used to analyze the collected data of different parameters will be described and presented in the next chapter.

Chapter 3

The techniques of processing signals associated to vital signs

3.1 Introduction

In order to accurately estimate the heart and respiration rate from the signal reflected from the displacement of the chest, various signal processing methods have been proposed in the literature. Although the RF-reflected signal from the human body is corrupted by noise of the radar, the clutter and random body movements. Given these limitations, the interest information, the heart and respiration rate can be difficult to extract. The different sections of this chapter present the state of the art of the different techniques in signal processing to estimate and extract the heart and respiration rate. Then, we have chosen to carry out simulations of an existing method based on demodulation and ellipse adjustment to separate the respiratory and cardiac frequencies.

Traditional Fourier analysis fails to detect the heart and breathing frequencies. In this effort, cyclostationary analysis has been used to improve the radar performance for non-invasive measurement of respiratory rate and heart rate. However, the preliminary works focus only on one frequency and do not include the impact of attenuation and random movement of the body in the analysis. Hence in this PhD, we evaluate the impact of distance and noise on the cyclic features of the reflected signal from the person's chest. Furthermore, we explore the assessment of second and third orders cyclic features of the cyclostationary signal processing performance by developing the cyclic statistics of each order. The cyclic mean for the first order, the conjugate cyclic autocorrelation and the second cyclic temporal cumulant for the second order. Then, the third cyclic temporal moment and cumulant was also developed. In addition, the analysis is carried out using a reduced number of samples to reduce the response time and complexity of system radar.

3.2 State of the art on existing signal processing techniques

Respiration rate (RR) and heart rate (HR) are considered the most important physiological parameters indicating the body's functioning state. Since the early development of radars for the detection of vital signs, they incorporated analog and digital signal processing to separate the small heart signal from the much larger respiratory signal, hence the subject did not need to hold their breath for the heart rate to be measured. Thus the heart and respiration could be measured simultaneously. Therefore, the existing work is done in controlled environments where noise is eliminated and the person under test remains stationary. Thus the heart rate is corrupted in noise and can not be extracted correctly.

According to radar theory for monitoring vital signs, as presented in Chapter 2, a continuous wave radar with the chest of a person stationary as the target should receive a signal similar to the transmitted signal with its phase-shift modulated by the mechanical displacement of the chest varying in time. When the phase-shift is demodulated, the thoracic displacement over time can be inferred, from which heart and respiratory rates can be determined. Analog and digital signal processing removes clutter and other noise, while discriminating the desired signal from interference, separates cardiac and respiratory signals and determines heart and respiratory rates. Advanced detection signal processing methods have been reported in the literature. Different filtering techniques was introduced [6, 19, 57, 55, 48], varying the type and the order of the filter, as well as the cutoff frequencies of each filter, in order to isolate the cardiac signal from the respiratory signal. For example, in [48] the heartbeat signal was first separated from the respiration signal by a Butterworth bandpass filter (BPF) with pass-band 0.7 to 3 Hz. The filtered signal was then windowed and auto-correlated. After that, the author propose to use a fast Fourier transform (FFT) to the auto-correlated signal to obtain the heartbeat rate.

There are many efforts in literature for removing random body motions for vital signs detection. In fact, the vital signs detection can be achieved when the body of the subject is stationary, otherwise any random motion creates harmonics and distortions in the signal such that accuracy detecting the vital signs becomes impossible. For example in [47], Ghanzhi Li et al. suggested a solution based on two-Doppler radar system by which they cancelled random body motions. They presented the use of two radars placed on the front and back sides of the body in order to have two different samples of the phase-shift modulation. By having them and considering the fact that the signs of the modulated phase-shifts due to body motion are different, they can be combined such that the output contains only the vital signs' phase-shift modulation. To implement the signal processing, they used phase-shift demodulation, which has advantages compared to the complex signal analysis [76]. To exploit the benefits of the phase-shift demodulation, the DC offset and IQ imbalances of the complex signal should have been removed before moving to the phase-shift domain. However, since the chest displacement caused by respiration is between 4 and 12 mm, and the chest displacement due to heartbeat alone ranges between 0.2 and 0.5 mm, the respiration signature is therefore much larger and stronger than the heartbeat component [39]. Heartbeat is more sensitive to the interference introduced by respiration harmonics and noise from remote sensing and the environment, which makes an accurate estimation difficult.

To solve the harmonic problem, the wavelet transform (CWT) [52] combined with either empirical mode decomposition (EMD) was introduced in [35]. In [52], the author proposed a wavelet transform based data length variation technique for the purpose to realise fast detection of heart rate utilizing CW Doppler radar. Compared to the traditional FT method, the accuracy is improved dramatically, because the proposed method is able to distinguish respiratory harmonics from the heartbeat signal by examining the peak property of the combined wavelet frequency spectrum. In a follow-up paper [36], Ensemble Empirical Mode Decomposition (EEMD) was used. This technique consists of applying the EMD decomposition several times, then calculating the average of the modes. A curvelet transform was applied in [51] in order to remove the direct coupling wave and background clutters, then the signal was denoised using a singular value decomposition. Both the FFT and the Hilbert–Huang transform were applied in order to separate and extract HR and RR.

Other works have focused on the linear and nonlinear methods, such as arctangent demodulation [76], complex demodulation [46], and adaptive DC calibration [114, 30], have been proposed to directly demodulate the return signal phase-shift to obtain vital-sign information. In [76], Park et al. propose the arctangent demodulation in single receiver-channel Doppler radar, combined with dc offsets removing by using a high-pass filter.The accurate phase-shift demodulation can be achieved by combining the two channels using a quadrature receiver. An other technique of demodulation is presented in [46], which is a complex signal demodulation. This method is proposed due to its robustness against DC offset in direct conversion system and to eliminate the null detection point problem in non contact vital sign detection.

In the case of a low signal-to-noise ratio (SNR) and body motion interference, the modulated back-scattered radar signal is non-stationary with hidden periodicities, which lead to use a nonlinear transformation based on cyclic statistics which is the cyclostationarity theory [39, 38]. This non-stationary approach have a cyclic pattern of statistical properties. It mainly uses the cyclic statistics to analyze, detect, and estimate signals with extracting the hidden periodicities without any needing phase-shift unwrapping or demodulation. It was first introduced for this purpose in [39, 38]. In these reported works, Somayeh Kazemi et al. proposed using simulations tools for cyclostationarity to estimate the Spectral Correlation Function (SCF) with a very large number of samples. An other work using a high order of the same approach was reported in [109]. It introduces the Third-Order Cyclic Cumulants (TOCC). However, the authors describe the higher-order cyclostationary for a zero mean value signal, this consideration makes the second cyclic cumulants and the third order cyclic cumulants both equivalent to their respective moments, while that is not true in the case of signal reflected from the chest's person. For this type of signal, the mean value is non-zero. Therefore, the second cyclic cumulants and the third cyclic cumulants are different from their respective moment and cyclic moment.

In this PhD, we propose to develop the theoretical vital sign detection analysis based on the cyclostationary approach, using cyclic moments and cyclic cumulant for the three first orders. To verify the detecting performances of the proposed method, a series of simulations and experiments considering different person under tests are carried out to confront the theory. Moreover, we evaluate the impact of the numbers of samples and the noise while considering a small number of samples to reduce both the computational cost and the response time of the digital signal-processing block.

3.3 Modeling of vital signals for radar

The modeling of vital signals is essential for radar analysis and simulation. In this section, we discuss the modeling of respiratory and cardiac signals used for our modeling.

3.3.1 modeling of the cardiac signal by a sinusoidal signal

Since the cardiac signal a priory does not have a mathematical model for specifying cardiac activity, we sought to establish an approximate model to use it in our Matlab codes for the first simulation. The first idea we investigated was that the cardiac signal is quasi periodic motion with a time-varying period to simplify the study.It can be further developed as follows:

$$x_h(t) = a_h \cos\left(2\pi f_h t + \theta_h(t)\right) \tag{3.1}$$

The amplitude and phase-shift variations $h(t)$ and $\theta_h(t)$ are zero mean random processes. They model the phenomenon of heart rate variability [34]. However, for the first study we consider a constant approximation of these values, by carefully choosing the sensing interval T, so that:

$$x_h(t) = a_h \cos\left(2\pi f_h t\right), \quad t \in [(k-1)T, kT] \tag{3.2}$$

3.3.2 modeling of the cardiac signal by an ECG signal

Modeling the heartbeat is an essential step for the automatic identification of characteristic waves. Its aim is to find a representation, as simple and compact as possible, of the shape of each constituent wave of the heartbeat. Indeed, the representation of waves would consist in describing the signal by its amplitude at each instant for each wave constituting the cardiac signal. The data used for the generation of the sequence of events and waves in a cardiac cycle is based on part 2.2.3 [67].

3.3.3 respiration signal pattern

The respiration signal $x_r(t)$ is nearly periodic, with a time-varying period. It can be further developed as follows:

$$x_r(t) = a_r \cos\left(2\pi f_r t + \theta_r(t)\right), \tag{3.3}$$

where the amplitude and phase-shift variations $\alpha_r(t)$ and $\theta_r(t)$ are zero mean random processes. They model the phenomenon of respiration rate variability [34]. So that:

$$x_r(t) = a_r \cos(2\pi f_r t), \quad t \in [(k-1)T, kT]. \tag{3.4}$$

3.3.4 Chest signal pattern

The movement of the left ventricle of the heart within the chest is the primary cause of movement of the chest due to heart beats. The contraction of the diaphragm during inhalation causes air to flow into the lungs and pushes the abdomen and ribs outward. This causes the expansion of the chest due to respiration. The chest movements due to heart beating and breathing is $x_{HR}(t) = x_r + x_h$. It denotes the displacement generated by respiration and heartbeat.

The zoom on the signal of the chest motion see in the Figure (3.1), we can see the inhales and exhales of the person under test. The blips on the signal allows to his heartbeats.

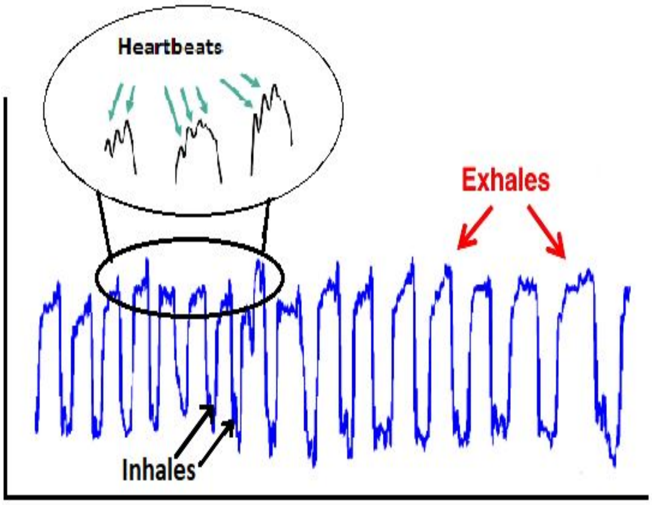

Figure 3.1: The signal of chest motion

3.3.5 Reflected signal pattern

The CW transmitted signal, which is also the local oscillator signal, can be written as follows:

$$T(t) = \cos(2\pi f t + \varphi(t)) \tag{3.5}$$

Let us consider that the target is located at a distance d_0. Furthermore, let us define the time-varying chest displacement as $x_{HR}(t)$ and the random body motion as $x_I(t)$, then the transmitted signal T(t) travels the distance $2\,d(t)$, where $d(t) = d_0 + x_{HR}(t) + x_I(t)$ and becomes the received signal R(t).

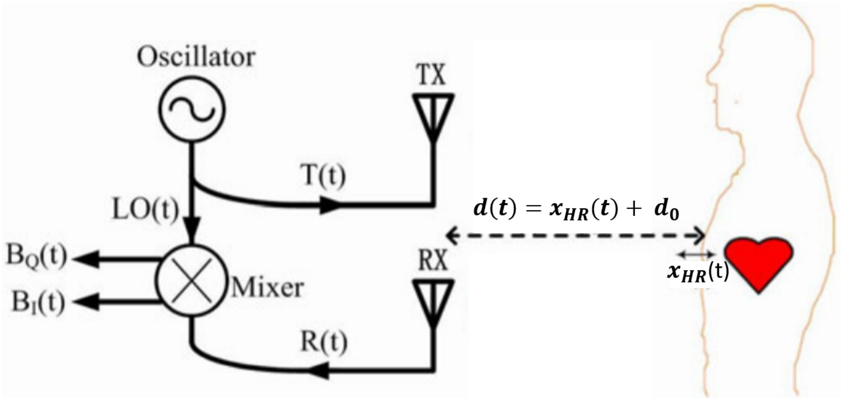

Figure 3.2: Functional diagram of Doppler radar.

The chest displacement $x_{HR}(t)$ varies between 4 mm and 12 mm due to RR, while it ranges between 0.2 mm and 0.5 mm due to HR. It is achieved with phase-shift variation $\Delta\theta$ based interferometry technology, and the variation of $x_{HR}(t)$ between two adjacent instants can be given as (3.6):

$$\Delta\theta = \frac{4\pi x_{HR}(t)}{\lambda}, \tag{3.6}$$

where λ is the free-space wavelength of the transmitted signal and $\lambda = \frac{c}{f}$ (c represents the speed of light and f RF frequency of operation). Hence the received signal from the body can be expressed as follows:

$$R(t) = A_{HR}\cos\left[2\pi ft - \frac{4\pi d}{\lambda} - \frac{4\pi x_{HR}(t)}{\lambda} - \frac{4\pi x_I(t)}{\lambda} + \varphi\left(t - \frac{2d_0}{c}\right)\right] + N(t) \tag{3.7}$$

where $x_I(t)$ can be modeled as a two-dimensional (2D) quasi-periodic motion considered as two independent 1D motions [39]. Each 1D motion is modeled as a stationary random process with a uniform distribution in a specified direction.

The receiver captures and down-converts the signal by comparing the phase-shift of the reflected wave with the local oscillator LO(t). In quadrature receiver configuration, two orthonormal components at the baseband are obtained, namely, $B_I(t)$ and $B_Q(t)$. The baseband signal is proportional to the cosine or sine of a constant phase-shift shift θ , which is determined by hardware and d_0 , summed with a time-varying phase-shift shift proportional to the time-varying chest motion $x_{HR}(t)$, and with the residual phase-shift noise $\Delta\varphi$(t). The two receiver output channels can be expressed as follows:

Once the reflected signal is mixed with the local oscillator, the baseband quadrature signals can be expressed as follows:

$$B_I(t) = A_{HR}\cos\left[\frac{4\pi d_0}{\lambda} + A_r\cos\left(2\pi f_r t\right) + A_h\cos\left(2\pi f_h t\right) + \frac{4\pi x_I(t)}{\lambda} + \Delta\varphi\left(t\right)\right] + N_I(t) \tag{3.8}$$

$$B_Q(t) = A_{HR}\sin\left[\frac{4\pi d_0}{\lambda} + A_r\cos\left(2\pi f_r t\right) + A_h\cos\left(2\pi f_h t\right) + \frac{4\pi x_I(t)}{\lambda} + \Delta\varphi\left(t\right)\right] + N_Q(t), \tag{3.9}$$

where

$$\Delta\varphi\left(t\right) = \varphi(t) - \varphi\left(t - \frac{2\pi}{c}\right) \tag{3.10}$$

$$A_r = a_r\frac{4\pi}{\lambda} \quad and \quad A_h = a_h\frac{4\pi}{\lambda}. \tag{3.11}$$

The baseband signal can be simplified to its complex form:

$$B_b(t) = A.M(t)exp\left[jA_r cos(2\pi f_r t)\right] exp\left[jA_h cos(2\pi f_h t)\right] + Z(t) \tag{3.12}$$

where

$$A = A_{HR}exp(j\frac{4\pi d}{\lambda}) \tag{3.13}$$

$$M(t) = exp\left[j(\frac{4\pi x_I(t)}{\lambda} + \Delta\varphi\left(t\right))\right] \tag{3.14}$$

and $Z(t) = N_I(t) + jN_Q(t)$ is the complex noise. According to Jacobi Anger expansion:

$$e^{jzcos\alpha} = \sum_{q=-\infty}^{\infty} j^q J_q(z)e^{jq\alpha} \tag{3.15}$$

where J_q represents the q-th-order Bessel function of the first kind, the heart and respiration signals in (3.12) can be expanded as Bessel series. Therefore, the baseband signal can be simplified into the following equation:

$$B_b(t) = AM(t)\sum_{q=-\infty}^{\infty}\sum_{l=-\infty}^{\infty} j^{q+l}J_q(A_r)J_l(A_h)exp\left[j2\pi(qf_r + lf_h)t\right] + Z(t) \tag{3.16}$$

3.4 Overview of signal processing definitions

Before launching into the simulations, it is necessary to take into consideration several parameters and conditions, in order to have successful results.

3.4.1 Frequency resolution

To compute the spectrum of an analog signal digitally, a finite-duration record of the signal is sampled and the resulting samples are transformed to the frequency domain by a DFT or FFT algorithm. The sampling rate fs must be fast enough to minimize aliasing effects. If necessary, an analog anti-aliasing prefilter may precede the sampling operation [92].

3.4.2 Fourier transform

The fast Fourier transform (FFT) is a fast implementation of the discrete Fourier transform (DFT). It is used to determine the frequency characteristics of a signal; when used for a sampled signal, the discrete Fourier transform (DFT) is used. With N time domain samples, the DFT determines the spectral content of the input at N equally spaced frequency bins. The frequencies at which the analysis is performed is determined by the sampling frequency f_s and N:

$$f_{analysis}(m) = \frac{mf_s}{N} a_h, 0 \leq m \leq N \tag{3.17}$$

There are several ways to calculate the DFT, such as solving simultaneous linear equations or the correlation methods. The FFT is another method for calculating the DFT. While it produces the same result as the other approaches, it is incredibly more efficient, often reducing the computation time by hundreds [92].

The signal is made up of N points. The FFT operates by decomposing an N point time domain signal into N time domain signals each composed of a single point. The second step is to calculate the N frequency spectra corresponding to these N time domain signals. Lastly, the N spectra are synthesized into a single frequency spectrum.

3.4.3 Shannon theory

The sampling theorem known also as Shannon sampling theorem, or the Nyquist sampling theorem. According to the Shannon Sampling Theorem, you can completely reconstruct properly a continuous-time signal from discrete, equally spaced samples if the highest frequency in the time signal is less than half the sampling frequency. Half the sampling frequency equals the Nyquist frequency. The Shannon Sampling Theorem bridges the gap between continuous-time signals and digital-time signals [92].

3.5 Simulation results: detection and identification techniques

3.5.1 The use of error correction methods

The objective of this part was to develop an algorithm able to detect and separate a respiration and heartbeat from data obtained by CW radar. To answer this problem, we have chosen to carry out simulations and some tests in order to test an existing technique in the literature and to evaluate it according to the needs of our application. We worked on the ellipse adjustment method in order to improve and eliminate errors when receiving the signal, so phase-shift demodulation happens more easily and we get more accurate vital sign frequencies. The two error detection and correction methods that are based on the fit of the ellipse, namely the algebraic and geometric method were developed. Therefore, the three methods applied on our type of signals.

Figure 3.3 shows the methodology used to estimate and correct phase-shift imbalance errors as well as DC compensation and then extract vital signs. The process used to achieve this goal is divided into three main stages:

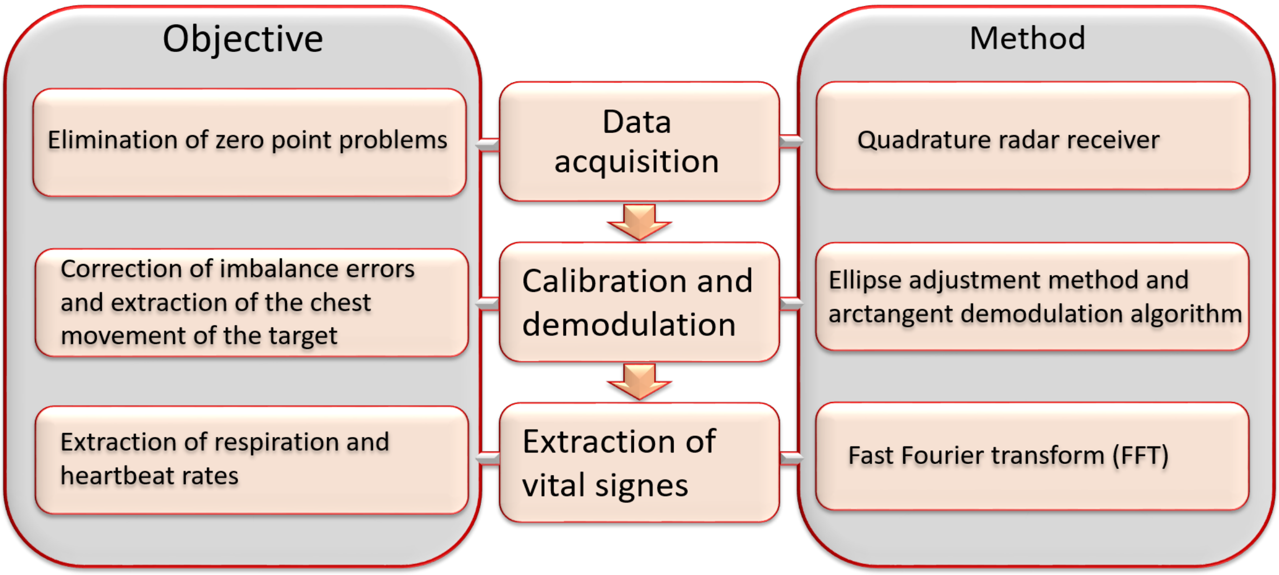

Figure 3.3: Representation of the approach deployed to estimate and correct the phase-shift as well as DC compensation

The first step in this methodology is the data acquisition, we choose to use a Doppler radar with a quadrature receiver to avoid zero point errors, which allows us to obtain a phase-shift linearly proportional to the movements of the chest $x_{HR}(t)$ during the phase-shift extraction step (third step). The second step is correcting the imbalance errors and extracting the target's chest displacement, this step itself is divided into two parts. The first part consist on removing amplitude and phase-shift errors as well as DC offsets [59].Then using the ellipse fit methods of two different families: geometric fit and algebraic. The suitability of these two methods was tested for our application with respect to two parameters:

- The length of the arc, which in our case depends on the frequency of the radar and / or the amount of data in the signal.
- The value of the phase-shift error.

These parameters affect the precision of the ellipse adjustment method, this hypothesis has been tested with simulation signals and real signals. The second part consists in demodulating the signal in the baseband, using the arctangent demodulation to obtain the movement of the chest of the target $x_{HR}(t)$. Indeed, among the methods studied in the state of the art for estimating the phase-shift of signals, arctangent demodulation remains the most interesting [110]. It is the best compromise for application which require both good precision and little computing time. The third step is to extract the heartbeat and the respiration rates by Fast Fourier Transform (FFT). The most important power peaks correspond to the frequency of the heart.

3.5.2 Simulation

In this part, we will start by simulating the chest displacement signal $x_{HR}(t)$ as well as the heartbeat signals and respiration. The values used are presented in Table 1. These values come from the literature and correspond to the performances announced by several existing solutions.

3.5.3 Estimation and correction of I / Q imbalances and DC offsets with the ellipse adjustment method

In this part, we will estimate the imbalances (amplitude error and phase-shift error), as well as the DC offsets from equations.

3.5.3.1 I / Q Imbalances and DC Offsets

In quadrature Doppler radar systems, the receiving I and Q channels are suffering from imbalance in amplitude and phase-shift I / Q, as well as direct

Table 3.1: Parameters defined for the simulation

Radar frequency	5.8 GHz
Cardiac frequency f_h	1.25 Hz
Heart amplitude a_h	0.5 mm
Breathing frequency f_r	0.25 Hz
Breathing amplitude a_r	10 mm
Distance between antenna and target	20 cm
Amplitude error A_e	0.9
DC Offset of Chain I (V_i)	0.1
DC Offset of Chain Q (V_q)	0.1
phase-shift Error (E_r)	40 °

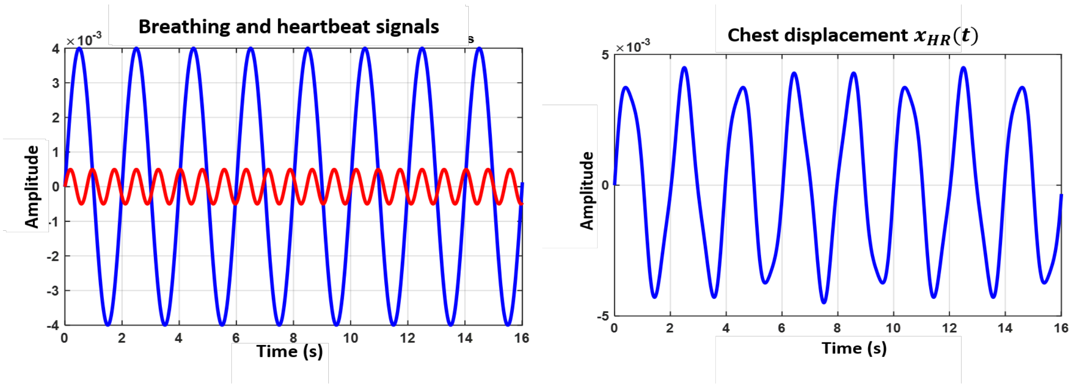

Figure 3.4: Representation of the breathing and heartbeat signals and the chest displacement

current (DC) shifts resulting from reflections from stationary objects, imperfections in circuit components and clutter reflections. There are several work concern the compensation of the DC offset in Doppler radars. However, these methods are either inaccurate or sensitive to environmental changes. With these imperfections, the baseband signals 3.8 and 3.9 are written as follows [104, 51] [102]:

$$B_I(t) \approx V_I + A_B \cos\left[\theta + \frac{4\pi x_{HR}(t)}{\lambda} - \theta_0 + \Delta\phi\left(t\right)\right] \tag{3.18}$$

$$B_Q(t) \approx V_Q + A_B A_E \sin[\theta + \frac{4\pi x_{HR}(t)}{\lambda} - \theta_0 + \Delta\phi(t) + \phi_E] \tag{3.19}$$

Where

$$\Delta\phi\left(t\right) = \phi(t) - \phi\left(t - \frac{2d_0}{c}\right) \tag{3.20}$$

is the residual phase-shift noise and

$$\theta = \frac{4\pi d_0}{c} + \theta_0 \tag{3.21}$$

is the constant phase-shift shift dependent on the nominal distance to the target d_0 and V_I, V_Q correspond to the DC offsets in the I and Q quadrature channels. The amplitude error A_E is defined as the ratio of signal amplitude Q to signal amplitude I (RF signals). $\varnothing_E$ is defined as the difference between the phase-shifts of the two LO signals minus $\frac{\pi}{2}$ (the phase-shift of the wave generated in transmission and that of the wave generated in reception to bring the signal back to baseband) [35].

By representing in the complex plane the signal of channel Q as a function of that of channel I, the respiration forms an arc of a circle, the radius of the circle is A_B and the center of the circle is (V_I, V_Q). The method exploits the I / Q plane, if the two channels are perfectly balanced, a target moving in the radial direction forms a circle in the I / Q plane. Any imbalance in the channels results in an ellipse, as shown in Figure 3.5 . The measurements on this ellipse are made to estimate DC and amplitude and phase-shift errors [35]. The central of the ellipse indicates the DC offsets of the two channels, and the difference in rotation and length between the two axes indicates the amplitude error A_E and phase-shift error ϕ_E: Find the width A and the height B; Thus, A_E is equal to $\frac{B}{A}$. It is the distance between two joints that is decided by the center line parallel to the I axis and the ellipse, the ϕ_E can be calculated as an $arcsin(\frac{C}{A})$. These errors and offsets are then removed from the $B_I(t)$ and $B_Q(t)$ signals using the Gram-Schmidt orthogonalization method. The orthogonal signals obtained come from equation 3.22.

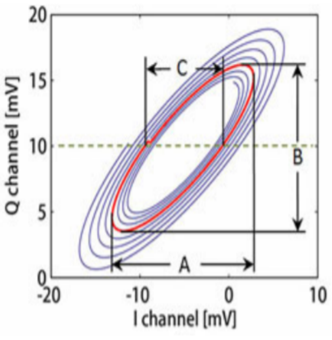

Figure 3.5: Complex plot of the Q channel as a function of the I channel

3.5.3.2 Correction of errors: Geometric method of fitting the ellipse (Gram-Schmidt procedure)

To avoid any distortion of the signal, the imbalances must be calculated and eliminated before demodulation with the arc tangent function [35]. Known amplitude and phase-shift imbalances, as well as DC offsets can be corrected using the Gram-Schmidt (GS) procedure. For this application, the vectors B_i and B_q are converted into orthonormal basis vectors B_{ii} and B_{qq}. B_{ii} is assumed to be B_i then B_q is converted to be normal to B_{ii}:

$$\begin{bmatrix} B_{I,orth} \\ B_{Q,orth} \end{bmatrix} = \begin{bmatrix} 1 & 0 \\ -tan(\phi_E) & \frac{1}{A_E cos(\phi_E)} \end{bmatrix} \begin{bmatrix} B_I - V_I \\ B_Q - V_Q \end{bmatrix} \tag{3.22}$$

This method is insufficient in wideband systems where the phase-shift imbalance varies with frequency. However, the Doppler radar system is an extremely narrow band, so none of these concerns apply. The geometric method was evaluated using a radar at frequency 5.8 GHz. The phase-shift of each filtered component is extracted by applying the arc tangent method to the I and Q output ratios, it is always possible to obtain an accurate phase-shift demodulation regardless of the position of the target [76].

$$\theta' = arctan(\frac{B_Q}{B_I}) \tag{3.23}$$

The displacement of the chest can be recovered by enveloping the demodulated phase-shift signal. Then measure the impact of the various errors after demodulation (Amplitude error A_E, phase-shift error Φ_E and DC offset).

Figure 3.6 shows the evolution of error Δx as a function of amplitude, phase-shift (Figure 3.6c) and DC offsets errors (Figure 3.6b), before correction and after correction. No error is observed on the signal by increasing the error on the amplitude (Figure 3.6a). on the other hand, we notice that more the value of the DC offsets increase, more the error on the signal δx increases. However, their impact on the signal remains low. In addition, DC offsets are fully corrected after using the correction algorithm. In Figure 3.6c, we notice that the value of the error δx increases with the phase-shift error up to a value of 40%, after that it starts to decrease and becomes much smaller.

By applying our correction algorithm, we are able to correct the phase-shift errors and therefore reduce the impact of the error on the signal. The increase in DC offsets and the amplitude error generate an increase in the error δx.

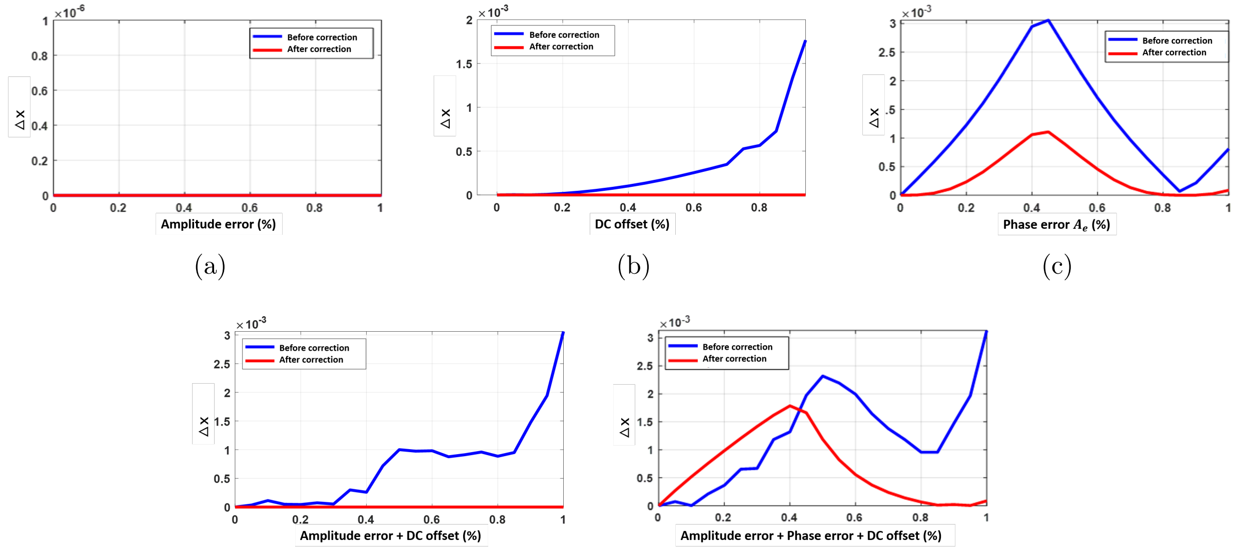

(a) (b) (c)

(d) (e)

Figure 3.6: Evolution of the error Δx according to each of the errors. (**a**) Amplitude error A_e; (**b**) DC offset; (**c**) phase-shift error; (**d**) Amplitude error and DC offset; (**e**) All errors

The impact of these errors on the signal remains low (Figure 3.6d). We also observe that the errors are completely corrected after using the correction algorithm. Therefore, including the phase-shift error ϕ_E into our simulation shows that the correction algorithm becomes less efficient (Figure 3.6e).

3.5.3.3 Correction of errors:Algebraic ellipse adjustment method

This method consists of estimating the center of an arc to be studied intensively. Different methods are used to estimate the center of the arc [111], among them the Least squares adjustment method with Levenberg-Marquardt [63].The last method (LM) is a recursive least squares (LSF) adjustment problem solving algorithm. This method is the classical Gauss-Newton method with LM correction. Once the errors are removed, the ellipse becomes a circle centered on (0,0) with a radius A_b.
We implemented the LM method [17] and evaluate its performance in simulation for the same frequencies used above.

Figure 3.7 and 3.8 show the evolution of error Δx as a function of amplitude, phase-shift and DC offsets errors, before error correction and after correction. With the algebraic correction method we observe similar trends with the geometric method. The error on the signal x (t) is non-existent by varying the amplitude error (Figure 3.7a). It increases as a function of the DC offsets (Figure 3.7b), but the impact of the DC offset remains low and is removed after correction. The error Δx increases according to the phase-shift error in a linear way to reach its maximum at a value of 43% then it goes down again until becoming zero (Figure 3.8a). Our algorithm does not allow us to correct for phase-shift errors, as can be seen in Figure 3.8a and 3.8b, the value of Δx increases significantly after the correction. The algorithm is therefore efficient only in the absence of the phase-shift error.

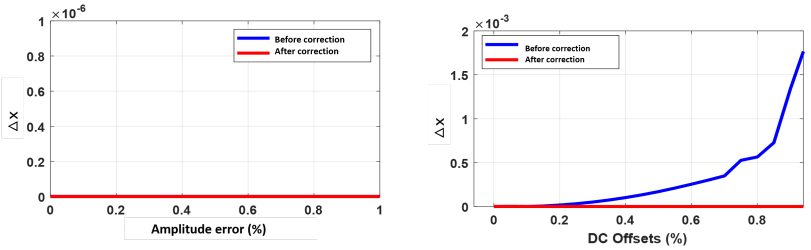

(a) (b)

Figure 3.7: Evolution of the error Δx according to each of the errors. (**a**) Amplitude error A_e; (**b**) DC offset

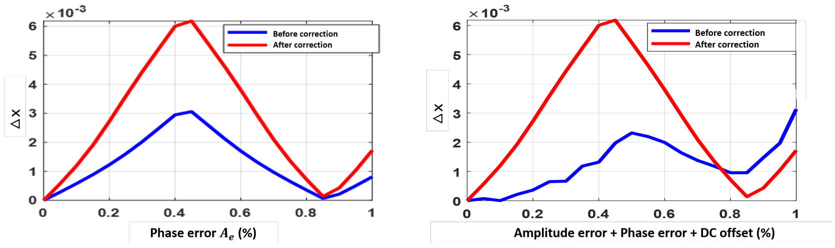

(a) (b)

Figure 3.8: Evolution of the error Δx according to each of the errors.(**a**) phase-shift error; (**b**) All errors

3.5.4 Detection of the breathing and the heartbeat rates

The accuracy of the error detection methods is greatly affected by two parameters, the arc length, which in our case depends on the frequency of the radar and the value of the phase-shift error. Both the algebraic and the geometric methods offer very acceptable results for the correction of DC offset and amplitude errors. On the other hand, they remain very sensitive to the phase-shift variation.

Regarding the algebraic method, for a radar frequency of 5.8 GHz, the algorithm does not allow to correct the phase-shift errors. It only performs well in the absence of this error. For low frequencies, it cannot estimate the errors because the arc length is too small, which means that the resulting curve was a hyperbola or a parabola instead of an ellipse. However, the geometric method, the error estimation and correction algorithm is efficient for the amplitude errors A_E and DC offsets. For the phase-shift error in the case of the frequency system 5.8 GHz, the algorithm detects and corrects the phase-shift errors separately (not added to the amplitude error and the DC offsets) but for low frequencies, its works only from a certain value. By comparing these two methods, it emerges that the geometric ellipse adjustment method is more efficient. To extract heart and respiratory beats, geometric method and the Fast Fourier Transform (FFT) were applied. Then the most important power peaks are equivalent to heart rate and respiration rate. We can clearly identify the respiratory rate and a little less obviously the heart rate. However, by applying the method developed on these signals, only the respiratory frequency is extracted. Heart rates are completely erased by this operation. The work carried out brought a considerable gain compared to the results existing in the literature, however, improvements remain possible, especially to deal with phase-shift problems. To extract heart and respiratory beats, the Fast Fourier Transform (FFT) was applied. Then the most important power peaks are equivalent to heart rate and respiration rate.

Both of these methods offer very acceptable results for the correction of DC offset and amplitude errors. On the other hand, they remain very sensitive to the phase-shift variation. By comparing these two methods, it emerges that the geometric adjustment method is more efficient. We use the geometric method and apply it for signal processing and for the purpose of extracting heart and respiratory rhythms. We can clearly identify the respiratory rate and a little less obviously the heart rate. However, by applying the method developed on these signals, only the respiratory frequency is extracted. Heart rates are completely erased by this operation. The work carried out brought a considerable gain compared to the results existing in the literature, however, improvements remain possible, especially to deal with phase-shift problems.

3.6 Proposed approach: cyclostationarity at higher orders

The principle of radar for monitoring vital signs is based on phase-shift modulation induced by movement of the thorax. In fact, the human chest wall has a variable position over time, due to respiration and heart rate. In order to accurately estimate the information of interest, various signal processing techniques were used, including the theory of cyclostationarity. This theory makes it possible to estimate and detect vital signs without demodulation and at low SNR in the presence of interference.

3.6.1 General theory of cyclostationary process in the time domain

Pioneering work in cyclostationarity date back to the early 1958s with the work of Bennett [4] and 1963s with Gladyshev [27]. But it is began to arouse practical interest in recent years with the development of the telecommunications field. Since then, several contributions have enriched this theory of cyclostationary processes. As an example, we cite Gardner and his collaborators [26].

3.6.1.1 Definitions

Cyclostationary processes, sometimes called periodically stationary processes, are special cases of non-stationary processes in the sense that their statistical properties vary over time but in a periodic manner. These cyclostationary processes are generally generated by systems with random output and periodically disturbed over time. Examples of physical systems are meteorological processes that are disturbed by the effect of the earth's rotation or by noises produced by rotating machines [106]. In the important case of communications systems, information messages of a random nature combine with the periodicity introduced by modulations, coding, etc. to acquire cyclostationarity.

Let x(t) be a continuous time random process with complex values, x(t) is a cyclostationary process of order m if and only if its statistical properties up to order m vary periodically in time. It is mean that a time-series is considered to be m-th order wide sense cyclostationary if its m-th order time varying temporal moment and cumulant is periodic in time. In the literature, when the word cyclostationary is used alone and without further specification, the term is supposed to mean wide-sense cyclostationary, so in the rest of this report, we adopt the same terminology.

Both moments and cumulants are useful to characterize an m-th order cyclostationarity of signal. The m-th order lag product of the signal x(t) is define as follow :

$$L_x(n,\tau)_{m,p} = \prod_{j=1}^{n} x^{(*)_j}[n + d_j] \tag{3.24}$$

where $(*)_j$ denotes an optional conjugation, p denote the number of possible conjugations and $\tau = [d_1 .....d_m]$.

The higher order cyclic statistics of a cyclostationary signal x(t) are defined as follows:

- **Cyclic Temporal Moment Function CTMF:**

  $M_x^{\alpha}[\tau]_{m,p}$ defines the m-th order Cyclic Temporal Moment Function (CTMF)[112]:

  $$M_x^{\alpha}[\tau]_{m,p} = \lim_{N \to \infty} \frac{1}{N} \sum_{n=0}^{N-1} L_x[n,\tau]_{m,p} \quad exp(j2\pi\alpha n) \tag{3.25}$$

  where $A_\alpha = \{\alpha | L_x[t;\tau]_{m,p}] \neq 0\}$. It should be noted that the set of discrete cyclic frequencies A_α, is defined as $\alpha \in [\frac{-1}{2}, \frac{1}{2}[$, where the cyclic resolution is of order $\Delta\alpha = \frac{1}{N}$.

- **Cyclic Temporal Cumulant Function CTCF:**

  The n-th order cyclic temporal cumulant function (cyclic cumulant) is a Fourier coefficient of the cyclic temporal cumulant function. The cyclic cumulants are pure sine-wave amplitudes, and they can be computed by combining cyclic moment amplitudes.

  $C_x^{\nu}[\tau]_{m,p}$ defines the m-th order Cyclic Temporal Cumulant Function, and is a Fourier coefficient such that:

  $$C_x^{\nu}[\tau]_{m,p} = \lim_{N \to \infty} \frac{1}{N} \sum_{n=0}^{N-1} cum[x^{(*)_1}(n+d_1)...x^{(*)_m}(n+d_m)]exp(-j2\pi\nu n) \tag{3.26}$$

  $A_\nu = \{\nu \quad | \quad C_x^{\nu}[\tau]_{m,p} \neq 0\}$ denotes the entire set of cyclic frequencies.

- **Moments to cumulants conversion formula:**

  CTCF can be directly computed from the CTMF which represents the cyclic moment to cyclic cumulants conversion that is given by the combination of products of lower-order cyclic temporal moment functions:

  $$C_x^{\nu}[\tau]_{m,p} = \sum_{D_m} \left[(-1)^{d-1}(d-1)! \sum_{\alpha^\intercal 1 = \nu} \prod_{i=1}^{d} R_x^{\alpha_i}[\tau_{bi}]_{m_i,p_i} \right] \tag{3.27}$$

  where ν is the pure sine wave of the lower order cyclic frequencies and α is the impure sine-wave of order m. The vector of cycle frequencies

α is the vector of cyclic temporal moment cycle frequencies, and they must sum up to the cyclic-cumulant cycle frequency ν.

In (3.27), the sum is over distinct partitions of the index set { 1,...,m }, referred to as D_m, d is the number of elements in a partition,$1 \leqslant d \leqslant m$. The set of indexes belonging to a partition is denoted as $\{b_i\}_{i=1}^{d}$.
The cyclic moments to cyclic cumulants conversion is a powerful tool in signal processing, as it allows the derivation of cyclic cumulants directly from the data and that is what we will use in our algorithm.

The conversion of cyclic moments into cyclic cumulants has the following interpretation. In fact,in the literature, the set of cyclic frequencies defined from the cyclic moments is referred to as “impure cyclic frequencies”, as it can be the result of a combination of lower order cyclic frequencies. Whereas, the cyclic frequencies defined from the cyclic cumulants are known as the “pure cyclic frequencies”, as they characterize the m-th order additive sine-waves only. In other words, cyclic cumulants isolate the cyclic feature of the m-th order from products of lower orders. They represent the part of the m-th order moment sine wave that is independent of all lower-order moment sine waves. Hence, all possible products of lower-order pure sine-waves can be subtracted from the m-th order cyclic moment sine waves to obtain the cyclic cumulant of order m [112].

3.6.1.2 The first-order cyclic moment (the cyclic mean)

The first order of the algorithm which is the cyclic mean is a Fourier transform in terms of the cyclic frequencies, in contrast to the standard Fourier analysis which as a function of the frequency. Those cyclic frequencies are is a combination of the respiratory rate and the heart rate, which differ from one order to another. Then, we proposed the second order of the approach to make more difference. The cyclic mean of the baseband received signal can be defined as follows [16]:

$$CM_{B_b}(\alpha) = \lim_{T \to \infty} \frac{1}{T} \int_{\frac{-T}{2}}^{\frac{T}{2}} B_b(t)\ e^{-j2\pi\alpha t} dt \tag{3.28}$$

$$CM_{B_b}(\alpha) = \lim_{T\to\infty} \frac{1}{T} \int_{\frac{-T}{2}}^{\frac{T}{2}} E[AM(t) \sum_{q=-\infty}^{\infty} \sum_{l=-\infty}^{\infty} j^{q+l} J_q(A_r) J_l(A_h) exp[j2\pi(qf_r + lf_h)t] \\ + Z(t)] exp(-j2\pi\alpha t) dt \tag{3.29}$$

The noises $Z(t)$ and $M(t)$ are uncorrelated and stationary [2]. Furthermore, using the Dirac delta identity

$$lim_{T\to\infty} \frac{1}{T} \int_{\frac{-T}{2}}^{\frac{T}{2}} exp(\pm j2\pi f t)\ dt = \delta(f) \tag{3.30}$$

the cyclic mean in (3.16) can be derived as:

$$CM_{B_b}(\alpha) = A\mu_M \sum_{q=-\infty}^{\infty} \sum_{l=-\infty}^{\infty} j^{q+l} J_q(A_r) J_l(A_h) \delta(\alpha - (qf_r + lf_h)) + \mu_Z \delta(\alpha) \tag{3.31}$$

where μ_M and μ_Z represent the mean of the multiplicative noise $M(t)$ and the additive noise $Z(t)$ respectively.

If $\mu_M \neq 0$, then the baseband received signal is first order almost-cyclostationary, with a set of cyclic frequencies $A_{\alpha 1} = \{\pm(qf_r + lf_h), 0\}$. As it be noticed, the cyclic frequencies are a combination of heart and respiration rates. Hence, in this case, the vital signs can be extracted from the first-order cyclic moment (the cyclic mean). However, if $\mu_M = 0$, then defining the cyclic autocorrelation of $y(t)$ is of a great use.

3.6.1.3 The second-order cyclic moment

The continuous-time process $B_b(t)$ is said to be a second-order cyclostationary if its first and second-order moments are periodic functions of time. The second-order cyclic moment is defined as follows [112]:

$$R_{B_b}(\alpha, \tau) = \lim_{T\to\infty} \frac{1}{T} \int_{\frac{-T}{2}}^{\frac{T}{2}} B_b(t) B_b^*(t+\tau) exp(-j2\pi\alpha t)\ dt. \tag{3.32}$$

Superscript $(*)$ denotes an optional complex conjugation (see [65] for clarification on this notation) which is a continuous function of the variable τ and discrete of the variable α. It is non-zero for some $\alpha \neq 0$. If the conjugation is present, then it is the cyclic autocorrelation function. If the conjugation is absent, then it is the conjugate cyclic autocorrelation function. Both second-order moments are needed for a complete second-order characterization in the wide-sense of complex-valued processes [65].

Replacing $y(t)$ with the signal model in (3.16), we can write:

$$R_{B_b}(\alpha,\tau) = A^2 R_M(\tau) \lim_{T\to\infty} \frac{1}{T} \int_{\frac{-T}{2}}^{\frac{T}{2}} \sum_{q=-\infty}^{\infty} \sum_{l=-\infty}^{\infty} \sum_{q'=-\infty}^{\infty} \sum_{l'=-\infty}^{\infty} J_q(A_r) J_l(A_h) J_{q'}(A_r) J_{l'}(A_h)$$
$$exp\left[j2\pi((q-q')f_r + (l-l')f_h)t\right] exp\left[-j2\pi(q'f_r + l'f_h)\tau\right] exp(-j2\pi\alpha t)\ dt + R_Z(\tau) \tag{3.33}$$

where $R_M(\tau)$ and $R_Z(\tau)$ are the autocorrelation functions of the stationary noises $M(t)$ and $Z(t)$. Using the aforementioned Dirac delta identity, the cyclic autocorrelation function of the baseband signal can simplified to:

$$R_{B_b}(\alpha,\tau) = A^2 R_M(\tau) \sum_{q=-\infty}^{\infty} \sum_{l=-\infty}^{\infty} \sum_{q'=-\infty}^{\infty} \sum_{l'=-\infty}^{\infty} J_q(A_r) J_l(A_h) J_{q'}(A_r) J_{l'}(A_h)$$
$$exp\left[-j2\pi(q'f_r + l'f_h)\tau\right] \delta(\alpha - ((q-q')f_r + (l-l')f_h)) + R_Z(\tau) \tag{3.34}$$

Provided that $R_M(\tau) \neq 0$, the conjugate cyclic autocorrelation of $B_b(t)$ function is defined for the set of cyclic frequencies $A_{\alpha 2} = \{\pm((q-q')f_r + (l-l')f_h), 0\}$.

Note that in the stationary case, this cyclic autocorrelation function (CAF) is zero for all frequencies $\alpha \neq 0$. Indeed, for $\alpha = 0$, the CAF function becomes exactly the classical autocorrelation function. This property of the cyclostationary model makes it an attractive model.

3.6.1.4 The second-order cyclic cumulant

For the second cyclic cumulant, we apply the moments to cumulants conversion formula (3.26) since we have already calculated the second cyclic temporal moment.

Table 3.2 presents the set of partitions for the order $m = 2$. The number of possible partitions increases with the order, and is given by the Bell' s number.

Table 3.2: Partitions, example for $m = 2$.

$\boldsymbol{D_m}$	**{1,2 }**	**{1} {2}**
d	1	2
b_i	$b_1 = \{1, 2\}$	$b_1 = \{1\}$ $b_2 = \{2\}$

To better understand the conversion formula, in this section we illustrate an example with real values of the cyclic frequencies. From the previous sections, $A_{\alpha 1} = \{\pm(qf_r + lf_h), 0\}$ and $A_{\alpha 2} = \{\pm((q - q')f_r + (l - l')f_h), 0\}$ represent the formula of the first order and second order respectively. To simplify, we take $q' = -q$ and $l' = -l$, so both formulas become: $A_{\alpha 1} = \{\pm(qf_r + lf_h), 0\}$ $A_{\alpha 2} = \{\pm(2qf_r + 2lf_h), 0\}$.

For this example, we fix the value of ν and we choose $-1 \leqslant q \leqslant 1$ and $-1 \leqslant l \leqslant 1$, therefore the possible combinations of cyclic frequencies are presented in the table 3.3.

Table 3.3: Cyclic frequencies of the first and second order of the cyclic moment

Index	1	2	3	4	5	6	7	8	9
α_1	$f_r - f_h$	$-f_r$	$-f_r + f_h$	$-f_h$	f_h	f_r	$f_r - f_h$	$f_r + f_h$	0
α_2	$-2(f_r - f_h)$	$-2f_r$	$-2(-f_r + f_h)$	$-2f_h$	$2f_h$	$2f_r$	$2(f_r - f_h)$	$2(f_r + f_h)$	0

For $\nu = \alpha_2(5) = 2f_h$, the alpha values that sum towards the ν are: $\alpha_1(3) - \alpha_1(1)$, $\alpha_1(5) - \alpha_1(4)$, $\alpha_1(8) - \alpha_1(7)$ and $\alpha_1(5) + \alpha_1(5)$. The second-order cyclic-cumulant of $B_b(t)$ can be expressed as follow for $\nu = 2f_h$:

$$\begin{aligned} C_x^{\alpha}(\tau)_{2,0} = M_x^{\alpha_2(5)}(\tau)_{2,0} - [&M_x^{\alpha_1(3)}(\tau)_{1,0} M_x^{\alpha_1(5)}(\tau)_{1,0} + M_x^{\alpha_1(5)}(\tau)_{1,0} M_x^{\alpha_1(4)}(\tau)_{1,0} \\ &+ M_x^{\alpha_1(8)}(\tau)_{1,0} M_x^{\alpha_1(7)}(\tau)_{1,0} + M_x^{\alpha_1(5)}(\tau)_{1,0} M_x^{\alpha_1(5)}(\tau)_{1,0}] \end{aligned} \tag{3.35}$$

3.6.1.5 The third-order cyclic moment(TOCM)

The third-order cyclic-moment of $B_b(t)$ can be expressed as follow:

$$M_x^{\alpha}(\tau)_{3,p} = \lim_{T\to\infty}\frac{1}{T}\int_{\frac{-T}{2}}^{\frac{T}{2}} B_b(t)B_b(t+\tau_1)B_b(t+\tau_2)exp(-j2\pi\alpha t)\ dt \quad (3.36)$$

After some mathematical manipulations, the 3-th order cyclic moment of the reflected signal is given by:

$$\begin{gathered} M_x^{\alpha}(\tau)_{3,p} = A^3 m(t)m(t+\tau_1)m(t+\tau_2)\sum_{q=-\infty}^{\infty}\sum_{l=-\infty}^{\infty}\sum_{q'=-\infty}^{\infty}\sum_{l'=-\infty}^{\infty}\sum_{q''=-\infty}^{\infty}\sum_{l''=-\infty}^{\infty} \\ j^{(q+q'+q''+l+l'+l'')}J_q(A_r)J_l(A_h)J_{q'}(A_r)J_{l'}(A_h)J_{q''}(A_r)J_{l''}(A_h) \\ exp[j2\pi(f_r(q'\tau_1-q''\tau_2)+f_h(l'\tau_1-l''\tau_2)]\delta(\alpha-[(q+q'-q'')f_r+(l+l'-l'')f_h] \end{gathered}$$

where the set of cyclic frequencies is given by:

$A_{\alpha 3} = \{\pm((q+q'-q'')f_r + (l+l'-l'')f_h), 0\}$.

3.6.1.6 The third-order cyclic cumulant(TOCC)

The third-order cyclostationary of the received signal retains the fundamental frequency along the cyclic axis. We calculate the third-order cyclic cumulant (TOCC) of the signal by using the formula (3.26) to convert the third-order cyclic moments to the third-order cyclic cumulants conversion since we already have the third-order cyclic moments.

Table 4 presents the set of partitions for the order m= 3. The number of possible partitions increases with the order, and is given by the Bell' s number.

Table 3.4: Partitions, example for $m = 3$

D_m	**{1,2,3}**	**{3}{1,2}**	**{1}{2,3}**	**{2}{1,3}**	**{1}{2}{3}**
d	1	2	2	2	3
b_i	$b_1 = \{1,2,3\}$	$b_1 = \{1,2\}$ $b_2 = \{3\}$	$b_1 = \{2,3\}$ $b_2 = \{1\}$	$b_1 = \{1,3\}$ $b_2 = \{2\}$	$b_1 = \{1\}$ $b_2 = \{2\}$ $b_3 = \{3\}$

Table 3.5: Partitions, example for $m = 3$

$\boldsymbol{D_m}$	d	b_i
{1,2,3}	1	$b_1 = \{1, 2, 3\}$
{3}{1,2}	2	$b_1 = \{1, 2\}$ $b_2 = \{3\}$
{1}{2,3}	2	$b_1 = \{2, 3\}$ $b_2 = \{1\}$
{2}{1,3}	2	$b_1 = \{1, 3\}$ $b_2 = \{2\}$
{1}{2}{3}	3	$b_1 = \{1\}$ $b_2 = \{2\}$, $b_3 = \{3\}$

3.7 Simulation and discussions

In this section of the simulation part, we define the amplitude and the frequency of the respiratory and cardiac signal to build the signal which describes the movement of the rib cage, which will allow us to have the signal in base band reflected by the antenna. The proposed treatment is based on applying the first-order, the second-order and the third-order of cyclostationary algorithm on the received signal, in order to extract the values of the heart rate and the respiratory rate by varying several parameters, such as the system frequency and the distance, to see their influence on the results.

The flowchart shows in Figure 3.9, describes the different steps performed in the simulation part for the generation of the baseband signal reflected by the antenna and the associated processing, in order to extract the heart and respiratory rates.

For the first part of the simulation, we apply the algorithm on the received signal while modelling the cardiac signal with a sinusoidal signal, and in the second part we mediate the cardiac signal by a real format signal. For the two parts, we do the simulations without and with the noise.

3.7.1 First case: Modulation of the heart signal by a sinus

To evaluate the influences of the noise, the frequency system, and the distance between the antenna and the person under test, we make different simulations with different parameters to see the behavior of the cyclic features. These simulations allow to find a compromise for the best extraction of vital signs.

3.7.1.1 The cyclic frequencies of the cyclic features

The distinct cyclic features are defined for different cyclic frequencies. We have considered simulation values shown in Table 3.6 to visualised the different combination of cyclic frequencies of each order.

The set of cyclic frequencies defined from the cyclic temporal moments and

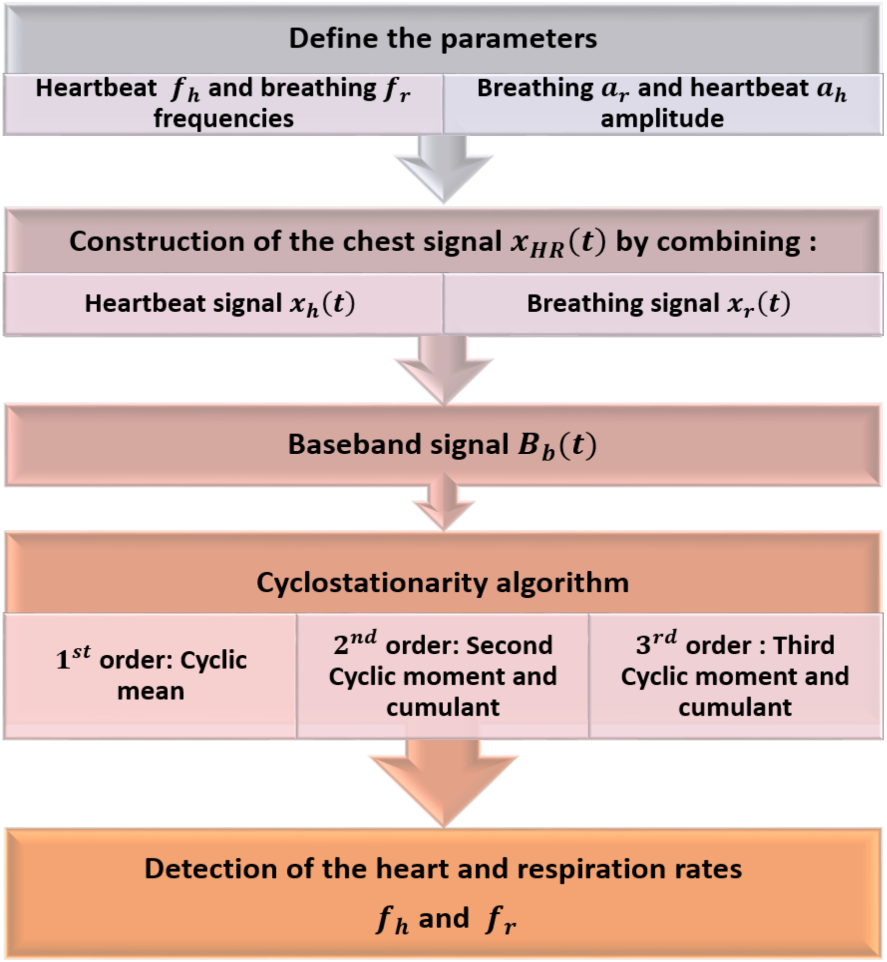

Figure 3.9: Flowchart of the cyclostationarity block to extract the respiration and heart rates

Table 3.6: Parameters defined for the simulation

System frequency f	10 GHz
Cardiac frequency f_h	0.5 Hz
Heart amplitude a_h	0.5 mm
Breathing frequency f_r	1.3 Hz
Breathing amplitude a_r	4 mm
Distance between antenna and target	60 cm
Sampling frequency	100 Hz

the cyclic cumulant are different. For the cyclic frequencies occurring with the moment, which is the impure cyclic frequencies, it can be the result of a combination of lower order cyclic frequencies.The first order cyclic moment contain the different combination of the heart and respiration rates which is defined by the set of cyclic frequencies $A_{\alpha 1} = \{\pm(qf_r + lf_h), 0\}$. Then by replacing the q and l in the equation, with different integers, the equation will be solved and the different frequencies which constitutes the cyclic mean will be obvious as in the figure 3.10(a). The same processing for the second and the third order, which are defined respectively for the set of cyclic frequencies $A_{\alpha 2} = \{\pm((q-q')f_r + (l-l')f_h), 0\}$ and $A_{\alpha 3} = \{\pm((q+q'-q'')f_r + (l+l'-l'')f_h), 0\}$. All the different combination for the two sets, are visualized in the figure 3.10(b) and figure 3.11.

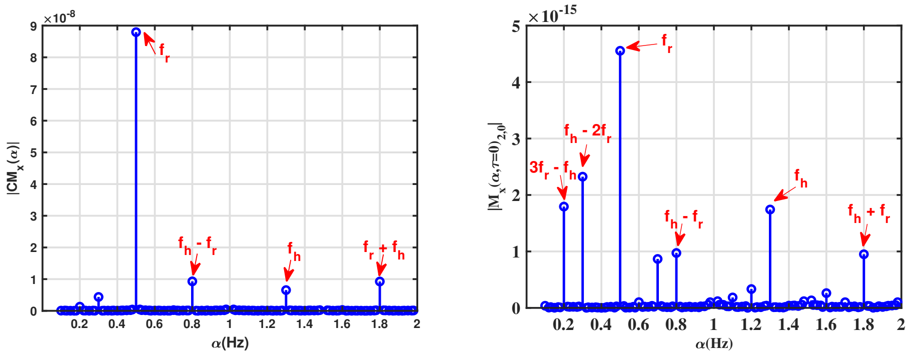

(a) (b)

Figure 3.10: The cyclic temporal moment: (a) The cyclic mean and (b) the second-order cyclic temporal moment $|M_x(\alpha, \tau = 0)_{2,0}|$

Although, the cyclic frequencies defined from the cyclic temporal cumulants characterise the m-th order additive sine-waves only. For our case, the second and the third order. For the second cyclic cumulant, the different conjugations are useful and complementary, because one gives us information on breathing rate $|C_x(\alpha, \tau = 0)_{2,0}|$ and the other on heart rate $|C_x(\alpha, \tau = 0)_{2,1}|$.The two cyclic features contain the respiratory rate $f_h = 1.3Hz$ and the heart rate $f_r = 0.5Hz$ and other frequencies as shown in the figure 3.12 $f_h - f_r = 0.8Hz$ $f_h + f_r = 1.8Hz$.

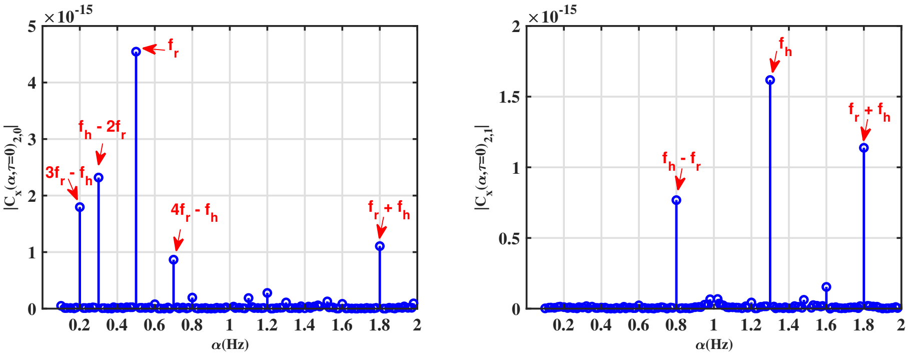

(a) (b)

Figure 3.11: The second-order cyclic temporal cumulant statistics of reflected signal with different number of conjugation: (a) $|C_x(\alpha, \tau = 0)_{2,0}|$ and (b) $|C_x(\alpha, \tau = 0)_{2,1}|$

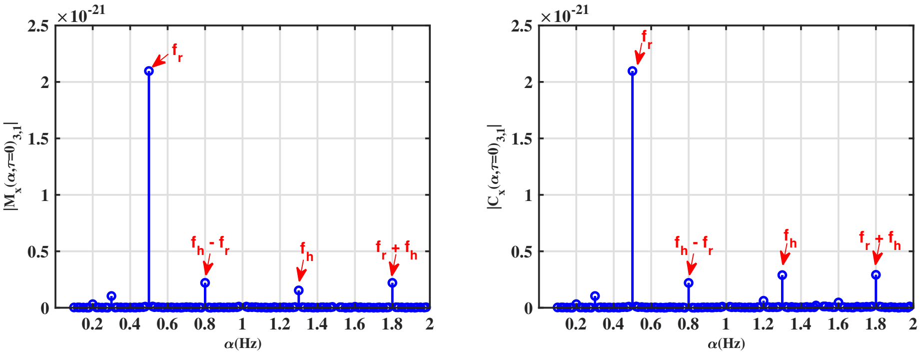

(a) (b)

Figure 3.12: The third-order cyclic statistics of reflected signal: (a) third cyclic temporal moment $|M_x(\alpha, \tau = 0)_{3,1}|$ and (b) third cyclic temporal cumulant $|C_x(\alpha, \tau = 0)_{3,1}|$

3.7.1.2 Effect of additive and multiplicative noise

In order to focus only on the cyclic features of vital signs, at first, the signal is generated without additive noise or multiplicative noise. In this case, the attenuation A_{H_R} has been taken into account. The second part consists to simulate the reflected signal with all its components, to get closer to the real signal. The additive noise $Z(t)$,the attenuation A_{H_R} and the multiplicative noise $M(t)$. In these examples, we have considered simulation values shown in Table (3.7):

Table 3.7: Parameters defined for the simulation

System frequency f	10 GHz
Cardiac frequency f_h	0.5 Hz
Heart amplitude a_h	0.5 mm
Breathing frequency f_r	1.3 Hz
Breathing amplitude a_r	4 mm
Distance between antenna and target	60 cm
Sampling frequency	100 Hz

The observation time is 60 seconds and the sampling frequency is 100 Hz, which gives a number of points of 6001. Figure (3.13) shows the baseband signal $B_b(t)$ resulted from the modeling of the respiratory and cardiac signal by a sinusoidal in the time domain. We consider the baseband signal $B_b(t)$ is presented in both cases with the noise component and without noise.

The processing chain carried out for, the calculation of the functions of the cyclic mean, the cyclic moments and cyclic cumulants of order two and three, on a signal composed essentially of a respiratory and cardiac components in

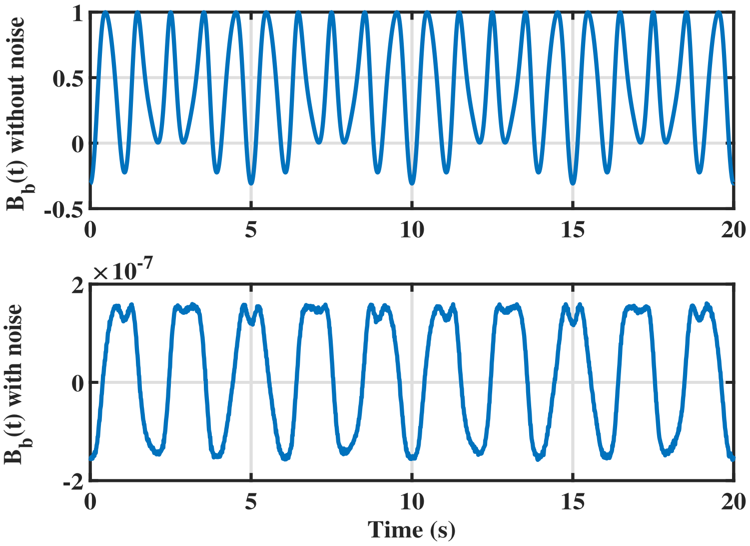

Figure 3.13: The baseband signal $B_b(t)$ in both cases: with and without noise component

the sinusoidal form. The two components evolve at distinct average frequencies, namely $0.5Hz$ for the respiratory rate, and $1.3Hz$ for the heart rate. Figures (3.14) (3.16) and (3.18) represent the cyclic statistics of the baseband signal in the case of a signal without additive and multiplicative noises. While the Figures (3.15) (3.17) and (3.19) show the cyclic features of the reflected signal for the case of with additive and multiplicative noise.

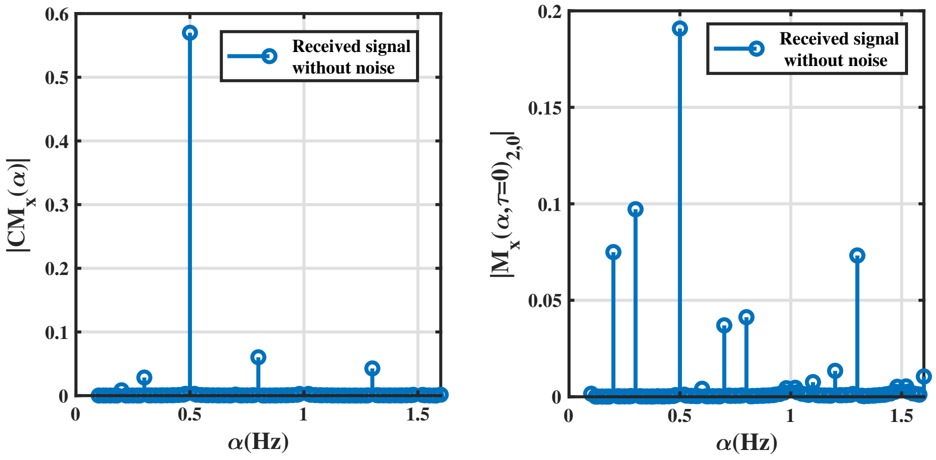

(a) (b)

Figure 3.14: (**a**) The first order (the cyclic mean) and (**b**) the second cyclic moment of the reflected signal without additive noise

The amplitude level of the cyclic features is very large for the case of in the case of the received signal from the person's chest without any noise (additive and multiplicative) compared to the case with the noise. For example, the second cyclic temporal moment $|M_x(\alpha, \tau = 0)_{2,0}|$ for the case without noise

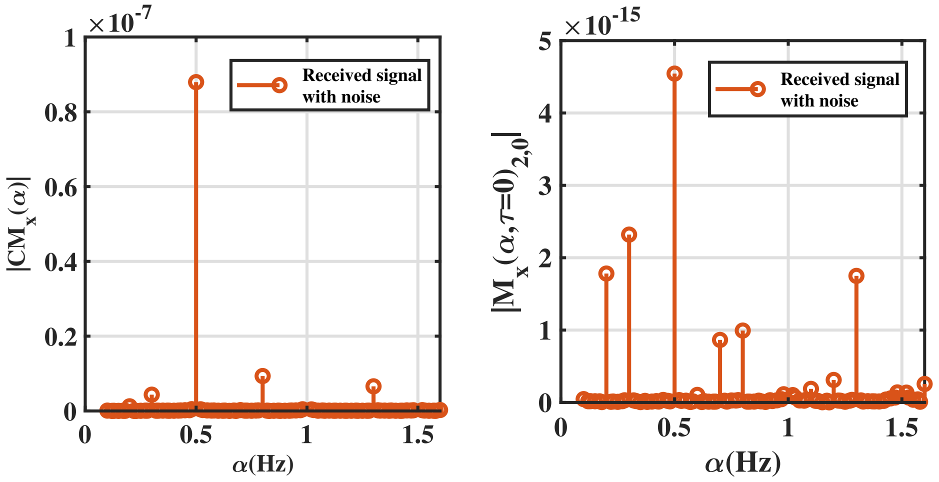

(a) (b)

Figure 3.15: (**a**) First order (the cyclic mean) and (**b**) the second cyclic moment of the reflected signal with additive noise

is of the order of 0.2 against $5e^{-15}$ for the case with noise.

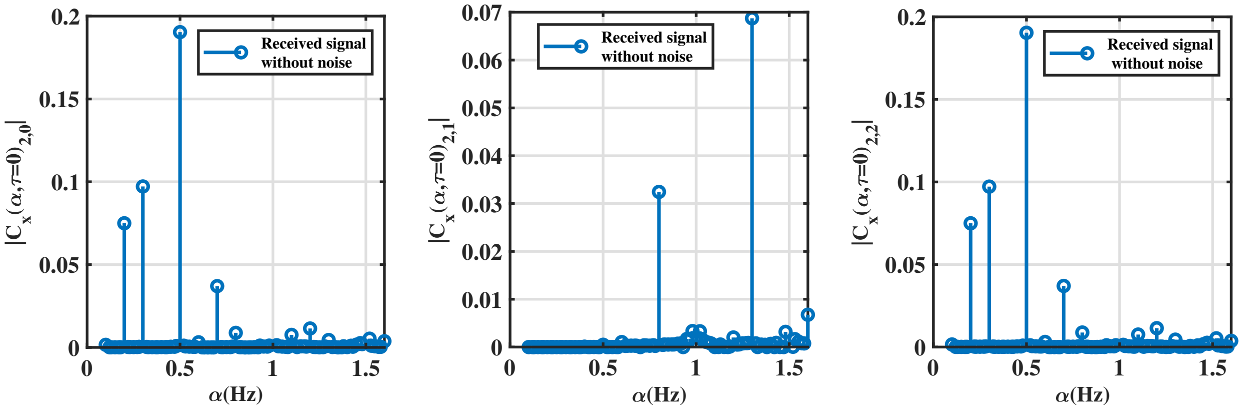

(a) (b) (c)

Figure 3.16: Second-order temporal cyclic cumulant of reflected signal without additive noise for different number of conjugation: (**a**) $|C_x(\alpha, \tau = 0)_{2,0}|$, (**b**) $|C_x(\alpha, \tau = 0)_{2,1}|$ and (**c**) $|C_x(\alpha, \tau = 0)_{2,2}|$

The amplitude of the baseband signal depends on the received power and phase-shift modulation. Noise sources include residual phase-shift noises from the down converting system, additive white Gaussian noise (AWGN), and the baseband noise of the receiver circuits. Then the backscattered signal from the heart and the respiration should be stronger than other noise sources at the receiver's baseband output. To solve the above problem, the property of cyclostationarity is used to reduce noise. In the figures of cyclic features, all the cyclic statistics contain the heart and respiration frequencies, $f_h = 1.3Hz$

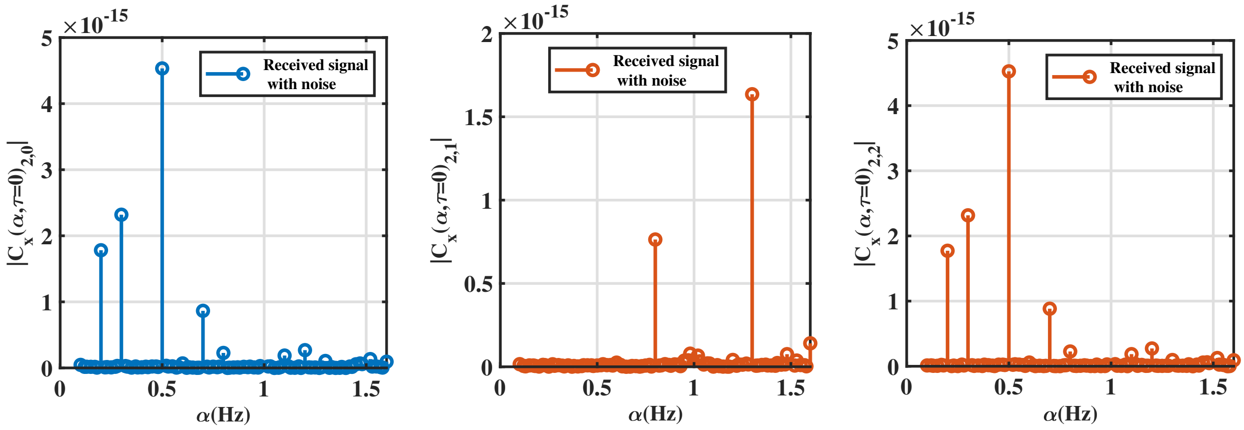

(a) (b) (c)

Figure 3.17: Second-order temporal cyclic cumulant of reflected signal with additive noise with different number of conjugation (**a**) $|C_x(\alpha, \tau = 0)_{2,0}|$, (**b**) $|C_x(\alpha, \tau = 0)_{2,1}|$ and (**c**) $|C_x(\alpha, \tau = 0)_{2,2}|$

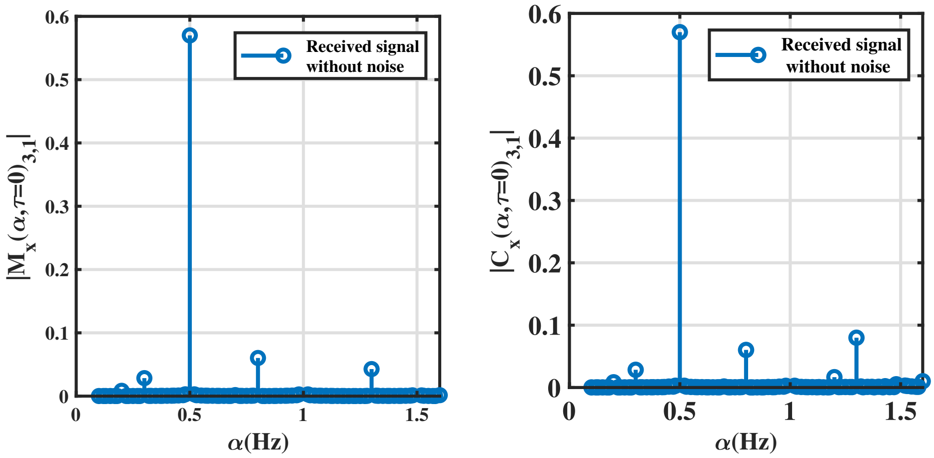

(a) (b)

Figure 3.18: The third-order cyclic statistics of reflected signal without additive noise: (**a**) Cyclic temporal moment and (**b**) Cyclic temporal cumulant

and $f_r = 0.5Hz$ and all the frequencies combination which describes each order. One of our main goals is to require the cyclic features even with the presence of noise. The cyclostationary approach allows the extraction the the interest frequencies in the presence of noise (multiplicative and additive).

To further assess the impact of the additive noise on detection of vital signs, we computed the probability of detection as a function of SNR, in order to detect the presence of both heart and respiration rates. We performed the detection as a function of the SNR (Figure 3.20), using sampling time value $T_s = 0.01$ ($f_s = 100$ Hz), which leads to $N_s = 6001$ samples. Therefore,

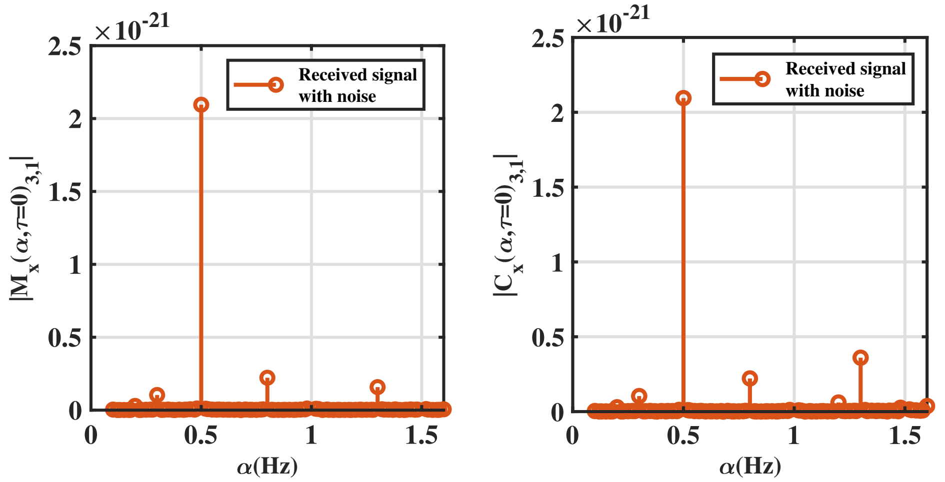

(a)

(b)

Figure 3.19: The third-order cyclic statistics of reflected signal with additive noise: (**a**) Cyclic temporal moment and (**b**) Cyclic temporal cumulant

for simulation, we tested if the estimate values using the cyclostationary algorithm f_h' and f_r' of HR and RR respectively, are the same values set for the transmitted signal f_h and f_r.

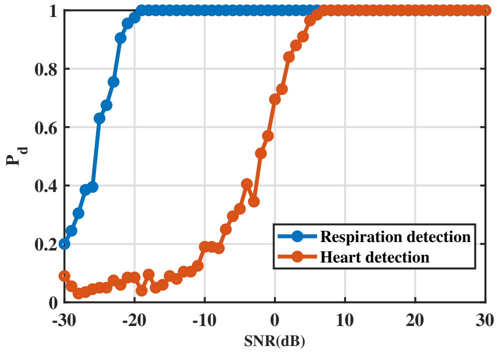

Figure 3.20: Probability of detection of respiration and heartbeat as a function of the signal-to-noise ratio (SNR) and $d = 60$ cm, N_s= 6001

Thus we simulate both probabilities $P_d = P(f_r' = f_r)$ and $P_d =$ P $(f_h' = f_h)$. The blue curve corresponds to RR, while the red one corresponds to HR. The probability of detection of the respiration rate is $P_d = 1$ from the value of SNR $=$ -20 dB because the respiratory signal is the strongest component in the reflected signal. On one hand, the heart rate detection is $P_d = 1$ from the value of SNR 6 dB. On the other hand, the probability of detection of the heart rate is increasing with the SNR.

The simulation results demonstrate that the cyclostationary theory is a powerful tool to extract the cyclic frequencies from noisy non-stationary signals independent of the SNR level, having taking into consideration the body movements, the attenuation and the additive and the multiplicative noises.

3.7.1.3 Effect of respiration amplitude on the detection of the respiration and heart rates

The respiration signal is usually the component of the lowest frequency in cyclic components and is at the same time the strongest component of the signal because of the chest movement due to respiration is between a_r= 4 mm and a_r= 8 mm. It is therefore ten times greater than the heartbeat a_h= 0.5 mm. This makes it easier to extract the breathing frequency, while precise heart rate detection is the main challenge. The next simulation allow to visualize the effect of different value of the respiration amplitudes on the detection of the heart and respiration rates.
The cyclic features of the received signal for the 10 GHz frequency and distance d= 60 cm, with a number of samples 6001 for two distinct configurations of respiration amplitude a_r= 4 mm and a_r= 6 mm. The result of the simulation are presented in figures 3.21 Figure 3.22 and Figure 3.23 .

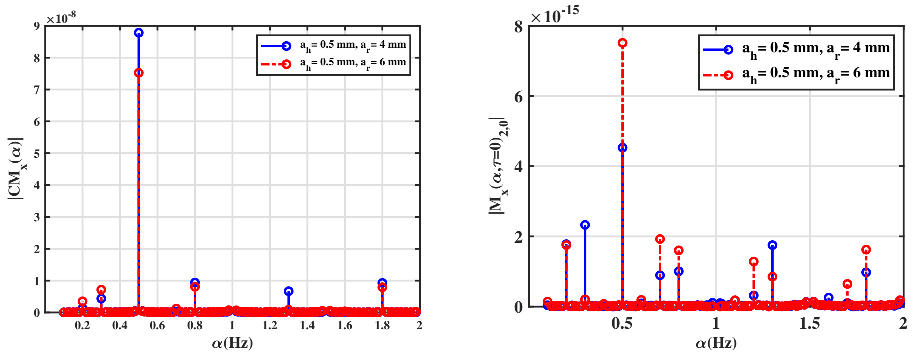

(a) (b)

Figure 3.21: Cyclic features of the reflected signal without and with noise: (**a**) cyclic mean $|CM_x(\alpha)|$ and (**b**) second order cyclic temporal moment $|M_x(\alpha,\tau=0)_{2,0}|$

In the first configuration, where a_r= 4 mm these harmonics are less significant than the heart peak. However, in the second configuration a_r= 6 mm, the harmonics are greater than the heart peak for some features. In both cases, the extraction of the frequencies of interest is possible. The cyclic cumulant eliminate the impure cyclic frequencies.

To evaluate the impact of the breathing amplitude, in particular the heart rate, we calculated the probability of detection as a function of SNR, in order to detect the presence of both heart and respiration rates for two different value of the respiration amplitude. We performed the impact using sam-

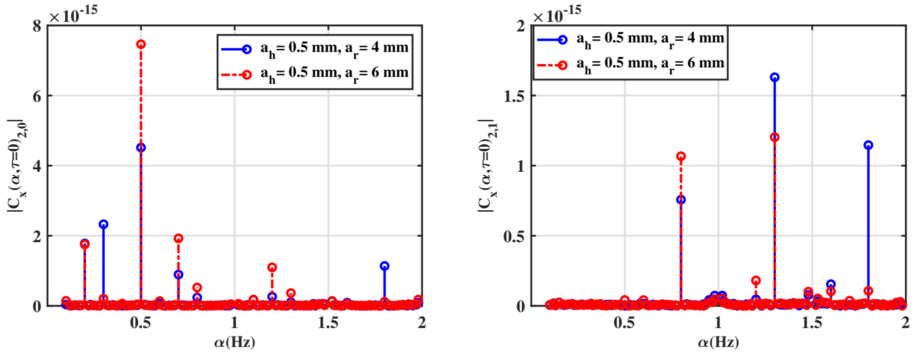

(a) (b)

Figure 3.22: Second-order cyclic temporal cumulant statistics of the reflected signal without and with noise with different number of conjugation: (**a**) $|C_x(\alpha, \tau = 0)_{2,0}|$ and (**b**) $|C_x(\alpha, \tau = 0)_{2,1}|$

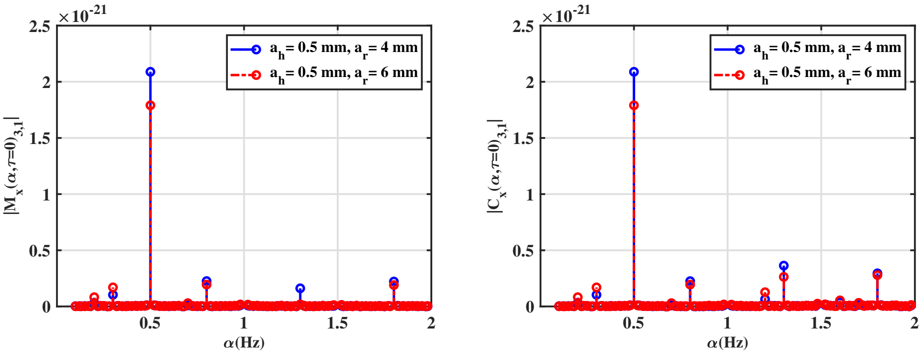

(a) (b)

Figure 3.23: Third-order cyclic statistics of the reflected signal without and with noise: (**a**) cyclic temporal moment and (**a**) cyclic temporal cumulant

pling time value $T_s = 0.01$ ($f_s = 100$ Hz), which leads to $N_s = 6001$ samples. Therefore, for simulation, we tested if the estimate values using the cyclostationary algorithm f_h' and f_r' of HR and RR respectively, are the same values set for the signal f_h and f_r in the initialization part. The Figure 3.24 shows the results.

We simulate both probabilities $P_d = P(f_r' = f_r)$ and $P_d = \mathrm{P}\ (f_h' = f_h)$. The Figure 3.24(a) corresponds to the probability of detection of respiration rate for both different value of the breathing amplitude, which equal to 1 from the value of SNR= -20 dB. For the both value of a_r the P_d are very similar. While in the Figure 3.24 (b), which represent the probability of detection of the heart rate, which seems different from one value to another of a_r. The probability of detection of the heart rate is increasing with the SNR.

The greater the displacement of the rib cage due to the increased respiration,

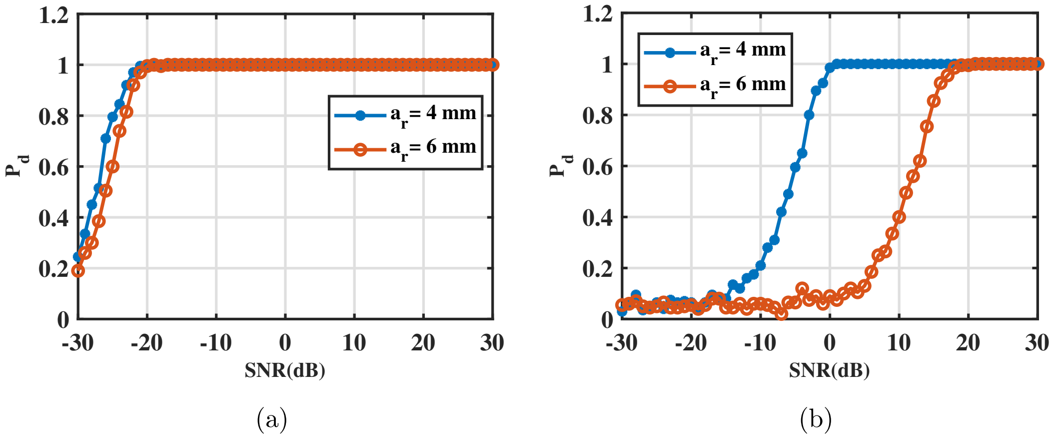

(a)

(b)

Figure 3.24: Probability of detection of vital signs as a function of the SNR for both respiration amplitude 4 and 6 mm:(**a**) respiration rate and (**b**) heart rate

the greater the lag between the respiratory rate and the heart rate becomes, which lowers the probability of detecting the heart rate. Indeed, when the amplitude of the respiratory rate increases, the harmonics and the combinations constituting it become more important, which disturbs the detection of small displacement of the heart rate.

3.7.1.4 The impact of the number of samples on detection of heart and respiration rates

The effect of the number of samples is considered in Figure 3.25. The cyclic features of the received signal for the 10 GHz frequency and distance d= 60 cm, with a small number of samples ($N_s = 601$) are presented. All frequencies of interest are present. We present just the second order cyclic moment and cumulant.

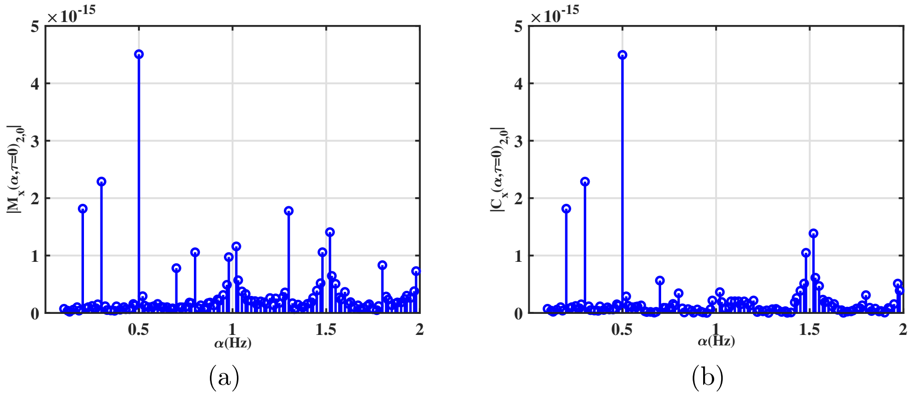

(a)

(b)

Figure 3.25: Second-order cyclic statistics of the reflected signal with small number of samples 601: (**a**) cyclic temporal moment; (**b**) cyclic temporal cumulant

As the heart rate is in the range of $0.83 - 1.5Hz$, the minimum sampling frequency allowing reconstruction of cyclostationarity should be at least twice the maximum target frequency $f_s \geqslant 2max(f_h)$, in this case $f_s \geqslant 4Hz$. In figure 3.21 3.22 and 3.23, The sampling rate is then chosen to minimize the computational cost, $f_s = 100Hz$. Hence, the signal is generated with a sampling time of $T_s = 0.01s$, and for a total observation time $T = 60s$, which leads to $N_s = 6001$ samples. While in figure 3.25, the second cyclic moment and cumulant estimation are corrupted with the noise. This means that the cyclostationarity process requires a high number of samples to accurately estimate the cyclic features. In [39], the results are obtained using 131,072 samples. One of our main goals is to require cyclic features by reducing the measurement time and the numbers of samples, hence we carry out our data using small sample sizes, which is reduced comparing to the number cited in the literature. It should be noted that increasing the number of samples would lead to a better estimation of cyclic features at the expense of higher computational costs, which leads to a longer processing time. The Figure 3.26 shows the probability of detection of the vital signs using a small number of sample. We observe that reducing the number of sample to 601 samples, leads to a bad detection of HR, because we have a small probability of detection of HR compared to the one of 6001 samples used previously in the Figure 3.20.

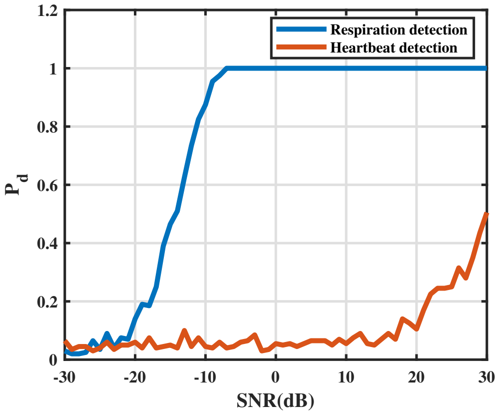

Figure 3.26: Probability of detection of respiration and heartbeat as a function of the signal-to-noise ratio (SNR) for 601 samples and d= 60cm

3.7.1.5 Influence of distance on cyclostationary detection

This study concerning the impact of the distance between the subject under test and the antennas, on cyclic features detection. So from the attenuation Equation (2.14) we can derive the maximum distance at which detection of vital signs is possible:

$$d_{max} = \left[\frac{P_{Tx} G_T G_R \sigma_h L_h \lambda^2}{(4\ \pi)^3 A^2_{HR_{min}}} \right]^{\frac{1}{4}}. \tag{3.37}$$

where P_{Tx} is the transmitted power, G_T and G_R are transmitter and receiver antenna gains. σ_h is the RCS, L_h is the reflection loss of the heart. A_{HR} is the attenuation of the reflected signal. Equation (3.37) shows that the detection distance is related to the transmitted power, antenna parameters, as the frequency. These variables are constant and transceiver-dependent, while the target RCS σ_h and loss L, are related to the human body.

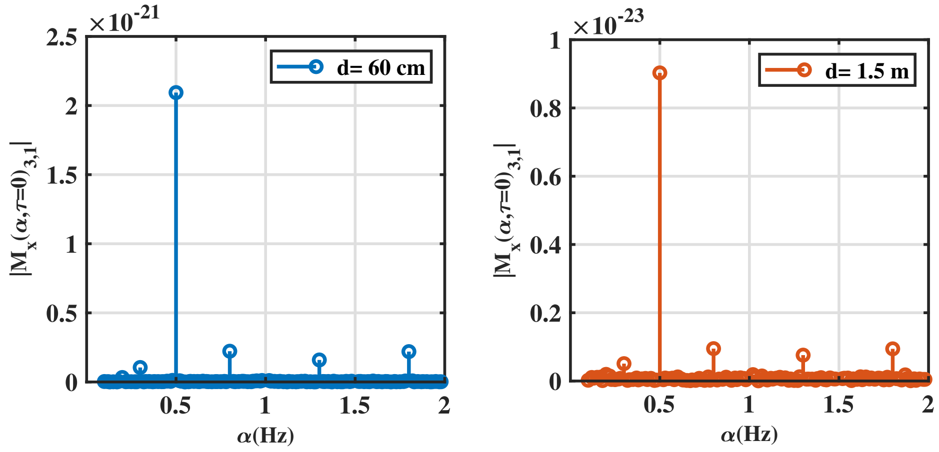

(a) (b)

Figure 3.27: Third-order cyclic temporal moment of the reflected signal: (**a**) d= 60 cm and (**b**) 1.5 m

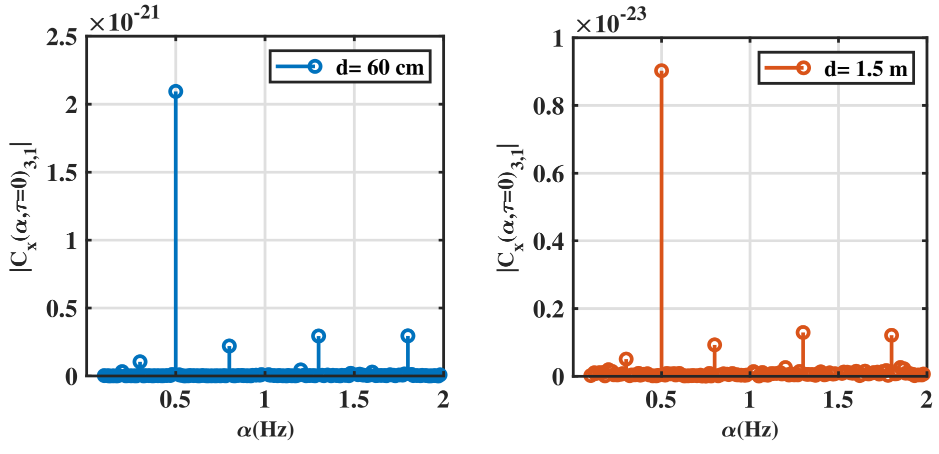

(a) (b)

Figure 3.28: Third-order cyclic cumulant of the reflected signal: (**a**) d= 60 cm and (**b**) 1.5 m

Figure 3.27 and Figure 3.28 represent the third-order cyclic features of the received signal for the 10 GHz frequency and two distinct distances d= 60 cm and d= 1.5 m. For the first and second order cyclic moment and cumulant figures, can be found in Appendix A. The number of samples was set at 6001 so the sample frequency 100 Hz. In these examples, HR and amplitude were f_h = 1.3 Hz and a_r = 0.5 mm, respectively, while RR and amplitude were f_r = 0.5 Hz and a_r = 4 mm, respectively. In Figures, all frequencies of interest are present and the number of samples is sufficient to reconstruct the cyclic spectrum. However, for d= 1.5 m, the different combination between RR and HR are more obvious than HR.

3.7.1.6 Influence of the frequency system on Cyclostationary Detection

The choice of the frequency system is justified by the tendency of the system to miniaturize and belonging to the Industrial Scientific and Medical band (ISM). Two frequencies considered in this simulation 2 GHz and 17 GHz, which can compared to the previous studies at 10 GHz. For the first and second order cyclic moment and cumulant figures, can be found in Appendix B.

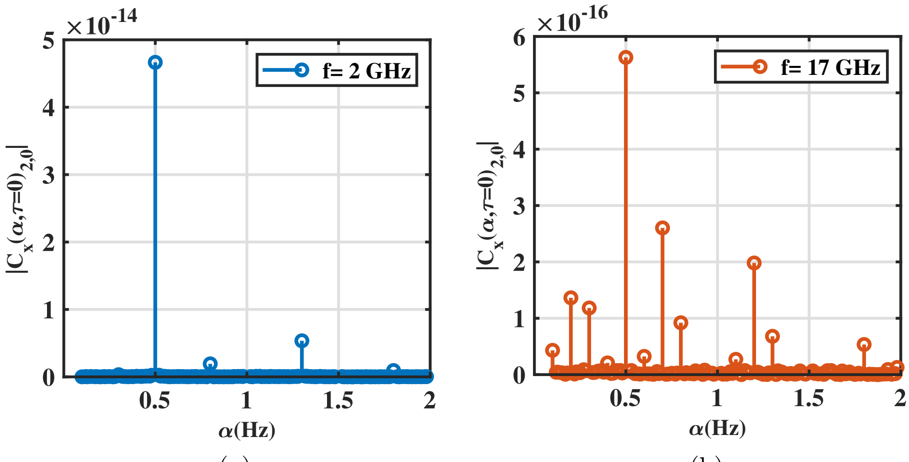

(a) (b)

Figure 3.29: Second cyclic cumulant $|C_x(\alpha, \tau = 0)_{2,0}|$ of the reflected signal at: (**a**) 2 GHz and (**b**) 17 GHz

Figure 3.29 3.30 and 3.31 show the cyclic characteristics of the reflected signal for two separate frequencies 2 GHz and 17 GHz for a distance of d = 60 cm and 6001 points. Regarding both frequencies, all cyclic frequencies are present. Respiratory frequencies are clearly identified and correspond to expected values. However, the heart frequencies are drowned in noise.

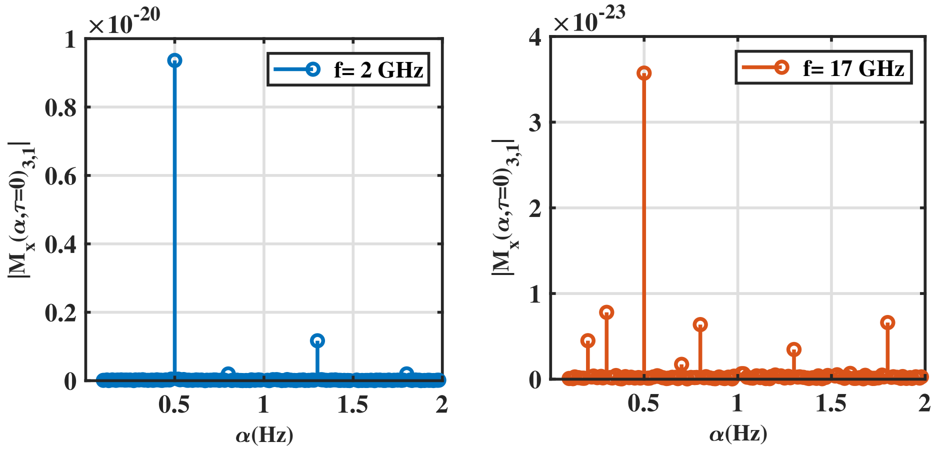

(a) (b)

Figure 3.30: Third-order cyclic temporal moment $|M_x(\alpha, \tau = 0)_{3,1}|$ of the reflected signal for the frequency system: (**a**) 2 GHz and (**b**) 17 GHz

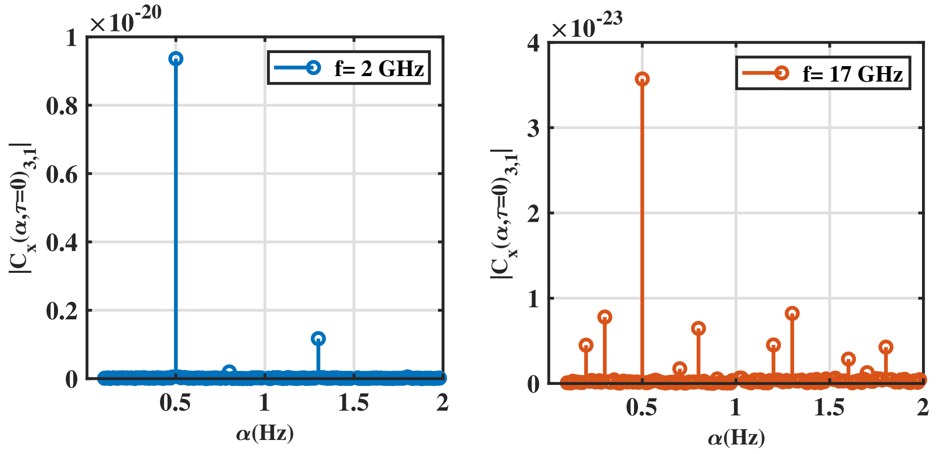

(a) (b)

Figure 3.31: Third-order cyclic temporal cumulant $|C_x(\alpha, \tau = 0)_{3,1}|$ of the reflected signal for the frequency system: (**a**) 2 GHz and (**b**) 17 GHz

3.7.2 second case: the heart signal ECG model

3.7.2.1 Simulation without noise

The reflected signal is essentially composed of a respiratory component in the sinusoidal form, and a cardiac component close to the shape of the signal given by the electrocardiogram (see Figure (3.32)). The two components evolve at distinct average frequencies, namely 0.5 Hz for the respiratory rate, and 1.3 Hz for the heart rate. Having a priory no mathematical model to specify cardiac activity, we sought to establish an approximate model to use in our Matlab codes while respecting the values described in the section (1.1.2). The new function replaces the sinusoidal pattern used in the first part. This new function is the best representation of vital signals.

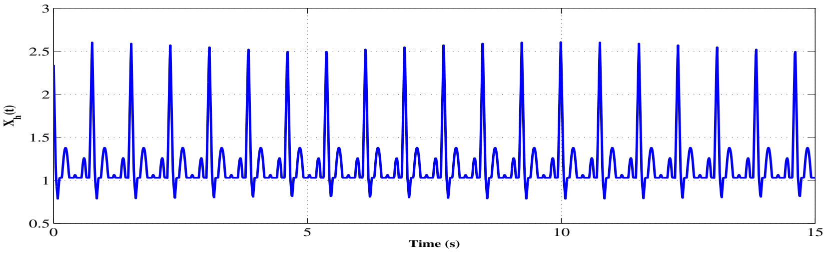

Figure 3.32: $X_h(t)$ Cardiac signal ECG model

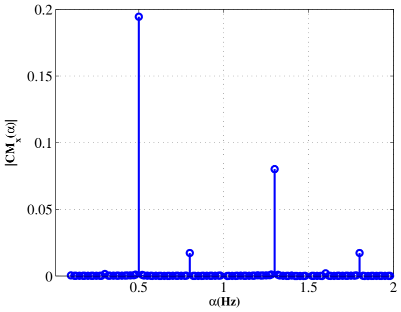

Figure 3.33: First order of the reflected signal without additive noise: the cyclic mean

Figures (3.33) (3.34) and (3.35) represent the cyclic statistics of the received signal in (3.16) in the case of a signal without the additive noise. As can be seen in all the figures, all the cyclic frequencies of interest are present and the number of samples is sufficient to reconstruct the cyclic spectrum for each order.

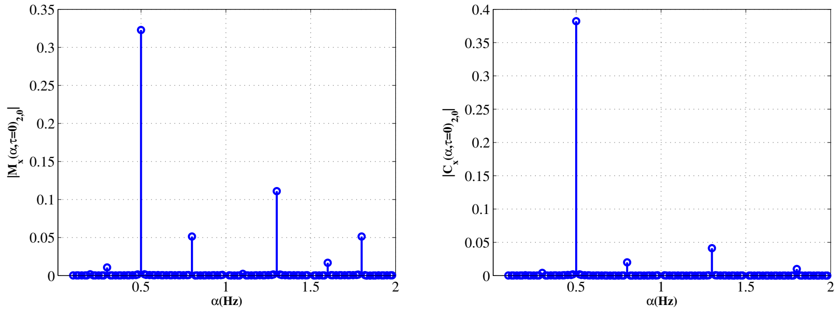

(a)

(b)

Figure 3.34: Second-order cyclic statistics of reflected signal without additive noise: (**a**) cyclic temporal moment; (**b**) cyclic temporal cumulant

3.7.2.2 Simulation with noise component

Figures (3.36) and (3.37) represent the cyclic statistics of the received signal in (3.16) in the case of a signal without the additive noise. As can be seen in all the figures, all the cyclic frequencies of interest are present and the

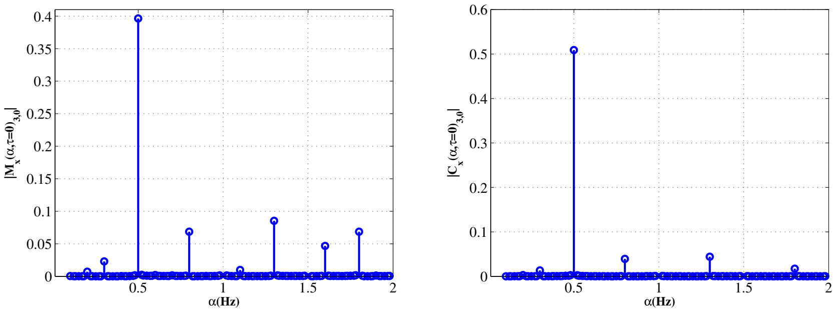

(a) (b)

Figure 3.35: Third-order cyclic statistics of reflected signal without additive noise: (**a**) cyclic temporal moment; (**b**) cyclic temporal cumulant

number of samples is sufficient to reconstruct the cyclic spectrum for each order.

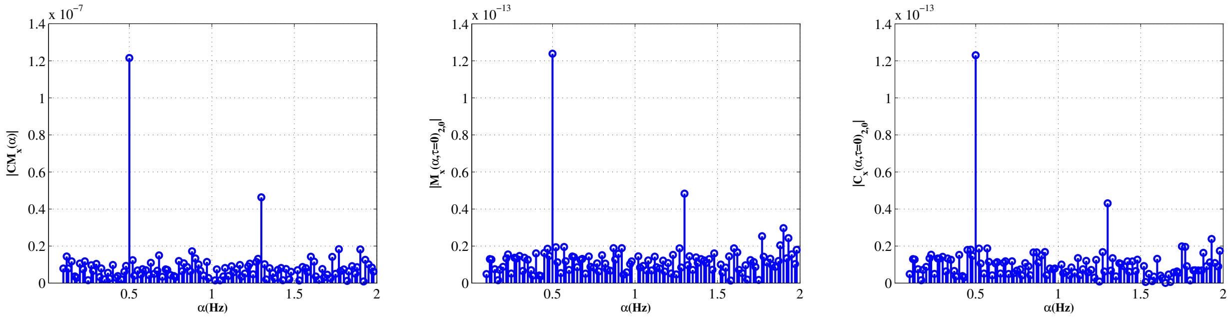

(a) (b) (c)

Figure 3.36: First and second order cyclic statistics of reflected signal with noise, SNR= 0 dB: (**a**) cyclic mean (**b**) Cyclic temporal moment; (**c**) Cyclic temporal cumulant

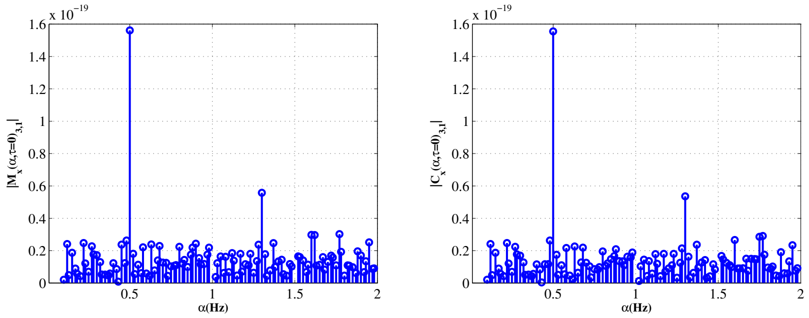

(a) (b)

Figure 3.37: Third-order cyclic statistics of reflected signal with noise, SNR= 0 dB: (**a**) Cyclic temporal moment; (**b**) Cyclic temporal cumulant

To evaluate the impact of the additive noise on detection of vital signs, in the case where the cardiac signal is modeled by an ECG signal instead of a sinusoidal. We computed the probability of detection in function of SNR for the second and the third order of cyclostationary algorithm. The Figure 3.38 shows the result of the simulation for the heart and the breathing detection in the both cases second and third order inf unction of the SNR.

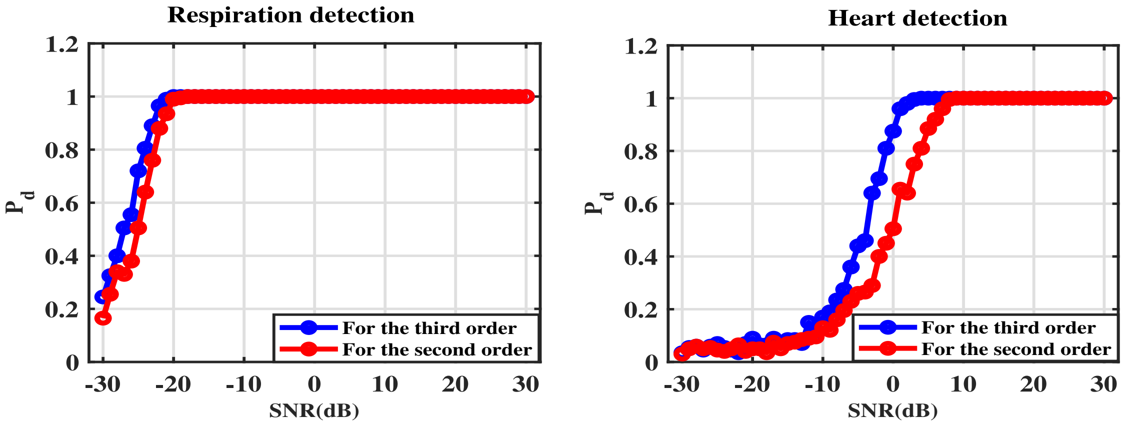

Figure 3.38: Probability of detection of respiration and heartbeat as a function of SNR

The probability of detecting heart and respiratory rates is higher with order three than with order two of the cyclostationary approach. As the previous results, the detection of respiration is still high compared to cardiac. Even with the modeling of the heart rate with an ECG signal we arrive at the extraction of information of interest with the same precision than modeling with sinusoidal.

3.7.2.3 Simulation of different cases of ECG

Taking into account the state of the art of the signal processing part for the ECG signal, each case of pathology, the signal is defined according to the values of the amplitude and the duration of each wave constituting the ECG signal which varying the HR. Figure 3.39 shows three cases of the cardiac signal, a normal rhythm with the cardiac frequency $1.3Hz$ which belongs to the normal interval and two abnormal rythm the hypothermia with slow heartbeat frequency $0.4Hz$ and the tachycardia with high heart rate $2Hz$.

Figure 3.40 shows the second order temporal moment applied to the three different baseband signal of the three cases of cardiac signal. In all the cases, the detection of the heart rate is possible.

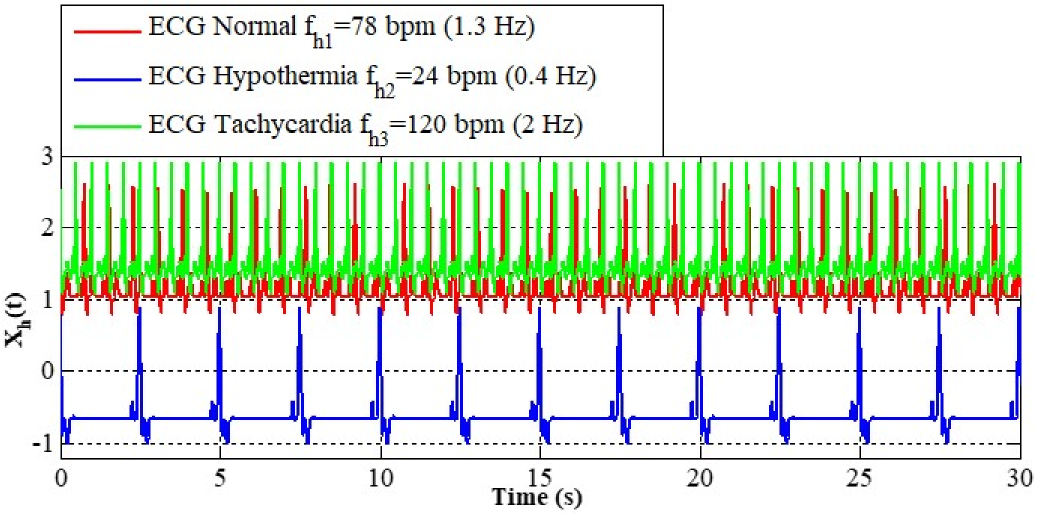

Figure 3.39: Three cases of cardiac signal: the cyclic mean, SNR= 0 dB

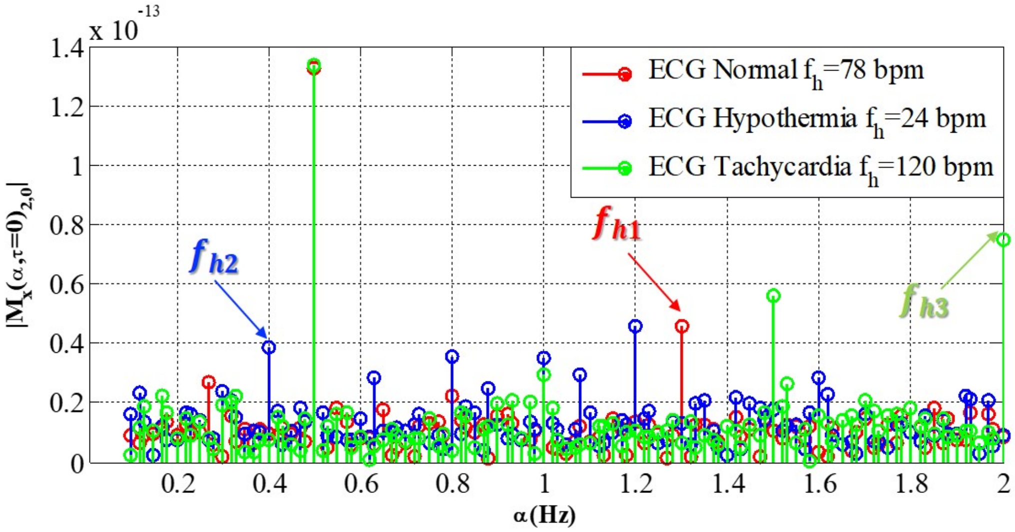

Figure 3.40: Second-order cyclic temporal moment of reflected signal with noise, SNR= 0 dB with three cases of cardiac signal

3.8 Conclusion

In the first part of this chapter, we have presented the state of art of the several techniques of signal processing for detection and estimation of the vital signs. Then, we have focused on the exploitation of error correction methods and the evaluation of their contribution to the separation of cardiac and respiratory signals obtained by Doppler radar. The result was a definite improvement in what already existed by deploying the method of geometric adjustment of the ellipse. However, this method, which is very robust to variations in amplitudes and DC offsets, is very sensitive to phase-shift errors. More in-depth work or even coupling with other error correction methods remains to be done.

To remedy these problems we have presented the cyclostationary statistical approach for the estimation of the respiration and the heart rates.The algorithm developed in the second part of the project is based on the first, second and the third orders cyclostationarity approach, which allows to calculate the cyclic statistics of the reflected baseband signal like the cyclic temporal moment and the cyclic temporal cumulant . The analytical closed-form of the m-th order cyclic moment and cumulants of the baseband signal from the radar for monitoring vital are first derived.The results of simulations obtained by this method are very encouraging. This method is very tough in the face of noise without any demodulation of the reflected signal from the chest's person.

To prove the ability and accuracy of the proposed algorithm of cyclostationary for vital signs monitoring technique, actual experiments were performed on human subjects, the results of which are presented in the following chapters starting by optimizing the measurement bench and identifying the sources of noises.

Chapter 4

Free-space modelling and calibration for microwave radar vital signs

4.1 Introduction

Continuous Wave (CW) microwave radars have attracted the interest from the research community for contactless, low-power and non-ionizing detection of human respiratory and heart frequencies. Optimum radar architecture design and optimization require the identification of systematic and non-systematic errors in both guided and radiating microwave paths of the system. In this effort, an heterodyne CW radar built up with reference measurement instrument is used to accurately identify sources of errors.

The aim of this chapter is to carry out a study that will allow us to optimize the measurement bench before starting the first application measurements. Several parameters influence the signal of interest, which reflects the mechanical displacement of the rib cage in millimeter order. The figure 4.1 below shows the parameters studied in this chapter.

The parameters influencing the quality of the signal of interest are: The amplitude of the variation of the amplitude and phase-shift of the signal and the fluctuation of the parasitic signal. The parametric study will allow us to know the level and the parasitic fluctuations brought by each component of the instrumentation.

4.2 Experimental equipment and Setup

Doppler-radar motion-sensing systems typically transmit a continuous-wave (CW) signal, reflected off the chest's target and then demodulated in the receiver. Due to unwanted mismatching effects, propagation losses and phase-

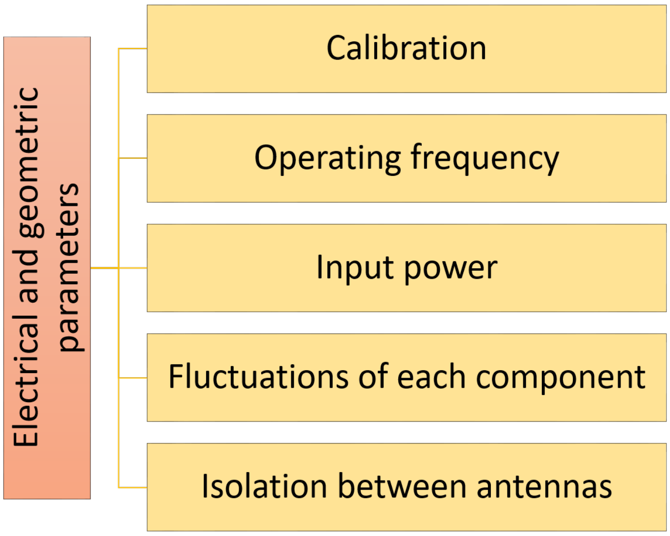

Figure 4.1: Block diagrams showing the different parameters studied

shift-shifts, interferometric free-space reflections between antennas and target, the measured microwave complex signal, namely I and Q components, is mixed with unwanted signals. The direct solution consists to optimize the entire microwave path at the expense of the circuit complexity. The second solution, commonly adopted in microwave network analysis, is based on the identification of both systematic and non-systematic errors. Whereas systematic errors can be removed by an appropriate calibration procedure, the non-systematic errors must be eliminated or reduced to guaranty accurate extraction of vital signs. The study of the noise of the instrumentation chain will be studied.

In this effort, we propose a framework to identify both systematic and non-systematic errors. In particular, measurements parameters such as RF power, frequency, intermediate frequency bandwidth (IFBW) stand-off, separation between antennas play a major role in the combination of unwanted signals with the signal of interest. The measurement system is a reference system based on the heterodyne architecture, which uses the vector network analyzer (N5242A Agilent Technologies, 10 MHz–26.5 GHz), coaxial cable and two horn antennas (SAS-571 700 MHz–18 GHz) Fig 4.2.

The SAS-571 Double Ridge Guide Horn Antenna is lightweight and compact. It has been used as reference antenna, for their good compromise between high bandwidth and directivity for a parametric study. The double ridge guide horn antenna is intended for general laboratory use in a wide variety of industrial and scientific applications. Table 4.1 shows the features of The SAS-571 double ridge guide horn antenna. The antenna gain depends

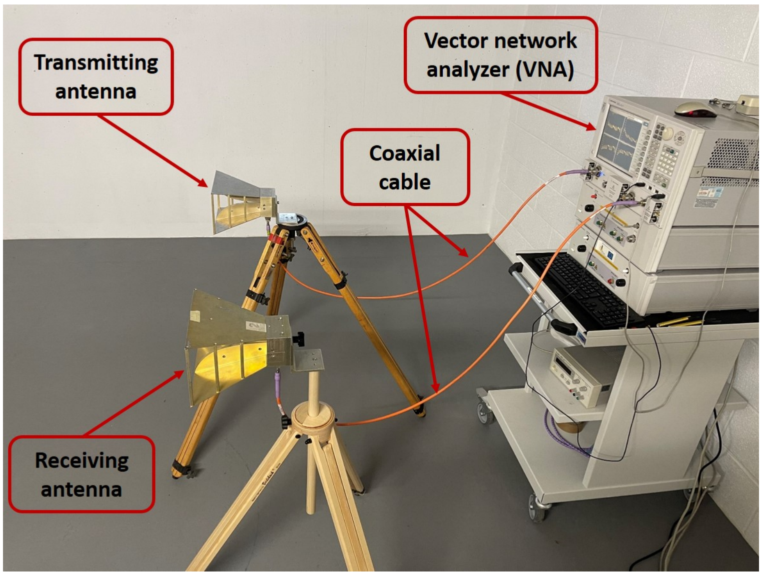

Figure 4.2: Measurement system in a close room clear of all obstacles

on the frequency. Table 4.2 shows the antenna gain for different operating frequencies [17].

Table 4.1: Features of the horn antenna

Block	**Specifications**
Frequency range	700 MHz–18 GHz
Gain (dBi)	1.4 to 15
Maximum Power	300 Watts

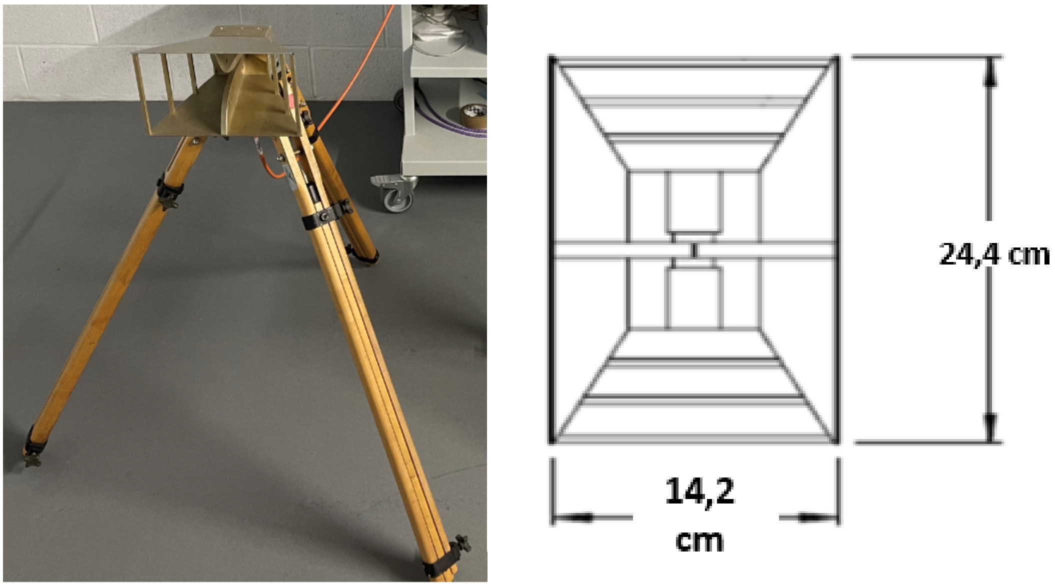

(a) (b)

Figure 4.3: A.H. Systems Double Ridge Guide Horn Antenna SAS-571 700 MHz - 18 GHz

Table 4.2: Antenna gain

Frequency (GHz)	**Gain (dBi)**
2.5	8.96
10	11.56
17	12.71

The measurements presented in this section are carried out in in a close room clear of all obstacles. Prior to measurements, system noise is characterized in multiple configurations (with / without cables / antennas). As an illustration, impact of the isolation between the antennas is removed by considering three distances between the antennas, keeping the radiating elements to the subject under test, and subtracting the “isolation vector” (measurement in free-space conditions).

4.3 Relevance of non calibration

As mentioned in section 2.7.2, the VNA is used to determine the amplitude and phase-shift of the S-parameters of a test device. The system used has advantages. The main aim was to determine the best parameters including frequency, power, IFBW for the most accurate operation of the radar for monitoring vital signs. The VNA presented the obvious choice to perform this study as it allows to test several configurations, provides a wide range of these parameters that can be changed very easily.

It is necessary to separate between the S-parameters measured inside the VNA in the plane of the IQ demodulator without vector calibration, then the S-parameters of the coaxial cables with the calibration. The parameters of interest S_{11} and S_{21} are functions of terms of errors and of all the parameters S_{i_j} $(i = 1, 2; j = 1, 2)$ measured inside the VNA equations 4.1 and 4.2. The measured S-parameters are linked to the S-parameters of interest by error terms determined by calibration. These equations make it possible to express the parameters S of interest as a function of the set of parameters S measured. Between the data measured by the VNA inside and measured in the cable bridges, phase shifts and losses are introduced; therefore we represent it with an error model called the 12-term model.

There are systematic errors associated with network measurements. These errors relating to signal leakage are directivity and crosstalk. Errors related to signal reflections are source and load match. The final class of errors are related to frequency response of the receivers and are called reflection and transmission tracking. The full two-port error model includes all six of these terms for the forward direction and the same six (with different data) in the reverse direction, for a total of twelve error terms. This is why it often refer to two-port calibration as twelve-term error correction Figure 4.4 [85]. Before using an RF vector network analyzer, VNA, it is necessary to calibrate the system so that cable lengths and other uncertainties cited before are removed.

$$S_{11} = \frac{(\frac{S_{11_M} - e_{00}}{e_{10}e_{01}})[1 + (\frac{S_{22_M} - e'_{33}}{e'_{23}e'_{32}})e'_{22}] - e_{22}(\frac{S_{21_M} - e_{30}}{e_{10}e_{32}})(\frac{S_{12_M} - e'_{03}}{e'_{23}e'_{01}})}{D} \tag{4.1}$$

$$S_{21} = \frac{(\frac{S_{21_M} - e_{30}}{e_{10}e_{32}})[1 + (\frac{S_{22_M} - e'_{33}}{e'_{23}e'_{32}})(e'_{22} - e_{22})]}{D} \tag{4.2}$$

However, it is always interesting to study the noise of the instrumentation chain in order to know what happens between the vector network analyzer and the antennas. With the noise study, we have directly the signal levels, the variations and the fluctuations compared to the noise of the receiver.

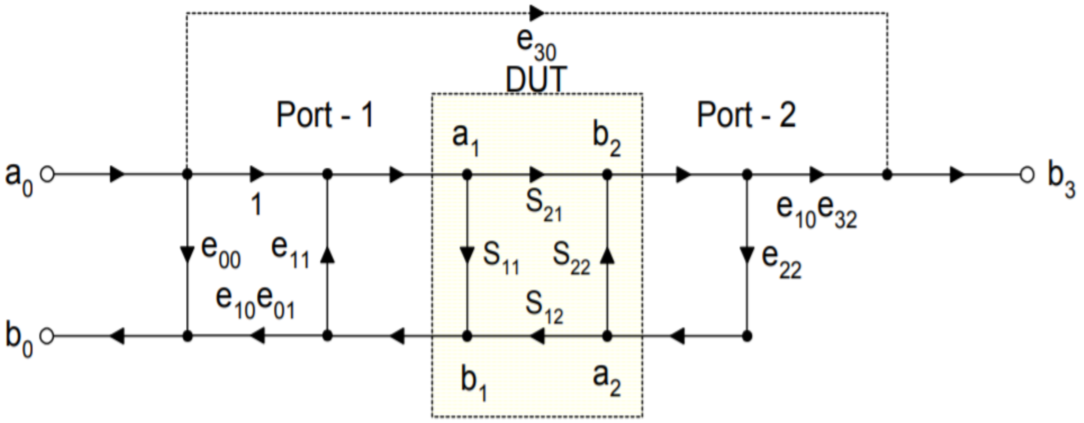

Figure 4.4: Dual-port 12-term (direct chain) error model[85]

The branches of the flow graph are the error terms that describe the linear microwave errors of the system. In the forward direction from Figure 4.4:

- e_{0_0} = Directivity
- e_{1_1} = Port-1 Match
- $(e_{1_0}e_{0_1})$ = Reflection Tracking
- $(e_{1_0}e_{3_2})$ = Transmission Tracking

- e_{2_2} = Port-2 Match
- e_{3_0} = Leakage

We have two measurement scenarios, calibrated $\frac{b_2}{a_1}$ and uncalibrated $\frac{b_3}{a_0}$, and for each scenario, we have two measurements, one for the free space without obstacle figure 4.5(a) and the other with DUT (a seated individual) figure 4.5(b). This study allows knowing the losses and phasing shifts introduced by the cables. The parameters fixed for these measurements are described in Table 4.3.

Table 4.3: The parameters set for the measurements

VNA frequency	10 GHz CW mode
IFBW	100 Hz
Number of points	8001
Acquisition time	72 seconds
Input power	0 dBm
Distance between the antenna and the person	1 m

(a)

(b)

Figure 4.5: The two measurement scenario: (**a**) free space measurement and (**b**) measurement with a seated individual

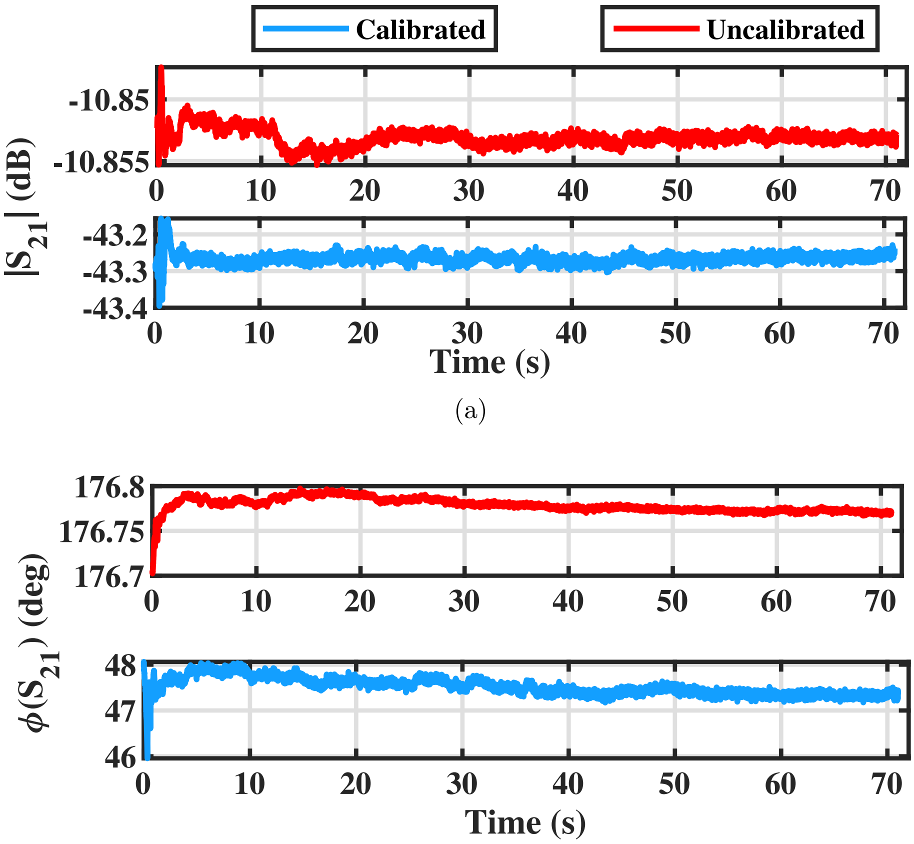

(a)

(b)

Figure 4.6: Transmission coefficient in free space with or without the calibration: (**a**) the amplitude variation and (**b**) the phase-shift variation of S_{21}

The comparison of measurements calibrated in CW mode and non-calibrated will allow us to evaluate the losses. The phase and amplitude variations obtained from the two figures 4.6 and 4.7 are shown in table 4.4.

Table 4.4: Variation of the module and the phase-shift of S_{21} for calibrated and uncalibrated measurement free space and subject located at 1 m

	Calibrated		Uncalibrated	
Variations	$\Delta\lvert S_{21}\rvert$ [dB]	$\Delta\phi S_{21}$ [°]	$\Delta\lvert S_{21}\rvert$ [dB]	$\Delta\phi S_{21}$ [°]
Free space	0.04	0.21	0.001	0.01
With subject at 1 m	0.01	0.46	1.62	18.35

The variations of the amplitude and the phase-shift of the transmission signal S_{21} displayed in the two figures 4.6 and 4.7, is more important and higher for the uncalibrated test in the case of measurements with subject at the distance 1 m, compared to the calibrated test. Indeed, we observed that the variation of the amplitude for the uncalibrated case is 1.6166 dB compared to

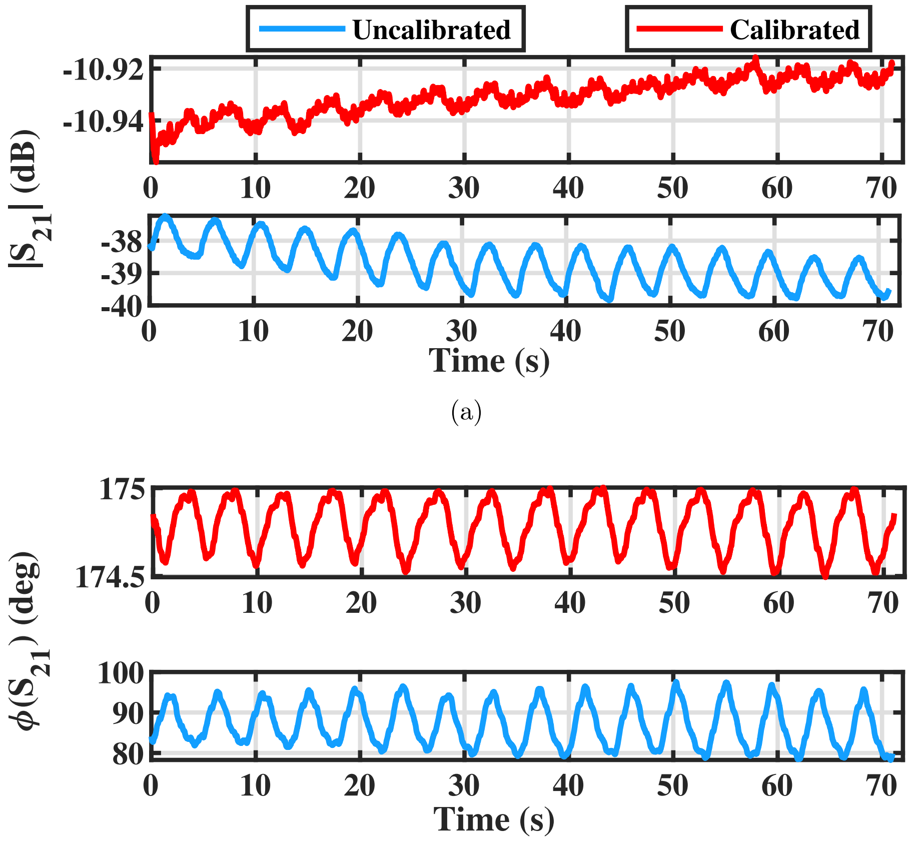

(a)

(b)

Figure 4.7: The measurement with the subject located 1m from the antennas and the distance between the two antennas 22 cm: (**a**) the amplitude variation and (**b**) the phase-shift variation of S_{21}

0.0113 dB for the calibrated case. As far as the phase-shift variation is 0.46° for the calibrated test beside 18.355° for the uncalibrated. In the calibrated case the VNA corrects with default values and therefore incorrect. In fact, for the vector network analyzer calibration in CW mode to be correct, the wave must be inserted into the two VNA ports at the same time, which is impossible.

The two equations 4.1 and 4.2 implies that it is necessary to measure simultaneously, and in real time the parameters S on each side, and to inject the signal on the two ports of the VNA at the same time, which is impossible. This is the reason why any vector calibration in full two port in CW mode is excluded and not relevant for our measurement case. The only two calibrations that can be used in CW mode are a free space calibration [84] in the plane of the device under test [32], or the calibration only in reflection at the level of the cables.

To better understand the phenomenon of propagation between the opening of the antenna and the reference plane, we model our measurement system by a quadrupole with 4 complex terms [Γ_1,Γ_2,T_1,T_2] to characterize the propagation of the wave between the antenna and the human body and on the other hand a quadrupole [t_{01},t_{10},r_{01},r_{10}] to characterize the human body air interface, Figure 4.8.

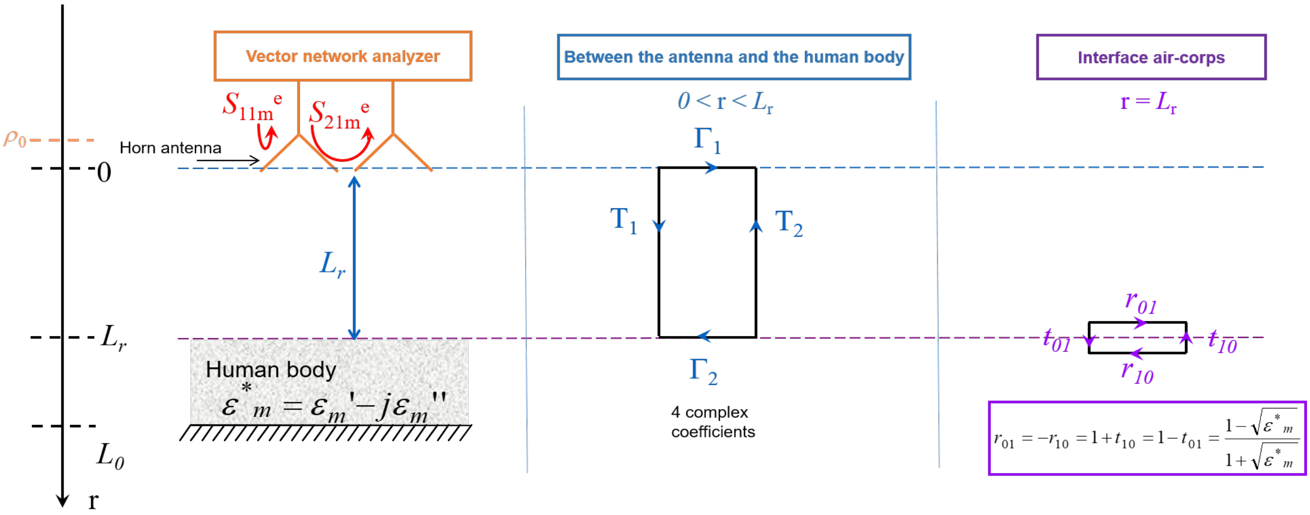

Figure 4.8: Measurement configuration

In the case of an aperture propagation of the antenna / reference plane, the complex terms [Γ_1,Γ_2,T_1,T_2], represent respectively in the case in transmission, the isolation vector, the re-radiation (any energy not transmitted to the antenna), the phase shift losses of a wave propagating from the antenna towards the reference plane (human body) and the phase shift losses of a wave propagating from the reference plane towards the opening of the antenna.

In the case of propagation at the air / body (thorax) interface, r_{01} and r_{10} represent the body (thorax) / air reflections and the body (thorax) / air transmissions t_{01} and t_{01}. The measured parameter S_{21m} is therefore dependent on the distance between the antenna and the individual, the permittivity, G_1, G_2 r_1, r_2 $S_{21m} = \mathrm{f}\ (\ L_r\ ,\ \epsilon^*_m\ ,\ \rho_0\ ,\ \Gamma_1\ ,\ \Gamma_2\ ,\ T_1\ T_2\ )$. For the calculation of these terms can be done by free space calibration.

4.4 Characterisation of system noise in multiple configurations

The measuring bench is a reference system based on the heterodyne architecture, which is the vector network analyzer (VNA).The analyzer module receives and interprets the IF signal for phase-shift and amplitude data. All electronic circuits which constitutes the VNA, make a contribution in terms of noise. Which are unpredictable since they vary with time in a random way. Thus, they cannot be removed by calibration. The main contributors to random error are instrument noise (source phase-shift noise, sampler noise, IF noise). The most common form of random errors is the thermal noise, which increases as the temperature of the circuit increases. Contrary to systematic errors, which are due to imperfections in the analyzer and test setup. They are repeatable (and therefore predictable) and are assumed to be time invariant.

4.4.1 The intrinsic noise of a network analyzer

A series of measurements are made to reveal the noise of the measurement system. The figure 4.9 shows a flow chart resume different parameters studied, in order to assess the intrinsic noise of the vector network analyzer.

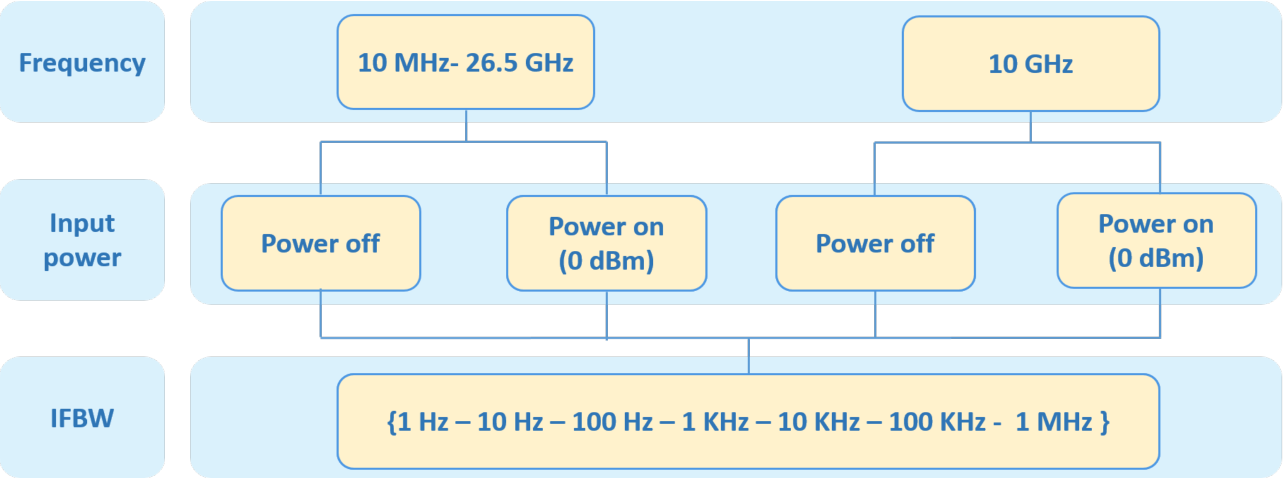

Figure 4.9: Flow chart of the parametric study to assess the intrinsic noise of the network analyzer

To begin, a matched load is placed on the two ports of the VNA for isolation, and the measurement is launched over the entire frequency band of the VNA [10 MHz – 26.5 GHz], with a variable Intermediate Frequency Band Width (IFBW). The choice of the IFBW has a significant effect on overall measurement speed and on the measurement result. To understand the effect of IF bandwidth on measurement performance, it's worthwhile to take measurements on the entire range of IFBW. However, the number of points has fixed at 3001 points, which leads to different time of measurements for each IFBW (Table 4.5).

The variations of the module of S_{21} for the two scenarios of measurement

Table 4.5: Time of measurement for each value of IFBW for 3001 samples

IFBW	Time of measurements [seconds]
1 Hz	$2.6e^3$
10 Hz	$2.7e^2$
100 Hz	$2.7e^1$
1 KHz	3.2
100 KHz	$4.2e^{-5}$
1 MHz	$3.9e^{-5}$

with the VNA: power off and power on 0 dBm are presented in the Table 4.6 for each value of IFBW. We can see in Table 4.6, that the signal level goes from -73 dB for an IFBW of 1 MHz to -130 dB for an IFBW of 1 Hz with a power on 0 dBm. This is because a smaller IFBW leads to a higher SNR, so the variations of the signal are more obvious.

Table 4.6: Variation of the module of S_{21} for each IFBW and both cases Power on and off

$\lvert S_{21} \rvert$ [dB] IFBW	Power off	Power on
1 Hz	-8.5	-130.9
10 Hz	-8.1494	-122.6
100 Hz	-8.2	-112.8
1 KHz	-8.3	-102.8
100 KHz	-8.1	-83.3
1 MHz	-7.9	-73.2

The standard deviation is a measure of the amount of variation of a set of values. For a random variable vector A made up of N scalar observations, is the square root of the variance and it is defined as:

$$S = \sqrt{\frac{1}{N-1}\sum_{i=1}^{N} |A_i - \mu|^2} \tag{4.3}$$

where μ is the mean of A.

The standard deviation of the results of the measurement are presented in both cases: power off and power on with the power is fixed at 0 dBm figure 4.10. It allows seeing the natural noise of the vector network analyzer even if the source is off. It is a noise generated by the local oscillator of the IQ demodulator.

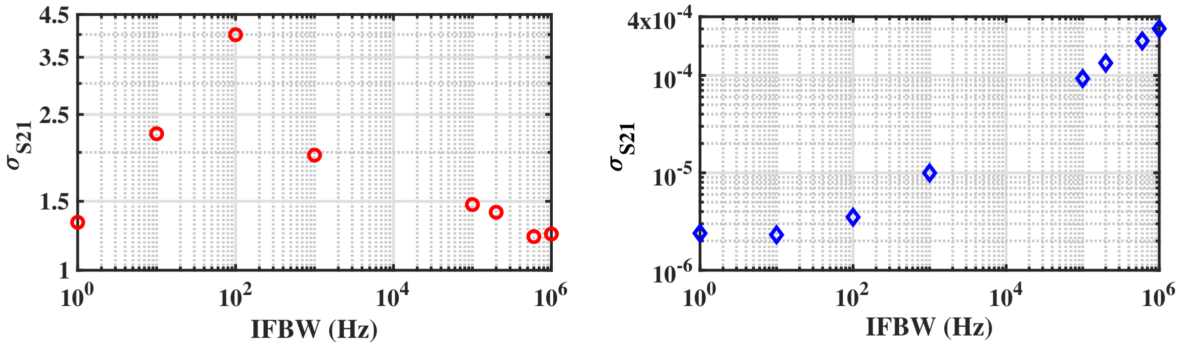

(a) (b)

Figure 4.10: Standard deviation of the measurement (VNA without cable) in the frequency band [10 MHz- 26.5 GHz]: (**a**) power off and (**b**) power on 0 dBm

The same experiments were carried out at the 10 GHz frequency, to observe the impact of IFBW on the reflection coefficient and the transmission coefficient in the time domain figure 4.11. .

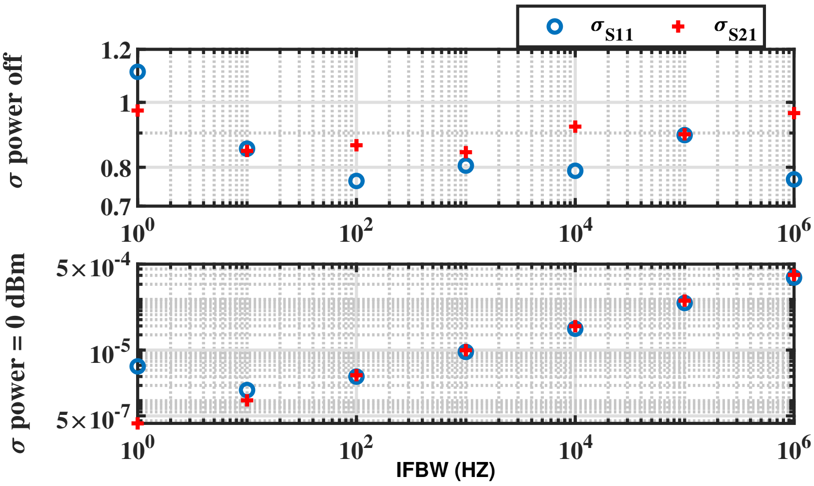

Figure 4.11: Standard deviation of S_{11} and S_{21} (VNA without cable) for the input power 0 dBm and the power off, F= 10 GHz

The results of the measurements made it possible to know the fluctuations and the level of the intrinsic noise of the VNA without the additional instrumentation (antenna and cable) for each value of the IFBW. The measurement with lower IFBW yields better detection capability with less noise and higher resolution. So the smaller the IFBW, the better the signal-to-noise ratio. Otherwise, wider IFBW translate to faster measurement speeds, for an IFBW 1MHz, the time of measurements is $3.9e^{-5}$. By contrast, narrow

IFBW configurations lead to longer measurement times, for an IFBW 1Hz, the time of measurements is $2.6e^3$. For our case (low noise and reduced acquisition time) it is preferable to work at an IFBW of 100 Hz to 1 KHz.

To complete the previous measurements, we carried out in the same configuration as previously a study at the power -20 dBm. The figure 4.12 shows the standard deviation of the measurements result of both reflection and transmission coefficients for each value of IFBW.

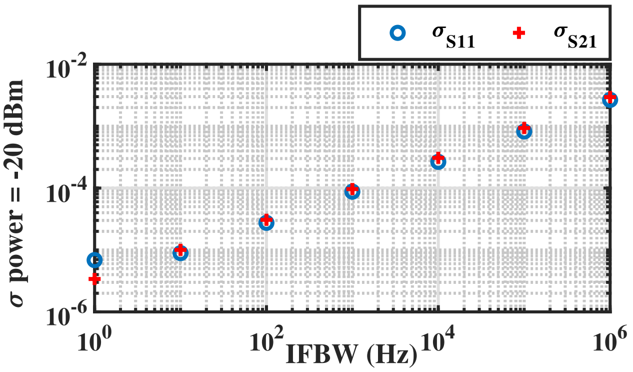

Figure 4.12: Standard deviation of S_{11} and S_{21} (VNA without cable) for the input power -20 dBm, F= 10 GHz

The Table 4.7 resume the result of comparison. This measurement companion allows highlighting the proportionality that exists between the IFBW and the input power. Indeed, working in a power configuration $P_1 = 0$ dBm and $IFBW_1 = 1$ MHz is equivalent to working in the power configuration $P_2 =$ -20 dBm and $IFBW_2 = 10$ KHz. The resulting proportionality formula is:

$$\frac{P_1}{P_2} = \frac{IFBW_1}{IFBW_2} = k \tag{4.4}$$

Where k=100 , $P_1 > P_2$ and $IFBW_1 > IFBW_2$.

Table 4.7: The proportionality between the IFBW and the power

IFBW $\sigma_{S_{21}}$	1 MHz	100 KHz	10 KHz	1 KHz	100 Hz	10 Hz	1 Hz
Power -20 dBm	0.0029	9.34e-4	3.079e-4	9.65e-5	3.07e-5	1.005e-5	3.400e-6
Power 0 dBm	3.06e-4	9.48e-5	2.97e-5	9.92e-06	3.19e-6	1.014e-6	3.56e-7

4.4.2 The effect of a coaxial cable on measurement

The following studies concern the study of signal fluctuations when the two ports of the VNA are connected by a coaxial cable. The measurements will be performed in two configurations: power off and power on (0 dBm). The cable used in the measurements is constructed with MegaPhase's industry, The length of the cable used is 2 m with an attenuation of 3 dB at the operating frequency 10 GHz.

Figure 4.13: The coaxial cable MegaPhase

According to the measurement results, in frequency corresponds to the VNA band, or in CW mode at 10 GHz figure 4.14, we see that the cable adds fluctuations. In the case of the VNA without cable with the power 0 dBm and at the frequency 10 GHz Figure 4.11, we have the standard deviation which is of the order of 10^{-4} compare to 10^{-3} in the case of the VNA with the cable connecting the port 1 to 2 Figure 4.14. Indeed, when the power is off the fluctuations are low, and the more the power is increased, the cable will go through variations in the environment (temperature, humidity,etc.).

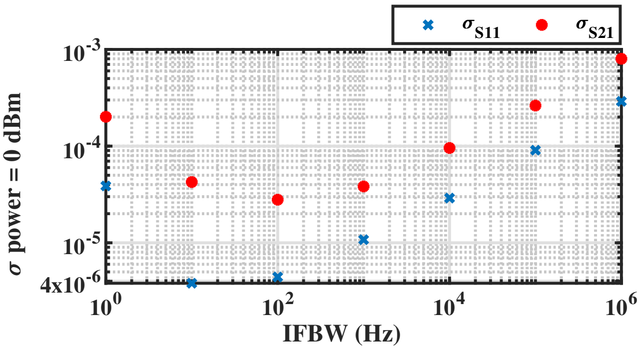

Figure 4.14: Standard deviation of S_{11} and S_{21} (VNA with cable) for the input power 0 dBm, F= 10 GHz

In addition to the VNA, the measurement system includes coaxial cable and two horn antennas, one for transmission, and the other for reception. The model of the both antenna is SAS-571 Double Ridge Horn antenna, which is a broadband High gain antenna with low VSWR. It has an input handling capability up to 300 watts CW.

We are interested in this part in the contribution of each instrument (VNA, cable, Antenna) and to know the variations of parameters S introduced by each component. The measuring bench is characterized in multiple configurations (with / without cables / antennas). To do this, a first measurement of the S-parameters is carried out on the VNA alone, the same measurement will be carried out with the VNA and the cables, to end up inserting the antennas on the cables and the VNA and see the variations of these S-parameters. This study will highlight amplitude and phase-shift variations of each component of the instrumentation chain (VNA, cables and antennas. The figure 4.15 shows the S_{11} reflection and S_{21} transmission coefficients of each configuration.

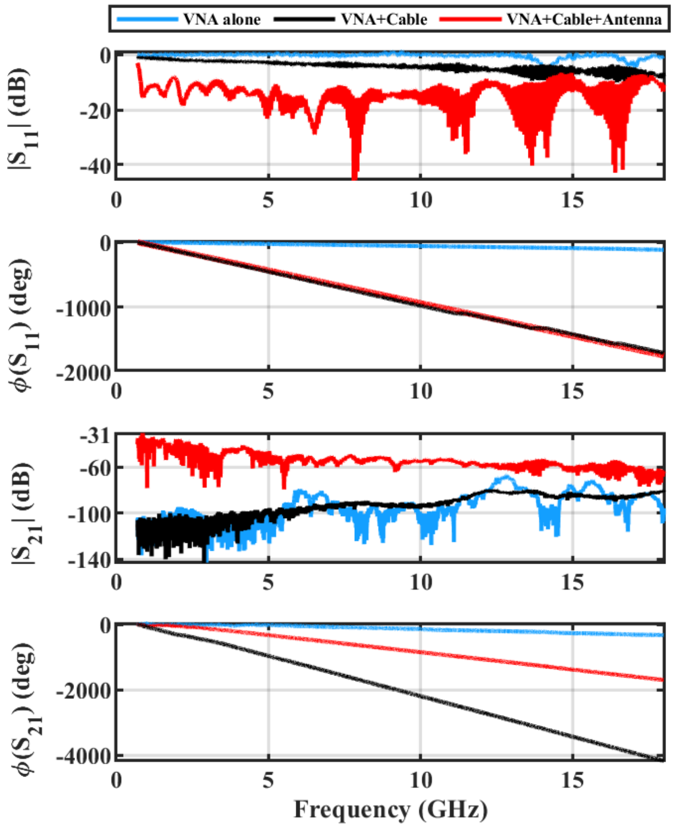

Figure 4.15: S_{11} and S_{21} of the three configurations: VNA alone, VNA plus cable and VNA plus cable plus antenna

We observe that when the VNA is alone, the reflection coefficient is greater than when the VNA is connected to the antenna. indeed the S_{11} is of the order of -0.4 dB (at 10 GHz) with the VNA and -14 dB (at 10 GHz) with the connected antenna. Conversely, the transmission coefficient is smaller when the VNA is alone than when it is connected to the antenna. When the VNA is alone the whole wave is reflected towards the VNA is therefore S_{11} is large and S_{21} is small. In the other case, when the VNA is connected to the antenna, the energy transmitted by the VNA is transmitted to the antenna thus generating a decrease in the reflection coefficient S_{11} is an increase in the transmission coefficient S_{12}.

The increase in the number of points is closely related to the increase in scan time, and it is evident that using IFBW reduction to attain increased dynamic range has an impact on measurement speed. The VNA provides a large number of intermediate frequency bandwidth to choose from, which gives the wide flexibility in reducing the desired background noise.

4.5 Impact of the isolation between the antennas on the measurement

The ideal electrical performance of the antenna can be dictated by an infinite gain, lack of side or back lobes, no return loss. However, microwave noncontact vital sign adds new requirements in terms of sensitivity to the environmental clutter, limited cross-section of the target and compactness. In this effort, an extensive review on different antenna designs for non-contact vital signals measurements was presented in [29]. In this section, we consider double ridge and linearly polarized horn antennas (SAS-571) with frequency range 700 MHz – 18 GHz and 1.4 to 14 dBi gain. Among the antenna technologies, this antenna presents a good compromise in terms of electrical performance to achieve a parametric study. We have preliminary characterized the antenna by measuring the radiation pattern at 10 GHz as showing in the Figure 4.16.

There is coupling noise due to the distance between the transmitting antenna and the receiving antenna. The following study shows the impact that this distance has on the amplitude and the phase-shift of the S-parameters. The distance between the individual under test and the antennas is fixed arbitrary at 60 cm. The test frequency is set at 10 GHz, while the number of samples at 10001, and the IFBW at 100 Hz which leads to time of measurements 88.7 seconds. This study will allow us to know how close can the transmit and receive antennas be to each other. However, it is necessary to judiciously

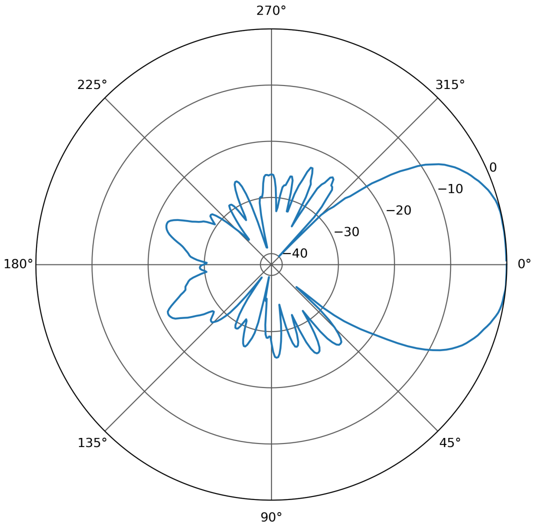

Figure 4.16: Measured radiation pattern at 10 GHz – Double ridge horn antenna SAS-571

choose the separation distance between the two antennas in order to obtain two uncorrelated signals and prevent the interference problems. Optimal spacing is always a trade-off. For that, the antennas are placed on an arc of a circle to vary the position between the transmitting antenna and the receiving antenna, in order to find the optimum point to have the least coupling. As an illustration, the impact of the leakage between the antennas is removed by considering three position distances between the antennas(Figure 4.17), keeping the radiating elements to the subject under test, and subtracting the “leakage vector” (measurement in free-space conditions). Table 4.8 shows the distance fixed for each position.

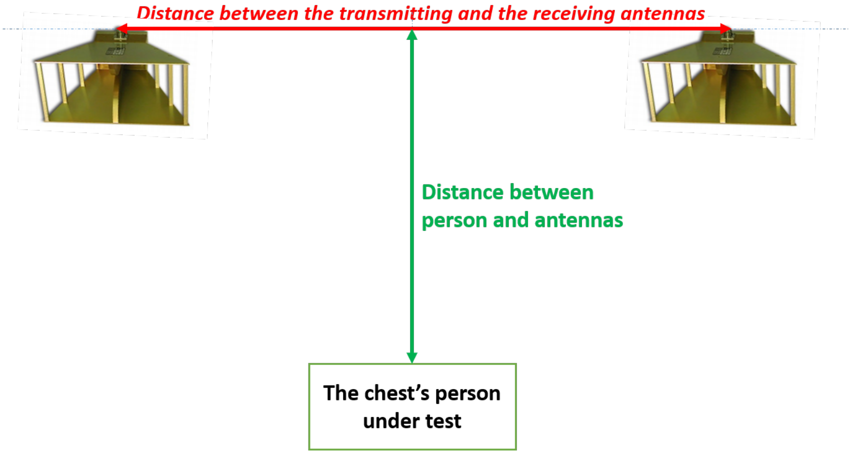

Figure 4.17: Distance between the transmitting and the receiving antennas

The Figures 4.18, 4.19 and 4.20 show the results of this measurement in S-

Table 4.8: Distance separation between the two antenna fixed for each position

Different position	Distance between the transmitting and the receiving antenna
Position 1	24.4 cm
Position 2	80.4 cm
Position 3	54.4 cm

parameters and IQ diagram for the three positions. The measured signal comprises two things: the signal emitted on the thorax of the person under test, and the parasitic vector, which is a fixed vector, represents the isolation. As we have fluctuations, so we take the mean amplitude and phase-shift vector of each signal for the representation using the real and imaginary parts of the complex values of the S_{21}.

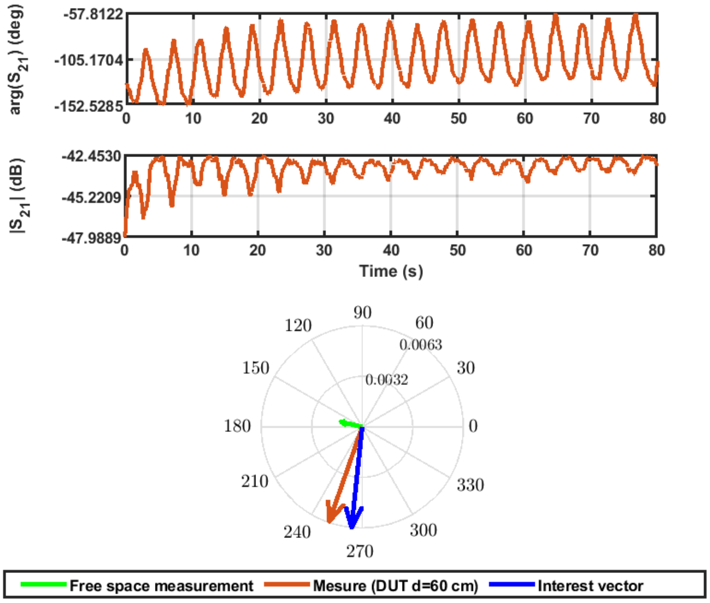

Figure 4.18: Amplitude and phase-shift of S_{21} (Position 1). IQ diagram

The variations on the amplitude and phase-shift are resumed in the Table 4.9. For position 1, there are weak variations on the amplitude and significant on the phase-shift, which means that most of the information is supported mainly by the phase-shift of S_{21} , because the parasitic vector influences the amplitude. On the other hand for position 3, the parasitic vector is large and influences the amplitude and the phase-shift of the vector of interest even if the variants are large. When the antennas move apart, the signal becomes weak and the errors will be large, which explains why for position 3, the parasitic vector is enormous. The losses in free space increase with the frequency.

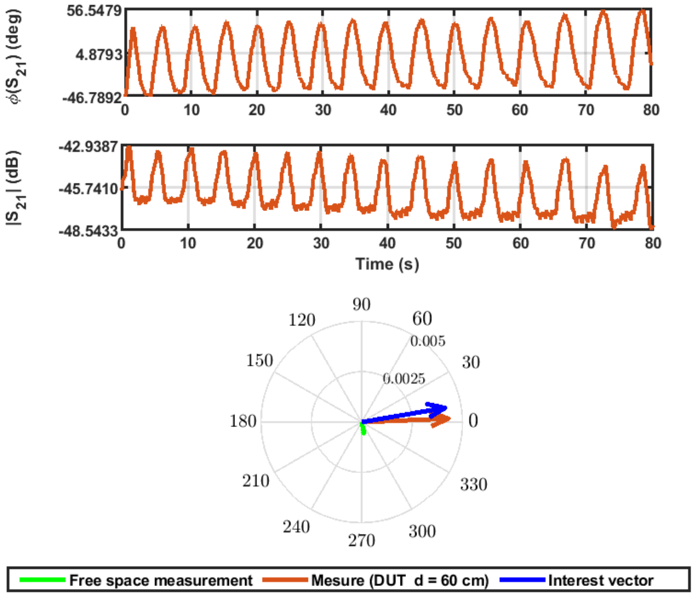

Figure 4.19: amplitude and phase-shift of S_{21} (Position 2). IQ diagram

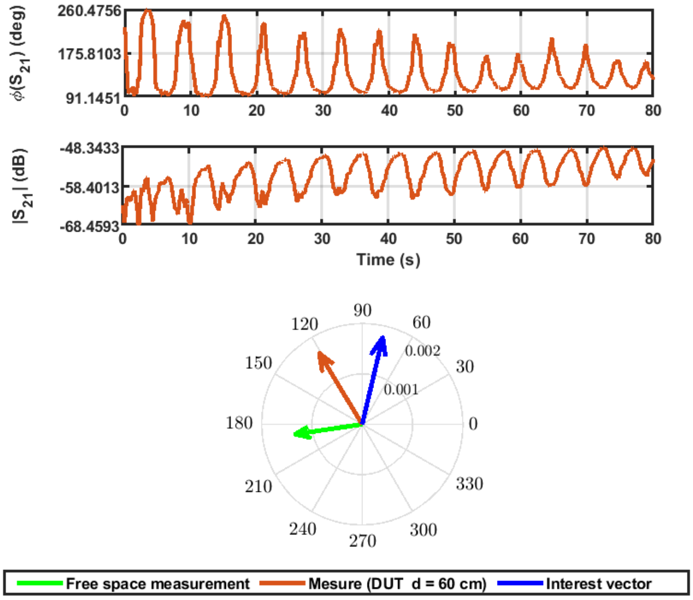

Figure 4.20: Amplitude and phase-shift of S_{21} (Position 3). IQ diagram

Table 4.9: Variation of the module of S_{21} for each position

	Before		After	
Variations	$\Delta\|S_{21}\|$	$\Delta\phi S_{21}$	$\Delta\|S_{21}\|$	$\Delta\phi S_{21}$
Position 1	5.53	94.72	0.00418	95.09
Position 2	20.12	169.3	0.0039	184.3
Position 3	5.69	104.4	0.0038	104.8

For position 2, the parasitic vector is much smaller than the signal reflected by the person's chest and does not influence the measurement and there are no disturbances. therefore it has a negligible influence which is the reason why the curves are cleaner, it does not affect either the amplitude or the phase-shift.

4.6 Conclusion

To resume these experiments, a hard compromise between, input RF power, IFBW, acquisition time and speed of operation must be done to provide optimal solution to reduce the microwave signal fluctuations. A general study aimed to identify both systematic and non-systematic errors in CW microwave vital sign detection has been proposed. Measurement parameters such as RF power, intermediate frequency bandwidth (IFBW), separation between antennas significantly contributes in the combination of unwanted signals with the signal of interest. Prior to vital sign application, full characterization of the microwave system in terms of noise / signal fluctuations should be ideally performed to derive the intrinsic performance in terms of phase-shift sensitivity and resolution. To resume these experiments, a hard compromise between, input RF power, IFBW, acquisition time and speed of operation must be done to provide optimal solution to reduce the microwave signal fluctuations.

The main drawback in CW bistatic radar remains the leakage between the two antennas. In particular, a part of the transmitted microwave signal goes directly to the receiving antenna, causing a leakage. The leakage can be eliminated or reduced by using microwave absorbent between the antennas or by spacing the antennas. So, all the next measurements are made with an absorbent between the transmitting antenna and the receiving antenna.

The performance of the measurement system depends on the propagation environment, noise and system settings. A parametric study is therefore necessary to know the optimum parameters thus allowing the correct detection of vital signs. The following chapter 5 will therefore be devoted to a parametric study of the propagation system and environment.

Chapter 5

Methodology for the analysis of microwave devices on board Continuous Waves (CW)

5.1 Introduction

As discussed in previous chapters, current methods of heart and respiratory rate monitoring are either expensive or uncomfortable, or both. There is a need for non-invasive, more comfortable, reliable and robust alternative methods. In this chapter, we will prove that the cyclostationary approach associated to the transmission coefficient amplitude and phase of a bistatic radar attached to a person's chest is capable of monitoring the respiration and the heart rate of that person with excellent accuracy compared to a reference system.

To verify the detecting performances of our proposed method based on cyclostationarity, a series of experiments considering different parameters are carried out to confront the theory and the simulations results. Moreover, we evaluate the impact of the numbers of samples and the noise impact, we also propose to evaluate these results using a small number of samples to reduce both the computational cost and the response time of the digital signal-processing block. The measurements are performed at the ISM frequency 2.5 GHz in a bi-static scenario using a CW radar, built up with a vector network analyzer interfaced with two horn antennas.

This parametric study is carried out with the aim of providing a comprehensive guide to the detection of vital signs with CW radar. It is divided into two parts Figure 5.1, one part concerns study of the internal parameters of the VNA including the IFBW, the power and the frequency. The other part concerns the parameters of the measurement environment, the polarization of the antennas, the distance between the antenna and the subject under test in different scenarios.

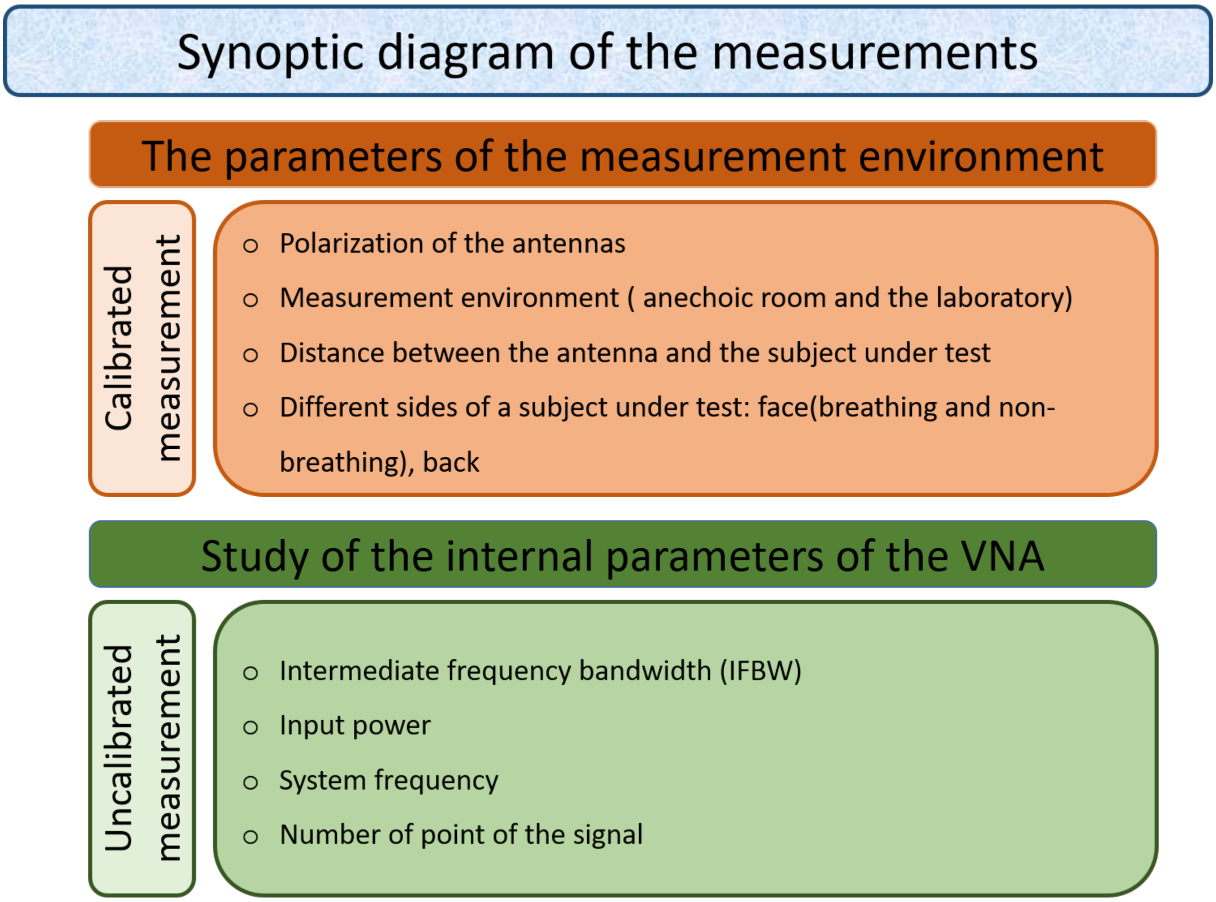

Figure 5.1: Synoptic diagram of the measurements

5.2 Experimental validation of the parametric study: measurement environment

5.2.1 Experimental setup

A radar system generally consists of a transmitter, antennas, a receiver and signal processing hardware and/or software. The transmitter creates a waveform. Then, a directional antenna focuses the beam in the direction of the target's rib cage. The receiver converts the signal from the transmission frequency to an intermediate frequency or to a baseband. Signal processing is used to reject clutter and out-of-band noise while passing the desired signal, and to derive information from the signal. The radar system shown in Figure 5.3 is built up with a reference measurement system, i.e., vector network analyser (VNA 24 from Rohde and Schwarz $R\&S$, 0.7–24 GHz) interfaced with two horn antennas (AH Systems SAS-571 Double Ridge Horn Antenna 700 MHz–18 GHz through stable coaxial cables with 2 m long each. The figure 5.2 shows the VNA used in the measurements and the table 5.1 shows the characteristic of this VNA.

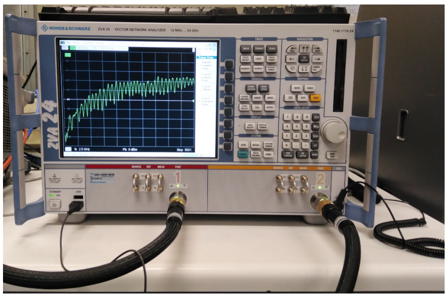

Figure 5.2: The VNA used in the measurement (ZVA 24)

Table 5.1: Specifications of the ZVA 24

Network analyzer series	ZVA 24
Number of test ports	2 ports
Frequency range	10 MHz to 24 GHz
Connector type	3.5 mm (f)
Number of test points per trace	1 to 60001
Measurement bandwidths	1 Hz to 1 MHz
Sweep times	Depend on the number of measurement points, the measurement bandwidth and the start and stop frequencies.

The VNA provides continuous waves at the desired frequency 2.5 GHz with an RF that corresponds to 0.25 mW. The Table 5.2 shows the parameters defined for the VNA. The antenna is directed to the person under test's thorax which is placed at a distance d from the subject under test.

The transmitting antenna connected to port 1 of the VNA radiates the RF signal (a_1) to the person. the receiving antenna connected to port 2 of the VNA, receives the RF signal reflected (b_2) by the chest of the seated person. The reflected signal is modulated by the movement of the rib cage. The VNA, measures the amplitude and the phase-shift of the transmission coefficient $|S_{21}| = \frac{b_2}{a_1}$. Hence, it contains information about the heartbeat and the breathing frequencies. In this study, the reflected signal from the rib cage is extracted in the time domain while fixing the CW mode of the VNA,

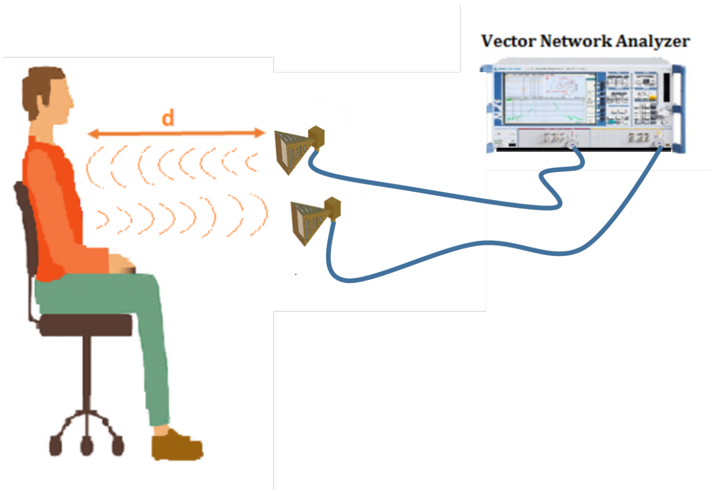

Figure 5.3: Measurement configuration considering a vector network analyser (VNA) and two horn antennas

either as a function of the number of points or as a function of the time of acquisition.

Table 5.2: Specifications of the measurement system

Block	**Specifications**
Acquisition time	160.58 seconds
Distance	60 cm and 1 m
Transmitted Power	-6 dBm
Number of points	8001
IFBW	100 Hz

According to equation (3.6), the phase-shift-shift variation, for the test frequency 2.5 GHz ($\lambda = 120$ mm) is 1.2° for a chest displacement of 0.2 mm, and 3° for 0.5 mm. Many parameters are accessible to be set by using a VNA, such as the frequency, the number of measurement points, the sweep time, and hence, the sampling rate. It is necessary to reduce the transmitted power in order to reduce the radiated energy to which the person under test is exposed during the measurements. Various organizations and countries have developed exposure standards for radio frequency energy (section 2.3). These standards recommend safe exposure levels for the general public and workers,so the output power set to -6 dBm. Then, it is important to note that the selected frequency belongs to the Industrial Scientific Band (ISM) and the radiated power is fixed at -6 dBm, which does not exceed the limits specified by several organizations.

For this quantitative measurement campaign, we consider a reference commercial kit of Libelium MySignals [64] for HR and RR (Figure 5.4). MySignals is a development platform for medical devices and eHealth applications. It can measure more than 15 different biometric parameters with several sensors, Figure 5.4. For our case, we use the two sensors ECG and AIRFLOW that are fixed on the person under test and at each test we note the value of the HR in beats per minute (BPM) and RR. The data gathered by MySignals is encrypted and sent to the developer's private account at the Libelium Cloud. Table 5.3 presents general features of MySignals.

Table 5.3: General features of MySignals

Features	**MySignals SW**
Number of sensors	16
Sensor Readings	From any sensor (16) to one interface
Architecture	Libelium IoT Core
Radios on board	BLE(Bluetooth Low Energy), WiFi

To validate the proposed system, the algorithm of cyclostationarity and its ability to detect the breathing and the heartbeat rates, the radar measurements were performed simultaneously with ECG and the airflow measurements. To validate the proposed system and its ability to detect heartbeat rate, the radar system measurements are performed simultaneously with ECG measurements.

Figure 5.4: Libelium MySignals Kit

5.2.2 Environment (controlled / uncontrolled)

For the purpose of determining the effect of the measurement environment on the detection of vital signs, the measurements are done in two environment as shown in the Figure 5.5: the controlled room (anechoic chamber) and the uncontrolled room (laboratory environment).The anechoic chamber is a room designed to absorb the reflections of electromagnetic radiation and to minimise interfering energy disturbances from external sources and their surroundings.

As a first step, in order to validate and assess the performance of the proposed algorithm and avoid disturbing the measurements by any other type of signal coming from the environment or multi-path or noise, we carried out a series of tests on a clothed person seated in front of the system (30-year-old man) in an anechoic chamber. The second step consists of redoing the same measurement with the same subject under test, but this time in a laboratory environment.
The Figure 5.6 shows the variation of the amplitude and the phase-shift of the Transmission coefficient S_{21} in the two environment. In both cases, the distance between the antennas and the person under test was fixed at 60 cm and breathing normally.

(a) (b)

Figure 5.5: Measurement environment: (**a**) in anechoic chamber and (**b**) in the laboratory environment

We show that the phase-shift variation of S_{21} in the uncontrolled room is noisier and smaller than the phase-shift variation of S_{21} an anechoic chamber. In addition, the amplitude of S_{21} in the uncontrolled room is much smaller than the one in the anechoic room. This difference, could be related to the nature of the measurement environment, because in the measurement laboratory,

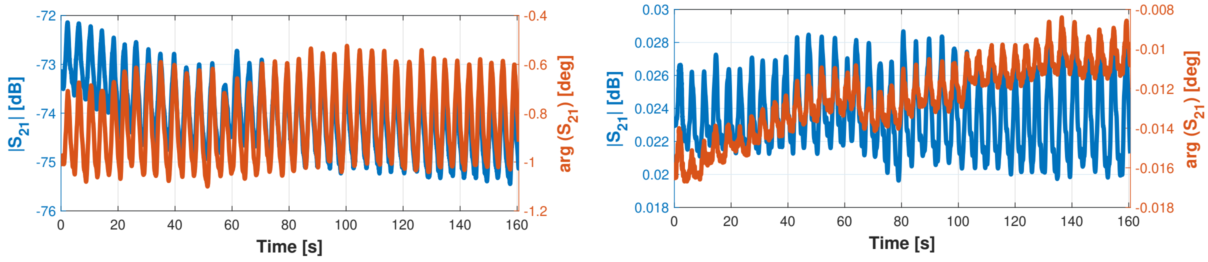

(a)

(b)

Figure 5.6: Amplitude and phase-shift variation of the transmission coefficient S_{21} in the two environment : (**a**) anechoic chamber and (**b**) uncontrolled room (the laboratory)

Table 5.4: The variation of the amplitude and phase of the transmission coefficient for both case anechoic chamber and uncontrolled room

	anechoic chamber	Uncontrolled room
$\Delta\lvert S_{21}\rvert[dB]$	1.9	$5.6e^{-3}$
$\Delta\phi S_{21}[°]$	0.5	$2.2e^{-3}$

with the presence of different sources of noise and the multi-path, the signal to noise ratio decrease. The temporal signal from the measurements in the anechoic chamber is more stable and clear than that of the measurement laboratory, which contains other motions, multiple paths, clutters and movements of other machines, due to the environment and materials that exist in the laboratory.

The Figure 5.7 and Figure 5.8 show the second and the third order temporal cyclic moment and temporal cyclic cumulant of the transmission signal S_{21} in both cases : anechoic chamber and uncontrolled room, respectively.

Whatever the order of the cyclostationarity algorithm, the level of the cyclic features are greater for the measurements carried out in the anechoic chamber ($2.5e^{-4}$ for the anechoic chamber against $1e^{-4}$ for the uncontrolled room for $|M_x(\alpha, \tau = 0)_{2,0}|$). It is also noted that the more the order increases, the more the difference between the cyclic features in the measurements carried out in the anechoic chamber and that carried out in the uncontrolled room increase (about $1.5e^{-4}$ to the second order against $3.5e^{-4}$ to the third order).

As the respiration signal is a relatively strong signal (compared to the heart signal). Indeed, it is not affected as much as the heart signal by the free space losses, clutter and noise from the environment. The peaks corresponding to the harmonics of RR can sometimes be very close to HR which can make

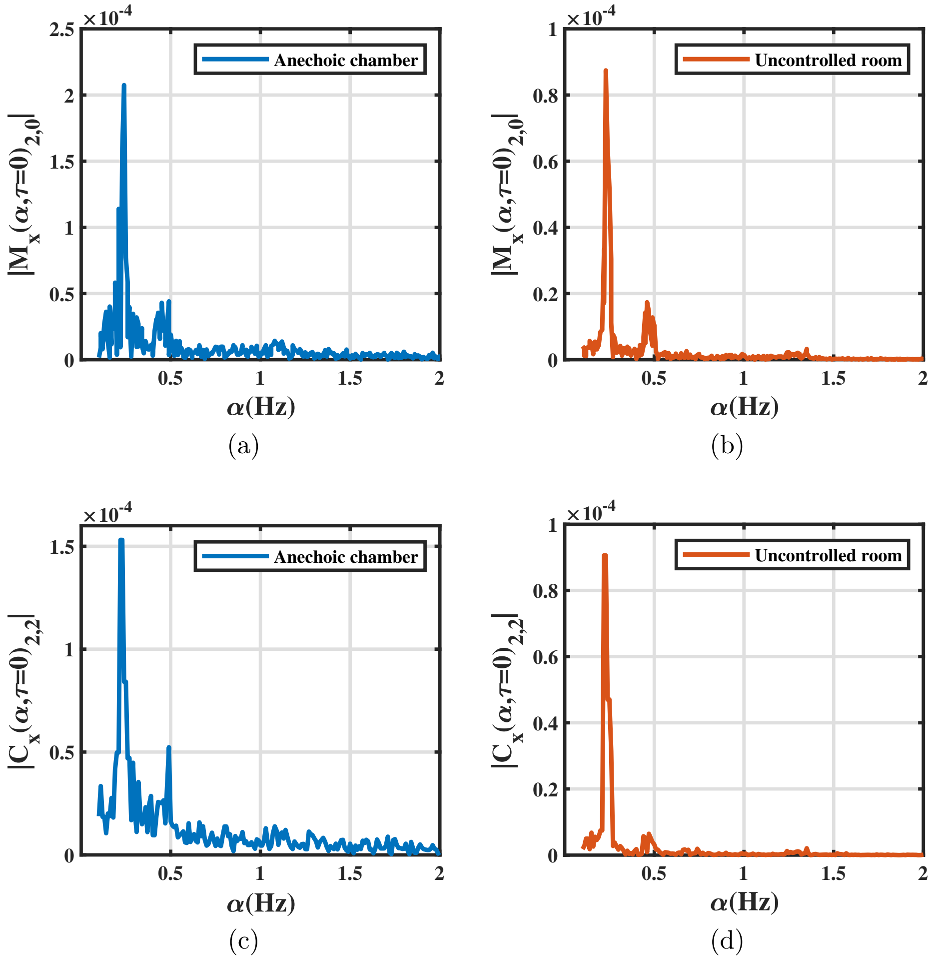

(a) (b) (c) (d)

Figure 5.7: The cyclic features $|M_x(\alpha, \tau = 0)_{2,0}|$ and $|C_x(\alpha, \tau = 0)_{2,2}|$ of S_{21} in the two environment anechoic chamber and the laboratory

it difficult to evaluate this frequency, for example in this case RR is equal 0.22 Hz while HR is 1.1 Hz which corresponds to $5 \times RR$. The level of the parasitic noise, the body motion, linked to the environment infects the detection of the HR which is a small component of the signal comparing to the RR.

Table 5.5 presents the heartbeat and the respiration rates extracted from the chest movement of the person under test by applying the cyclostationarity algorithms and by the reference device MySignal. Then the relative error between the HR and RR from the cyclostationarity and from the MySignals reference is calculated.

The relative error for the detection of RR in anechoic chamber and in Uncontrolled room is equal to zero, which mean that the RR extracted by the cyclostationarity algorithm is equal to the one detected by the reference sys-

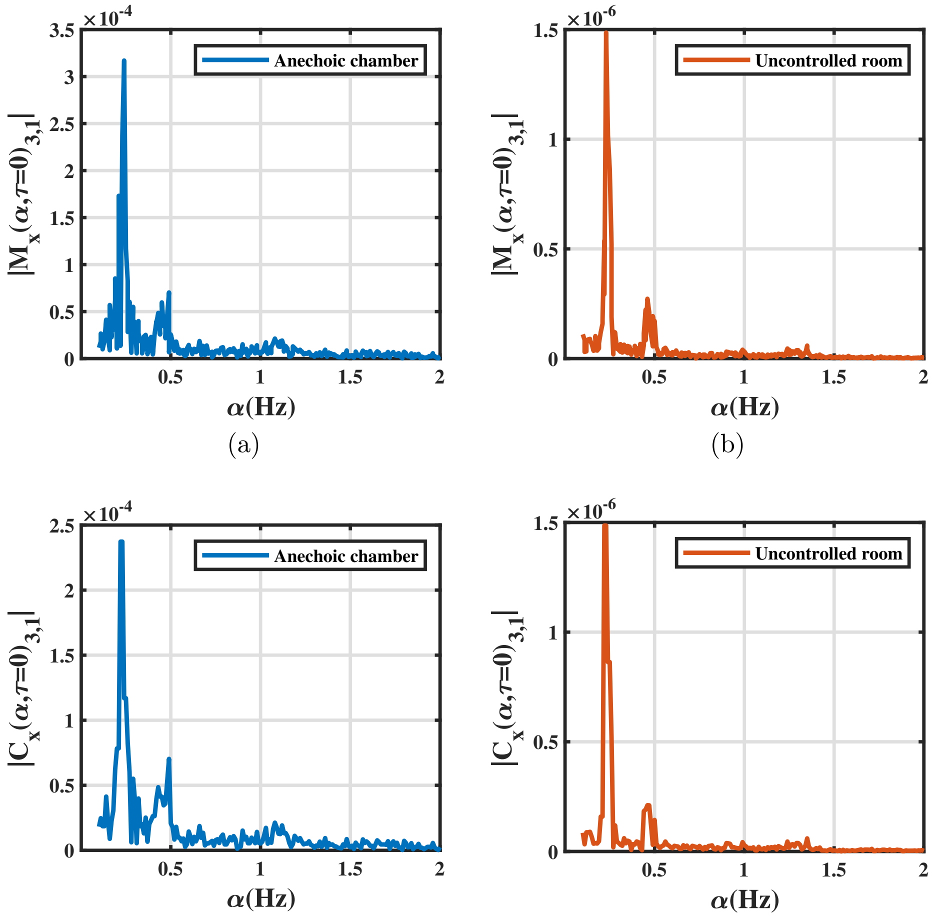

(a) (b)

(c) (d)

Figure 5.8: The cyclic features $|M_x(\alpha, \tau = 0)_{3,1}|$ and $|C_x(\alpha, \tau = 0)_{3,1}|$ of S_{21} in the two environment anechoic chamber and the laboratory

Table 5.5: Comparison of the results for the heart and respiration rate

	MySignals		Cyclostationarity		Relative Error (%)	
	RR (Hz)	HR (Hz)	RR (Hz)	HR (Hz)	RR (Hz)	HR (Hz)
Anechoic chamber	0.22	1.10	0.220	1.081	<1	1.75
Uncontrolled room	0.22	1.32	0.220	1.350	<1	2.22

tem MySignal. While the relative error for the detection of HR is 1.82(%) for the anechoic chamber whilst 2.27(%) for the uncontrolled room. This difference between the detection values of RR and HR is due to the fact that the respiration signal is a relatively strong signal (compared to the heart signal)and it is not affected as much as the heart signal by the free space losses, clutter and noise from the environment.

5.2.3 Impact of the distance between the antenna and the target

For the purpose of determining the impact of the distance between the antenna and the subject detected chest, the distance is set in two values d= 60 cm and d = 1 m, the test frequency is set at 2.5 GHz, while keeping other parameters constant and using the same experimental setup as described in Table 5.2. The subject sits on a chair for the duration of the measure, which is 160.58 seconds. The antennas are mounted on a fixed platform, which are directed and parallel to the subject's chest. The person is breathing normally. The variation of the distance is made for two configuration of the antennas: vertical and horizontal polarization, for the purpose to choose the best antenna position which can lead to have a better detection of vital signs.

Figure 5.9 shows the two configurations of the measurement system when the measurement is made with the antennas in vertical and horizontal polarization are considered.

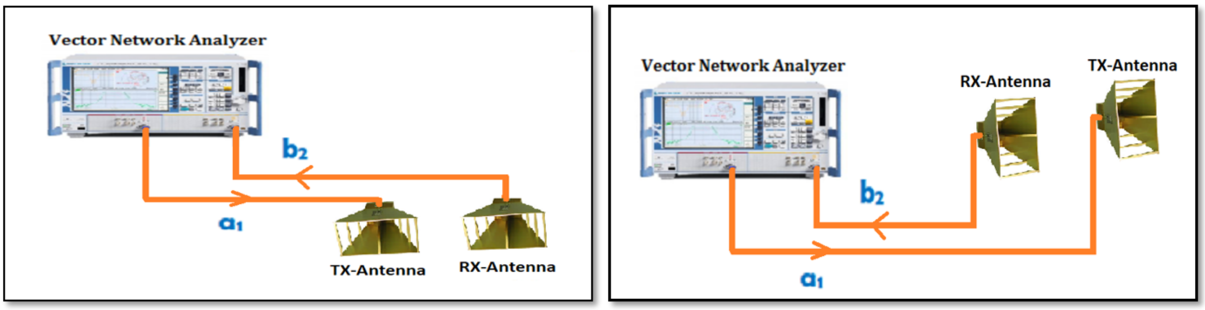

(a) (b)

Figure 5.9: The two different configuration : (**a**) horizontal polarization and (**b**) vertical polarization of the antennas used in the measurement

Figure 5.10 presents S_{21} amplitude and phase-shift extracted for different distances 60 cm and 1 m, in both antenna polarizations. Gain of each antenna at 2.5 GHz is 8.96 dB.

The transmitted signal applied to the horn antenna, generates out electromagnetic waves in the free space at the operating frequency 2.5 GHz ($\lambda = 12$ cm). The different limits of electromagnetic zones are illustrated in the Table 5.6 and the biggest dimension of the horn antenna used in the measurement is D= 24.4 cm (Figure 4.3).

Figures (5.11a) (5.11b) (5.11c) (5.11d) (5.12a) (5.12b) (5.12c) and (5.12d) represent the cyclic statistics, the second-order cyclic moment $|M_x(\alpha, \tau =$

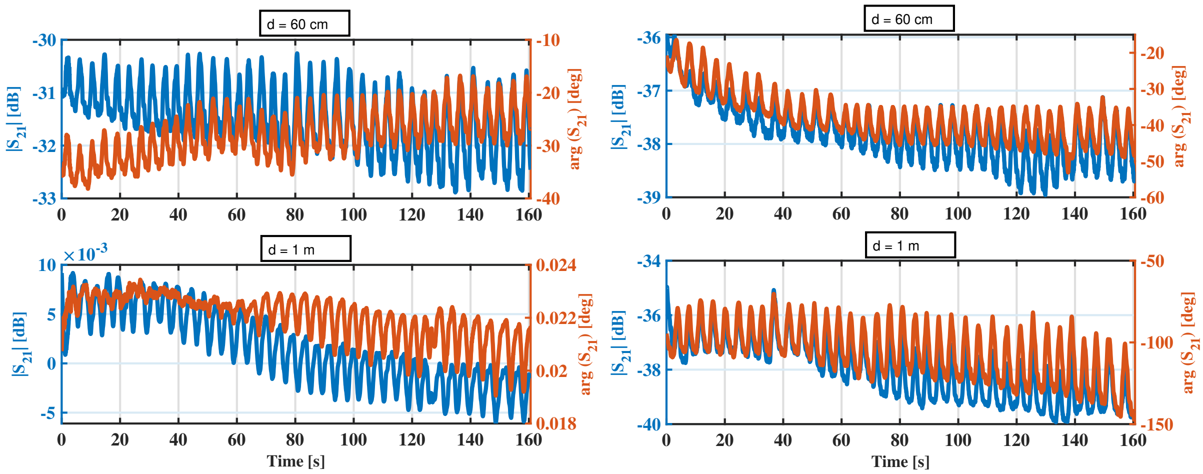

(a) (b)

Figure 5.10: Transmission coefficient S_{21} for both distance 60 cm and 1 m with the two configurations: (**a**) horizontal and (**b**) vertical polarization of the antennas.

Table 5.6: The distance limit for each zone of propagation, f= 2.5 GHz.

Frequency (GHz)	**Wavelength** (cm)	**Rayleigh area (m)** $\frac{\lambda}{2\pi} \leq r \leq \frac{D^2}{2\lambda}$	**Fresnel area (m)** $\frac{D^2}{2\lambda} < r < \frac{2D^2}{\lambda}$	**Far Field (m)** $r \geq \frac{2D^2}{\lambda}$
2.5	12	$0.019 \leq r \leq 0,25$	$0.25 < r < 0.99$	$r \geq 0.99$

$0)_{2,2}|$ d= 60 cm, the second-order cyclic moment $|M_x(\alpha, \tau = 0)_{2,2}|$ d= 1 m, the second-order cyclic cumulant $|C_x(\alpha, \tau = 0)_{2,0}|$ d= 60 cm, the second-order cyclic cumulant $|C_x(\alpha, \tau = 0)_{2,0}|$ d= 1 m, the third-order cyclic moment $|M_x(\alpha, \tau = 0)_{3,1}|$ d= 60 cm, the third-order cyclic moment $|M_x(\alpha, \tau = 0)_{3,1}|$ d= 1 m, the the third-order cyclic cumulant $|C_x(\alpha, \tau = 0)_{3,1}|$ d= 60 cm, the third-order cyclic cumulant $|C_x(\alpha, \tau = 0)_{3,1}|$ d= 1m, respectively, of the reflected signal from the person (5.10b). These measures was performed in the case of a horizontal polarization of the antennas.

Figures (5.13a) (5.13b) (5.13c) (5.13d) (5.13e) (5.13f) (5.13g) and (5.13h)represent the cyclic statistics, the second-order cyclic moment $|M_x(\alpha, \tau = 0)_{2,0}|$ d= 60 cm, the second-order cyclic moment $|M_x(\alpha, \tau = 0)_{2,0}|$ d= 1 m, the second-order cyclic cumulant $|C_x(\alpha, \tau = 0)_{2,0}|$ d= 60 cm, the second-order cyclic cumulant $|C_x(\alpha, \tau = 0)_{2,0}|$ d= 1 m, the third-order cyclic moment $|M_x(\alpha, \tau = 0)_{3,2}|$ d= 60 cm, the third-order cyclic moment $|M_x(\alpha, \tau = 0)_{3,2}|$ d= 1 m, the the third-order cyclic cumulant $|C_x(\alpha, \tau = 0)_{3,1}|$ d= 60 cm, the third-order cyclic cumulant $|C_x(\alpha, \tau = 0)_{3,1}|$ d= 1m, respectively, of the reflected signal from the chest person (5.10b). These measures was performed in the case of a vertical polarization of the antennas.

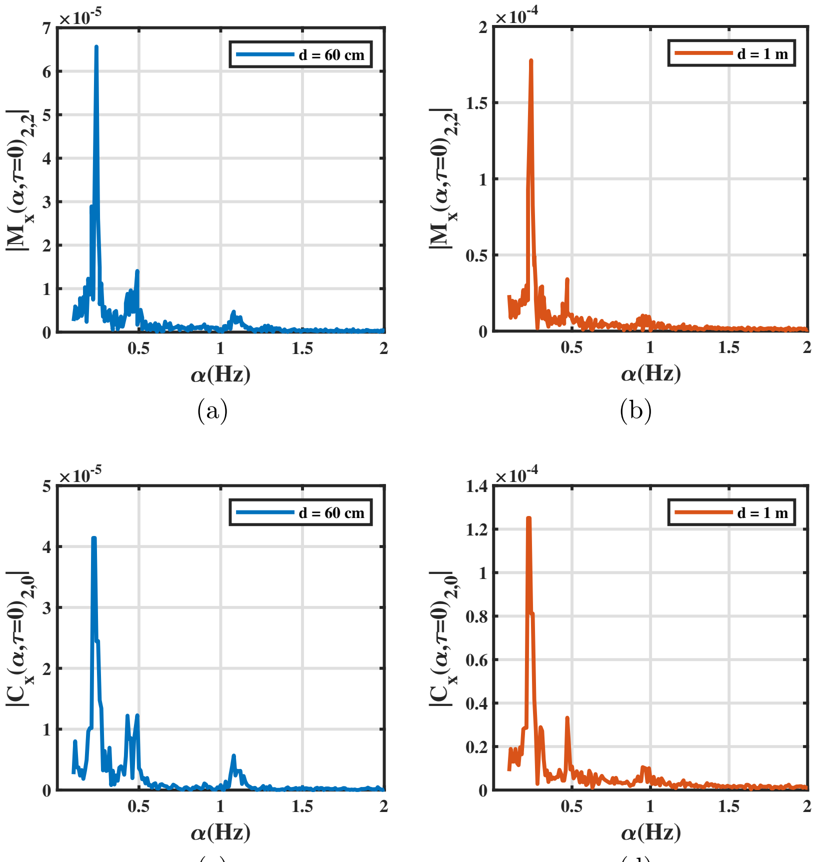

(a) (b)

(c) (d)

Figure 5.11: Second order cyclic features of the transmission signalS_{21} in case of the horizontal polarization of the antennas: (**a**) $|M_x(\alpha,\tau=0)_{2,2}|$ d= 60 cm , (**b**) $|M_x(\alpha,\tau=0)_{2,2}|$ d= 1 m , (**c**) $|C_x(\alpha,\tau=0)_{2,0}|$ d= 60 cm and (**d**) $|C_x(\alpha,\tau=0)_{2,0}|$ d= 1 m

The decision algorithm identifies the maximum peak as RR. For the detection of HR, all related harmonics to RR are removed, then the cyclic statistics in the interval 0.8 – 2 Hz related to HR are identified. The RR is detectable with considerable accuracy for any distance, because it is less affected by noise (environment noise, interference motion body,etc.) as well than the HR. The results show that increasing the distance between the antenna and the chest decreases the accuracy of the vital signs detection specially for the HR. The signal to noise ratio (SNR) of the input of the radar system made of VNA and two horn similar antenna is expressed as a function of the signal power at the input of the system P_s and the noise power at the system input P_b as showing in the equation 5.1 [86]:

$$SNR_{input}(dB) = P_s(dBm) - P_b(dBm) \tag{5.1}$$

Where the signal power at the input of the system is given by equation

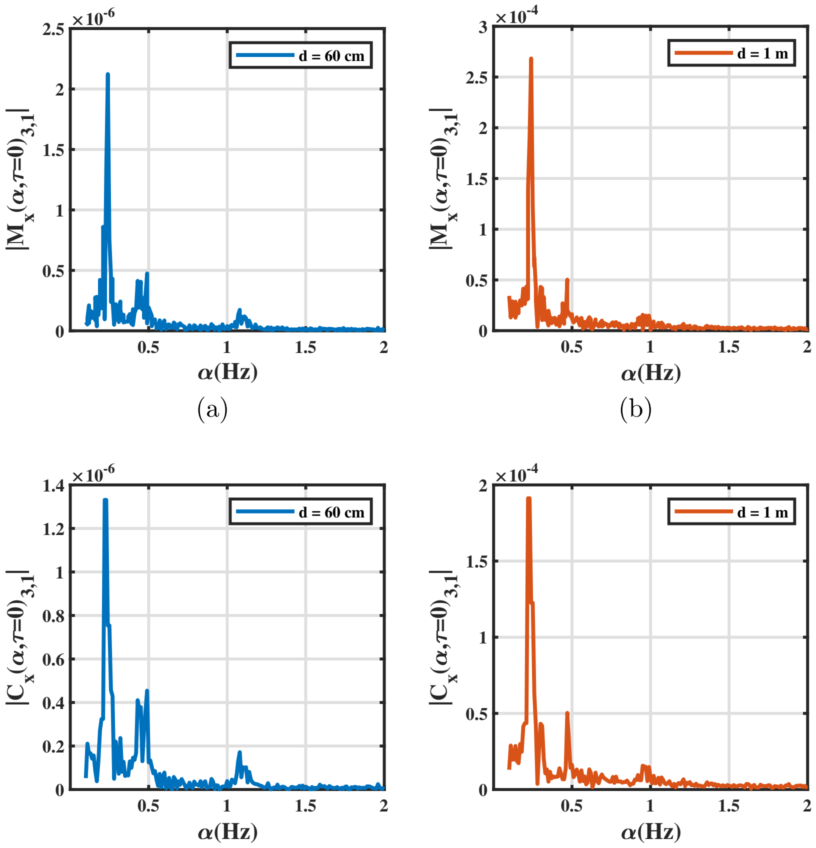

(a) (b)

(c) (d)

Figure 5.12: Third order cyclic features of the transmission signalS_{21} in case of the horizontal polarization of the antennas: (**a**) $|M_x(\alpha, \tau = 0)_{3,1}|$ d= 60 cm , (**b**) $|M_x(\alpha, \tau = 0)_{3,1}|$ d= 1 m, (**c**) $|C_x(\alpha, \tau = 0)_{3,1}|$ d= 60 cm and (**d**) $|C_x(\alpha, \tau = 0)_{3,1}|$ d= 1 m

(5.2) [86]:

$$P_s(dBm) = P_e(dBm) + 2G_e(dB) - A_1(dB) - Refl(dB) - A_2(dB) \quad (5.2)$$

Where G_e is the antenna gain one for the emission and the other one for the reception because they are similar , $A_1 + A_2 = A(dB) = 40\log(\frac{4\pi d}{\lambda})$ are the round trip free space losses which is the global free space losses, Refl is the reflection loss on the human body and P_e is the emitted power. Figure 5.14 presents the signal power at system input for distance between 40 cm and 3 m at the operating frequency 2.5 GHz .

Based on the equation 5.1, the SNR of the input signal decrease when the person is getting farther to the system of measurement. As seen in equation 5.2, for each emitted power of a fixed distance between the person and the radar, signal power at the VNA input is fixed. The second and the third orders of the cyclic statistics for $d = 1$ m were very attenuated compared

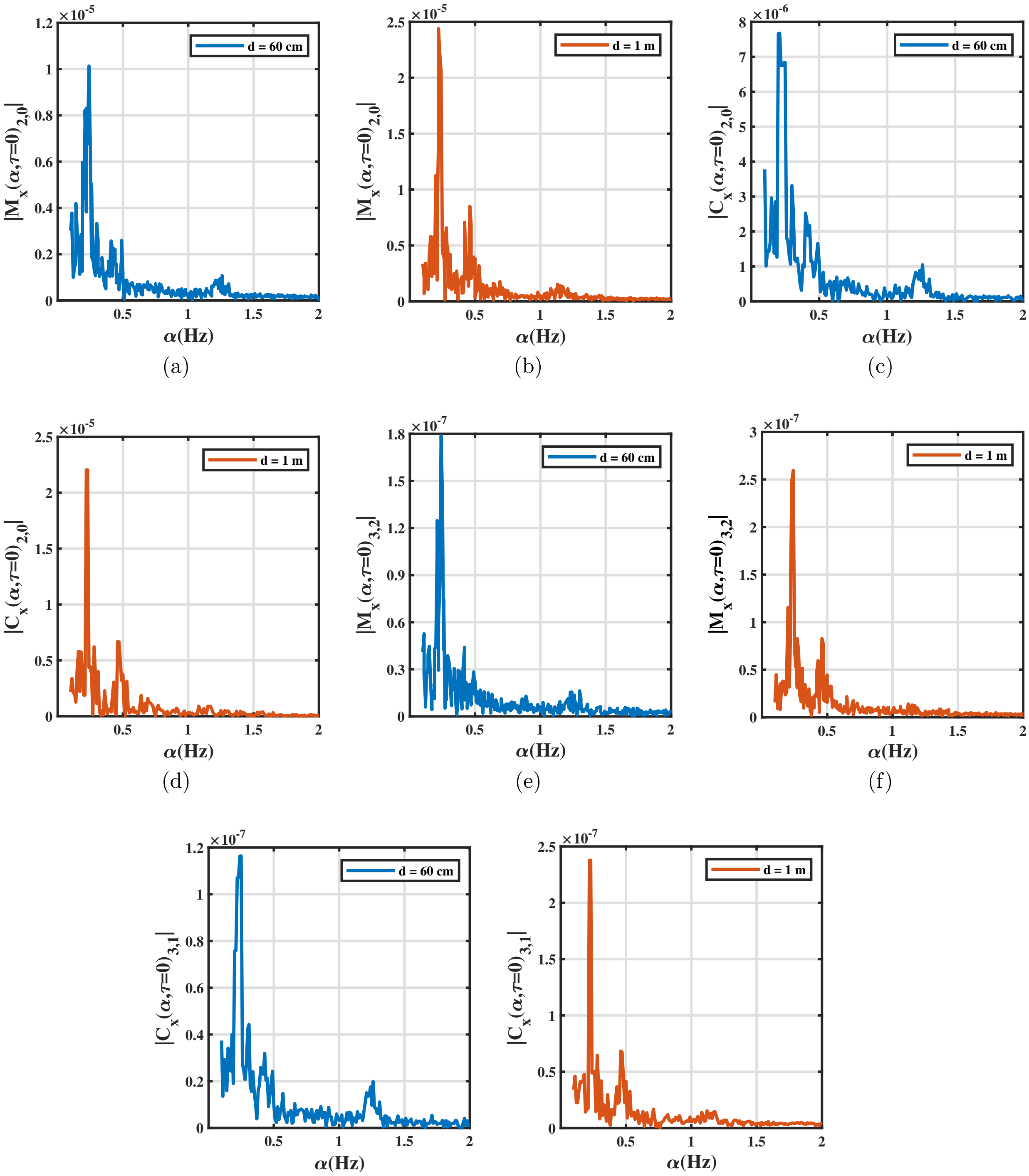

(a) (b) (c)

(d) (e) (f)

(g) (h)

Figure 5.13: Second and third order cyclic features of the transmission signalS_{21} in case of the vertical polarization of the antennas: (**a**) $|M_x(\alpha, \tau = 0)_{2,0}|$ d= 60 cm , (**b**) $|M_x(\alpha, \tau = 0)_{2,0}|$ d= 1 m , (**c**) $|C_x(\alpha, \tau = 0)_{2,0}|$ d= 60 cm and (**d**) $|C_x(\alpha, \tau = 0)_{2,0}|$ d= 1 m, (**e**) $|M_x(\alpha, \tau = 0)_{3,2}|$ d= 60 cm , (**f**) $|M_x(\alpha, \tau = 0)_{3,2}|$ d= 1 m , (**g**) $|C_x(\alpha, \tau = 0)_{3,1}|$ d= 60 cm and (**h**) $|C_x(\alpha, \tau = 0)_{3,1}|$ d= 1 m

to d = 60 cm. However, the cyclic features of vertical polarization of the antennas are more closer to the horizontal polarization for both distance 60

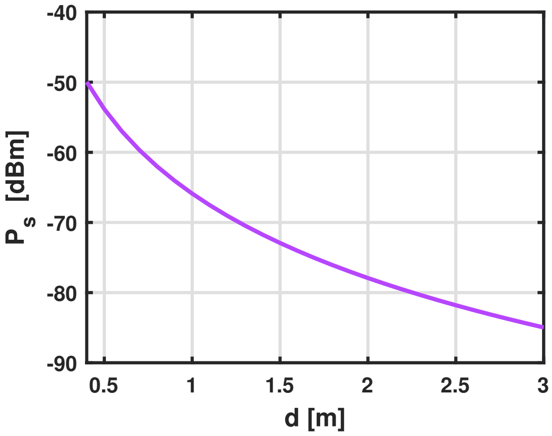

Figure 5.14: Signal power at system input vs. distance at P_e= -6 dBm and f = 2.5 GHz

cm and 1 m. During the measurements, the two Libelium sensors of the heart and respiratory rate are fixed on the person under test, the table 5.7 illustrates the values displayed by these two sensors and the values found by the cyclostationarity algorithm which are almost the same values of the sensors.

Table 5.7: Comparison between the detection of RR and HR resulting from the cyclostationarity algorithm and the reference system

		MySignals		Cyclostationarity		Relative Error (%)	
		RR (Hz)	HR (Hz)	RR (Hz)	HR (Hz)	RR (Hz)	HR (Hz)
Polarization horizontal	d= 60 cm	0.22	1.07	0.220	1.080	<1	0.93
	d= 1 m	0.23	0.96	0.230	0.95	<1	1.04
Polarization vertical	d= 60 cm	0.24	1.27	0.240	1.260	<1	0.79
	d= 1 m	0.23	1.12	0.230	1.130	<1	0.89

Regardless of the configuration of antenna (60 cm, 1m), the error is of the order of 1% in a controlled environment. The VNA is sensitive and precise enough to address this application. There is nevertheless a minor degradation due to the distance. Note that it is not a good idea to operate at a large distance here to assess the impact, as the radar surface area increases.

5.2.4 The impact of the number of samples on the detection

In this section, we evaluate the impact of the numbers of samples, while considering two number 1201 and 8001 samples. Note that a small number of samples reduce both the computational cost and the response time of the digital signal-processing block. The cyclostationarity process requires a high number of samples to accurately estimate the cyclic features (131072 point in [39]). The impact of the number of samples is considered in Figure 5.15 with horizontal polarization of the antennas, and in Figure 5.16 with vertical polarization of the antennas.

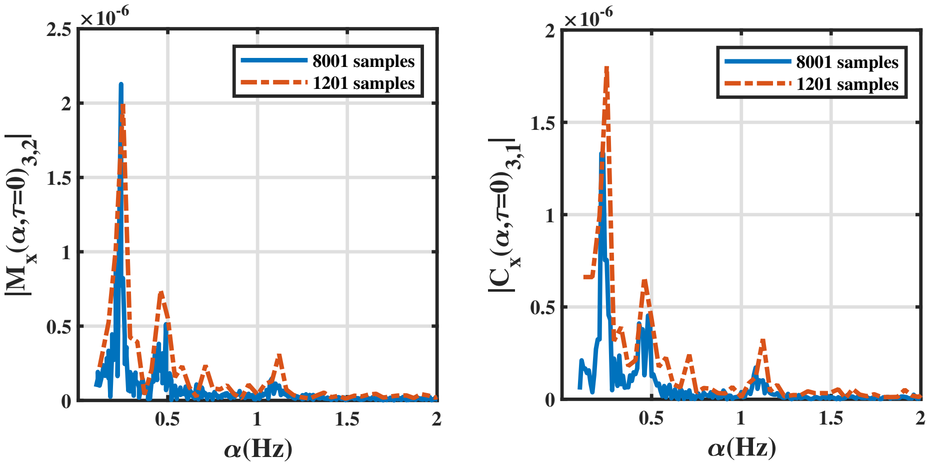

(a) (b)

Figure 5.15: Third orders cyclic features of the signalS_{21} for two different number of points with horizontal polarization of the antennas: (**a**) $|M_x(\alpha, \tau = 0)_{3,2}|$ and (**b**) $|C_x(\alpha, \tau = 0)_{3,1}|$

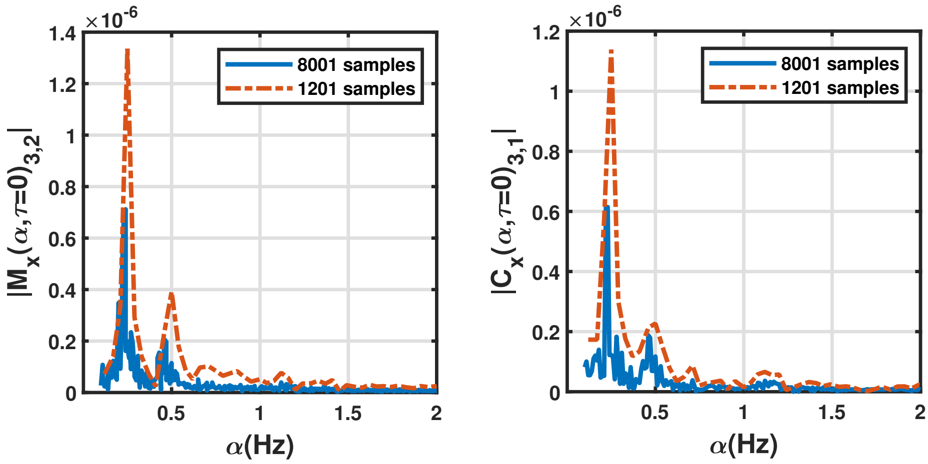

(a) (b)

Figure 5.16: Third orders cyclic features of the signalS_{21} for two different number of points with vertical polarization of the antennas: (**a**) $|M_x(\alpha, \tau = 0)_{3,2}|$ and (**b**) $|C_x(\alpha, \tau = 0)_{3,1}|$

The cyclic features of the received signal at frequency 2.5 GHz and $d = 60$ cm, with two different number of samples $N_{s_1} = 1201$ and $N_{s_2} = 8001$ are presented. The sampling frequency is 49.82 Hz. All frequencies of interest, RR and HR, are present. However, the cyclic features with the horizontal polarization, are more obvious than the features with the vertical polarization. The measurement time for N_{s_1} is 24.10 seconds, which remains insufficient to have all the information, compared to that of N_{s_2} 160.58 seconds. Thus, The number of samples N_{s_2} is sufficient to reconstruct the cyclic features. It should be mentioned that increasing the number of samples would lead to a better estimation of cyclic features at the expense of higher computational costs, which leads to a longer processing time.

5.2.5 The study of different scenarios of the person

The aim of this section is to provide the possibility of extracting the heartbeat activity of the human body at different sides (front and back). In addition, different scenarios are considered: the person under test is breathing normally and sitting at a 60 cm distance from the system, as well as the person under test hold his breathing. The all measurement of the subject was carried out when the target was sitting on a chair. The measurement time is determined by the VNA after choosing the number of samples and the bandwidth. This latter is set to 100 Hz resulting from a compromise between the signal noise reduction and sweep time. The number of samples is set to 8001 samples corresponding to a sweep time of 160.58 sec. Therefore, the sampling frequency is 49.8 Hz. The Figure 5.17 shows the variations of the amplitude and phase-shift of the transmission coefficient measured at 2.5 GHz, for two sides of the subject: back side and front side. The two scenarios of breathing normally and holding breath were considered for each side.

For the case front side, the reflected signal contains two cycles of the person holding his breath (1) and (2). The total signal measured was 160.58 seconds. The person breathes and blocks his breathing for 24 seconds, then the person resume his breathing and blocks it again. At the end, the person resume his breathing again.

The amplitude and phase-shift variation of the transmission signal S_{21} due to the chest movement, caused by the cardiopulmonary activities is more clear from the front side of the subject than the back side, when the subject is breathing. Which could be related to the physiology and anatomical position of the lungs in the chest (Section 2.2). The detection of HR is studied when the person is in the state of holding his breath. The blocs (1) and (2) on the figure 5.17 represents the cycles where the person blocks his breathing, of each side the front and the back. The figure 5.18 shows the blue dotted frames in Figure 5.17.

The figures 5.19 and 5.20 show the second order cyclic moment $|M_x(\alpha, \tau = 0)_{2,0}|$, the second order cyclic cumulant $|C_x(\alpha, \tau = 0)_{2,0}|$, the third or-

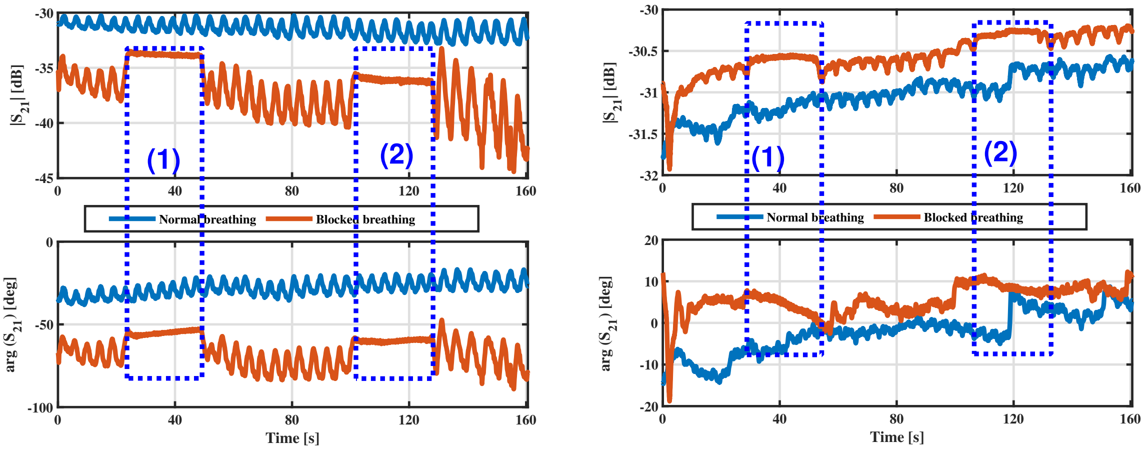

(a) (b)

Figure 5.17: Amplitude and phase-shift variation of S_{21} owing to the chest movement at different sides and at -6 dBm: (**a**) front side and (**b**) back side

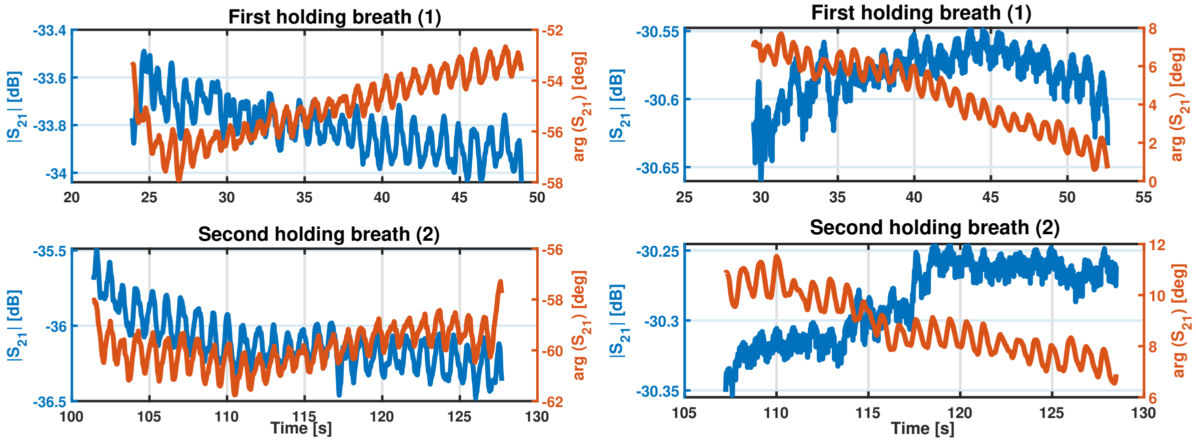

(a) (b)

Figure 5.18: Amplitude and phase-shift variation of S_{21} owing to the chest movement at different sides of the blocks (1) and (2), P= -6 dBm: (**a**) front side and (**b**) back side

ders cyclic moment $|M_x(\alpha, \tau = 0)_{3,2}|$ and the third order cyclic cumulant $|C_x(\alpha, \tau = 0)_{3,1}|$ of the complex transmission signal S_{21} for different sides of the subject front side and the back side respectively. The level of the amplitude of each features are different than order to an order.

The interval correspond to the normal respiratory rate for an adult between 10 and 20 breaths per minute correspond to 0.16 Hz and 0.33 Hz. Thus, the cyclic frequency correspond to the maximum amplitude frequency in this interval is attributed to the RR. Then, we remove the harmonics of the breath and we are interested in the interval between 0.83 Hz and 1.6 Hz

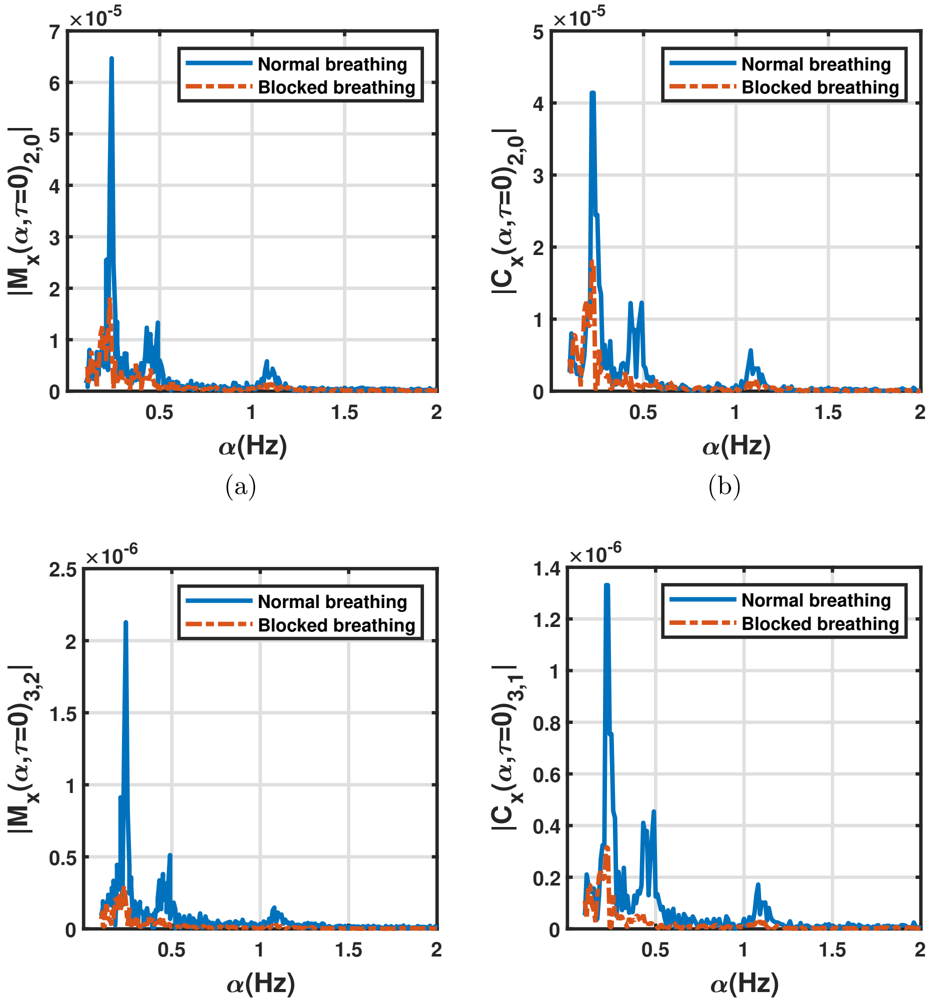

(a) (b)

(c) (d)

Figure 5.19: Second and third orders cyclic features of the signal S_{21} for the front side: (**a**) $|M_x(\alpha,\tau=0)_{2,0}|$, (**b**) $|C_x(\alpha,\tau=0)_{2,0}|$, (**c**) $|M_x(\alpha,\tau=0)_{3,2}|$ and (**d**) $|C_x(\alpha,\tau=0)_{3,1}|$

which corresponds to the heart rate. The HR is attributed to the frequency corresponds to the maximum amplitude in this interval Figure 5.21.

The figures 5.22 and 5.23 shows the second and the third orders of cyclostationarity applied on the blocs of temporal signals 5.18 corresponding to the person holding his breath for the both side front and back,respectively, in order to extract the respiration and the heart rate.

Through the back, the lungs are located deeper, and the signal is further attenuated by human tissue. Nonetheless, it might make it easier to measure the heartbeat. The level of the heartbeat signal is weak and difficult to measure due to the noise level.

Through the back, the lungs are located deeper, and the signal is further

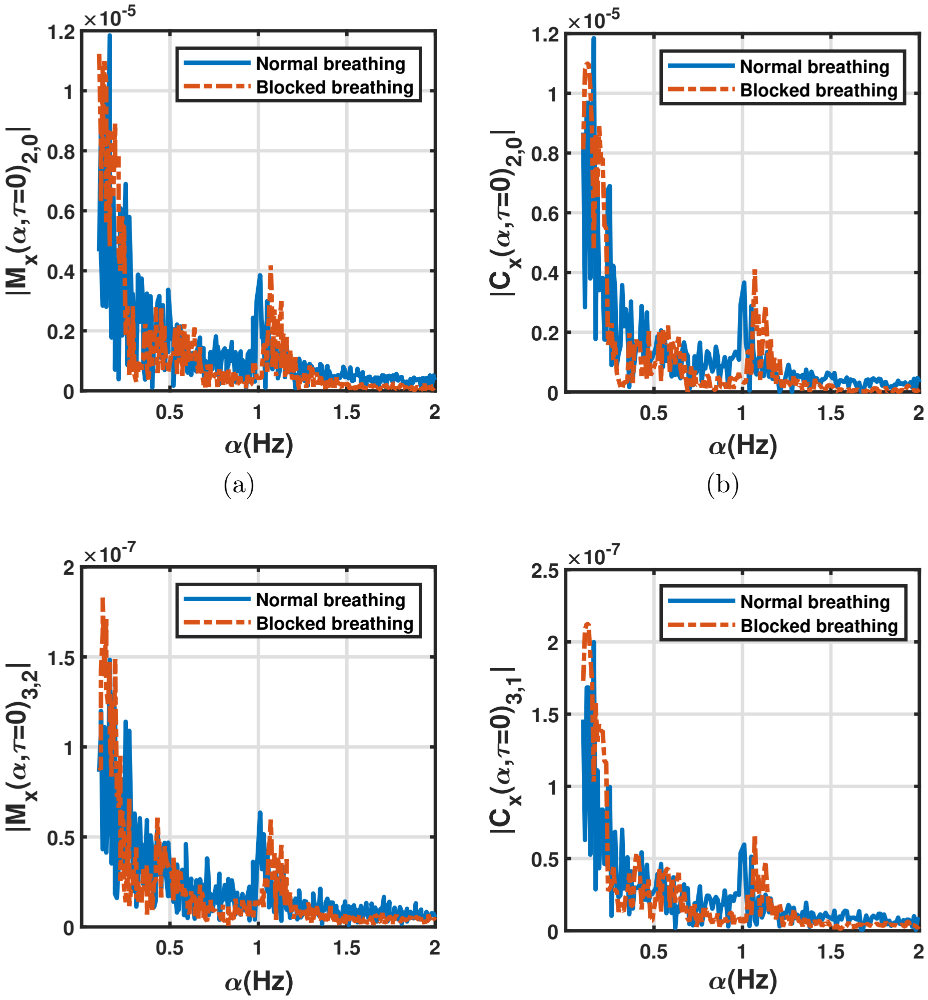

(a) (b) (c) (d)

Figure 5.20: Second and third cyclic features of the signal S_{21} for the back side of the persons: (**a**) $|M_x(\alpha, \tau = 0)_{2,0}|$, (**b**) $|C_x(\alpha, \tau = 0)_{2,0}|$, (**c**) $|M_x(\alpha, \tau = 0)_{3,2}|$ and (**d**) $|C_x(\alpha, \tau = 0)_{3,1}|$

attenuated by human tissue. However, it could make it easier to measure the heartbeat. When the person hold his breath, the heart rate is dominate in the cyclic frequencies for both sides front and back, but from the front the signal is clear and more obvious than the one from the back.

5.3 Parametric study of the electric parameters and free-space set-up arrangement

In order to present a complete guide to campaign measurement, a different measurement were carried out for different variation of the internal parameters of the VNA. Accurate detection of small mechanical movements by radar techniques is conditioned mainly by the sensitivity and accuracy of the IQ demodulator, main of the radar architecture. In particular, if electrical pa-

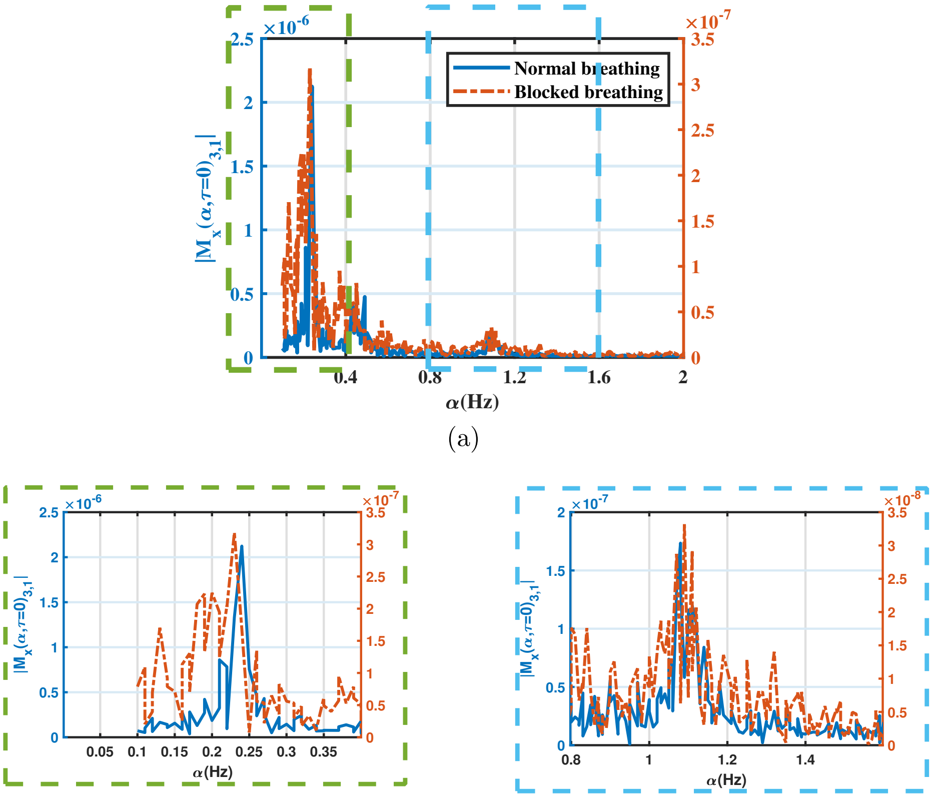

(a)

(b)

(c)

Figure 5.21: Third cyclic moment $|M_x(\alpha, \tau = 0)_{3,1}|$ of S_{21} for the front side in different interval: (**a**) $|M_x(\alpha, \tau = 0)_{3,1}|$ (**b**) zoom on the part corresponds to RR and (**c**) HR)

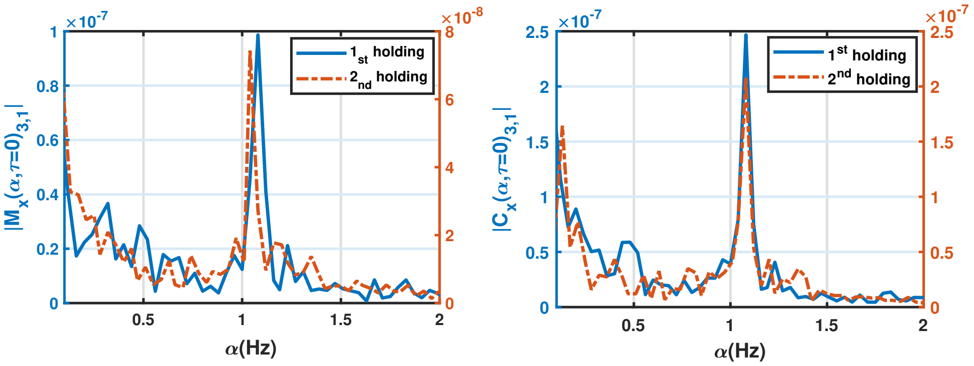

(a)

(b)

Figure 5.22: (**a**) $|M_x(\alpha, \tau = 0)_{3,1}|$ and (**b**) $|M_x(\alpha, \tau = 0)_{3,1}|$, holding breath front side

rameters are not properly set it can have a significant effect on measurement quality. The first parameter concerns the operating microwave frequency. In particular, there is a trade-off between relatively low and high frequency that impact directly free-space propagation and phase-shift sensitivity. The optimum solution can be found in the interplay between input RF power and intermediate frequency bandwidth (IFBW). A narrow IFBW setting helps reduce trace noise but at the expense of the measurement time. Therefore,

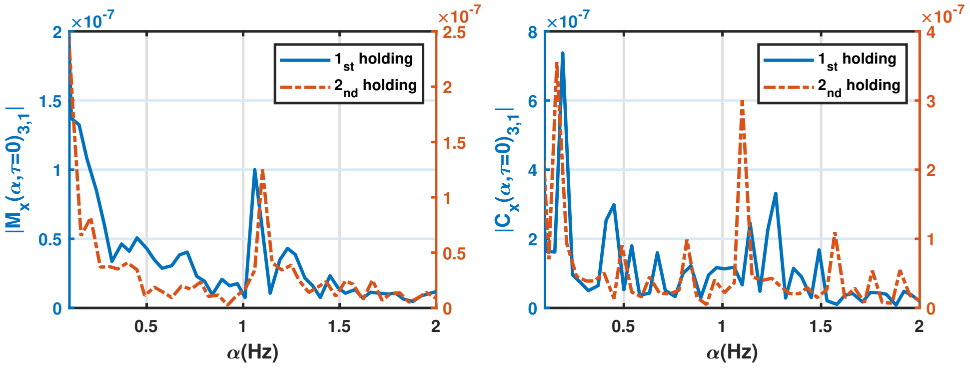

(a) (b)

Figure 5.23: (**a**) $|M_x(\alpha, \tau = 0)_{3,1}|$ and (**b**) $|C_x(\alpha, \tau = 0)_{3,1}|$, holding breath for the back side

a hard compromise with optimum electrical parameters is required. In this part, a parametric study considering different levels of input RF power and IFBW is described. An attention is paid to maximum RF power imposed by the regulation organisms for the radiation exposure for the health of the human body. Then, the operating frequency of the measurement system to find a good compromise between the hardware complexity and the precision of detection. Finally, experiments are conducted considering a measurement environment close to the targeted application. The flowchart of different measurement at the operating frequency 10 GHz is presented in Figure 5.24.

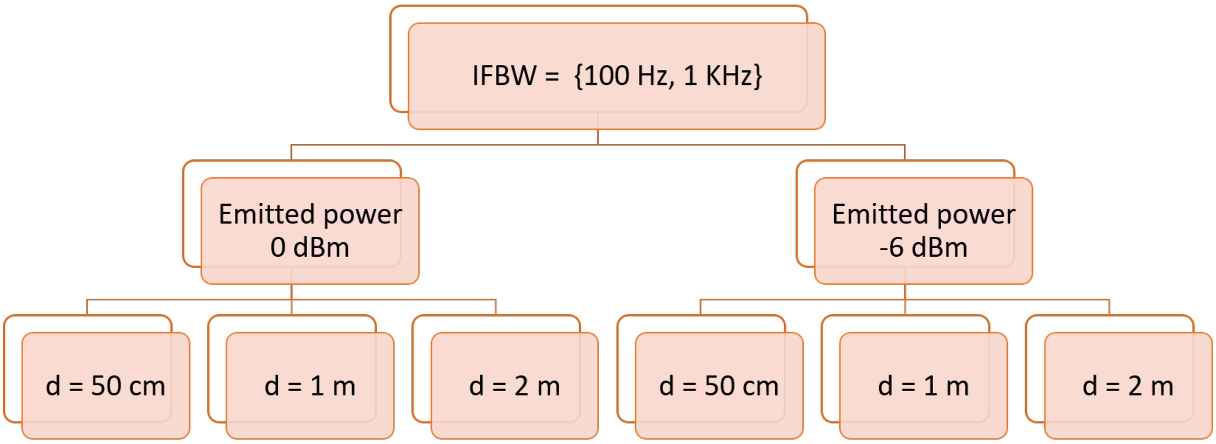

Figure 5.24: Flowchart of the measurement at 10 GHz

5.3.1 Impact of the operating frequency

For the purpose of determining the impact of the operating frequency on the CW radar vital signs detection accuracy, the frequency was varied using a VNA connected to two horn antennas to form a bi-static heterodyne radar. Two distance of 50 cm and 1 m separating the antenna and the person under test chest are considered. The person under test is a 37 year old man sitting on a chair and breathing normally. The input RF source power is set to 0 dBm (1 mW). Therefore, the radiated power of the antenna depends on the transmitted power measured at the input of the transmitting antenna and the gain of the antenna in each frequency. The parameters and other measurement conditions are summarized in Table 5.8.

Table 5.8: Specifications of the measurement system.

Parameters	**Specifications**
Acquisition time	120.43 seconds
Distance	50 cm and 1 m
Transmitted Power	0 dBm
Number of points	12001
IFBW	100 Hz
Cable losses	3 dB
Antenna polarization	Horizontal

The effect of frequency is investigated by performing experiments varying this parameter. Three different test ISM frequencies 2.5 GHz, 10 GHz and 17 GHz was considered. The chest displacement $x_{HR}(t)$ varies between 4 mm and 12 mm due to breathing, while it ranges between 200 μm and 500 μm due to cardiac activity. Thus, the chest displacement due to the cardiopulmonary activities is between 4.2 mm and 12.5 mm. Applying the equation given in 3.6, the resulting theoretical values of the phase-shift variations related to the chest displacement due to heartbeat an respiration activities are computed in Table 5.9 for the three test frequencies considered.

It can be seen that the phase-shift variation due to the cardiopulmonary activities increases when the rate increases. Thus, a higher sensitivity to small displacements is obtained at higher frequencies. Using higher frequencies will reduce the noise effect and increase the accuracy of detecting signal peaks. Figure 5.25 and Figure 5.26 show the amplitude and the phase-shift

Table 5.9: phase-shift variations related to the chest displacement for the three test frequencies 2.5, 10 and 17 GHz

Frequency (GHz)	Free-space wavelength (λ) (mm)	phase-shift variation of x_{HR}= 4.2 mm	phase-shift variation of x_{HR}= 12.5 mm
2.5	120	25.2 $^\circ$	75 $^\circ$
10	30	100°	300°
17	18	171°	150$(+2\pi)^\circ$

variation of the transmission coefficient S_{21} due to cardiopulmonary activities measured at 2.5, 10 and 17 GHz, for both distance 50 cm and 1m respectively.

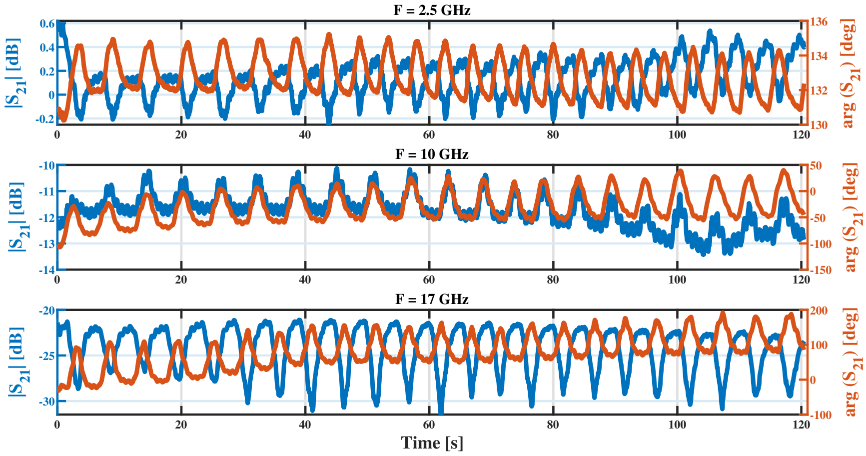

Figure 5.25: Amplitude and phase-shift of the transmission coefficient S_{21} at the test frequencies 2.5, 10 and 17 GHz (distance between antenna and the chest's person= 50 cm; input RF power= 0 dBm)

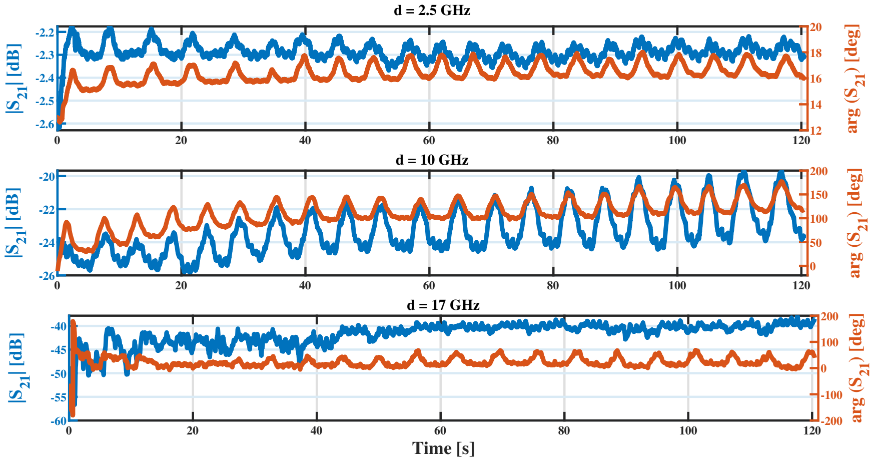

Figure 5.26: Amplitude and phase-shift of the transmission coefficient S_{21} at the test frequencies 2.5, 10 and 17 GHz (distance between antenna and the chest's person= 1 m; input RF power= 0 dBm)

From the measured data, different qualitative conclusions can be drawn. First, the signals fluctuations attributed to the chest movement can be easily detected for all the test frequencies considered. It is difficult to compare the phase-shift variations to the theoretical values as waves interference occur. Indeed, the amplitude variations should be negligible given the limited mechanical movement of the target. At the first order, the isolation between the antennas plays a major role. By vector recombination with the signal of interest, i.e. reflected wave by the chest, one part of the phase-shift variation is reversed on the amplitude signal. Furthermore, free-space losses increase with distance whereas phase-shift sensitivity is enhanced. Incidentally, as observed at 10 GHz, the optimum frequency is in between. Besides, the radiation pattern of the antennas plays a major role as it varies as a function of the frequency of operation, as illustrated in Figure 5.28 for the three cases. This figure shows the distribution of the radiation energy as a function of angle about the antenna measured in the far filed region (3 m).

Figure 5.27 shows radiation pattern measurements in an RF Anechoic chamber. The antenna directivity is better at 10 GHz whereas radiation patterns are degraded at 2.5 and 17 GHz. From these data, the apertures determined at -20 dB are 100°, 70° and 300°, at 2.5, 10 and 17 GHz respectively. It has to be mentioned that the frequency range of the antenna is 700 MHz – 18 GHz. Therefore, the performance are obviously affected in the lower and upper bound frequency limits.

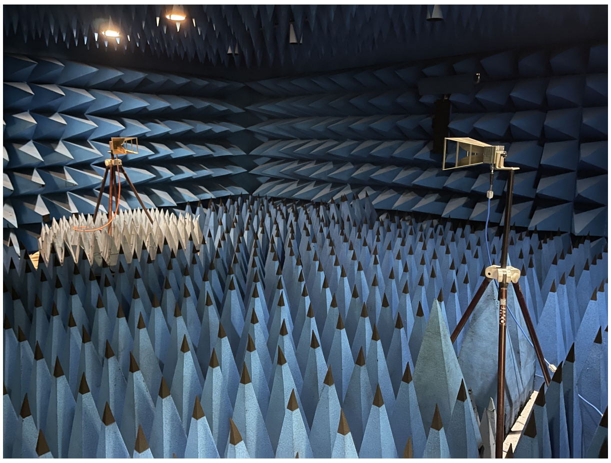

Figure 5.27: Radiation pattern measurements in an RF Anechoic chamber

The vital sign detection method based on applying the third-order cyclostationary analysis on the measured complex transmission coefficient S_{21}. The cyclostationary process in the next subsection will show the possibility to extract the heartbeat signal from the cardiopulmonary signal over all frequencies and different distances. In Figure 5.29 and Figure 5.30 , it depicts the third-order cyclic cumulant of the reflected signal at the operating frequencies 2.5 , 10 and 17 GHz for both distance 50 cm and 1 m respectively. The third order temporal cyclic cumulant presented in the Figure 5.29 and Figure 5.30 is applied to three different cyclic frequencies interval, Figure 5.29a and 5.30a for 0 - 2 Hz, then Figure 5.29b and 5.30b correspond to 0.1 - 0.4 Hz interval for the detection of RR and Figure 5.29c and 5.30c correspond to 0.83 - 1.6 Hz for the detection of HR.

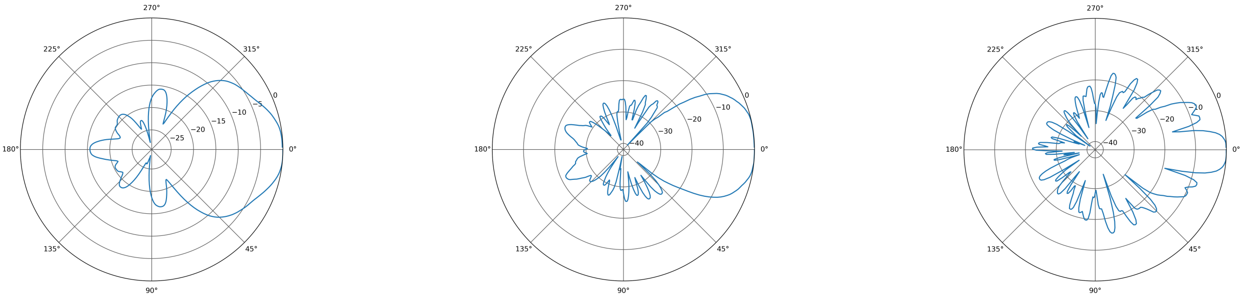

(a) a (b) b (c) c

Figure 5.28: The measured radiation pattern of the horn antenna used in the measurement at the frequencies: (**a**) 2.5 GHz, (**b**) 10 GHz and (**b**) 17 GHz

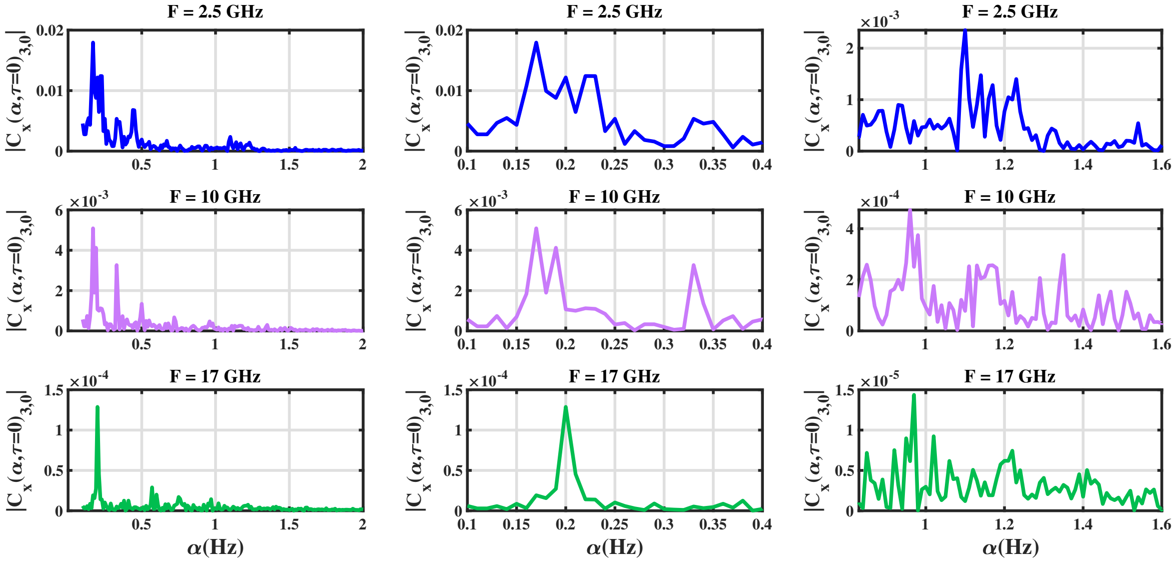

(a) (b) (c)

Figure 5.29: Cyclic cumulant of the third order of cyclostationary signal S_{21} for three test frequencies 2.5 , 10 and 17 GHz (distance = 50 cm; input RF power = 0 dBm)

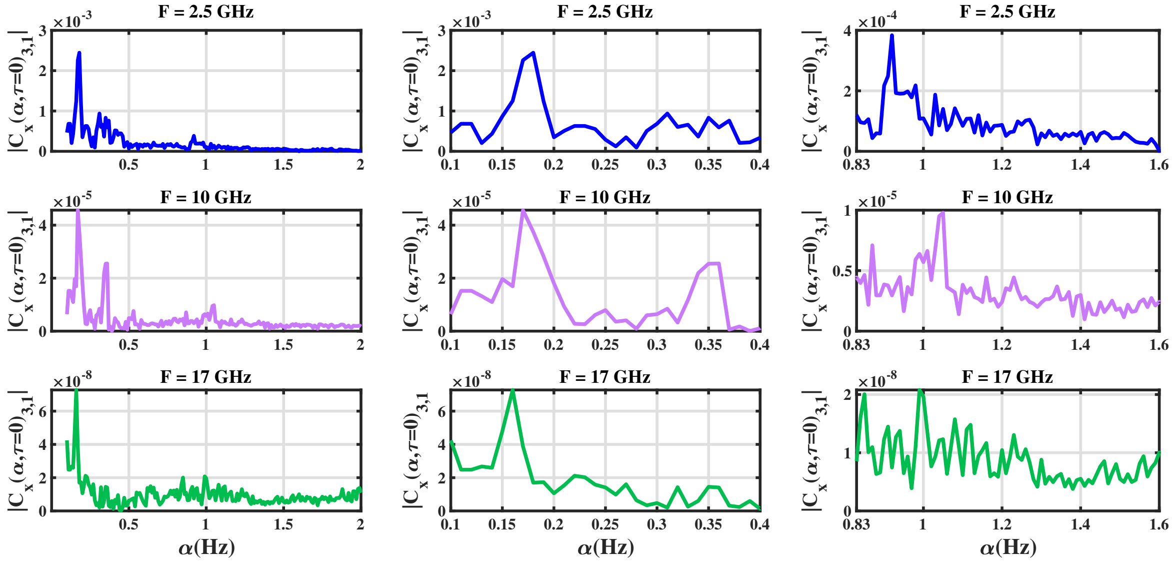

(a) (b) (c)

Figure 5.30: Cyclic cumulant of the third order of cyclostationary signal S_{21} for three frequencies 2.5 , 10 and 17 GHz (distance between antenna and the chest's person = 1 m; input RF power = 0 dBm)

As is obvious from Figure 5.29b and 5.29c for the distance 50 cm and the Figure 5.30b and 5.30c for the distance 1 m, the respiration and heartbeat frequencies can be estimated for the three frequencies 2.5, 10 and 17 GHz for the emitted power 0 dBm and the IFBW 100 Hz. However, the accuracy of the cyclic features at 10 GHz is more better, and the signal reflected from the person under test chest is more clearer than the other frequencies. As well, the next experiments will be carried out at the operating frequency 10 GHz. The Table 5.10 resume the results of the RR and HR at the three test frequencies and both distance (50 cm and 1 m) and the relative error for each case.

The relative error for the detection of RR is zero and for HR is very low in the case of the test frequency 10 GHz for the two distances 50 cm and 1 m. While the error is low for the detection of RR and HR for short distances (50 cm) in the two cases of operating frequency 2.5 and 17 GHz, which confirms the previous conclusion.

5.3.2 Impact of the parameters setting (IFBW and input RF power)

The received signal is converted from its source frequency to a lower intermediate frequency bandwidth (IFBW). The bandwidth of the IF bandpass

Table 5.10: Comparison between the detection of RR and HR resulting from the cyclostationarity algorithm and the reference system

		Cyclostationarity		MySignals		Relative Error (%)	
Frequency (GHz)	Distance (cm)	RR (Hz)	HR (Hz)	RR (Hz)	HR (Hz)	RR (Hz)	HR (Hz)
2.5	50	0.171	1.101	0.17	1.09	0.5	0.99
	100	0.175	0.928	0.17	0.98	2.85	5.6
10	50	0.170	0.961	0.17	0.96	<1	0.1
	100	0.170	1.050	0.17	1.03	<1	1.9
17	50	0.200	0.971	0.2	0.98	<1	0.92
	100	0.164	0.994	0.17	1.04	3.65	4.62

filter is adjustable from 1 MHz down to a minimum of 1 Hz. The value of IFBW is selected by scrolling through the values available in the IFBW text box. Several measurements have been performed for the two different IFBW 100 Hz and 1 KHz respectively. The source power is set to 0 dBm. The same subject and the same measurements conditions are considered except the distance set to 50 cm, 1 m and 2 m respectively.

The VNA generates a Continuous Wave (CW) signal at the operating frequency 10 GHz. The reflected signal that carries the information about the mechanic movement of the chest is received by the receiving antenna and detected by the VNA where the variation of the amplitude and the phase-shift of S_{21} is computed. The both emitted and received antenna are similar, and the gain of this antenna at 10 GHz is 11.56 dB. There is a hard compromise between the IFBW and experiment duration. We adapt the values for each experiment. For example, an IFBW of 100 Hz considering 12001 measurement samples leads to a sweep time of 120.43 seconds. By increasing the IFBW by one order of magnitude (IFBW = 1 KHz), we consider 60001 samples for a sweep time of 62.10 seconds. For the both cases, the sampling frequency is 9.66 Hz.

To validate the proposed system, ECG measurements were started simultaneously with the RF measurements for further comparison. Table 5.11 summarizes the measurements parameters.

Figure 5.31 shows to the amplitude and phase-shift of the complex trans-

Table 5.11: Specifications of the measurement system.

Block	Specifications
Operating frequency	10 GHz
Acquisition time	120.43 seconds
Distance	50 cm, 1 m and 2 m
Transmitted Power	0 dBm
Number of points	12001
IFBW	100 Hz and 1 KHz
Cable losses	3 dB
Antenna polarization	Horizontal
Body position	Sitting

mission coefficient S_{21} at the test frequency 10 GHz. The measurement was carried out for the emitted power 0 dBm, three distance 50 cm, 1 m and 2 m. The IFBW set at 100 Hz and 1 KHz, for three different distance between the person and the antennas 50 cm, 1 m and 2 m.

Reducing the IF receiver bandwidth reduces the signal fluctuations and the effect of random noise on a measurement to optimize measurement speed. The smaller the IFBW, the better the signal-to-noise ratio (SNR). In the experiment, we study the effect of two different IFBW values on the detection of vital signs 100 Hz and 1 KHz.

The measured data present a better signal to noise ratio (SNR) for the lowest IFBW (100 Hz) for the three distances 50 cm, 1 m and 2 m. For example, at a distance of 1 m, the variations of the phase-shift and amplitude are 50° and 4 dB respectively for the IFBW 100 Hz and 30° and 1 dB for the IFBW 1 KHz. The signal processing applied on the raw data in the cyclic frequencies are presented in the following yields to quantitative data for validation.

The figure 5.32 shows detected results of the heartbeat and respiration rate, extracted from the cyclic moment and cumulant of cyclostationary signal S_{21} at the operating frequency 10 GHz, for the IFBW 100 Hz and source power power 0 dBm. It is obvious seen that heart and respiration peaks corresponding to heart and respiration frequencies are clearly displayed in the figure. It shows the detected results of the heart and respiration frequencies by applying the temporal cyclic moment and cumulant of the third

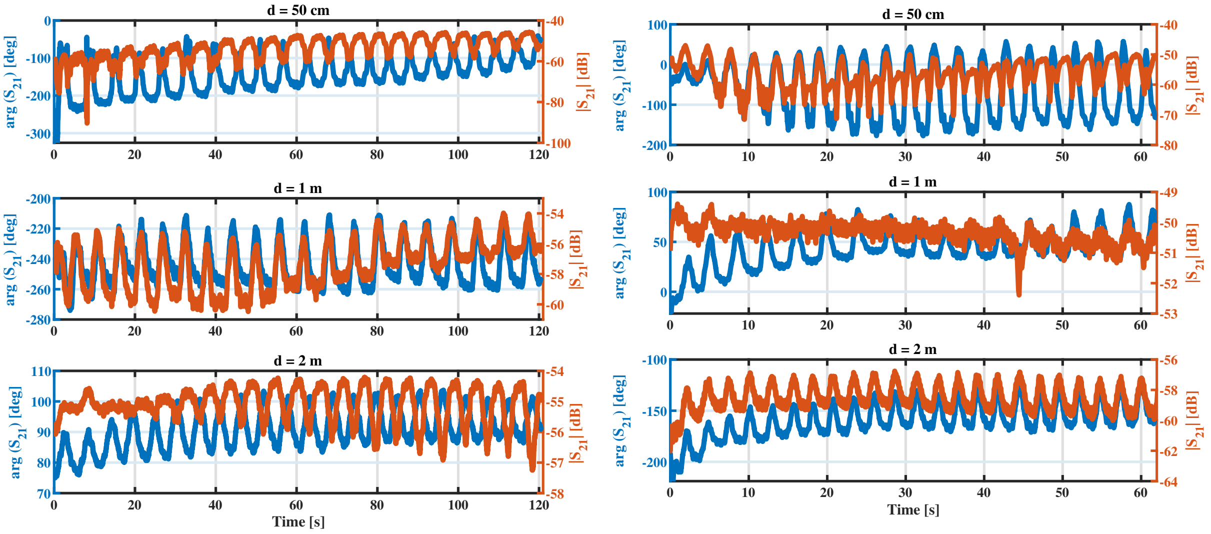

(a)

(b)

Figure 5.31: amplitude and phase-shift variation of transmission coefficient S_{21} for different distance (50 cm, 1 m and 2 m) at 10 GHz and 0 dBm: (**a**) IFBW = 100 Hz and (**b**) IFBW = 1 KHz

order of cyclostationary signal S_{21}. The zoom has been made on the two intervals corresponds to the respiratory rate and heart rate. The frequencies corresponding to maximum peaks in the range 0.17–0.4 Hz and 0.83–1.6 Hz are considered as estimated frequencies of respiration and heartbeat signals, respectively.

The same process for the IFBW 1 KHz was applied. The figure 5.33 shows the cyclic cumulant of the third-order of cyclostationary signal S_{21} for three distance (50 cm, 1 m and 2 m) and a zoom in the interval corresponds to breathing and heart rate at the frequency 10 GHz and the source power 0 dBm and IFBW = 1 KHz.

From the cyclic features extracted from the measured complex transmission coefficient S_{21}, the third cyclic cumulant for the 100 Hz IFBW, is more clean than at 1 KHz. While wider IFBW settings result in faster measurements, they also generate more noise and create a higher noise floor, which reduces dynamic range. The measurement made in the previous chapter demonstrate the link between the IFBW and the input power level of the system. In the next subsection, we study the impact of the input power while considering a fixed IFBW 100 Hz.

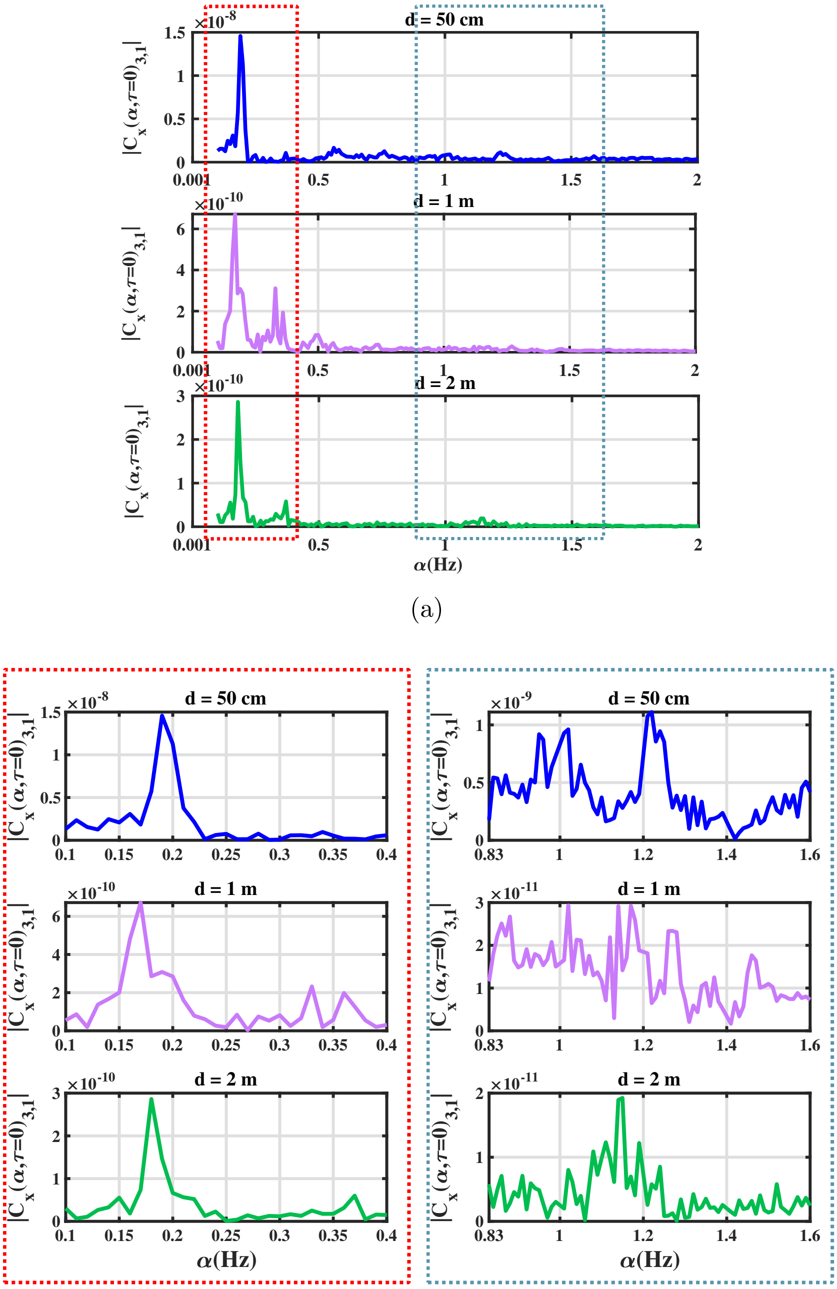

(a)

(b)

(c)

Figure 5.32: (**a**) Cyclic cumulant of the third-order of cyclostationary signal S_{21} for three distance (0.5, 1 and 2 m) and a zoom in the interval corresponds (**b**) to RR and (**c**) HR at 10 GHz, 0 dBm, IFBW = 100 Hz

The input power is set at -6 dBm for three distances 50 cm, 1 m and 2 m. Considering the antenna gain (11.56 dB) and cable losses of 3 dB, the source power -6 dBm corresponds to a radiated power of -3.56 dBm. The complex S_{21} measured at 50 cm, 1 m and 2 m respectively, for the 100 Hz IFBW and -6 dBm is shows in Figure 5.34.

Figure 5.35 shows the results of the third-order cyclic cumulant of the re-

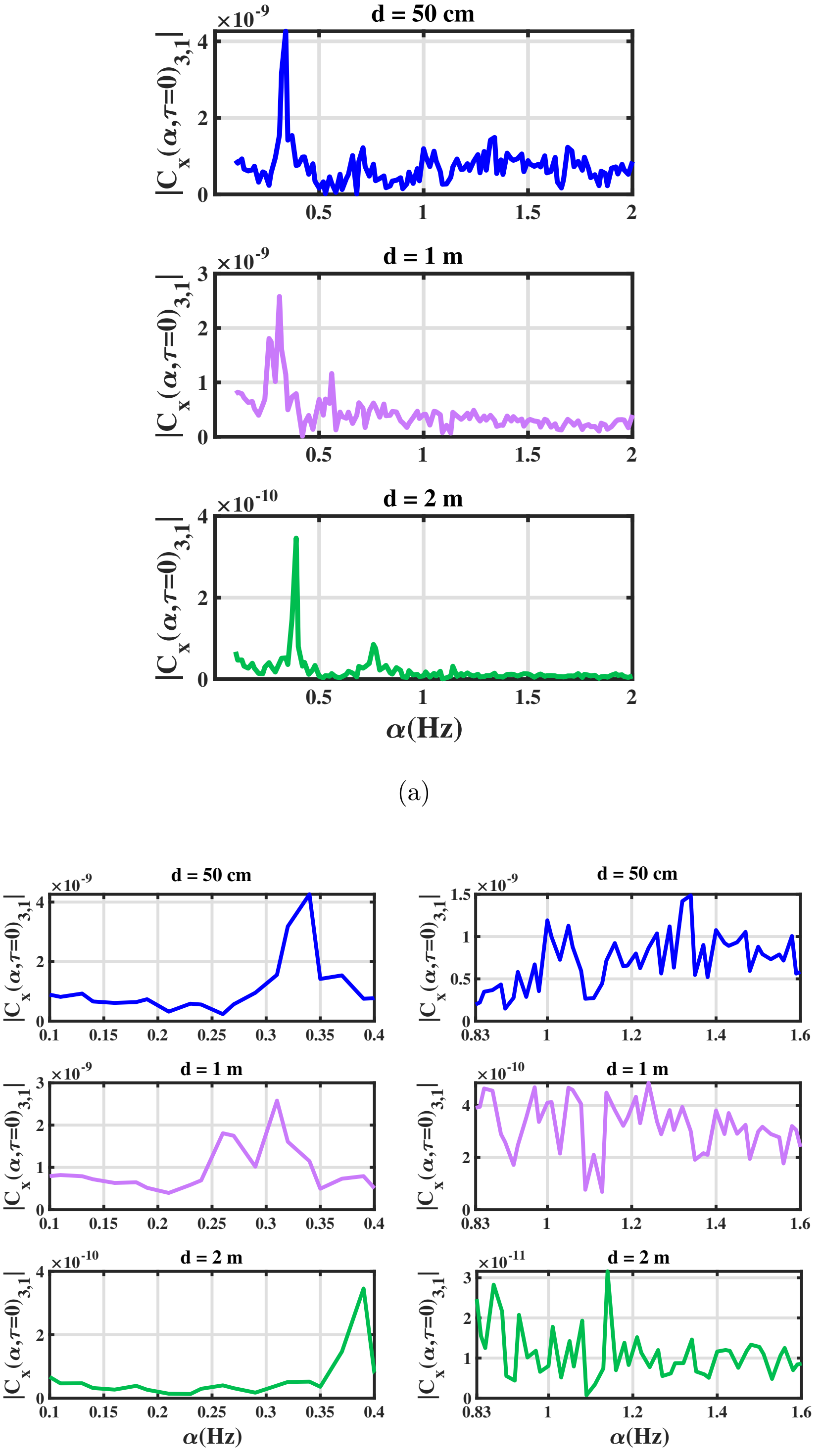

(a)

(b)

(c)

Figure 5.33: (**a**) Cyclic cumulant of the third-order of cyclostationary signal S_{21} for distance (0.5, 1 and 2 m) and a zoom in the interval corresponds (**b**) to RR and (**c**) HR at 10 GHz, 0 dBm and IFBW = 1 KHz

flected signal S_{21}. Simultaneously with the VNA, ECG and airflow sensors are used as references to extract the RR and HR, in order to compare with the

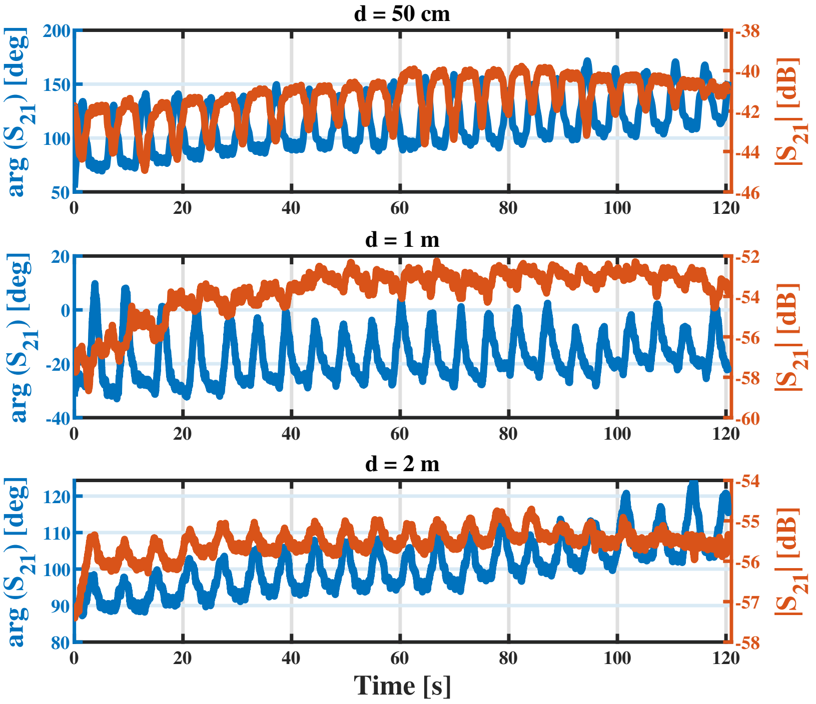

Figure 5.34: Amplitude and phase-shift variation of transmission coefficient S_{21} measured at 50 cm, 1 m and 2 m respectively, for the 100 Hz IFBW and -6 dBm

rates extracted by applying the cyclostationary process for precision calculation. The Table 5.12 shows the respiration and the heart rates calculated from the cyclic cumulant and the reference measurement system, thus the errors for both input power -6 dBm and 0 dBm at different distance. The relative errors increase by increasing the distance and the input power.

Table 5.12: Comparison between the detection of RR and HR resulting from the cyclostationarity algorithm and the reference system for both input power -6 dBm and 0 dBm at 100 Hz IFBW

		MySignals		Cyclostationarity		Relative Error (%)	
		RR (Hz)	HR (Hz)	RR (Hz)	HR (Hz)	RR (Hz)	HR (Hz)
Input power -6 dBm	d= 50 cm	0.2	1.17	0.201	1.190	0.49	1.68
	d= 1 m	0.2	1.17	0.194	1.153	3.09	1.47
	d= 2 m	0.18	0.96	0.173	1.00	4.04	4
Input power 0 dBm	d= 50 cm	0.19	1.23	0.190	1.220	<1	0.8
	d= 1 m	0.18	1.18	0.172	1.173	4.65	0.85
	d= 2 m	0.17	1.17	0.178	1.153	4.49	1.47

We note that when the power is lowered (from 0dbm to -6dbm) the signal to noise ratio decreases and the amplitude and phase variation decreases (for 2 dB for -6 dBm and 4dB for 0 dBm for the amplitude and for the phase-

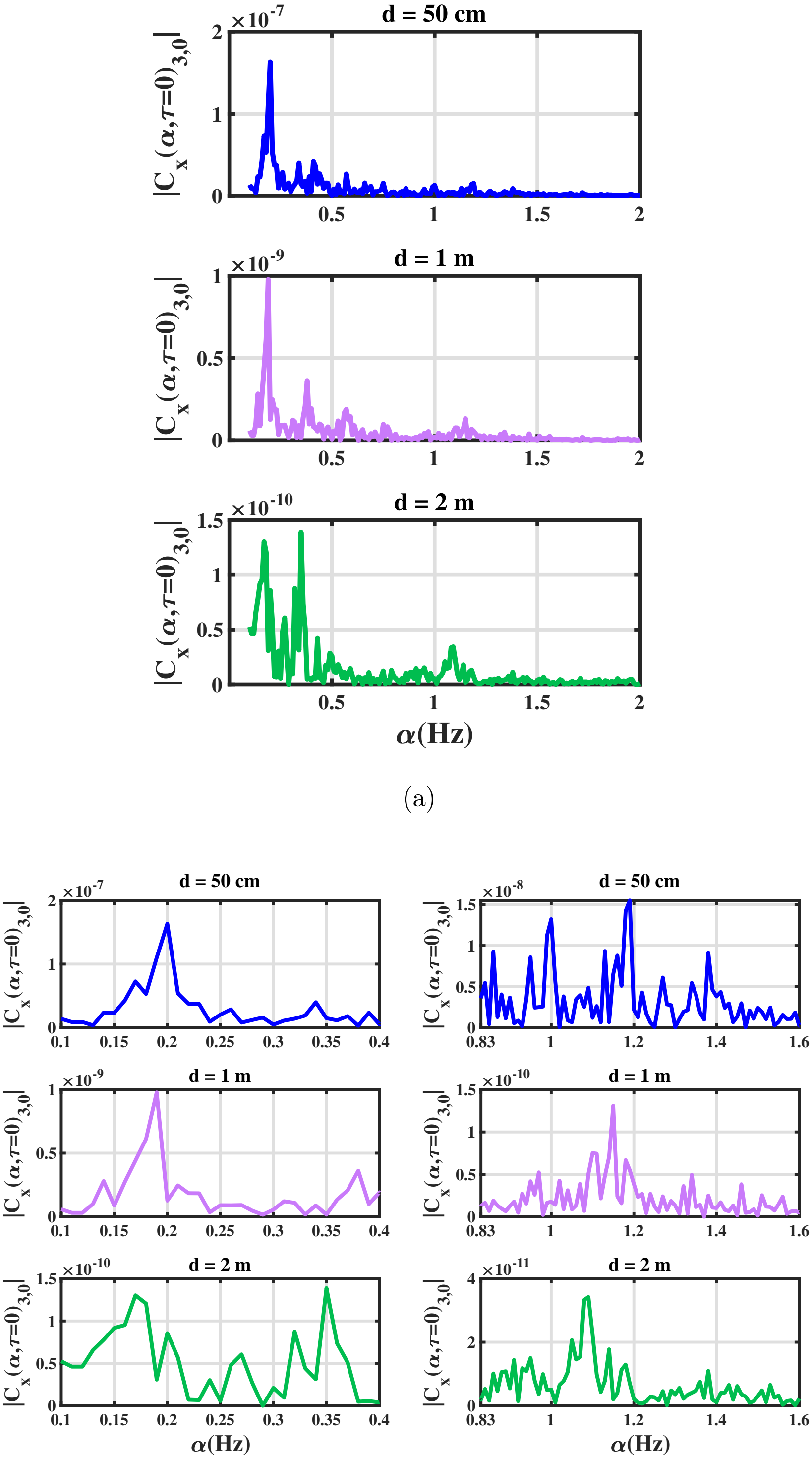

(a)

(b)

(c)

Figure 5.35: (**a**) The cyclic cumulant of the third-order of cyclostationary signal S_{21} for three distance (50 cm, 1 m and 2 m) and a zoom in the interval corresponds (**b**) to breathing and (**c**) heart rate at 10 GHz, -6 dBm and 100 Hz IFBW

shift 20° for -6 dBm and 40° for 0 dBm). In fact, when the power decreases, the transmitted signal is weaker and during its propagation attenuates and therefore loses power, causing a reduction in the variation of amplitude and phase-shift. For both input power 0 dBm and -6 dBm, the relative error is the same for the detection of RR and HR. However, the Table 5.12 shows that for the two powers (0 dBm and -6 dBm) emitted we manage to detect with an error of the order of 5% compared to the reference measurements the respiratory and cardiac frequency with a precision of the order of 0.01 Hz for the three studied distance (50 cm, 1 m and 2 m).

5.4 Improvement of the radar architecture for application in confined and perturbed environment

Operating in an anechoic environment or in a laboratory environment controlled in temperature and other parameters differs from real world applications. In particular, the electromagnetic propagation path is sensitive to the dielectric properties that are function of the temperature, mechanical vibrations, perturbations of natural or artificial electromagnetic radiated sources. The resulting clutter degrades significantly the overall measurement performance. Indeed, although there is an increasing interest in vital signs detection by radar techniques. On the first hand, detection of RR has been, in principle, addressed widely in the literature as the sensitivity and resolution of conventional radar architectures is suitable. On the other hand, detection of HR remains a challenging task. Efforts have been directed towards radar architectures or processing signals to eliminate or at least reduced the clutter. In the following, we improve the overall signal to noise ratio by low noise amplification as commonly found in radar implementation. In a second step, reflective metallic surface is considered in the propagation path to model at the first order the impact of a confined and perturbed environment such as a train driver's cabin.

For the first step, the low noise amplifier LCA-0218 illustrated in Figure 5.36, has a gain of 25 dB and noise figure of 4.5 dB (see Table 5.13). We can note that a power amplifier is usually added at the emission but is not compatible for low power applications on human beings as targeted in this work. For our application, the LNA is added after the receiving antenna, in order to amplify the signal coming from it while minimizing the noise figure of the receiver. In other words, the radar operates at low RF signal.

The figure 5.37 presents the vital signs measurements using the same system as before with adding the LNA at the reception after the receiving antenna. The bandwidth is 100 Hz. The number of points taken for the signals mea-

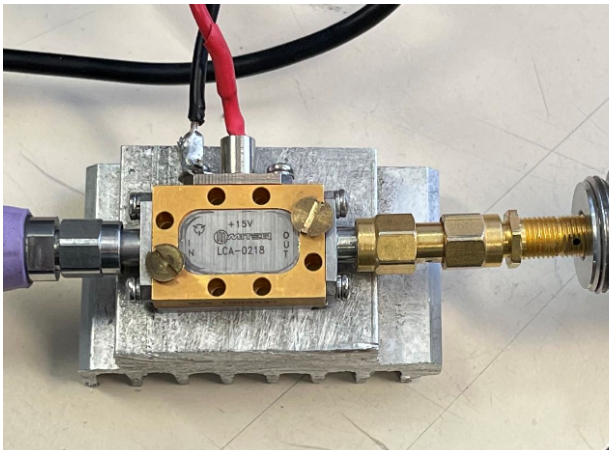

Figure 5.36: Low noise amplifier (LNA)

Table 5.13: General parameters of the LNA

Block	**Specifications**
Part Number	LCA-0218
Type	Power Amplifier, Low Noise Amplifier
Frequency	2 to 18 GHz
Gain	25 dB
Noise Figure	4.5 dB
Supply Voltage	15 V
Current Consumption	200 mA

sured with the VNA is 12001 points. The duration is 120 seconds, hence the sampling frequency is 99.65 Hz. Figure 5.38 shows The amplitude and the phase-shift of the complex transmission coefficient S_{21} at the operating frequency 10 GHz and source power 0 dBm. The distance between the person under test and the antenna aperture is varied (50 cm, 1 m and 2 m).

Figure 5.39 shows the third order of the cyclic moment and cyclic cumulant of the complex coefficient of transmission S_{21} reflected signal in the case of adding a LNA after the received antenna.

Comparing the measurement results with and without the LNA, it is observed that the level of the amplitude and the phase-shift of the complex coefficient of transmission S_{21} is increased without increasing the variation of the latter. Indeed, the LNA amplifies the reflected signal which is composed of the used signal and the noise.

For the second experiment, a simplified model of the driver's cabin is consid-

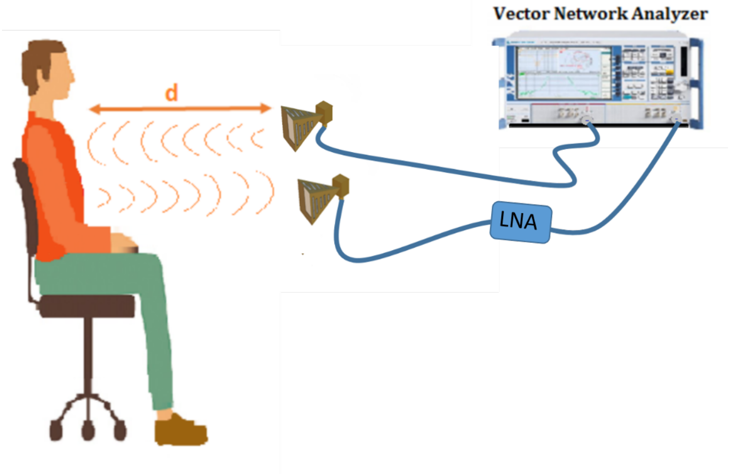

Figure 5.37: Measurement system with a LNA at the reception

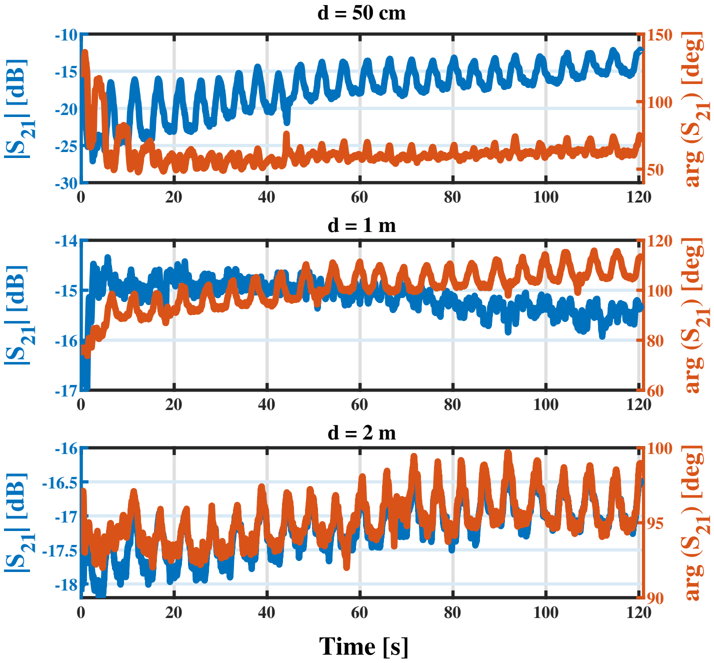

Figure 5.38: Variation of the transmission coefficient S_{21} with LNA at the reception for three distance 50 cm, 1 m and 2 m

ered. In particular, a metallic plate is first added behind the person under test as showing in the Figure 5.40. Then, two other metallic plates are added to form a three-sided close environment. The choice of metallic materials is justified by the idea to operate in the worst conditions.

Measurements are carried out during 120 seconds simultaneously with the reference system of MySignal. The transmitted wave (F= 10 GHz and P= 0 dBm) is directed toward the person's chest situated at two different distance,

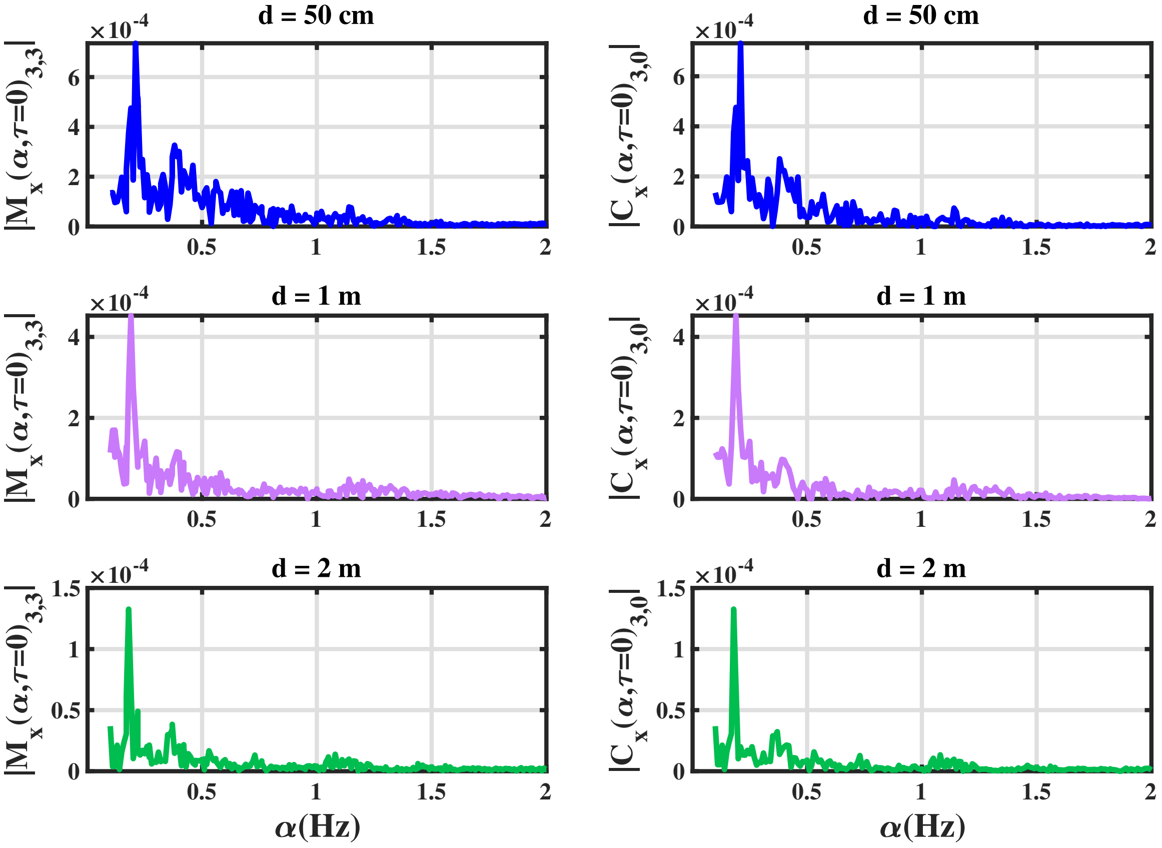

(a) (b)

Figure 5.39: Cyclic moment and cyclic cumulant of the third-order of cyclostationary signal S_{21} in the case of adding LNA at the reception

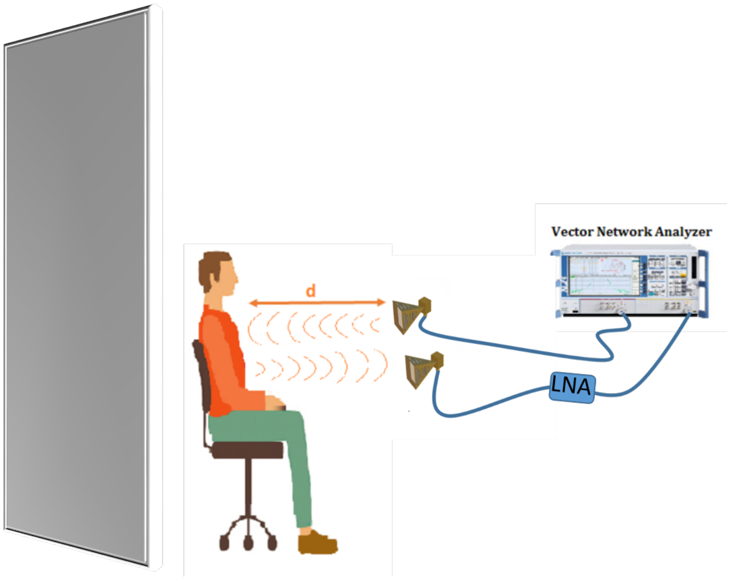

Figure 5.40: Measurement system with a metal plate behind the person

50 cm and 1 m from the horn antennas. The IFBW is set to 100 Hz, and the number of samples to 12001 samples.

The Figure 5.41 shows the amplitude and the phase-shift of the complex transmission coefficient reflected for both scenarios.

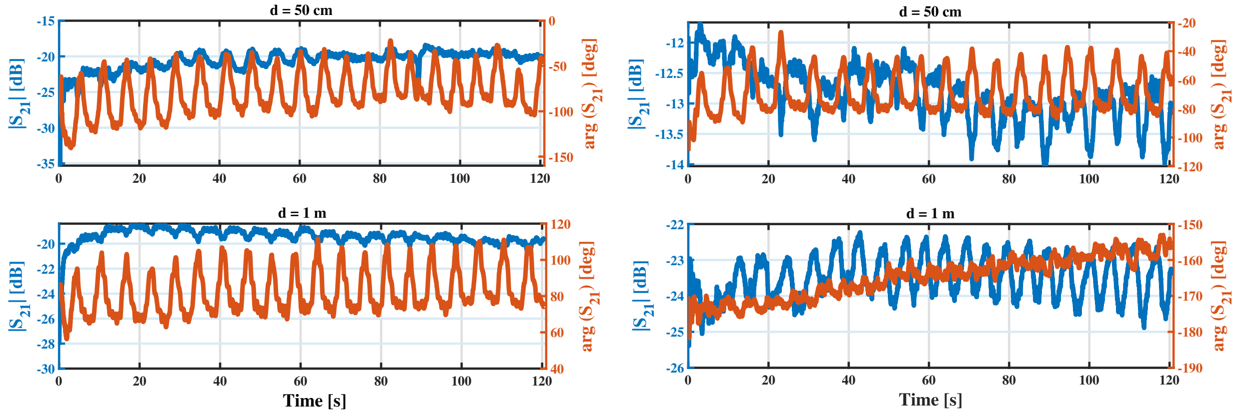

(a) (b)

Figure 5.41: Amplitude and phase-shift variation of the reflected signal S_{21} in the two cases: (**a**) First scenario with metal plate behind the person (**b**) second scenario with three-sided piece of metal

The breathing and heart rates extracted from the third-order cyclic cumulant of the reflected signal are compared to those extracted from the reference system Mysignal. Table 5.14 presents heartbeat and respiration rates extracted from Mysignal and the cyclostationary algorithm, as well as the relative error for each case and each scenario.

Table 5.14: Comparison between the detection of RR and HR resulting from the cyclostationarity algorithm and the reference system for both scenarios at 10 GHz

		MySignals		Cyclostationarity		Relative Error (%)	
		RR (Hz)	HR (Hz)	RR (Hz)	HR (Hz)	RR (Hz)	HR (Hz)
First scenario	d= 50 cm	0.2	1.08	0.197	1.060	1.52	1.85
	d= 1 m	0.18	1.07	0.174	1.06	3.44	0.93
Second Scenario	d= 50 cm	0.18	1.03	0.178	1	1.12	0.8
	d= 1 m	0.19	1.1	0.193	1.08	1.55	1.8

We observe that for the first case of a single metal plate behind the person, there is more variation on the phase-shift than on the amplitude of the

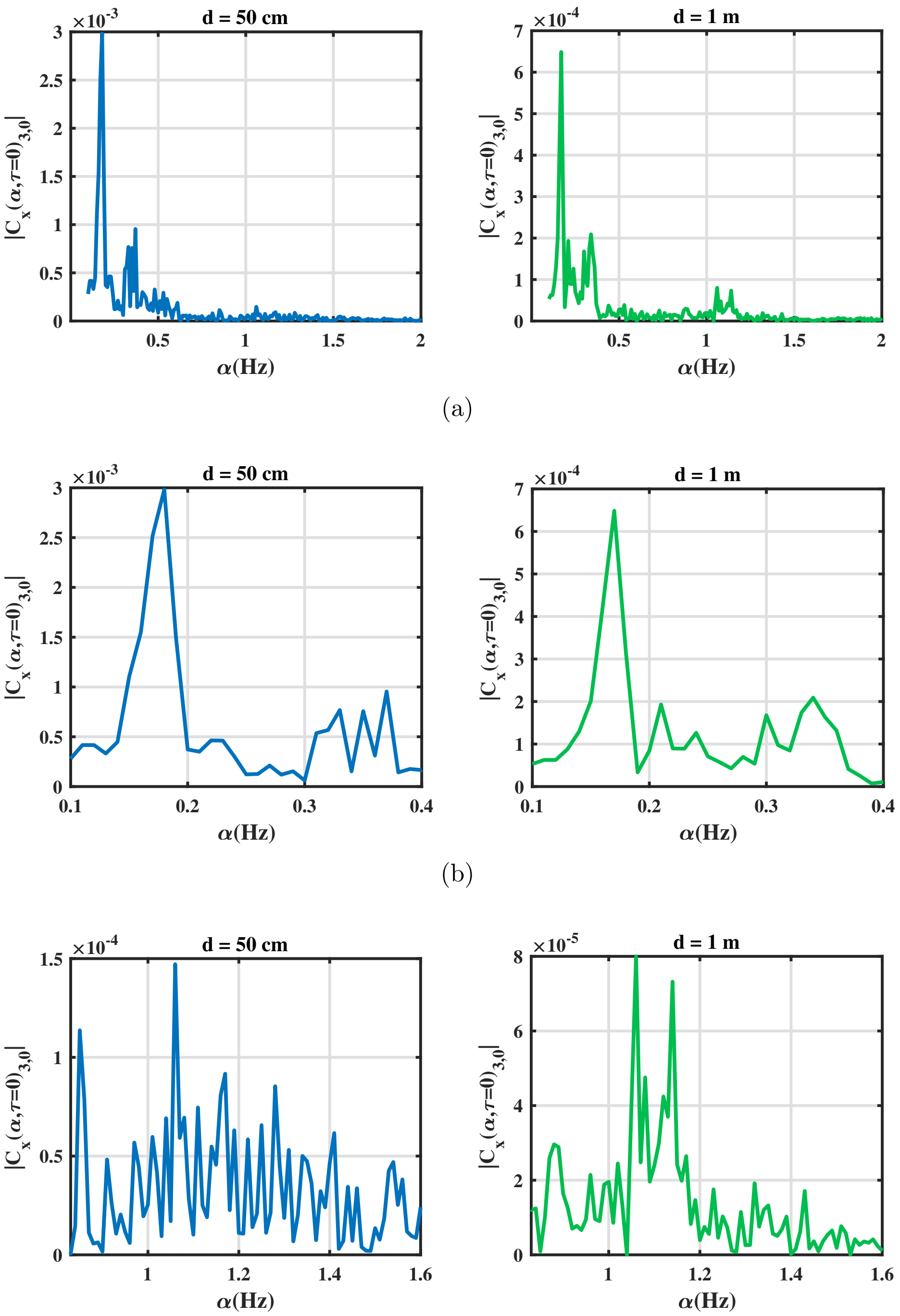

(a)

(b)

(c)

Figure 5.42: (**a**) Cyclic cumulant of the third-order of cyclostationary signal S_{21} for the distance 50 cm and 1 m in the case with 1 plaque, and a zoom in the interval corresponds (**b**) to breathing and (**c**) heart rate at 10 GHz

reflected signal from the chest's person. Unlike the second case with three-sided piece of metal plate, there is more variation on the amplitude than the phase-shift of the transmission coefficient S_{21}. Which may be due to multi-path. Indeed, with the metal plate, we have almost total reflections which is added to the interest signal. For the both cases, the relative error are the

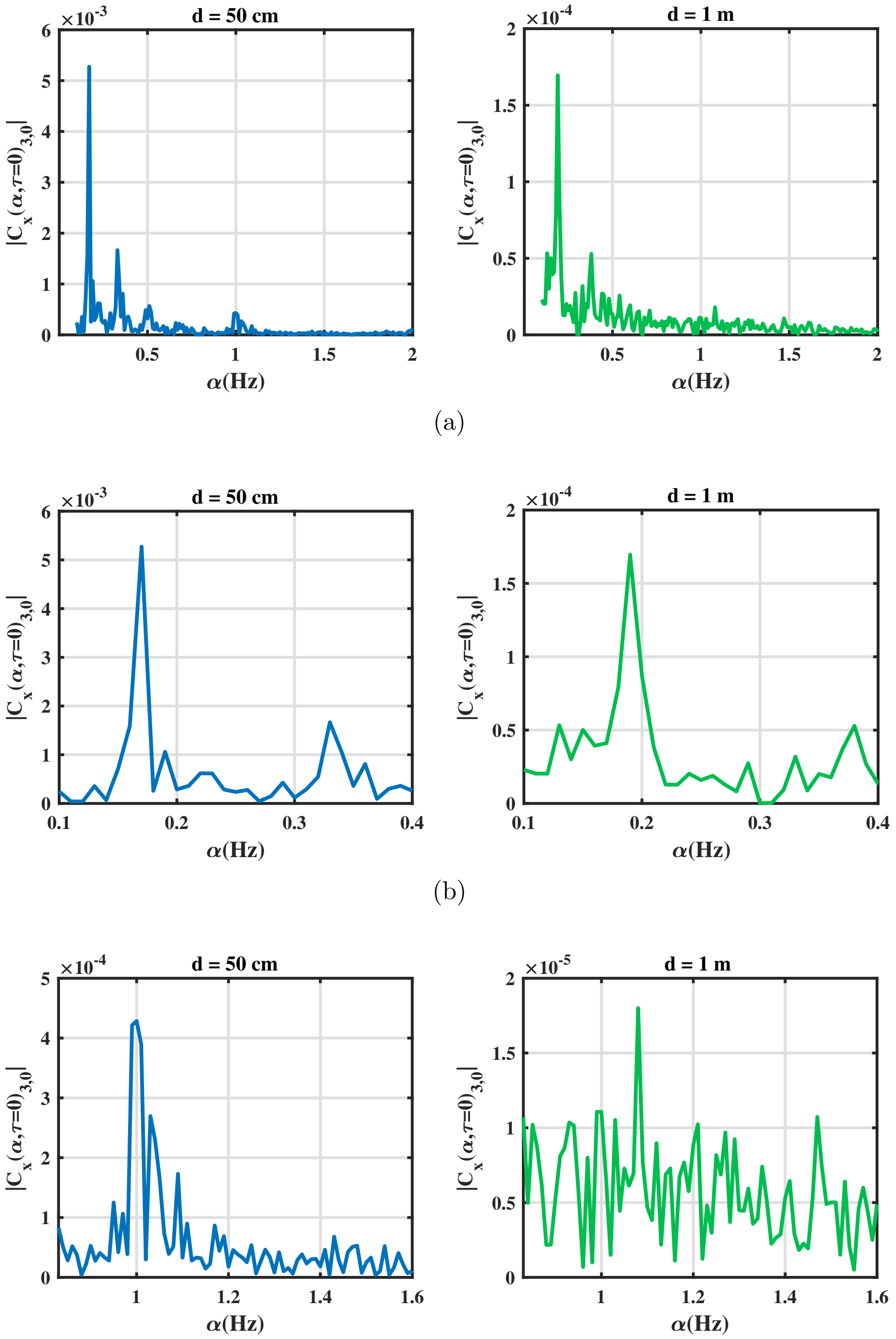

(a)

(b)

(c)

Figure 5.43: (**a**) Cyclic cumulant of the third-order of cyclostationary signal S_{21} for distance 50 cm and 1 m in the case with 3 plaques, and a zoom in the interval corresponds (**b**) to breathing and (**c**) heart rate at 10 GHz

same and is of the order of 5%.

5.5 Conclusion

The main aim of this chapter, was to determine the best parameters including frequency, power, distance, IFBW,etc. which lead to best accuracy for monitoring vital signs. The advantage of the VNA to vary several parameters easily, makes its the good choice for measurements. The use of Vector Network Analyzer (VNA) as a CW radar and to perform this study was presented.

In this chapter the capability of monitoring heart and breathing rate detecting from the movements of chest's person is studied and validated. A detailed description of the experimental setup and the algorithm approach applied to the transmission coefficient reflected from the person was analysed. For the purpose of having a general parametric study for the detection of vital signs, two studies have been proposed: a first parametric study concerning the parameters of the measurement environment (Polarization of the horn antenna, measurement in different environment anechoic room and the laboratory, the effect of distance between the antenna and the chest's person using different scenarios of the subject back or front side with breathing and holding breath). while the second part of the parametric study concerns the internal parameters of the vector network analyzer (Intermediate frequency bandwidth (IFBW), the input power, the operating frequency and the number of samples).

For the signal processing part, different order of the proposed algorithm based on the cyclostationary approach was applied to the results to detect the heartbeat and the breathing frequencies. The first, second and the third order cyclostationary properties of the radar signal with hidden periodicities and random motions are analyzed. The cyclic temporal moment and the cyclic temporal cumulant theory of each order was applied to the result of the experiments. Experimental results show that the third-order cyclostationary approach has better estimation accuracy for detecting the vital signs from the received radar signal under low SNR, strong clutter noise and random motion interference. For the quantitative measurement campaign, the results of the cyclostationary approach was compared to a reference commercial devices of Libelium MySignal using the two sensors Airflow and ECG. The results were very similar.

The investigation of these several parameters conducted to verify the accuracy of extraction of breathing and heartbeat of a person using the VNA, and its accuracy and working across a variety of different scenarios. All these experiments give a recommendations and an idea of the ideal design considerations for a practical device.

Other objectives included finding out the best parameters (frequency, number of samples, the position of antennas, power etc.), so that a prototype considering those parameters and recommendations can be designed in the future.

Conclusions and Perspectives

Conclusion

Vital signs are key indicators in assessing an individual's health. Conventional methods rely on direct contact with the person under test's skin and can therefore cause discomfort and reduce autonomy. A state of the art of different techniques for measuring vital signs including the microwaves method based on the radar was presented. The principle of several type of radar for measuring the movement of a person under test's chest was explained. Then, a brief background on radar was presented along with to the art and science of non-Contact cardiopulmonary monitoring with different type of radar.

Different type of radar was reported in this PhD, each of these type has it own advantages and disadvantages depending in the performance and accuracy of the architectures. The choice of the measurement system was presented. This choice based on the vector analyzer network (VNA) due to its simplicity of manufacture and therefore its allowing the access and controlling different parameters. For the purpose, a general parametric study for the detection of breathing and heartbeat has been done, considering two studies: a first parametric study concerning the parameters of the measurement environment, while the second part of the parametric study concerns the internal parameters of the system. Regarding these studies, the optimum parameters ware proposed.

The modulated reflected radar signal in the presence of high noise and body motion interference is non-stationary with hidden periodicities, and so conventional frequency analysis methods are not suitable to extract the hidden information. This leads to use a nonlinear transformation based on cyclic statistics which is the cyclostationary approach. The signal processing techniques used to analyze the collected data of different parameters based on the cyclostationary approach. Suppression of the non-cyclic components, attenuation of the random body motion interference, detection of the signal without any demodulation or filtering methods are the most advantages of this technique. These properties enhance the estimation accuracy of the heart and respiration rate when the detected subject lies in the complex environment with high noise and strong clutter. The theory, simulation and experiment results proved by using the first, second and the third order of the cyclic temporal moment and cyclic temporal cumulant. The second and the third-order cyclostationary approach proposed has better detection accuracy compared to the contact method (reference system), under complex circumstance with strong clutter, which makes it a promising method to be used with CW radar to analyze the vital signs.

The results obtained by the cyclostationary approach associated to the VNA are very encouraging and very similar to the results obtained by contact measuring devices. This method is very tough in the face of noise. The tests are carried out in a controlled environment (anechoic chamber) and in the uncontrolled room. Tests in real conditions with movement of the target are satisfied, due to improvement of the detection performance taking into account the propagation environment (noise, change of distance, frequency, input power and different scenarios,etc).

Future work

Despite the promising results presented in this work for the non-contact measurement of respiratory and cardiac frequencies, the approach followed to carry out our study either at the level of the RF system or signal processing part, as well as the different choices made open up various perspectives for additional works. Future work is needed to improve the techniques developed and realise more tests in real environments. Some potential solutions are presented below:

- **Short term**
    - To enrich the experimental part, we can consider a study taking into account the presence of several people in the same environment, which can caused extra noise in the acquired signals from other people or unwanted motion from the tested person or multi-path phenomena: studying the power of separation of the vital signs of different people. The prototype should be validated in larger population (according to their age, weight, sex,etc) to determine whether

  feasibility across such a wide population is achieved or not. Indeed, there may be some difference between the signals from the movement of the rib cage as shown in the work [96].

  - Taking into account other types of noise and canal effects propagation, which may interfere with the signal from the rib cage (impulsive noise, multi-path, etc.) in order to model the cabin environment of the train. Then, take measurements in a real environment (driving simulator and in a train cabin).

  - The proposed algorithm proposed in this work is suitable, but an extend and general algorithm for the detection can be performed. It is about the Time-warped (TW) almost-cyclostationary (ACS) process which is useful to describe signals with hidden imperfect periodicities [66]. A comparative study of this technique and our cyclostationarity technique can be accomplished.

- **Long term**
  - Based on the best configuration and parameters obtained from the parametric studies in this work, the obvious future work involves creation of prototypes for the radar monitoring by the implementation of the algorithm developed of the second and the third order of cyclostationarity on SDR system using NI-USRP cards.

  - The LINKing sEnsing & Driving (LINKED) project in progress, will allow us to perform measurements with industrial sensors to enhance our database, which will subsequently make it possible to use the contribution of artificial intelligence techniques for extraction and classification of vital signs.

5.6 Appendix

5.6.1 Appendix A: Influence of distance on cyclostationary detection

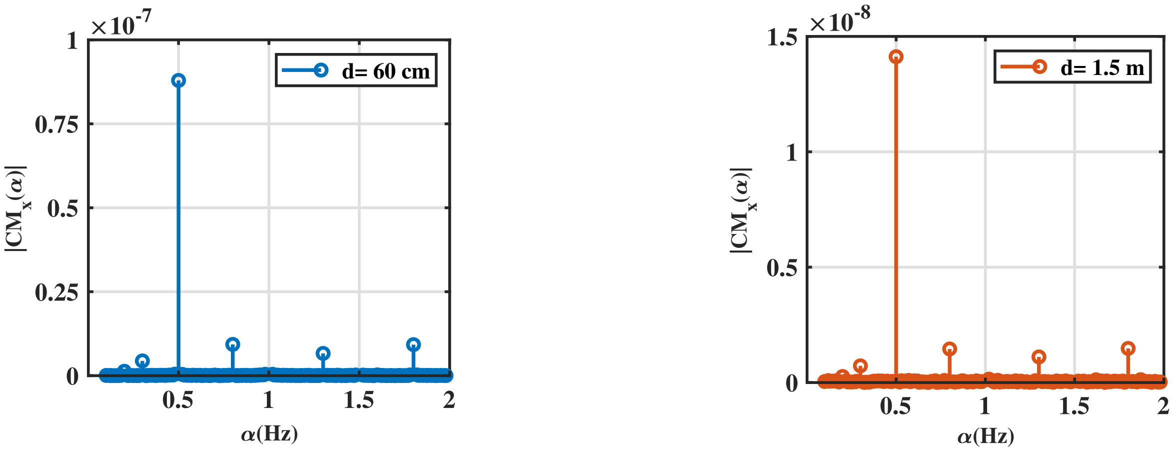

(a) (b)

Figure 5.44: The cyclic mean $|CM_x(\alpha)|$ of the reflected signal for the distance 60 cm and 1.5 m

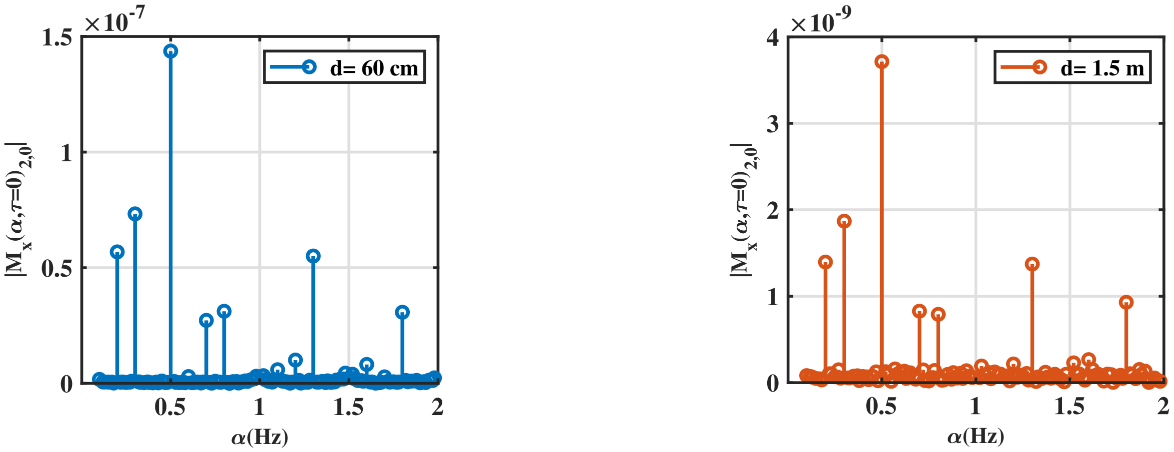

(a) (b)

Figure 5.45: The second-order cyclic temporal moment $|M_x(\alpha, \tau = 0)_{2,0}|$ of the reflected signal for the distance 60 cm and 1.5 m

5.6.2 Appendix B: Influence of the frequency system on Cyclostationary Detection

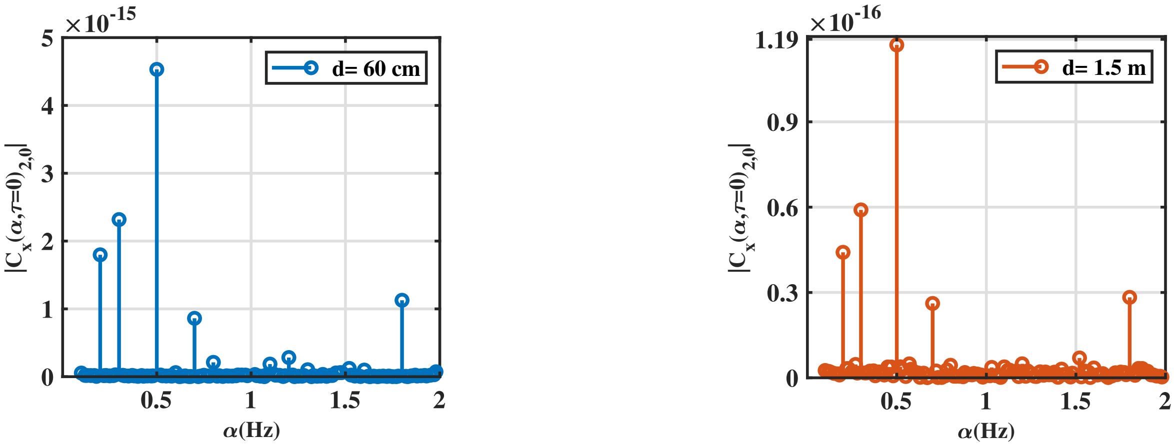

(a) (b)

Figure 5.46: The second-order cyclic temporal cumulant $|C_x(\alpha, \tau = 0)_{2,0}|$ of the reflected signal for the distance 60 cm and 1.5 m n

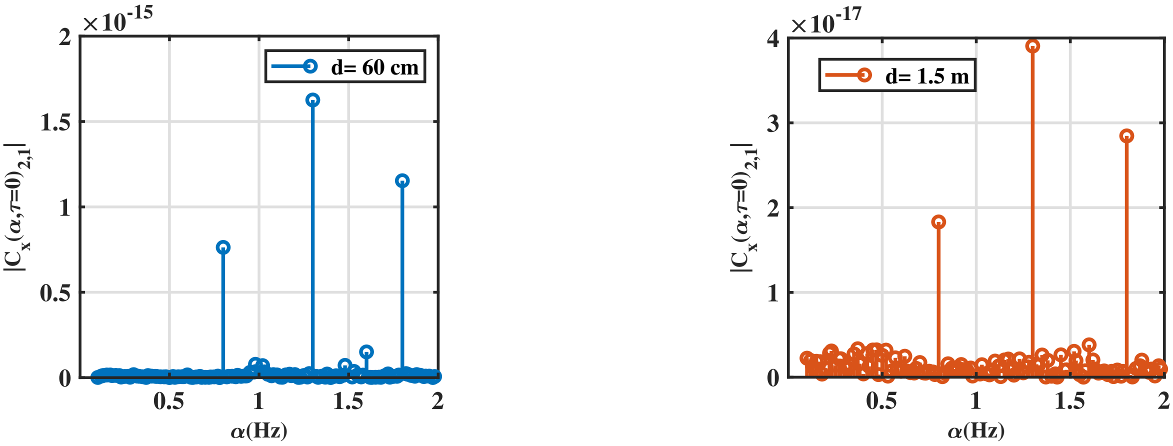

(a) (b)

Figure 5.47: The second-order cyclic cumulant $|C_x(\alpha, \tau = 0)_{2,1}|$ of the reflected signal for the distance 60 cm and 1.5 m

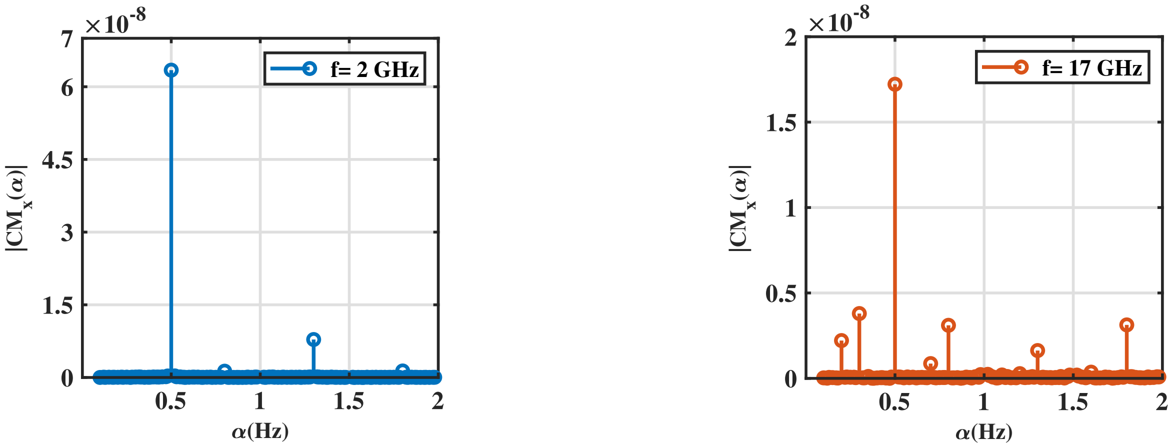

(a) (b)

Figure 5.48: The cyclic mean $|CM_x(\alpha)|$ of the reflected signal for the frequency system 2 GHz and 17 GHz

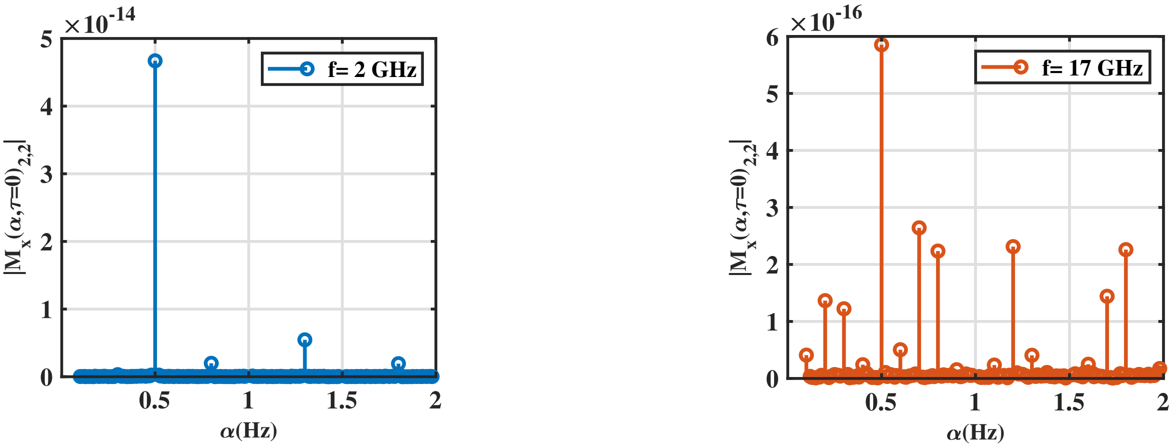

(a) (b)

Figure 5.49: The second-order cyclic temporal moment $|M_x(\alpha, \tau = 0)_{2,2}|$ of the reflected signal for the frequency system 2 GHz and 17 GHz

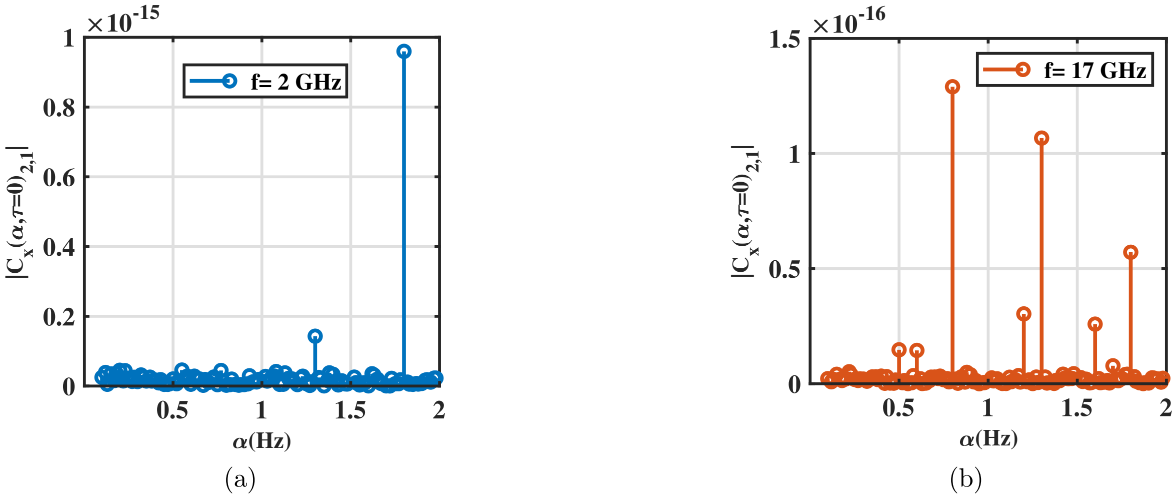

Figure 5.50: The second-order cyclic temporal cumulant $|C_x(\alpha,\tau=0)_{2,1}|$ of the reflected signal for the frequency system 2 GHz and 17 GHz

Bibliography

[1] URL: `https://aidal.fr/google-fit-suit-desormais-les-battements-et-les-respirations-directement-a-partir-des-smartphones-sur-les-pixels/`. (accessed: 29.06.2021).

[2] Vincent Aarts et al. "Performance of an accelerometer-based pulse presence detection approach compared to a reference sensor". In: *2017 IEEE 14th International Conference on Wearable and Implantable Body Sensor Networks (BSN)*. IEEE. 2017, pp. 165–168.

[3] Daniel E Becker. "Fundamentals of electrocardiography interpretation". In: *Anesthesia progress* 53.2 (2006), pp. 53–64.

[4] WR Bennett. "Statistics of regenerative digital transmission". In: *Bell System Technical Journal* 37.6 (1958), pp. 1501–1542.

[5] J Boyle, T Wark, and M Karunanithi. "Wireless personal monitoring of patient movement and vital signs". In: *Proceedings-Conference on Computational Intelligence in Medicine and Healthcare (CIMED 2005)*. 2005, pp. 141–146.

[6] Kun-Mu Chen et al. "Microwave life-detection systems for searching human subjects under earthquake rubble or behind barrier". In: *IEEE transactions on biomedical engineering* 47.1 (2000), pp. 105–114.

[7] Lydia Chioukh. "Système médical intégré de radar pour la surveillance de précision des battements cardiaques et du statut respiratoire". PhD thesis. École Polytechnique de Montréal, 2009.

[8] Lydia Chioukh et al. "Concurrent cardiopulmonary detection using 12/24 GHz harmonic multiport interferometer radar architecture". In: *IET Microwaves, Antennas & Propagation* 13.13 (2019), pp. 2396–2404.

[9] Lydia Chioukh et al. "Monitoring vital signs using remote harmonic radar concept". In: *2011 41st European Microwave Conference*. IEEE. 2011, pp. 1269–1272.

[10] Lydia Chioukh et al. "Multi-frequency radar systems for monitoring vital signs". In: *2010 Asia-Pacific Microwave Conference*. IEEE. 2010, pp. 1669–1672.

[11] Inoh Choi et al. "Robust Cardiac Rate Estimation of an Individual". In: *IEEE Sensors Journal* (2021).

[12] Charilaos Chourpiliadis and Abhishek Bhardwaj. "Physiology, Respiratory Rate". In: (2019).

[13] H Chuang, Y Chen, and K Chen. "Microprocessor-controlled automatic clutter-cancellation circuits for microwave systems to sense physiological movements remotely through the rubble". In: *7th IEEE Conference on Instrumentation and Measurement Technology*. IEEE. 1990, pp. 177–181.

[14] Huey-Ru Chuang, YF Chen, and Kun-Mu Chen. “Automatic clutter-canceler for microwave life-detection systems”. In: *IEEE Transactions on Instrumentation and Measurement* 40.4 (1991), pp. 747–750.

[15] Huey-Ru Chuang et al. “60-GHz millimeter-wave life detection system (MLDS) for noncontact human vital-signal monitoring”. In: *IEEE Sensors Journal* 12.3 (2011), pp. 602–609.

[16] Amod V Dandawate and Georgios B Giannakis. “Statistical tests for presence of cyclostationarity”. In: *IEEE Transactions on Signal Processing* 42.9 (1994), pp. 2355–2369.

[17] *Double Ridge Guide Horn Antenna SAS-571.* URL: `https://www.ahsystems.com/catalog/SAS-571.php`. (accessed: 27.05.2020).

[18] Amy Diane Droitcour. *Non-contact measurement of heart and respiration rates with a single-chip microwave doppler radar.* Stanford University, 2006.

[19] Amy D Droitcour et al. “0.25/spl mu/m CMOS and BiCMOS single-chip direct-conversion Doppler radars for remote sensing of vital signs”. In: *2002 IEEE International Solid-State Circuits Conference. Digest of Technical Papers (Cat. No. 02CH37315).* Vol. 1. IEEE. 2002, pp. 348–349.

[20] Amy D Droitcour et al. “Range correlation and I/Q performance benefits in single-chip silicon Doppler radars for noncontact cardiopulmonary monitoring”. In: *IEEE Transactions on Microwave Theory and Techniques* 52.3 (2004), pp. 838–848.

[21] Amy Droitcour et al. “A microwave radio for Doppler radar sensing of vital signs”. In: *2001 IEEE MTT-S International Microwave Sympsoium Digest (Cat. No. 01CH37157).* Vol. 1. IEEE. 2001, pp. 175–178.

[22] Glenn F Engen. “The six-port reflectometer: An alternative network analyzer”. In: *IEEE Transactions on microwave theory and techniques* 25.12 (1977), pp. 1075–1080.

[23] Guan-Wei Fang, Ching-Yao Huang, and Chin-Lung Yang. “Simultaneous detection of multi-target vital signs using EEMD algorithm based on FMCW radar”. In: *2019 IEEE MTT-S International Microwave Biomedical Conference (IMBioC).* Vol. 1. IEEE. 2019, pp. 1–4.

[24] *Federal Communications Commission FCC 13-39, P 1-202, Adopted: March 27, 2013 Released: March 29, 2013.* URL: `https://www.fcc.gov/engineering-technology/electromagnetic-compatibility-division/radio-frequency-safety/faq/rf-safety`. (accessed: 27.01.2020).

[25] Rich Fletcher and Jing Han. “Low-cost differential front-end for Doppler radar vital sign monitoring”. In: *2009 IEEE MTT-S International Microwave Symposium Digest.* IEEE. 2009, pp. 1325–1328.

[26] William A Gardner, Antonio Napolitano, and Luigi Paura. “Cyclostationarity: Half a century of research”. In: *Signal Processing* 86.4 (2006), pp. 639–697.

[27] EG Gladyshev. “Periodically and almost-periodically correlated random processes with a continuous time parameter”. In: *Theory of Probability & Its Applications* 8.2 (1963), pp. 173–177.

[28] DL Gorgas and J McGrath. “Vital signs and patient monitoring techniques”. In: *Clinical Procedures in Emergency Medicine: 4th ed.,(JR Roberts and JR Hedges, Eds.), Philadelphia,: Saunders* (2004), pp. 3–28.

[29] Carolina Gouveia et al. “Different antenna designs for non-contact vital signs measurement: A review”. In: *Electronics* 8.11 (2019), p. 1294.

[30] C Gu and C Li. “DC coupled CW radar sensor using fine-tuning adaptive feedback loop”. In: *Electronics letters* 48.6 (2012), pp. 344–345.

[31] Riadh WY Habash and P Eng. “Bioeffects and Therapeutic Applications of Electromagnetic Energy”. In: ().

[32] K Haddadi et al. “Contactless microwave technique based on a spread-loss model for dielectric materials characterization”. In: *IEEE Microwave and Wireless Components Letters* 19.1 (2008), pp. 33–35.

[33] Javier Hernandez, Daniel J McDuff, and Rosalind W Picard. “Biophone: Physiology monitoring from peripheral smartphone motions”. In: *2015 37th Annual International Conference of the IEEE Engineering in Medicine and Biology Society (EMBC)*. IEEE. 2015, pp. 7180–7183.

[34] Anders Høst-Madsen et al. “Signal processing methods for Doppler radar heart rate monitoring”. In: *Signal processing techniques for knowledge extraction and information fusion*. Springer, 2008, pp. 121–140.

[35] Wei Hu et al. “Noncontact accurate measurement of cardiopulmonary activity using a compact quadrature Doppler radar sensor”. In: *IEEE Transactions on Biomedical Engineering* 61.3 (2013), pp. 725–735.

[36] Xikun Hu and Tian Jin. “Short-range vital signs sensing based on EEMD and CWT using IR-UWB radar”. In: *Sensors* 16.12 (2016), p. 2025.

[37] Byung-Jun Jang et al. “Wireless bio-radar sensor for heartbeat and respiration detection”. In: *Progress In Electromagnetics Research C* 5 (2008), pp. 149–168.

[38] Somayeh Kazemi, Ayaz Ghorbani, and Hamidreza Amindavar. “Cyclostationary modelling of amplitude and frequency modulated signals in heart and respiration monitoring Doppler radar systems”. In: *IET Radar, Sonar & Navigation* 9.2 (2015), pp. 116–124.

[39] Somayeh Kazemi et al. “Cyclostationary Approach for Heart and Respiration Rates Monitoring with Body Movement Cancellation Using Radar Doppler System”. In: *arXiv preprint arXiv:1310.2293* (2013).

[40] Farah Q AL-Khalidi et al. “Respiration rate monitoring methods: A review”. In: *Pediatric pulmonology* 46.6 (2011), pp. 523–529.

[41] Faheem Khan and Sung Ho Cho. “A detailed algorithm for vital sign monitoring of a stationary/non-stationary human through IR-UWB radar”. In: *Sensors* 17.2 (2017), p. 290.

[42] John E Kiriazi, Olga Boric-Lubecke, and Victor M Lubecke. “Dual-frequency technique for assessment of cardiopulmonary effective RCS and displacement”. In: *IEEE Sensors Journal* 12.3 (2011), pp. 574–582.

[43] Alexander Koelpin et al. “Six-port based interferometry for precise radar and sensing applications”. In: *Sensors* 16.10 (2016), p. 1556.

[44] Alexander Koelpin et al. “The six-port in modern society”. In: *IEEE Microwave Magazine* 11.7 (2010), pp. 35–43.

[45] Hyunjae Lee et al. “A Novel Vital-Sign sensing algorithm for multiple subjects based on 24-GHz FMCW doppler radar”. In: *Remote Sensing* 11.10 (2019), p. 1237.

[46] Changzhi Li and Jenshan Lin. “Complex signal demodulation and random body movement cancellation techniques for non-contact vital sign detection”. In: *2008 IEEE MTT-S International Microwave Symposium Digest*. IEEE. 2008, pp. 567–570.

[47] Changzhi Li and Jenshan Lin. “Random body movement cancellation in Doppler radar vital sign detection”. In: *IEEE Transactions on Microwave Theory and Techniques* 56.12 (2008), pp. 3143–3152.

[48] Changzhi Li, Yanming Xiao, and Jenshan Lin. “Experiment and spectral analysis of a low-power Ka-band heartbeat detector measuring from four sides of a human body”. In: *IEEE Transactions on Microwave Theory and Techniques* 54.12 (2006), pp. 4464–4471.

[49] Changzhi Li et al. “A review on recent advances in Doppler radar sensors for noncontact healthcare monitoring”. In: *IEEE Transactions on microwave theory and techniques* 61.5 (2013), pp. 2046–2060.

[50] Changzhi Li et al. “Radar remote monitoring of vital signs”. In: *IEEE Microwave Magazine* 10.1 (2009), pp. 47–56.

[51] Jing Li et al. “Advanced signal processing for vital sign extraction with applications in UWB radar detection of trapped victims in complex environments”. In: *IEEE journal of selected topics in applied earth observations and remote sensing* 7.3 (2013), pp. 783–791.

[52] Meiyu Li and Jenshan Lin. “Wavelet-transform-based data-length-variation technique for fast heart rate detection using 5.8-GHz CW Doppler radar”. In: *IEEE Transactions on Microwave Theory and Techniques* 66.1 (2017), pp. 568–576.

[53] James C Lin. “Noninvasive microwave measurement of respiration”. In: *Proceedings of the IEEE* 63.10 (1975), pp. 1530–1530.

[54] James C Lin et al. “Microwave apexcardiography”. In: *IEEE Transactions on Microwave Theory and Techniques* 27.6 (1979), pp. 618–620.

[55] Bram Lohman et al. “A digital signal processor for Doppler radar sensing of vital signs”. In: *IEEE Engineering in Medicine and Biology Magazine* 21.5 (2002), pp. 161–164.

[56] Alexandra Sofia Dias Lopes. “Bio-Radar Applications for Remote Vital Signs Monitoring”. PhD thesis. 2021.

[57] Victor Lubecke, Olga Boric-Lubecke, and Eric Beck. “A compact low-cost add-on module for Doppler radar sensing of vital signs using a wireless communications terminal”. In: *2002 IEEE MTT-S International Microwave Symposium Digest (Cat. No. 02CH37278)*. Vol. 3. IEEE. 2002, pp. 1767–1770.

[58] Jaakko Malmivuo, Robert Plonsey, et al. “Principles and applications of bioelectric and biomagnetic fields”. In: *chapter* 15 (1995), p. 12.

[59] Wansuree Massagram et al. "Assessment of heart rate variability and respiratory sinus arrhythmia via Doppler radar". In: *IEEE Transactions on microwave theory and techniques* 57.10 (2009), pp. 2542–2549.

[60] T Matsui et al. "A novel apparatus for non-contact measurement of heart rate variability: a system to prevent secondary exposure of medical personnel to toxic materials under biochemical hazard conditions, in monitoring sepsis or in predicting multiple organ dysfunction syndrome". In: *Biomedicine & pharmacotherapy* 59 (2005), S188–S191.

[61] Steven McGee. *Evidence-based physical diagnosis e-book*. Elsevier Health Sciences, 2016.

[62] Fabian Michler et al. "A clinically evaluated interferometric continuous-wave radar system for the contactless measurement of human vital parameters". In: *Sensors* 19.11 (2019), p. 2492.

[63] Jorge J Moré. "The Levenberg-Marquardt algorithm: implementation and theory". In: *Numerical analysis*. Springer, 1978, pp. 105–116.

[64] *MySignals SW eHealth and Medical IoT Development Platform Technical Guide; P 1-304; Document version: v4.6 - 05/2019 © Libelium Comunicaciones Distribuidas S.L.)* URL: `https://www.the-iot-marketplace.com/mysignals-sw-ehealth-medical-biometric-complete-kit-ble`. (accessed: 27.01.2020).

[65] Antonio Napolitano. "Cyclic statistic estimators with uncertain cycle frequencies". In: *IEEE Transactions on Information Theory* 63.1 (2016), pp. 649–675.

[66] Antonio Napolitano. "Time-warped almost-cyclostationary signals: Characterization and statistical function measurements". In: *IEEE Transactions on Signal Processing* 65.20 (2017), pp. 5526–5541.

[67] R Joe Noble, J Stanley Hillis, and Donald A Rothbaum. "Electrocardiography". In: *Clinical methods: The history, physical, and laboratory examinations* (1990).

[68] International Commission on Non-Ionizing Radiation Protection et al. "ICNIRP statement on the "Guidelines for limiting exposure to time-varying electric, magnetic, and electromagnetic fields (up to 300 GHz)"". In: *Health physics* 97.3 (2009), pp. 257–258.

[69] Dany Obeid et al. "Multitunable microwave system for touchless heartbeat detection and heart rate variability extraction". In: *Microwave and optical technology letters* 52.1 (2010), pp. 192–198.

[70] Dany Obeid et al. "Noncontact heartbeat detection at 2.4, 5.8, and 60 GHz: A comparative study". In: *Microwave and Optical Technology Letters* 51.3 (2009), pp. 666–669.

[71] DG Osmond. "Functional anatomy of the chest wall". In: *The thorax* (1995), pp. 427–429.

[72] Gerald Ossberger et al. "Non-invasive respiratory movement detection and monitoring of hidden humans using ultra wideband pulse radar". In: *2004 International Workshop on Ultra Wideband Systems Joint with Conference on Ultra Wideband Systems and Technologies. Joint UWBST & IWUWBS 2004 (IEEE Cat. No. 04EX812)*. IEEE. 2004, pp. 395–399.

[73] Jianli Pan. "Medical applications of ultra-wideband (uwb)". In: *survey paper* (2007).

[74] W Pan et al. "Null point elimination using RF phase shifter in continuous-wave Doppler radar system". In: *Electronics letters* 47.21 (2011), pp. 1196–1198.

[75] Elena Pancera. "Medical applications of the Ultra Wideband technology". In: *2010 Loughborough Antennas & Propagation Conference*. IEEE. 2010, pp. 52–56.

[76] Byung-Kwon Park, Olga Boric-Lubecke, and Victor M Lubecke. "Arctangent demodulation with DC offset compensation in quadrature Doppler radar receiver systems". In: *IEEE transactions on Microwave theory and techniques* 55.5 (2007), pp. 1073–1079.

[77] Zhengyu Peng et al. "A portable FMCW interferometry radar with programmable low-IF architecture for localization, ISAR imaging, and vital sign tracking". In: *IEEE Transactions On Microwave Theory And Techniques* 65.4 (2016), pp. 1334–1344.

[78] Douglas T Petkie, Carla Benton, and Erik Bryan. "Millimeter wave radar for remote measurement of vital signs". In: *2009 IEEE Radar Conference*. IEEE. 2009, pp. 1–3.

[79] Vladimir L Petrović et al. "High-accuracy real-time monitoring of heart rate variability using 24 GHz continuous-wave Doppler radar". In: *IEEE Access* 7 (2019), pp. 74721–74733.

[80] Lingyun Ren et al. "Comparison study of noncontact vital signs detection using a Doppler stepped-frequency continuous-wave radar and camera-based imaging photoplethysmography". In: *IEEE Transactions on Microwave Theory and Techniques* 65.9 (2017), pp. 3519–3529.

[81] Natalia V Rivera et al. "Multi-target estimation of heart and respiration rates using ultra wideband sensors". In: *2006 14th European Signal Processing Conference*. IEEE. 2006, pp. 1–6.

[82] Christof Rohner. "Antenna basics". In: *Rohde & Schwarz* (1999).

[83] Sandy Rolfe. "The importance of respiratory rate monitoring". In: *British Journal of Nursing* 28.8 (2019), pp. 504–508.

[84] I Rolfes and B Schiek. "Calibration methods for microwave free space measurements". In: *Advances in Radio Science* 2.A. 1 (2005), pp. 19–25.

[85] Doug Rytting. "Network analyzer error models and calibration methods". In: *White Paper, September* (1998).

[86] Sarah Samad. "Contactless detection of cardiopulmonary activity for a person in different scenarios". PhD thesis. Rennes, INSA, 2017.

[87] C Saritha, V Sukanya, and Y Narasimha Murthy. "ECG signal analysis using wavelet transforms". In: *Bulg. J. Phys* 35.1 (2008), pp. 68–77.

[88] Joseph Seals. *Electromagnetic vital signs monitor*. Engineering Experiment Station, Georgia Institute of Technology, 1984.

[89] Fatima Sekak et al. "Cyclostationary-Based Vital Signs Detection Using Microwave Radar at 2.5 GHz". In: *Sensors* 20.12 (2020), p. 3396.

[90] Aditya Singh et al. "Considerations for integration of a physiological radar monitoring system with gold standard clinical sleep monitoring systems". In: *2013 35th Annual International Conference of the IEEE Engineering in Medicine and Biology Society (EMBC)*. IEEE. 2013, pp. 2120–2123.

[91] Merill I Skolnik. “An analysis of bistatic radar”. In: *IRE Transactions on Aerospace and Navigational Electronics* 1 (1961), pp. 19–27.

[92] Steven W Smith et al. “The scientist and engineer’s guide to digital signal processing”. In: (1997).

[93] David H Spodick. “Normal sinus heart rate: sinus tachycardia and sinus bradycardia redefined”. In: *The American heart journal* 124.4 (1992), pp. 1119–1121.

[94] Wei-Chih Su et al. “Stepped-frequency continuous-wave radar with self-injection-locking technology for monitoring multiple human vital signs”. In: *IEEE Transactions on Microwave Theory and Techniques* 67.12 (2019), pp. 5396–5405.

[95] Toshiyo Tamura et al. “Wearable photoplethysmographic sensors—past and present”. In: *Electronics* 3.2 (2014), pp. 282–302.

[96] Abubakar Tariq. “Vital signs monitoring using doppler radar and on-body antennas”. PhD thesis. University of Birmingham, 2013.

[97] Çağatay Tokgöz and Nicholas C Soldner. “Radar Hardware for Indoor Monitoring”. In: *Radar for Indoor Monitoring* (2017), pp. 21–38.

[98] *valeurs limites d’exposition du public aux champs électromagnétiques*. URL: `https://www.legifrance.gouv.fr/loda/id/JORFTEXT000000226401/`. (accessed: 27.09.2021).

[99] Gabor Vinci et al. “Microwave interferometer radar-based vital sign detection for driver monitoring syst”. In: *2015 IEEE MTT-S International Conference on Microwaves for Intelligent Mobility (ICMIM)*. IEEE. 2015, pp. 1–4.

[100] Gabor Vinci et al. “Six-port radar sensor for remote respiration rate and heartbeat vital-sign monitoring”. In: *IEEE Transactions on Microwave Theory and Techniques* 61.5 (2013), pp. 2093–2100.

[101] Toan Khanh Vodai et al. “Enhancement of Remote Vital Sign Monitoring Detection Accuracy Using Multiple-Input Multiple-Output 77 GHz FMCW Radar”. In: *IEEE Journal of Electromagnetics, RF and Microwaves in Medicine and Biology* (2021).

[102] Jing Wang et al. “An improved indoor localization solution using a hybrid UWB-Doppler system with Kalman filter”. In: *2018 IEEE Radio and Wireless Symposium (RWS)*. IEEE. 2018, pp. 181–183.

[103] Fu-Kang Wang et al. “An injection-locked detector for concurrent spectrum and vital sign sensing”. In: *2010 IEEE MTT-S International Microwave Symposium*. IEEE. 2010, pp. 768–771.

[104] Yazhou Wang, Quanhua Liu, and Aly E Fathy. “CW and pulse–Doppler radar processing based on FPGA for human sensing applications”. In: *IEEE Transactions on Geoscience and Remote Sensing* 51.5 (2012), pp. 3097–3107.

[105] *What should my heart rate be?* URL: `https://www.medicalnewstoday.com/articles/235710#target-training-heart-rates`. (accessed: 27.05.2020).

[106] K Worden, I Iakovidis, and EJ Cross. “New results for the ADF statistic in non-stationary signal analysis with a view towards structural health monitoring”. In: *Mechanical Systems and Signal Processing* 146 (2021), p. 106979.

[107] Y Xiao and J Lin. “Boric-Lubecke, and VM Lubecke,“Frequency tuning technique for remote detection of heartbeat and respiration using lowpower double-sideband transmission in Ka-band,”” in: *IEEE Trans. Microw. Theory Tech* 54.5 (2006), pp. 2023–2032.

[108] Xiang-Lin Yang et al. “The history, hotspots, and trends of electrocardiogram”. In: *Journal of geriatric cardiology: JGC* 12.4 (2015), p. 448.

[109] Zhibin Yu, Duo Zhao, and Zhiqiang Zhang. “Doppler radar vital signs detection method based on higher order cyclostationary”. In: *Sensors* 18.1 (2018), p. 47.

[110] Mari Zakrzewski. “Methods for doppler radar monitoring of physiological signals”. In: (2015).

[111] Mari Zakrzewski, Harri Raittinen, and Jukka Vanhala. “Comparison of center estimation algorithms for heart and respiration monitoring with microwave Doppler radar”. In: *IEEE Sensors Journal* 12.3 (2011), pp. 627–634.

[112] Kawtar Zerhouni et al. “Blind parameters estimation for Universal Filtered Multicarrier: a cyclostationarity approach”. In: *2019 Wireless Telecommunications Symposium (WTS)*. IEEE. 2019, pp. 1–6.

[113] Ting Zhang et al. “Estimation of human body vital signs based on 60 GHz Doppler radar using a bound-constrained optimization algorithm”. In: *Sensors* 18.7 (2018), p. 2254.

[114] Xi Zhao et al. “DC coupled Doppler radar physiological monitor”. In: *2011 Annual International Conference of the IEEE Engineering in Medicine and Biology Society*. IEEE. 2011, pp. 1909–1912.

[115] Nannan Zhu et al. “Vital signs monitoring using an IR-UWB radar based on edge computing”. In: (2021).